Effet thermoélectrique dans les métaux liquides sous champ magnétique.

Imants Kaldre

To cite this version:

Imants Kaldre. Effet thermoélectrique dans les métaux liquides sous champ magnétique.. Autre. Université de Grenoble, 2013. Français. NNT : 2013GRENI020 . tel-00961702

HAL Id: tel-00961702
https://theses.hal.science/tel-00961702

Submitted on 20 Mar 2014

UNIVERSITÉ DE GRENOBLE

LATVIJAS UNIVERSITATE
ANNO 1919
UNIVERSITY OF LATVIA

THÈSE

Pour obtenir le grade de

DOCTEUR DE L'UNIVERSITÉ DE GRENOBLE

Spécialité : **INGENIERIE-MATERIAUX MECANIQUE ENERGETIQUE ENVIRONNEMENT PROCEDES PRODUCTION**

Arrêté ministériel : 7 août 2006

Et de

DOCTEUR DE L'UNIVERSITÉ DE LETTONIE

Spécialité : **MECANIQUE DES FLUIDES**

Présentée par

« Imants / KALDRE »

Thèse dirigée par **« Yves / FAUTRELLE »** et

codirigée par **« Leonids / BULIGINS »**

préparée au sein du **Laboratoire SIMAP-EPM**

dans **l'École Doctorale IMEP2 MECANIQUE DES FLUIDES, PROCEDES, ENERGETIQUE**

et de

INSTITUTE DE PHYSIQUE UNIVERSITE DE LETTONIE

Effet thermoélectrique dans les métaux liquides sous champ magnétique

Thèse soutenue publiquement le **« 12.07.2013 »**, devant le jury composé de :

M. Hamda BEN HADID
Professeur UCB Lyon 1 (President)
M. Yves FAUTRELLE
Professeur INPG (Membre)
M. Leonids BULIGINS
Associé Professeur, University of Latvia (Membre)
M. Maris KNITE
Professeur, Riga Technical University (Rapporteur)
M. Bernard BILLIA
Investigateur Principal IM2NP (Rapporteur)

Acknowledgements

I would like to express my gratitude to my supervisors Prof. Yves Fautrelle from Grenoble Institute of Technology EPM-SIMAP laboratory and Assoc. Prof. Leonids Buligins from University of Latvia. I also wish to thank to my consultants Dr. Jacqueline Etay from Grenoble Institute of Technology EPM-SIMAP laboratory and Andris Bojarevics from Institute of Physics University of Latvia who took active part during the work of my thesis and helped with advises and fruitful discussions. I would like to thank to my colleagues in Institute of Physics University of Latvia and EPM-SIMAP laboratory in Grenoble for their support and exchange of ideas, and help in realization of experimental work and numerical simulations during my PhD studies.

This work was financially supported by ministry of education of France and European Social Fund project "Support for doctoral studies in University of Latvia".

This dissertation is prepared in EPM-SMAP laboratory in Grenoble and in Magnetohydrodynamics technology laboratory in Institute of Physics University of Latvia.

This work has been supported by the European Social Fund within the project «Support for Doctoral Studies at University of Latvia » and by French ministry scholarship.

Imants Kaldre
Grenoble 24.04.2013

Thermoelectric current and magnetic field interaction influence on the structure of binary metallic alloys

Abstract

If magnetic field is applied during directional solidification, liquid phase convection can be induced by means of thermoelectromagnetic effect. Temperature gradient at the solidification front can cause thermoelectric current circulation, which then interacts with field and creates convection (Thermoelectromagnetic convection-TEMC). Solute and energy transport conditions are affected by this convection, thus it influences dendrite spacing and macrosegregation of the alloys.

In this work magnetic field influence on the directional solidification of metallic alloys is studied. Experimental work of directional solidification of Sn-Pb and Sn-Bi alloys is done. Alloys are directionally solidified in Bridgman setup without or with applied magnetic field. Influence on the structure by magnetic field and applied electric current (AC and DC) is studied in this work. Analytical and experimental results are compared and interpreted.

Bridgman solidification under rotating transverse magnetic field is studied as well, field rotation value is chosen to be slow enough that electromagnetic stirring does not fully suppress effects of TEMC. At low pulling velocity and low field rotation velocity spiral shaped component macrosegregation can be achieved.

Keywords:

- Thermoelectromagnetic convection
- Directional solidification
- Sn-Pb alloys
- Slowly rotating magnetic field
- Absolute thermoelectric power measurements

Résumé

Lorsqu'un champ magnétique est appliqué au cours de la solidification directionnelle, une convection dans la phase liquide peut être induite par l'effet thermoélectrique. En effet la présence d'un gradient de température le long du front de solidification peut provoquer la circulation du courant thermoélectrique, qui interagit avec le champ magnétique appliqué pour créer un écoulement (convection thermo électromagnétique-TEMC). Les conditions de transport de soluté et de l'énergie sont affectées par cette convection, donc il y a influence sur l'espacement des dendrites et la macro-ségrégation des composants de l'alliage.

Dans ce travail, l'influence du champ magnétique sur la solidification directionnelle d'alliages métalliques est étudiée. Des travaux expérimentaux de la solidification directionnelle de Sn-Pb et Sn-Bi alliages sont réalisés. La solidification directionnelle dans la configuration Bridgman est effectuée avec ou sans champ magnétique appliqué. L'influence, sur la solidification, du champ magnétique et d'un courant électrique (AC et DC) appliqués est étudiée. Les mouvements du liquide provoquent de fortes macro-ségrégations ainsi qu'un modification des espacements interdendritiques. Les résultats expérimentaux sont interprétés à la lumière d'une modélisation heuristique.

Le cas d'un champ magnétique tournant a été aussi étudié. Ainsi, la valeur de la rotation du champ est choisie pour ralentir assez brassage électromagnétique sans pour autant supprimer les effets de TEMC. À faible vitesse de tirage et faible vitesse de rotation faible champ une macro-ségrégation en forme de spirale a pu être obtenue.

Mots clés:

- Convection thermoélectromagnétique
- Solidification directionnelle
- Sn-Pb alliage
- Champ magnétique tournant
- Puissance thermoélectrique absolu

Contents

List of figures

List of symbols and abbreviations

Symbols

Greek

Symbol	**Name**	**Unit**
μ	Dynamic viscosity Thomson coefficient Relative magnetic permeability	Pa·s V/K H/m
α	Thermal diffusivity	m^2/s
β	Thermal expansion	1/K
β_C	Volumetric expansion	1/%wt
Γ	Gibbs-Thomson coefficient	m·K
γ	Surface tension	N/m
δ	Boundary layer thickness Skin depth	m m
θ	Temperature gradient	K/m
ϑ	Wetting angle	
κ	Mean curvature	1/m
λ	Thermal conductivity	W/m·K
ν	Kinematic viscosity	m^2/s
Π	Peltier coefficient	V
ρ	Density	kg/m^3
σ	Electric conductivity Interface energy	s/m J/m^2
τ	Contact resistance	Ω/m^2
φ	Electric potential Concentration	V %wt
ω	Oscillation frequency	Hz
Ω	Angular velocity	rad/s

Latin

Symbol	Name	Unit
B	Magnetic field intensity	T
C_0	Nominal concentration	Wt.%
C_l	Liquid phase concentration	Wt.%
C_p	Heat capacity	J/K·kg
C_s	Solid phase concentration	Wt.%
D	Mass diffusivity	m^2/s
d	Characteristic size	m
E	Electric field intensity Fermi energy	V/m J, eV
f	Frequency	Hz
f_k	Form factor	
I	Nucleation rate	
k	Partition coefficient	
m	Liquidus slope	%/K
n	Nuclei density	m^{-3}
P	Differential thermopower	V/K
Q	Peltier heat density	W/m^2
q	Joule heat density Charge density	W/m^3 C/m^3
R	Resistance	Ω
S	Absolute thermoelectric power	V/K
T	Temperature	K
u	Flow velocity	m/s
V	Voltage	V
v	Growth velocity	m/s
w	Effective convection velocity	m/s
Z_{TE}	Thermoelectric figure of merit	A/W
ΔG	Activation energy	J/m^3
Δg	Differential Gibbs energy	J/m^3

Constants

Symbol	Name	Value
g	Fee fall acceleration	9.8 m/s^2
K_B	Boltzmann constant	$1.38\cdot10^{-23}$ J/K
e	Electron charge	$1.6\cdot10^{-19}$ C
μ_0	Magnetic permeability	$4\pi\cdot10^{-7}$ H/m

Acronyms

Acronym	Name
2D	Two Dimensional
3D	Three Dimensional
AC	Alternating Current
ATP	Absolute Thermoelectric power
CET	Columnar to Equiaxed Transition
DC	Direct Current
ESRF	European Synchrotron Radiation Facility
SEM	Scanning Electron Microscope
TE	Thermoelectric
TEMC	Thermoelectromagnetic Convection
TMF	Transverse Magnetic field
MHD	Magnetohydrodynamics

Dimensionless numbers

Symbol	Name	Expression
Bu	Buoyant number	$Bu = \frac{\rho\beta g d}{c\sigma PB}$
c	Current loop shape coefficient	$\frac{1}{1+\frac{\sigma_l d_l}{\sigma_s d_s}}$

Gr	Grasshof number	$Gr = \frac{\beta \Delta T g d^3 \rho^2}{\mu^2}$
Ha	Hartmann number	$Ha = Bd\sqrt{\frac{\sigma}{\mu}}$
N	Interaction parameter	$N = \frac{c\sigma B^2 d}{\rho u}$
Pe	Peclet number (thermal)	$Pe = \frac{T_{Cond}}{T_{Conv}} = \frac{du\rho C_p}{\lambda}$
Pe_C	Peclet number (diffusion)	$Pe_C = \frac{du}{D}$
Pr	Prandtl number	$\Pr = \frac{\nu}{\alpha}$
Ra	Rayleigh number	$Ra = \frac{g\beta\rho\Delta T d^3}{\mu\alpha}$
Re	Reynolds number	$\mathrm{Re} = \frac{\rho u d}{\mu}$
Rm	Magnetic Reynolds number	$Rm = \mu\sigma u d$
Sc	Schmidt number	$Sc = \frac{\nu}{D}$
Sh	Strouhal number	$Sh = \frac{\omega d}{u}$
Ta	Taylor number	$Ta = \frac{\sigma\pi f B^2 R^4 \rho}{\mu^2}$
Te	TE force/viscous force	$Te = \frac{\sigma P \Delta T B d^2}{\rho \nu^2}$
Z	Figure of merit	$Z = \frac{\sigma \cdot S^2}{\lambda}$
Z_{TE}	Thermoelectric figure of merit [A/W]	$Z_{TE} = \frac{\sigma \cdot \Delta S}{\lambda}$

Effet thermoélectrique dans les métaux liquides sous champ magnétique

1. Introduction

1.1. Structure de la thèse

Au cours de ce travail l'influence du champ magnétique appliqué sur la structure d'alliages métalliques est étudiée expérimentalement et théoriquement. L'attention principale du travail est focalisée sur l'étude de la convection thermo-électromagnétique (TEMC) dans la phase liquide lors de la solidification. La convection phase liquide a une influence sur la taille des grains ainsi que les macroségrégation et microségrégation. Ce phénomène est étudié expérimentalement et théoriquement au cours de nos travaux. Les résultats numériques et théoriques sont utilisés pour interpréter les résultats expérimentaux. Pour une meilleure compréhension des processus physiques lors de la solidification, des simulations numériques du courant thermoélectrique et de la TEMC sont développées (logiciels FLUENT et COMSOL). La thèse est divisée en chapitres suivants:

1. **Introduction.** La nouveauté scientifique du travail et la contribution d'auteur sont expliqués. Les hypothèses principales et les résultats sont brièvement résumés.
2. **Principes physiques.** La discipline physique jouant un rôle lors de la solidification est introduite. Les processus microscopique et macroscopique lors de la solidification d'alliages métalliques sont expliqués.
3. **Mesures des propriétés thermoélectriques**. La disponibilité de propriétés thermoélectriques fiables et détaillées demeure fragmentaire. Dans ce chapitre un dispositif expérimental est conçu pour mesurer le pouvoir absolu thermoélectrique (ATP) des alliages à l'état solide et liquide. Les propriétés d'ATP sont mesurées en fonction de la température et de la composition de Sn-Pb. Ces données sont nécessaires pour l'analyse de la TEMC et son influence sur la structure dans les chapitres qui suivent.
4. **Analyse théorique et simulations numériques.** Une revue de la littérature sur les problèmes thermoélectriques et des travaux théoriques est donnée dans ce chapitre. L'analyse théorique de la convection thermo-électromagnétique est présentée dans ce chapitre. L'estimation de l'importance de TEMC dans divers cas est effectuée, et les paramètres optimaux pour 'atteindre l'efficacité maximale de la TEMC est estimée. Les résultats des simulations numériques de courant thermoélectrique et TEMC créés par différents types de champs magnétiques sont présentés.

5. **Solidification sous champ magnétique statique**. Une revue de la littérature sur les travaux expérimentaux précédents dans le domaine de la solidification sous champ magnétique statique est donnée dans ce chapitre. Dans ce domaine un important travail expérimental a été réalisé avec de nombreux alliages et différentes intensités de champ magnétique. Les résultats de solidification directionnelle de Sn-Pb et Sn-Bi alliages réalisés dans le cadre de cette thèse, sont donnés dans ce chapitre. Les alliages sont solidifiés directionnellement sous champ magnétique axial ou transversal (jusqu'a 0.5 T). Les vitesses de solidification utilisées sont de 0.5 à 20 mm/s. Les résultats obtenus lors de l'observation directe de la solidification directionnelle sous champ magnétique statique effectué dans Installation Européenne de Rayons Synchrotron (ESRF) sont présentés et expliqués dans ce chapitre.

6. **Combinaison de TEMC et courant électrique**. Dans ce chapitre, on analyse les effets créés par un champ magnétique appliqué et combiné avec interaction électromagnétique provoqué par un courant électrique appliqué travers l'interface lors de la solidification. Deux effets différents peut être comparés pour trouver les paramètres qui sont inconnus. L'hypothèse que ce type d'interaction électromagnétique provoque, a été explorée analytiquement et expérimentalement. Des courants électriques AC et DC électriques a été utilisées.

7. **Solidification sous champ magnétique tournant lentement**. Un champ magnétique transversale tournant autour du creuset lors de la solidification directionnelle a été appliqué. Nous avons étudié la dépendance entre la vitesse de rotation du champ magnétique et la structure de l'alliage obtenue. Si la rotation de champ est plus lente que la vitesse de TEMC, une macroségrégation hélicoïdale dans lingot peut être obtenue. Si la rotation du champ magnétique est plus rapide, aucune macroségrégation n'est réalisée, mais les effets de TEMC affectent la structure à l'échelle de la dendrite. Différents cas ont été analysés théoriquement et vérifiés expérimentalement dans ce chapitre. La comparaison entre l'estimation théorique et les résultats expérimentaux est donnée.

8. **Conclusions et travaux futurs**. Dans ce chapitre, les conclusions générales sont données. Les principales préoccupations et les points critiques constatés lors des travaux sont décrits. Les perspectives de recherche future et les expériences nécessaires sont décrites.

1.2. Hypothèses principales et objectifs des travaux

L'objectif principal de cette thèse est d'analyser et de vérifier l'influence du champ magnétique statique sur la solidification des alliages métalliques binaires. Les hypothèses suivantes sont évaluées et vérifiées expérimentalement et théoriquement au cours de travail:

- le champ magnétique lors de solidification directionnelle peut causer de la macroségrégation et les changements de l'espacement des dendrites.
- l champ magnétique transverse statique provoque une macroségrégation importante, qui est plus grandes aux faibles vitesses de solidification.
- un écoulement de phase liquide similaire à la TEMC près de l'interface de solidification peut être induit par interaction du champ magnétique et du courant électrique.
- l'application d'un champ magnétique tournant lentement (l'effet d'agitation étant du même ordre de grandeur que celui de la TEMC) provoque une TEMC variant dans le temps. En tant que résultat, la qualité de la structure peut être améliorée ou une macroségrégation hélicoïdale peut être réalisée

1.3. Contribution de l'auteur et la nouveauté scientifique

Un système expérimental est développé pour la mesure de l'ATP à l'état solide et liquide. Les mesures du pouvoir thermoélectrique absolu d'alliage Pb-Sn en fonction de la température et de la composition ont été réalisées.

Le système expérimental utilisé dans les expériences solidification décrites dans cette thèse a été conçu et construit spécialement dans le cadre de ce travail par l'auteur de la thèse. Un système d'aimant permanent est utilisé pour atteindre un champ magnétique jusqu'à 0.5 T. La direction du champ magnétique peut être modifiée selon la direction transversale ou axiale, et il peut également être mis en rotation par un moteur programmable autour du creuset. Cette solution simplifie l'expérience et permet la réalisation des expériences sur une période plus longue.

Dans le cadre de cette thèse, un travail expérimental est réalisé pour étudier l'influence sur la structure des alliages du champ magnétique appliqué ayant des directions et des amplitudes différentes. Les alliages à basse température (Sn-Pb et Sn-Bi) sont utilisés pour l'étude de l'influence du champ magnétique sur la structure des alliages binaires. Ces alliages ont été largement utilisés pour des expériences de solidification directionnelle sous des conditions de solidification différentes. Les expériences sont réalisées avec un champ magnétique statique transversal ou axial et tournant.

La solidification directionnelle sous champ magnétique statique axial et transversal a été réalisée. Les résultats montrent que le champ magnétique transversal a une grande influence sur la macroségrégation. La distribution du soluté le long de la section transversale de l'échantillon est mesurée par microscopie électronique. Cette méthode est plus précise que l'analyse des micrographies. Il est démontré que l'application d'un champ magnétique transversal (0.3-0.5 T) provoque une macroségrégation significative si la vitesse de solidification est lente (dessous 10 μm/s). L'évolution de l'espacement des dendrites en fonction de la vitesse de croissance et du champ magnétique appliqué a été mesurée et comparée à d'autres résultats expérimentaux et des modèles théoriques.

La solidification directionnelle sous champ magnétique tournant lentement est effectuée. La rotation du champ magnétique a été choisie pour être suffisamment lente pour que la convection électromagnétique induite par rotation du champ soit comparable à la convection thermo-électromagnétique. Dans ce cas, la direction de la convection thermo-électromagnétique est variable dans le temps et donc la structure de l'alliage est affectée de manière différente par rapport au cas avec champ statique. Si la vitesse de rotation du champ magnétique est choisie correctement, il est possible de combiner l'effet de la convection thermo-électromagnétique et celui de l'agitation de la phase liquide par champ magnétique tournant. Des résultats expérimentaux montrent que, avec cette méthode, il est possible d'atteindre une structure plus homogène et fine et de prévenir la ségrégation du soluté. Si la vitesse de fluide créée par la rotation du champ magnétique est plus lente que la TEMC, une macroségrégation tridimensionnelle et hélicoïdale peut être obtenue, ce qui est un résultat nouveau et intéressant. La vitesse TEMC peut être déduite de ces résultats en trouvant la vitesse de rotation de champ lorsque l'effet de TEMC est dépassé par une agitation électromagnétique.

L'action combinée de la convection thermo-électromagnétique, de l'interaction du champ magnétique appliqué et du courant électrique travers le front de solidification, a été étudiée. L'idée heuristique sur les similitudes entre la TEMC et convection électromagnétique a été analysée et validée expérimentalement et numériquement.

Dans le cadre de ce travail, des expériences de solidification d'alliage sous champ magnétique à l'ESRF (European Synchrotron Radiation Facility) à Grenoble a été effectuée. Des expériences de solidification de Sn-Pb, Al-Cu, Al-Si sous champ magnétique modéré de 0.08 T ont été faites en filmant le processus in situ par rayons X à haute énergie. Ces expériences donnent des résultats utiles quant à la nature de l'écoulement près du front de solidification dendritique, et sur la fragmentation des dendrites causée par la force de Lorentz. L'estimation expérimentale de la grandeur de la TEMC et son influence sur la direction de croissance des dendrites et la morphologie a été mise en évidence dans ces expériences.

2. La théorie

2.1. L'effet thermoélectrique

En général, tout gradient de quantité physique induit une densité de flux. Le gradient de température crée le flux du chaleur et le gradient de tension crée flux du courant. Mais le gradient du température peut aussi créer un flux du courant et le gradient du tension peut créer un flux de chaleur. Ces effets sont appelés effets thermoélectriques.

Le pouvoir thermoélectrique absolu (ATP) est la propriété intrinsèque de chaque métal ou un alliage métallique. Il dépend de la température et des contraintes internes, et dans le cas d'un alliage, de la composition. Pour les métaux l'ATP varie entre -30 µV/K et 30 µV/K. Dans la pratique, le pouvoir thermoélectrique différentiel *P* est utilisé plus souvent, caractérise une paire de matériaux.

$$P = S_A - S_B \tag{2.1}$$

La tension thermoélectrique peut être calculée en appliquant la seconde loi de Kirchhoff au circuit constitué de deux conducteurs.

$$V = \int_{T_1}^{T_2} (S_B(T) - S_A(T))dT \tag{2.2}$$

où T_1 et T_2 sont les températures froides et chaudes, et *V* est la tension créée par le thermocouple. Si le gradient de température est appliqué, un champ électrique est généré par effet thermoélectrique, qui dans certains cas peut causer une circulation du courant thermoélectrique. La relation décrivant le flux de courant électrique dans le milieu continu est la loi d'Ohm et est donnée par l'équation (2.3).

$$\frac{\vec{j}}{\sigma} = \vec{E} + \vec{u} \times \vec{B} - S\nabla T \tag{2.3}$$

En application de la loi d'Ohm l'opérateur rotationnel dans la loi d'Ohm et dans le milieu stationnaire, nous pouvons voir qu'un courant électrique ne peut émerger que si le gradient de température n'est pas parallèle au gradient de *S*. Ce critère ne peut pas être rencontré si *S* est fonction de la température seulement. Le courant thermoélectrique peut émerger si *S* est fonction de la composition aussi ou sur la frontière entre deux substances différentes, soit :

$$curl(\vec{j} / \sigma) = -grad(S) \times grad(T) \tag{2.4}$$

L'échauffement ou le refroidissement provoqué par la circulation du courant dans les milieu ou à travers l'interface sont appelés effets Peltier et Thomson. Ces effets sont expliqués par les énergies différentes des électrons dans les différents milieux.

2.2. Thermoélectrique magnétohydrodynamique

Le terme thermoélectrique magnétohydrodynamique a été introduit par J.A.Shercliff (J. Shercliff 1979). Il a développé l'idée que courant thermoélectrique en présence d'un champ magnétique peut provoquer un pompage de fluides conducteurs. Il a également présenté l'estimation d'ordre de grandeur de la vitesse TEMC, montrant que la vitesse qui peut être atteinte dans le lithium liquide sous gradients de température élevés, ce qui peut être atteint dans les réacteurs de fusion (*grad (T)* ≈ 10 K / mm, $B = 1$ T, $S_{Li} = 25$ µV/K), peut atteindre jusqu'à 25 cm/s. La TEMC est créée par la force de Lorentz causée par l'interaction entre la courant thermoélectrique et le champ magnétique.

$$\vec{F} = \vec{j} \times \vec{B} \tag{2.5}$$

Le courant thermoélectrique dans les milieux liquides peut être exprimé à partir de la loi d'Ohm (2.3). Le mouvement du liquide est décrit par l'équation de Navier-Stokes:

$$\rho\left(\frac{\partial \vec{u}}{\partial t} + \vec{u} \cdot \nabla \vec{u}\right) = -\nabla p + \eta \nabla^2 \vec{u} + \sigma\left(\vec{u} \times \vec{B} \times \vec{B} - S\nabla T \times \vec{B}\right) \tag{2.6}$$

Deux nouveaux termes dans les équations de Navier-Stokes sont introduits par le champ magnétique appliqué. Le terme $\sigma S\nabla T \times \vec{B}$ est le terme thermoélectrique qui crée la TEMC. Le terme $\sigma\vec{u} \times \vec{B} \times \vec{B}$ est la force de freinage magnétohydrodynamique qui est créé par le mouvement d'un fluide conducteur dans le champ magnétique. Cette force agit toujours opposé à la vitesse du fluide. La force thermoélectrique est proportionnelle au champ magnétique, mais la force MHD de freinage est proportionnelle au B^2. En moyen ou faible champ magnétique, la force thermoélectrique est dominante, mais comme B augmente, la force de freinage croît plus vite et dépasse enfin la force thermoélectrique. Cet effet est utilisé pour limiter la convection naturelle indésirable (L. Davoust, 1997). Il existe une valeur du champ magnétique quand la TEMC est maximum pour chaque alliage et paramètres expérimentaux.

2.3. La solidification d'alliages binaires

La solidification d'un alliage est un processus multiphysique très complexe où nombreux phénomènes physiques peuvent avoir lieu simultanément. Il y a beaucoup d’alliages utilisés dans la technologie aujourd'hui. Même pour un alliage binaire de nombreux aspects différents peuvent influencer la structure finale de l'alliage solidifié, comme la vitesse de refroidissement, la direction d'extraction de chaleur, le champ de gravité et l’écoulement de la phase liquide à proximité de l'interface de solidification (Phillips, 2004). Un classique diagramme de phase d'alliage binaire est donnée dans la Figure 2.1.

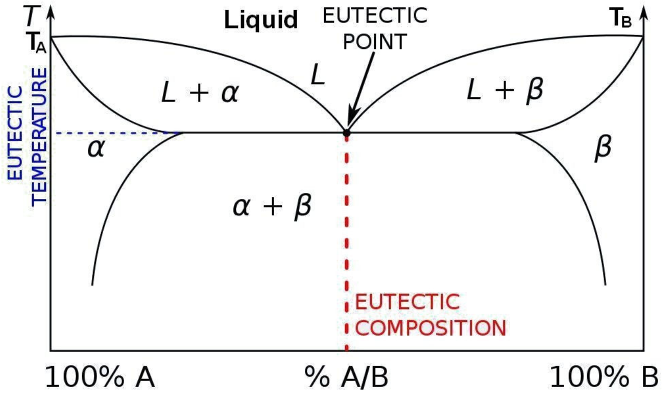

Figure 2.1: Diagramme de phases d'alliage à deux composants.

La structure en colonne se forme si la chaleur est extraite directionnellement, les colonnes se forment dans le sens de l’extraction de la chaleur. La structure equiaxe est obtenue lors de la solidification du liquide solidifié sans direction privilégiée. Plusieurs méthodes ont été développées pour contrôler la transition colonnaire-equiaxe (CET). En plus de la direction et du taux d'extraction de la chaleur, qui sont difficiles à contrôler dans le processus industriel, la transition entre ces deux structures est essentiellement déterminé par la convection de la phase liquide. Diverses méthodes ont été mises au point à contrôler ce flux et modifier la CET (Kurz, Bezencon and Gaumnn 2001), (Kurz and Fisher 1984)

Pendant la solidification dendritique, un changement de composition locale a lieu. La dendrite croissant ou noyau est susceptible d’attirer plus d'atomes constituant l’une que l'autre. Ceci est caractérisé par le coefficient de distribution k qui représente le rapport entre le concentration solide C_S et la phase liquide C_L sur l'interface solidification.

$$k = \frac{C_S}{C_L} \tag{2.7}$$

Ce rapport définit un gradient de concentration du soluté sur l'interface

$$\left(\frac{dC}{dx}\right) = -\frac{v}{D} C_l (1-k) \tag{2.8}$$

où D est le coefficient diffusion, v est la vitesse de solidification

2.4. La solidification directionnelle

La solidification directionnelle est un type particulier de solidification lorsque le front de solidification se déplace dans une direction en restant parallèle à lui-même. La solidification directionnelle est largement utilisée pour l'étude expérimentale dans les sciences de la solidification. La solidification directionnelle se fait habituellement dans la configuration Bridgman qui est également utilisée pour la croissance du silicone photovoltaique et électronique (renewable-energy-concepts, 2012). Cette méthode nous permet de connaître les paramètres essentiels du système à tout moment, les relations entre taille du grains et paramètres de solidification peuvent être validées expérimentalement.

Les dendrites apparaît parce que la température de solidification en chaque point dépend de divers facteurs et peut être exprimée comme équation (2.9).

$$T_i = T_0 - \frac{\Gamma}{L} T_0 \kappa - m_L (C_0 - C_i) - \frac{v}{\mu(\theta, \kappa)} \tag{2.9}$$

Où T_0 et C_0 sont la température de fusion et la concentration nominale, C_i est la concentration locale. Le second terme représente la surfusion supplémentaire crée par la courbure d'interface (κ-courbure moyenne, Γ la rigidité de surface). Le troisième terme représente la contribution au changement de température causé l'inhomogénéité de composition, et le quatrième terme tient compte des effets cinétiques du mouvement du front de solidification, $\mu(\theta, \kappa)$ est coefficient montrant la mobilité cinématique. La pointe de la dendrite croît plus vite à l'endroit plat au front de solidification en raison principalement de la contribution de terme de courbure.

Si les paramètres de solidification et les propriétés des alliages sont connus, il est possible de prévoir un espacement caractéristique principal des bras de dendrite lors de la solidification directionnelle (W. Kurz D. F., 1984). soit

$$\lambda = \frac{4.3(\Delta T_0 D \Gamma)^{0.25}}{k^{0.25} v^{0.25} \sqrt{\theta}} \tag{2.10}$$

où θ est le gradient de température, Γ est le coefficient de Gibbs-Thomson, ΔT_0 est l'intervalle de solidification.

2.5. Rôle de la convection lors de la solidification

Si la convection de la phase liquide est présente, la structure de solidification et de l'espacement peut être radicalement différent de celui prédit par l'équation (2.17) qui a été développé par l'analyse régime de solidification pleinement diffusif. En plus de la convection forcée il y a la convection naturelle (G. Müller, 1984) et la convection thermosolutale (W. Seifert, 1998) causées par l'expansion de liquide. L'importance de la convection naturelle est caractérisée par le nombre de Grashof (2.19) qui montre le rapport entre la flottabilité et les forces visqueuses.

$$Gr = \frac{\beta \Delta T g L^3 \rho^2}{\mu^2} \tag{2.11}$$

où L est la longueur caractéristique, ΔT est la différence de température sur cette longueur, β est coefficient de dilatation thermique, $\alpha = \lambda/\rho c_p$ est la diffusivité thermique, $Pr = \mu/\alpha\rho$ est le nombre de Prandtl. Convection thermosolutale peuvent être analysés de façon similaire.

Il existe plusieurs ouvrages sur la recherche de l'influence de la convection sur la structure de solidification (J. S. Wettlaufer, 1997), (J. Szekely, 1970). Ces travaux qualitativement accord que la présence de la convection lors de la solidification directionnelle réduit l'espacement des dendrites. Pour éliminer la convection complètement, les expériences sont fait en microgravité lors de vols paraboliques (M.D. Dupouy, 1989).

À l'interface de solidification la plupart des métaux et alliages métalliques présentent un saut de pouvoir thermoélectrique absolu. Le gradient de température est toujours présent au front de solidification. Ces conditions peuvent entrainer une circulation du courant thermoélectrique. En appliquant un champ magnétique externe, la force de Lorentz apparaît et convection forcée de la phase liquide prés du front de solidification peut être introduite (TEMC). Le gradient de température au front de solidification peut être très élevé donc même avec le champ magnétique modéré une convection assez fort peut être atteinte. La TEMC influence de la structure de l'alliage étudié est généralement lors de la solidification directionnelle d'un alliage appareil Bridgeman (P. Lehmann, 1998), (J.P. Garandet, 1999) ou similaire. Il est montré que la macrostructure et la microstructure peuvent être affectées par ce mécanisme (X. Li Z. R., 2012).

L'idée d'influencer la convection interdendritique par le champ magnétique lors de la solidification est relativement nouvelle et a été introduite par Moreau et Lehmann (P. Lehmann, 1998) dans l'années 90 du 20ieme siècle. Le transport d'énergie et de soluté du à cette convection peut alors affecter macroségrégation, structure cellulaire et morphologie dendritique. Ce type de convection et son influence sur la croissance, macroségrégation dendrite et morphologie interface sera analysé en plus détail dans les chapitres suivants de cette thèse.

3. Mesure des propriétés thermoélectriques

3.1. Introduction

En matériau monocristallin l'ATP est un tenseur (Marwaha, 1967). L'ATP est la propriété de transport d'électrons comme les conductivités électrique et thermique. Il peut être très dépendant des impuretés, des contraintes internes, et de la température. Pour ces raisons, il y a des difficultés pour mesurer avec précision cette propriété pour un alliage de composition certain. Il est important de connaître ces propriétés comme fonction de la température et de la composition dans le solide et le liquide pour une prédiction précise du phénomène thermoélectrique lors de la solidification. Dans ce chapitre les mesures d'ATP pour des alliages Sn-Pb et Sn-Bi est décrite et l'ATP est mesurée. Il existe des théories pour le calcul de l'ATP (Gasser, 2008), mais aucune d'elles n'est assez fiable.

Habituellement dans la littérature l'ATP est donnée pour les matériaux polycristallins tempérés. L'ATP pour divers métaux sont donnés par Shercliff (Shercliff, 1979). Un des plus grands recueils des propriétés thermoélectriques des métaux différents et certains alliages les plus populaires peut être trouvé dans le (Handbook of Physical quantities, 1991). L'ATP pour le plomb et l'étain à l'état solide et liquide a été mesurée par Cusack et Marwaha (N. Cusack, 1958), (A.S. Marwaha, 1965).

Dans notre cas, la quantité pour comparer l' alliage optimal pour des expériences de solidification sous champ magnétique modéré est le ratio de Z_{TE} (appelé facteur thermoélectrique de qualité) donne par équation (3.1). Z_{TE} a une dimension de [A/W] et il montre la capacité de matérielle pour générer du courant lorsque le flux de chaleur est appliquée.

$$Z_{TE} = \frac{\sigma \cdot \Delta S}{\lambda} \tag{3.1}$$

Li et K ont plus haut facteur thermoélectrique de qualité. Dans ce chapitre l'ATP de l'alliage Sn-Pb alliage sera mesurée en fonction de la température et de la composition afin de déduire la concentration optimale qui sera utilisée dans l'expérience de solidification. Le facteur thermoélectrique de qualité de Sn et Pb est environ 0.15 A/W qui est assez haut.

3.2. Installation expérimental pour les mesures d'ATP et procédure

Un système expérimental (Figure 3.1) a été conçu pour permettre la mesure de l'ATP en continu dans les états solides et liquides de la température ambiante jusqu'à 600 ^{0}C. Les alliages sont préparés en utilisant du plomb et de l'étain de haute pureté (99,99%). Les tubes en quartz d'un diamètre intérieur de 4 mm, épaisseur de paroi de 1 mm et une longueur de 120 mm sont remplis de ces alliages. Les tubes sont refroidis à la température ambiante, une paire d'électrodes de cuivre et constantan de 0,2 mm diamètre est soudée de chaque coté du tube. Une paire d'électrodes cuivre-constantan est choisie pour former un thermocouple de type T, pour lesquels les relations versa ITS90 de température et vice-tension sont connues avec une grande précision (National Institute of Standards, 2010).

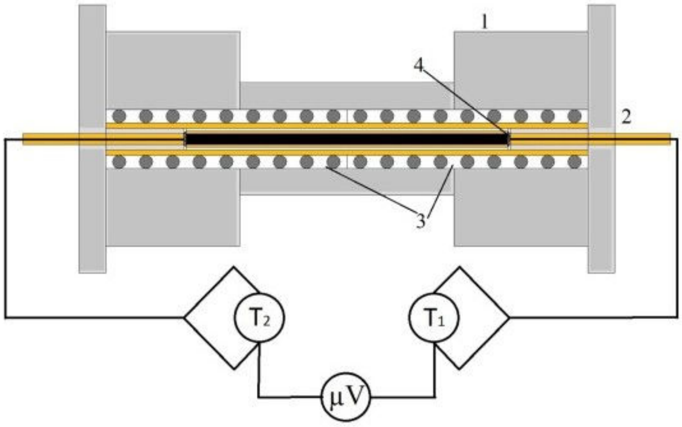

Figure 3.1: Installation pour la mesure d'ATP (1-isolant thermique, 2- tubes d'alumine à deux canaux avec des électrodes de cuivre et de constantan, 3 - radiateurs électriques Kanthal, 4- d'étanchéité céramique et de contacts d'électrode à l'extrémité du tube)

Le chauffage est effectué par deux appareils de chauffage électriques Kanthal, en permettant le contrôle de la différence de température entre les deux extrémités de l'échantillon. Le signal mesuré *V* est une somme de signaux générés par l'échantillon de métal V_0 et signal généré par deux électrodes en cuivre. En appliquant la deuxième loi de Kirchhoff au circuit composé d'électrodes en cuivre et d'échantillons de métal, on obtient:

$$V = \int_{T_0}^{T_2} S_{Cu}(T)dT + \int_{T_2}^{T_1} S(T)dT + \int_{T_1}^{T_0} S_{Cu}(T)dT \qquad (3.2)$$

où S_{Cu} et T_0 sont respectivement l'ATP du cuivre et la température de l'extrémité froide des thermocouples. Dans ce travail l'ATP du cuivre est prise égale à (Handbook of Physical quantities, 1991), (E.A. Brandes, 1992)

$$S_{Cu} = 1.684 + 0.00507 \cdot T \tag{3.3}$$

3.3. Résultats expérimentaux

Dans ce travail l'ATP de Sn et Pb purs sont mesurée. Les alliages à composition suivante ont été mesurés: Pb-20wt.%Sn, Pb-40wt.%Sn, Pb-60wt.%Sn and Pb-80wt.%Sn.

La précision des microvoltmètres utilisés dans la mesure de température est 2 μV, et l'exactitude des nanovoltmètres est de 100 nV. De là, nous pouvons calculer l'erreur totale d'ATP.

$$\Delta S = \frac{1}{(T_2 - T_1)^2} \sqrt{((V - \int_{T1}^{T2} S_{Cu} dT) \cdot \Delta T)^2 + (((T_2 - T_1))\Delta V)^2} \tag{3.4}$$

ΔT=0.1 K est la précision de mesure de température, ΔV=0.1 μV est la précision de mesure de tension. Ce calcul nous donne l'erreur d'ATP de 0.1 μV/K selon équation (3.4)

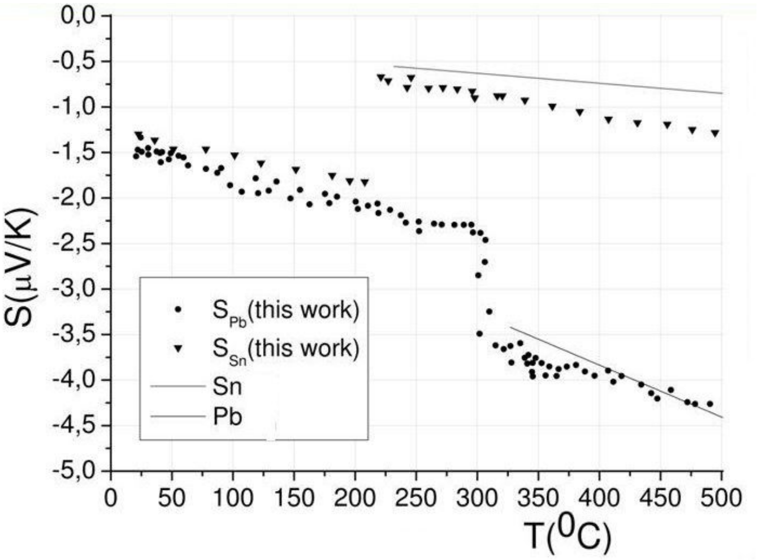

Figure 3.2: ATP de plomb et d'étain pur. Les résultats expérimentaux par rapport aux (N. Cusack, 1958).

La Figure 3.4 montre que l'ATP d'étain pur a un saut positif lors de la fusion, tandis que pour le plomb pur il est négatif. Dans les deux cas l'ATP augmente avec la température, en valeur absolue comme pour la plupart des métaux. La concentration pour laquelle il n'y a pas de saut de l'ATP lors de la solidification ou de fusion peut être vu dans la Figure 3.6, et il est à une concentration de Pb-35%wt.Sn. L'alliage Sn-Pb est largement utilisé pour le brasage de l'électronique et dans de nombreux cas, il y a des signaux thermoélectriques indésirables. Dans de telles applications de soudure avec cette composition pourrait être utilisé.

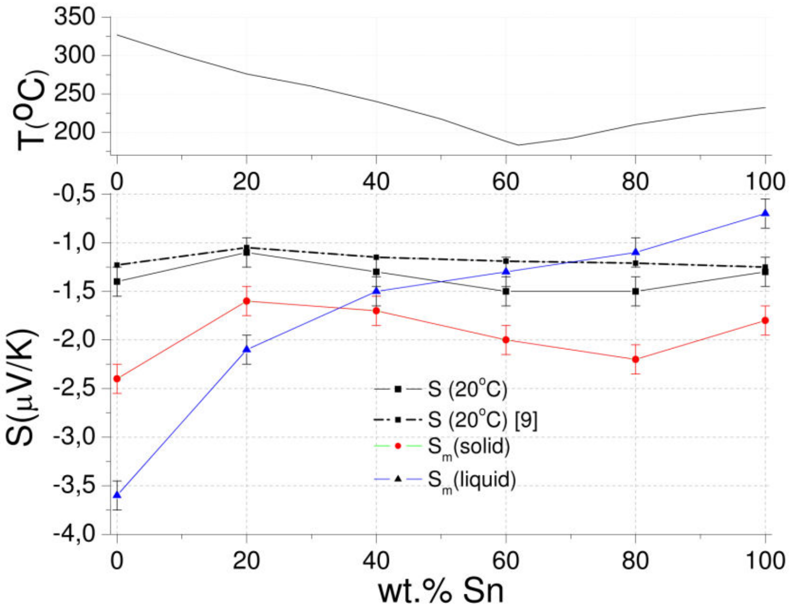

Figure 3.3: ATP mesurée pour alliage Pb-Sn). Ligne noire au-dessus indique la température de fusion en fonction de la fraction Sn. 9- (Pascore, 1976), S_m- ATP à la température de fusion

Table 3.1: Relation linéaire entre l'ATP et la température pour différentes compositions Pb-Sn.

Alliage (température de fusion)	Solide		Liquide	
	A (μV/K)	$B \cdot 10^3$ (μV/K^2)	A (μV/K)	$B \cdot 10^3$ (μV/K^2)
Sn (232 °C)	-1.25	-2.36	-0.18	-2.24
Pb-80wt.%Sn (210 °C)	-1.42	-3.68	-0.52	-2.76
Pb-60wt.%Sn (185 °C)	-1.44	-3.03	-0.95	-1.90
Pb-40wt.%Sn (241 °C)	-1.26	-1.82	-1.32	-0.77
Pb-20wt.%Sn (270 °C)	-1.06	-2.00	-0.93	-4.35
Pb (327 °C)	-1.36	-1.95	-2.27	-4.05

Les résultats montrent que, à l'état liquide, le plomb pur est beaucoup plus sensible aux impuretés que l'étain pur. L'ATP mesurée en fonction de la température pour Pb, Sn et ses alliages semble être presque linéaire à l'état solide et liquide dans la marge d'erreur. L'approximation linéaire est effectuée séparément pour chaque alliage à l'état solide et liquide, selon l'équation (3.12). Les coefficients de la fonction linéaire sont donnés dans le Table 3.2.

$$S[\mu V/K] = A + B \cdot T[°C] \tag{3.5}$$

3.4. Conclusions

Afin de choisir l'alliage et la concentration optimale pour les expériences de solidification prévues, l'ATP de l'alliage Sn-Pb a été mesurée en fonction de la température et de la composition.

Un nanovoltmètre de haute précision a été utilisé lors des mesures, et la précision des résultats est ± 0,10 μV/K en raison de difficultés de mesure.

Dans les mesures décrites, il a été trouvé que les concentrations de certains alliages Sn-Pb avait une différence significative d'ATP (environ 1 μV/K) entre le solide et la phase liquide à la température de fusion. C'est aspect important indique que l'effet sur la fluidité et la structure de solidification par le champ magnétique appliqué peut être prévu.

L'alliage Sn-10%wt.Pb a été choisi pour être l'alliage principal en vue de nos expériences de solidification. Cet alliage présente un changement d'ATP lors de la solidification de 1 μV/K, et il a un point de fusion bas (220 ^{0}C). La structure de solidification directionnelle des alliages Sn-Pb a été étudiée par Cadirli (E. Cadirli, 2000). La structure de l'alliage avec cette concentration est cellulaire, formée de grains d'étain avec une fraction riche en plomb entre elles.

4. Analyse théorique et simulations numériques

4.1. Introduction

Dans ce chapitre une solution simplifiée de l'équation de Navier-Stokes est fournie. La caractéristique de la vitesse de TEMC est estimée pour différents cas, en utilisant l'analyse d'ordre de grandeur. Ces résultats ont été pris en compte lors du choix des paramètres expérimentaux pour des expériences de solidification directionnelle. Une analyse détaillée de l'intensité de la TEMC et de son impact sur le transport de soluté dans la zone pâteuse est faite par Lehmann (P. Lehmann R. M., 1998) qui a analysé l'influence du champ magnétique appliqué sur le cas de la solidification directionnelle horizontale. Dans ce travail le courant thermoélectrique et la densité de force sont évalués analytiquement. La valeur obtenue pour la densité de courant est de l'ordre de grandeur de 10^4 A/m^2.

La simulation numérique de la distribution du courant dans la phase liquide en cours de solidification autour du noyau a été faite par Kao (A. Kao, 2012) , (A. Kao, 2012). La simulation numérique du courant thermoélectrique est réalisée par Xi Li (X. Li Y. F., 2009) montrant la répartition qualitative de la densité courant à l'interface de forme arbitraire statique.

4.2. Estimation analytique

Les propriétés de l'alliage Sn-10%wt.Pb, données par la Table 4.1, seront utilisées pour les estimations dans ce chapitre.

Table 4.1: Propriétés physiques de Sn-10%wt.Pb

Nom	Symbol	Value	Unit
Densité (l)	ρ	6974	kg/m^3
Conductivité électrique (s)	σ_s	$4 \cdot 10^6$	s/m
Conductivité électrique (l)	σ	$2 \cdot 10^6$	s/m
Viscosité dynamique (l)	μ	0.0021	Pa·s
Conductivité thermique (s)	λ_s	55	W/m·K
Conductivité thermique (l)	λ	30	W/m·K
Pouvoir thermoélectrique absolu (s)[1]	S_s	$-2 \cdot 10^{-6}$	V/K
Pouvoir thermoélectrique absolu (l)[1]	S	$-1 \cdot 10^{-6}$	V/K
Différentiel pouvoir thermoélectrique	P	$1 \cdot 10^{-6}$	V/K
Gradient du température	θ	8000	K/m
Coefficient de partage [3]	k	0.1	
Liquidus slope	m	1	%/K
s-solide, l-liquide 1- (I. Kaldre, 2010), 2- (E.A. Brandes, 1992), 3- (P. Lehmann, 1998)			

Dans l'étude expérimentale de la TEMC un champ magnétique statique est appliqué soit dans la direction axiale ou transversale par rapport à la direction de croissance. La convection de la phase liquide est induite par la force de Lorentz qui est le produit vectoriel du courant TE et du champ magnétique. La distribution quantitative du courant électrique et de la force TE sont présentés dans la Figure 4.1. Le champ magnétique axial induit une rotation liquide autour de chaque bras de dendrite, tandis que tout champ transversal provoque un écoulement macroscopique, somme des contributions de tous les bras de dendrite.

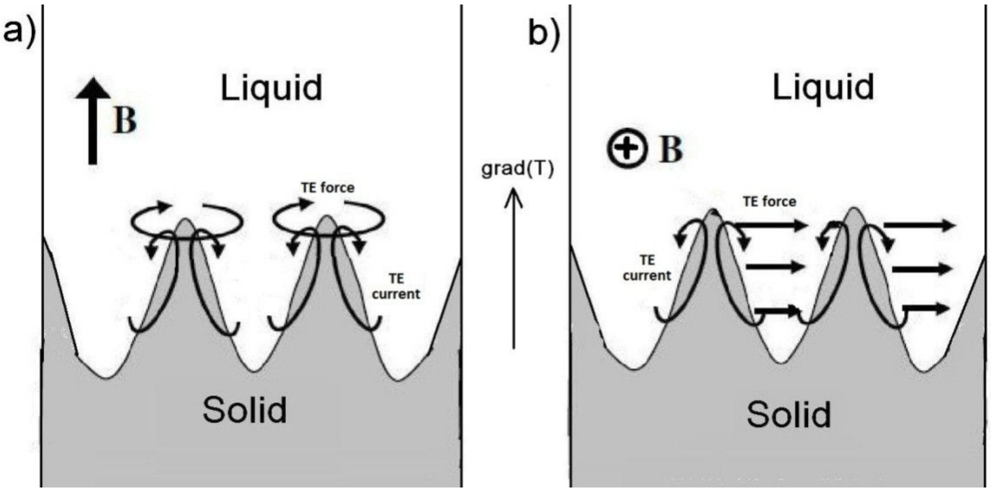

Figure 4.1: TEMC à l'interface de solidification dendritique: a) sous champ magnétique axial, b) sous champ magnétique transverse.

Si aucun champ magnétique n'est appliqué, cet effet est la seule source de courant et sa densité proche de l'interface de solidification peut être estimée en ordre de grandeur.

$$j = c\sigma P\theta \tag{4.1}$$

où c est le coefficient qui caractérise la forme du circuit de courant à l'interface de solidification (I. Kaldre, 2010). d_l et d_s sont les épaisseurs de trajet du courant dans les domaines liquide et solide.

$$c = \frac{1}{1 + \frac{\sigma_l d_l}{\sigma_s d_s}} \tag{4.2}$$

Si le champ magnétique est appliqué, la force de Lorentz apparaît, et le mouvement de la phase liquide est engendré. Dans ce cas, la situation devient plus compliquée parce que le mouvement du fluide introduit des forces électromagnétique et visqueuse. Le mouvement en phase liquide est régi par l'équation de Navier-Stokes:

$$\rho\left(\frac{\partial \vec{u}}{\partial t} + \vec{u}\cdot\nabla\vec{u}\right) = -\nabla p + \mu\nabla^2\vec{u} + \rho\vec{g}\beta\vec{\theta}L + \vec{j}\times\vec{B} \tag{4.3}$$

Pour estimer les ratios entre les forces, les nombres adimensionnels suivants sont définis:

Numéro Hartmann	Lorentz force/ viscosité	$Ha = BL\sqrt{\frac{c\sigma}{\mu}}$
Numéro Reynolds	Inertie/ viscosité	$\mathrm{Re} = \frac{\rho u L}{\mu}$
Paramètre d'interaction	Lorentz force/ inertie	$N = \frac{c\sigma B^2 L}{\rho u}$
Nombre de flottabilité	Force d'Archimède/ Lorentz force	$Bu = \frac{\rho\beta g L}{c\sigma P B}$
Nombre de Reynolds magnétique	Advection magnétique/ diffusion magnétique	$Rm = \mu\sigma u R$

Pour des dendrites primaires d'alliage Sn-Pb: Re=0.4, Ha^2=1, N=3, Bu=$1\cdot10^{-3}$, la flottabilité peut être donc négligée. Pour l'estimation d'ordre de grandeur, l'équation (4.3) est simplifiée comme suit :

$$\rho \frac{u^2}{L} + \mu \frac{u}{L^2} + c\sigma\ (uB^2 - P\theta B) = 0 \tag{4.4}$$

La solution de cette équation est

$$u = \frac{\left(\sqrt{\left(c\sigma\ LB^2 + \frac{\mu}{L} \right)^2 + 4\rho c P\theta B\sigma L} - \left(c\sigma LB^2 + \frac{\mu}{L} \right) \right)}{2\rho} \tag{4.5}$$

L'espacement primaire du bras de dendrite primaire est d'environ 100 µm. La vitesse maximum pour cette longueur est d'environ 1 mm/s pour un champ magnétique de 0.5 T.

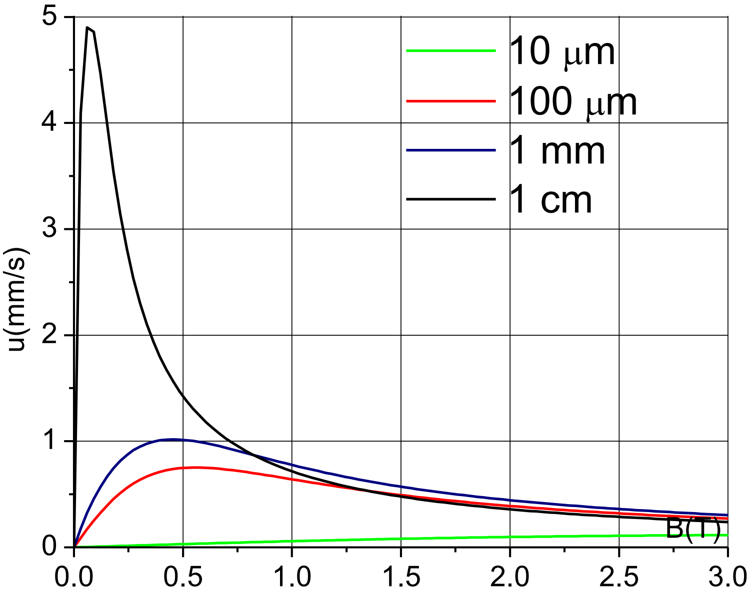

Figure 4.2: Ordre de grandeur de vitesse TEMC pour quatre différentes échelles de longueur (les propriétés de Sn-wt.10%. Pb sont utilisés).

4.3. Description de la frontière thermoélectrique

Pour le circuit ouvert composé de deux métaux différents la force électromotrice thermique générée dans le circuit peut être calculé d'après la loi de Kirchhoff selon l'équation (4.21).

$$\varepsilon_T = \int_{T_1}^{T_2} S_2(T) \cdot dT + \int_{T_2}^{T_1} S_1(T) \cdot dT \approx \Delta S \Delta T \tag{4.6}$$

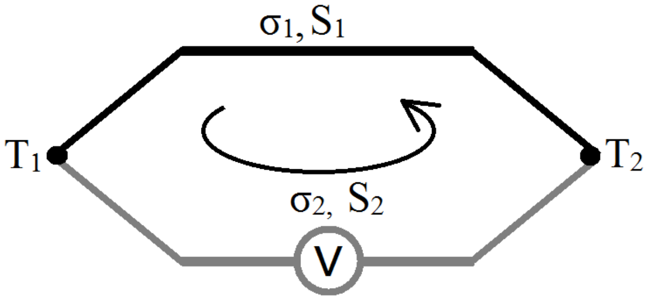

Figure 4.3: Schéma du circuit formé de deux conducteurs différents.

Si le circuit est fermé, il existe dans le circuit une circulation de courant TE. Dans ce cas, la situation est différente parce que la densité de courant doit être conservée aux points de contact. Dans des milieux continus, le principe est similaire, et la solution pour une distribution de potentiel et de courant à l'interface est complexe. Le potentiel électrique et la composante normale du courant doivent être conservés à l'interface.

$$\begin{aligned} U_1 &= U_2 \\ (\vec{j}_1 \cdot \vec{n}_1) &= \left(\vec{j}_2 \cdot \vec{n}_2\right) \end{aligned} \tag{4.7}$$

4.4. Simulation numérique

Le courant électrique dans les deux domaines est calculé par l'équation (4.8) en utilisant l'approximation consistant à négliger les courants induits par l'écoulement à travers le champ magnétique. Comme on peut le voir, le courant électrique se compose de deux parties, une due au gradient de potentiel électrique et l'autre due au gradient de température.

$$\vec{j} = -\sigma\nabla U - \sigma S\nabla T \tag{4.8}$$

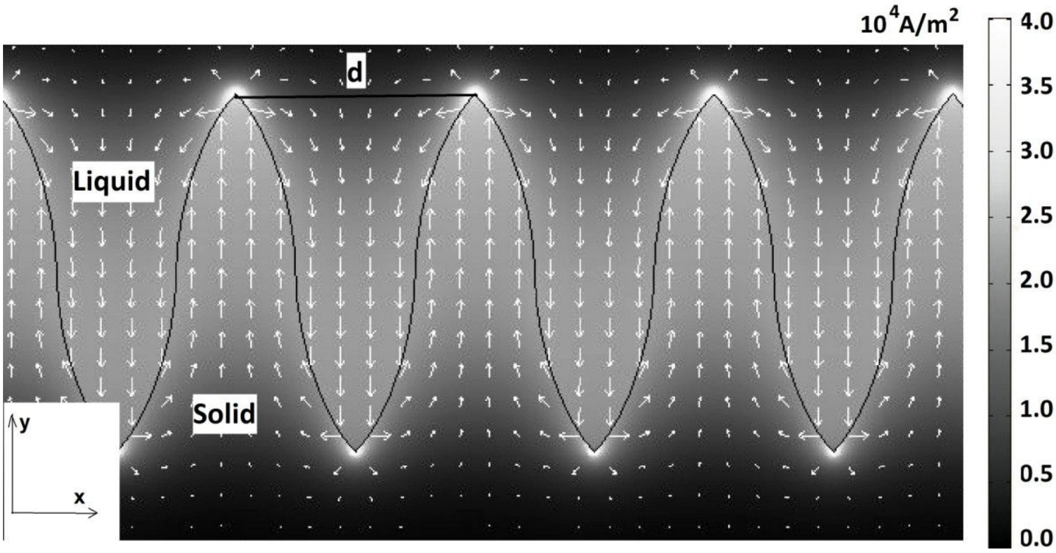

Figure 4.4: Répartition du courant thermoélectrique sur le front de solidification dendritique. Le calcul est fait pour Sn-10%wt.Pb alliage (*d*=100 µm, *h*=200 µm).

Si le champ magnétique est appliqué perpendiculairement au plan xy, les composantes de la force de Lorentz peuvent être calculée comme suit

$$\vec{F} = \vec{j} \times \vec{B} = \begin{pmatrix} j_x & j_y & 0 \\ 0 & 0 & B \\ \vec{i} & \vec{j} & \vec{k} \end{pmatrix} = j_y B\vec{i} - j_x B\vec{j} \tag{4.9}$$

Le flux TEMC est calculé numériquement dans la configuration axisymétrique comme indiqué dans Figure 4.5. La température de l'eau en bas de l'aiguille de cobalt est égale à T_1=50 ° C, tandis que T_0=17 °C. Le courant thermoélectrique est crée par un gradient de température à l'interface entre le cobalt et le GaInSn. Le cobalt a une valeur d'ATP plus haute à la température ambiante entre les métaux (-35 µV/K à la température ambiante).

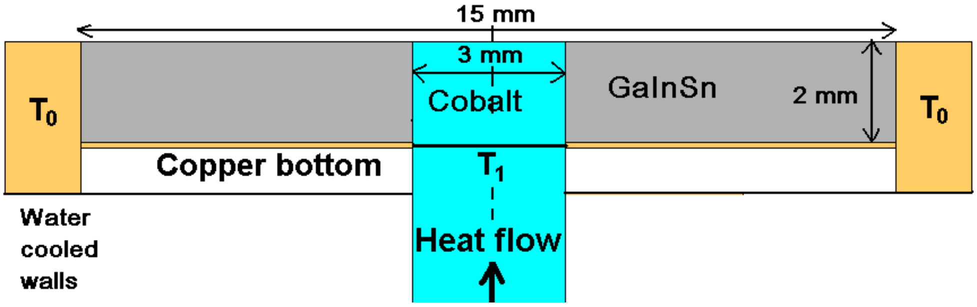

Figure 4.5: Géométrie et dimensions de la simulation numérique de la TEMC.

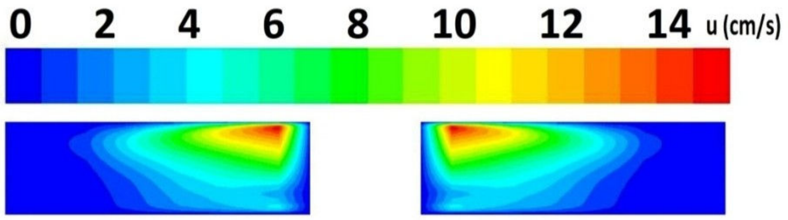

Figure 4.6: Composante de vitesse azimutale pour le champ magnétique axial appliqué (B_z = 0.2 T).

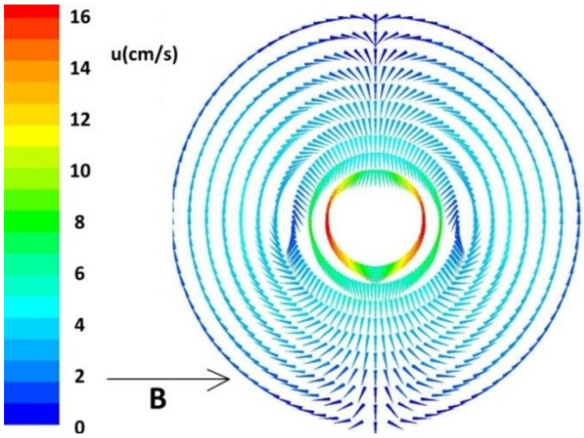

Figure 4.7: Vitesse TEMC provoquée par le champ magnétique transversal (B_x=0.2 T)

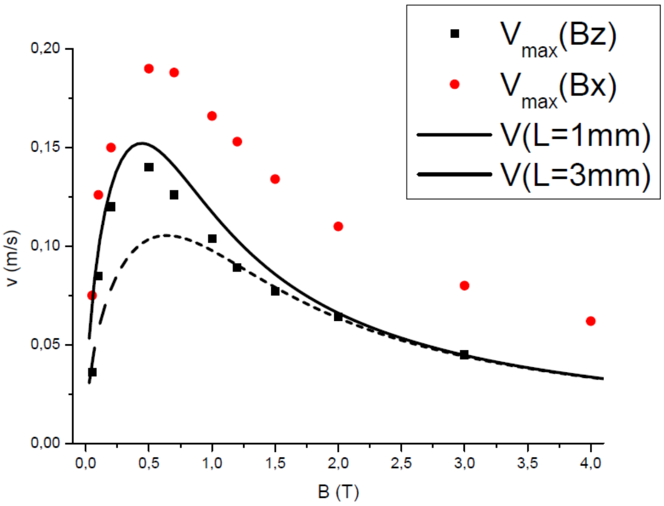

Figure 4.8: Comparaison entre l'ordre de grandeur issue de l'analyse des estimations (équation (4.5)) et la solution numérique.

4.5. Conclusions

L'analyse des estimations d'ordre de grandeur menée dans ce chapitre donne quelques indications intéressantes concernant l'influence du champ magnétique statique sur les caractéristiques du mouvement de fluide à proximité du front de solidification dans le cas de la solidification dendritique. Il a été confirmé que l'intensité de la TEMC augmentait avec le champ jusqu'à une certaine limite, mais une augmentation supplémentaire du champ magnétique réduisait la TEMC en raison de la force de freinage MHD qui devient dominante après un seuil. L'analyse de ces phénomènes à différentes échelles de longueur a révélé le fait que le champ magnétique critique pour lequel la TEMC était le plus élevé, était fortement dépendant de l'échelle caractéristique de l'écoulement provoquant la structure.

Les simulations numériques fournies dans ce chapitre confirment qualitativement les hypothèses précédentes sur les caractéristiques de l'écoulement sous champs magnétiques axial et transversal. La dépendance entre l'intensité de la TEMC l'intensité du champ magnétique a également été vérifiée numériquement, et un bon accord entre l'estimation et la simulation, concernant l'ordre de grandeur de vitesse, a été mis en évidence.

5. Solidification sous champ magnétique statique

5.1. Introduction

Dans ce chapitre nous étudions l'influence de la présence d'un champ magnétique sur les structures de solidification, la taille des grains et les macro-ségrégations d'un barreau métallique obtenu par solidification dirigée. L'alliage peut être de l'Etain-Plomb (Sn-Pb) ou de l'Etain-Bismuth (Sn-Bi). Le champ magnétique peut être axial ou transverse. Les vitesses de tirage peuvent varier.

Des travaux expérimentaux antérieurs (X. Li Y.F., 2007), (X. LI, 2007) et (P.Lehmann, 1998) ont montré que les effets thermoélectriques (TEMC) peuvent engendrer des changements importants de structures de grains, de morphologique et d'espacement interdendritique (Y.Y. Khine, 1998).

Ces recherches intéressent aussi le domaine de la croissance cristalline des semi-conducteurs, matériaux qui, dans l'état liquide, présentent en général un fort pourvoir thermoélectrique. (Yestilyurt, et al. 2004) et dans lesquels, par conséquent, des écoulements sont susceptibles d'être engendrés par effet TEMC.

5.2. Dispositif expérimental

Les échantillons sont élaborés dans un creuset d'alumine cylindrique de dimensions : longueur $L = 110\,mm$, diamètre intérieur $ID = 6mm$ et diamètre extérieur $OD = 10mm$. L'installation de solidification de type four de Bridgman (figure 5.1) utilisé offre de vitesses de tirage contrôlées pouvant aller de $0.5\mu m$ à $20\mu m$. Le champ magnétique est créé par un assemblage d'aimants permanents et engendre un champ magnétique maximal de $0.5T$.

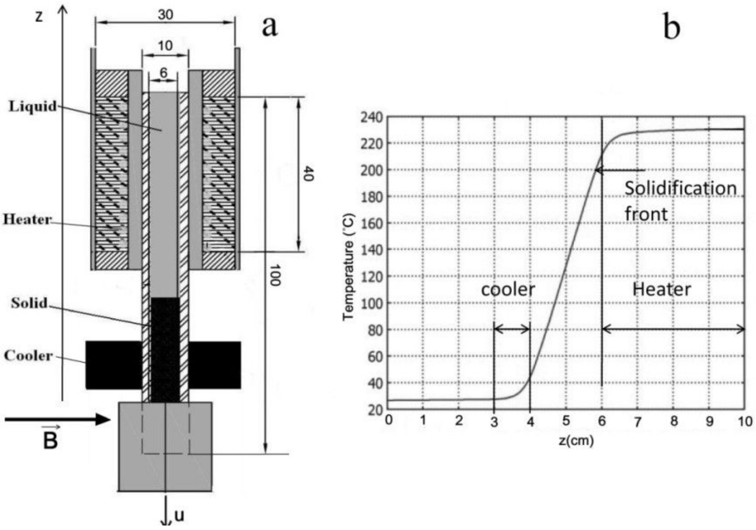

Figure 5.1: Configuration de solidification directionnelle: a) une section transversale de la configuration; b) distribution de la température dans l'installation.

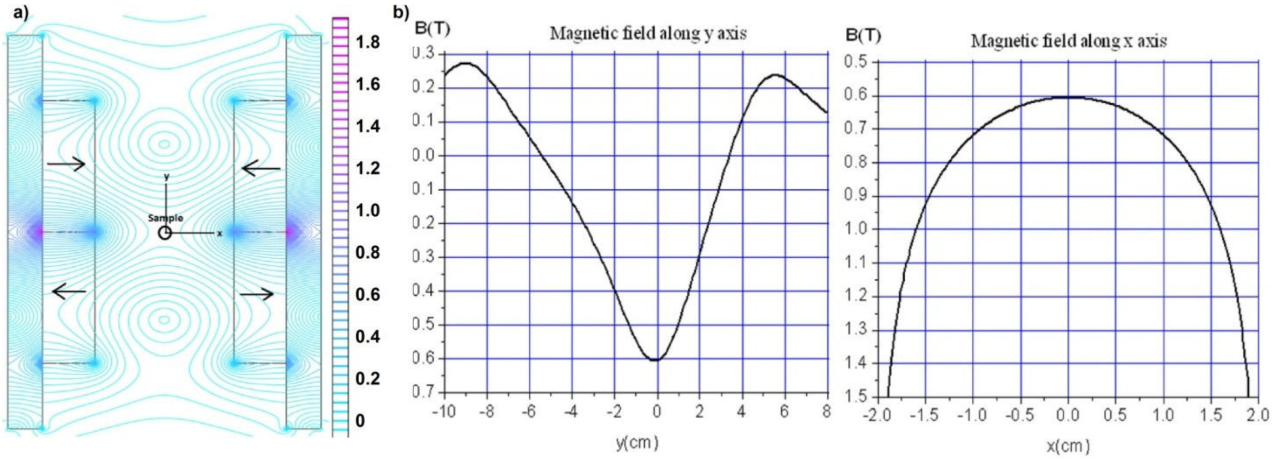

Figure 5.2: Système magnétique: a) isolignes du champ magnétique calculées avec Femm (Meeker 2011); b) distribution du champ magnétique le long de l'axes x et y.

5.3. Résultats expérimentaux

Des expériences de solidification directionnelle sont effectuées sous champ magnétique axial et vertical. Une cartographie du champ créé par l'assemblage des aimants est proposée sur la figure 5.2.a tandis que les profils axial et transversal sont présentés sur la figure 5.2.b.

Les figures 5.3. représentent des macrographies des sections axiale et transverse d'échantillons élaborés en présence d'un champ magnétique axial d'intensité $0.4T$ et pour des vitesses de tirage de $10, 2$ et 0.5 $\mu m/s$. Il apparait que les échantillons élaborés

- avec les vitesses de 10 et 2 $\mu m/s$ ne présentent pas de différence de structures selon qu'il y ait ou non champ magnétique

- tandis que avec la vitesse de tirage la plus faible ($0.5\ \mu m/s$) présentent des structures très différentes.

Cette différence est attribuable à la modification du champ des vitesses dû au freinage MHD, aux effets de convection thermique et solutale.

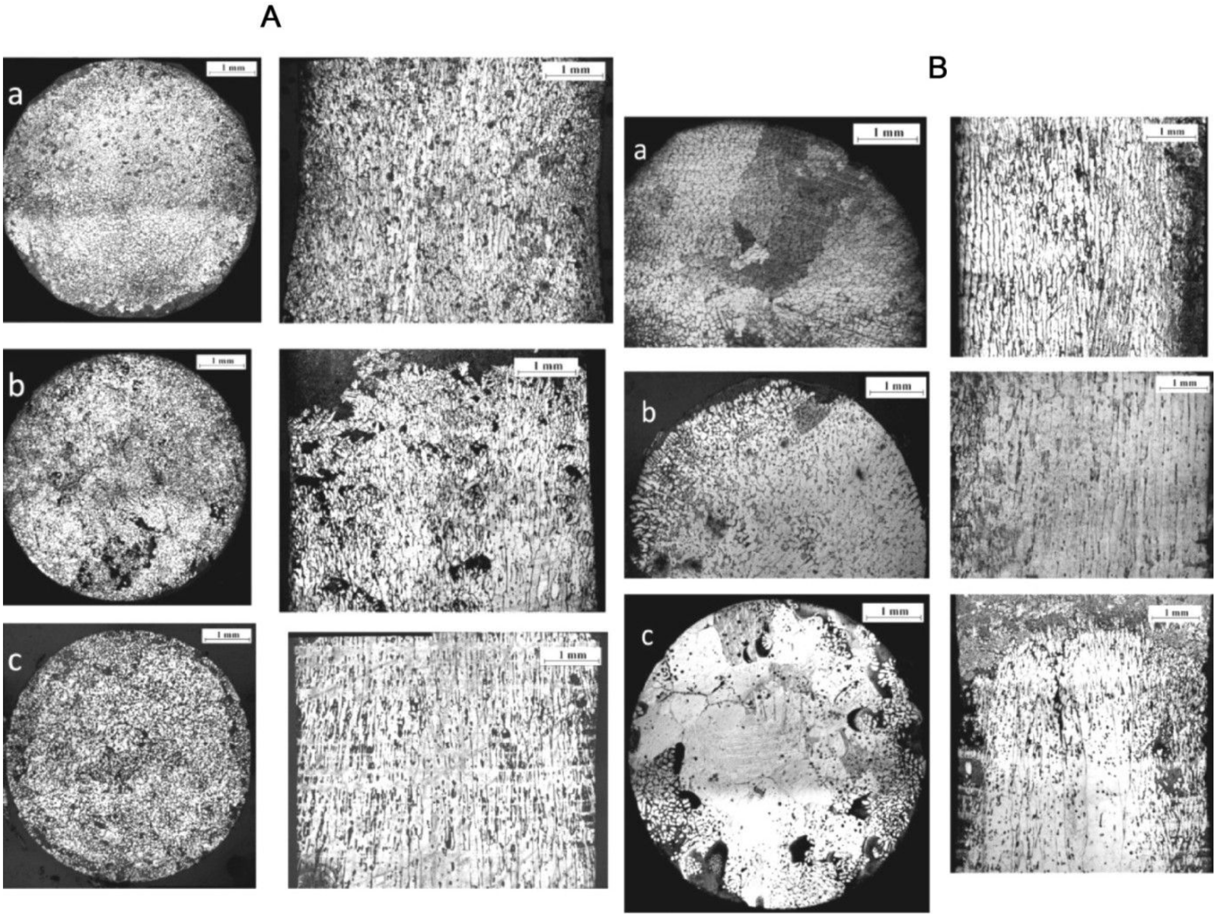

Figure 5.3: Sn-10%wt.Pb solidification directionnelle sous 0.4 T champ magnétique axial (A) et sans champ (B); a) 10 µm/s, b) 2 µm/s, c) 0.5 µm/s.

Les figures 5.4 représentent des macrographies d'échantillons élaborés sans et sous champ magnétique transverse d'intensité caractéristique$0.4T$. D'après les analyses théoriques et les calculs numériques, nous savons que ce type de champ peut créer un écoulement d'origine thermoélectrique au niveau de chaque dendrite et aussi de la taille du creuset susceptible d'engendrer des macroségrégations dans une section transverse de l'échantillon perpendiculaire au champ magnétique appliqué. Cet écoulement est engendré par des forces de Lorentz d'origine thermoélectrique localisée dans une région voisine du front dendritique ou zone pâteuse.

La variation de l'espacement interdendritique primaire en fonction de la vitesse de tirage est portée sur la figure 5.5 avec la courbe théorique issue de l'équation 4.3 est portée sur la figure 5.5.

Les profils de concentration correspondant aux échantillons des figures 5.4 sont mesurés au microscope électronique et sont représentés sur les figures 5.6.

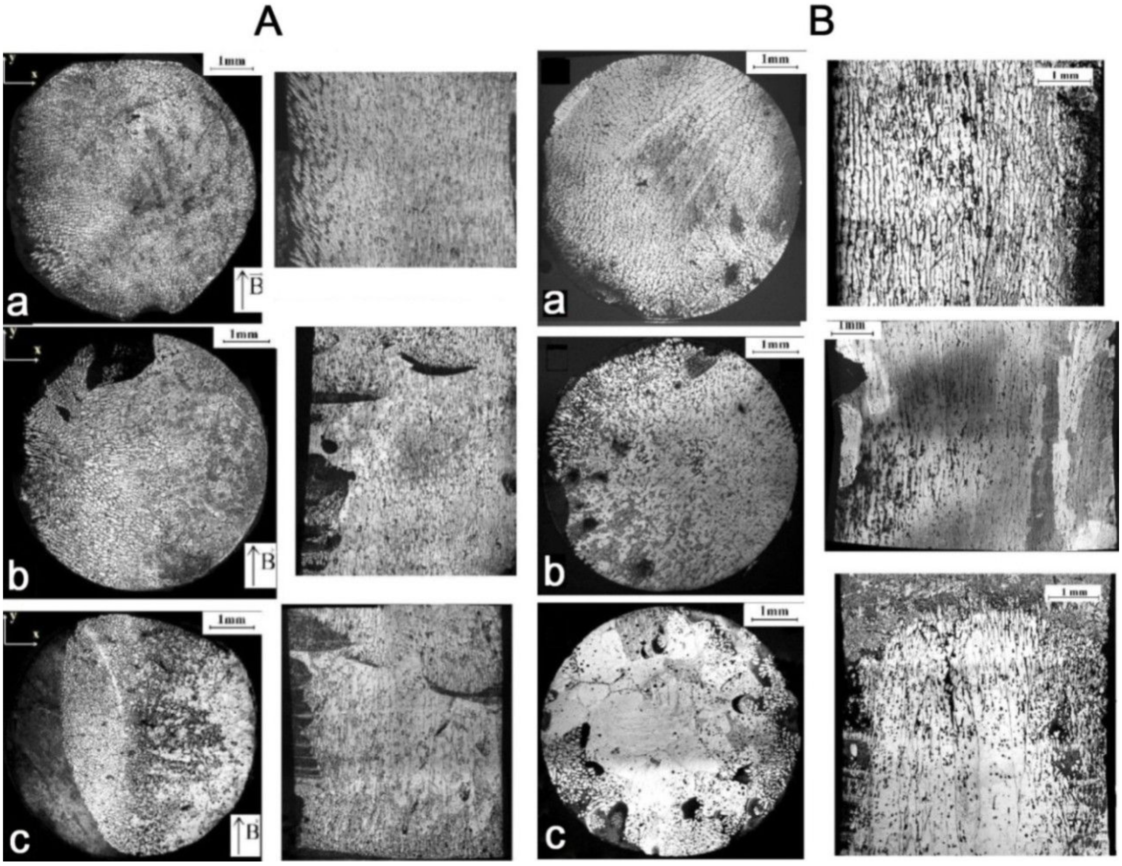

Figure 5.4: Solidification directionnelle Sn-10%wt.Pb de sous 0.4 T champ magnétique transversal (A) et sans champ (B); a) 10 µm /s, b) 2 µm /s, c) 0,5 µm /s.

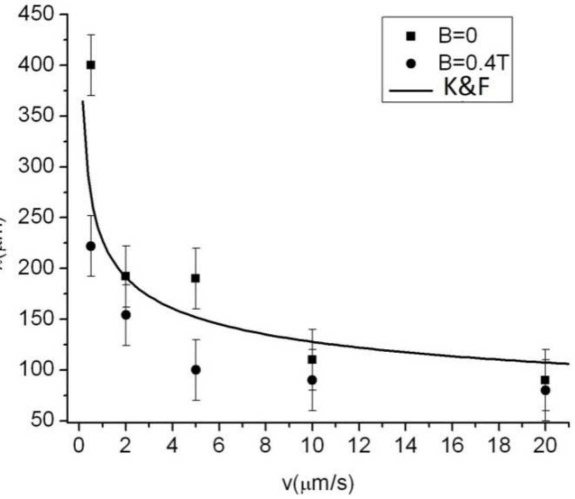

Figure 5.5: Comparaison entre l'espacement des dendrites primaires expérimentale et théorique (eq.(4.3)) de l'alliage à solidification directionnelle Sn-10% wt.Pb sans champ magnétique et sous le champ magnétique de 0.4 T.

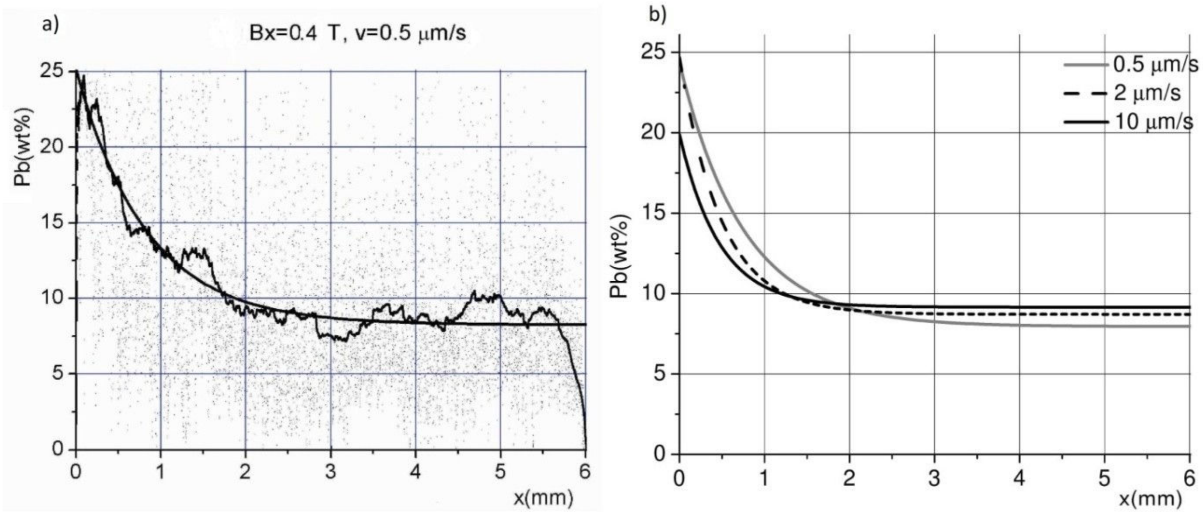

Figure 5.6: a) Pb concentration de la section transversale de l'échantillon à une vitesse de croissance 0.5 μm/s. Points expérimentaux, en moyenne de distribution et approximation exponentiel; b) le contenu en plomb d'alliage à solidification directionnelle Sn-10%wt.Pb en fonction des coordonnées à trois vitesses de solidification différentes.

5.4. Conclusions

Dans ce chapitre, nous avons présenté des expériences de solidification dirigée d'un alliage métallique binaire (Sb-10%wt.Pb) en absence ou en présence d'un champ magnétique axial ou transverse d'intensité caractéristique $0.4\,T$. Nous avons présenté des macroségrégations, mesuré l'espace interdendrique primaire des divers échantillons en fonction de la vitesse de tirage ainsi que les profils de concentration en plomb.

Lorsque la vitesse de tirage est faible et en présence d'un champ magnétique axial, les structures de solidification sont très différentes de celles qui sont observées pour des vitesses de tirage plus élevées. Nous avons attribué ce changement à l'amortissement de la convection naturelle par le freinage électromagnétique.

Lorsque le champ magnétique est appliqué dans la direction transverse à la vitesse de tirage, la taille des macroségrégations croit quand la vitesse de tirage diminue.

6. Superposition de l'effet thermoélectrique et d'un courant électrique imposé

6.1. Introduction

Dans ce chapitre, nous présentons des expériences menées avec le dispositif déjà décrit dans lequel une courant continue ou alternative est imposée aux extrémités de l'échantillon engendrant un courant électrique de direction axiale. L'interaction de ce courant avec le champ magnétique engendre des forces de Lorentz dont l'effet s'ajoute aux forces de Lorentz d'origine thermoélectrique.

Les conductivités électriques des phases solides et liquides d'un même alliage sont différentes. Il existe donc à l'interface solide/liquide une redistribution des courants électriques. Ainsi, une composante du courant perpendiculaire à l'interface de solidification apparait susceptible d'engendrer un mouvement semblable à celui d'origine TEMC. La figure 6.1. est un résultat de simulation numérique qui illustre cet effet.

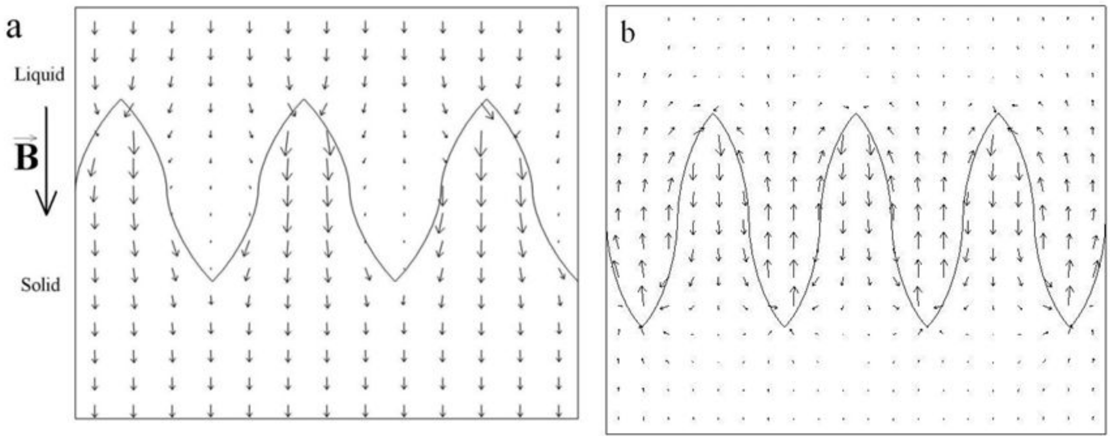

Figure 6.1: a) La distribution de courant à l'interface entre deux milieux des conductivités différentes, b) Lorsque le courant axial dans le volume est soustraite.

6.2. Simulation numérique

L'écoulement dans ma phase liquide engendré par les forces électromagnétiques produites par l'interaction d'un champ magnétique et d'un courant électrique appliqué est réalisé sur la géométrie présentée sur la figure 6.2.

Deux cas sont calculés : selon que le champ magnétique et la courant electrique soient parallèles (figure 6.3) ou perpendiculaires (figure 6.4).

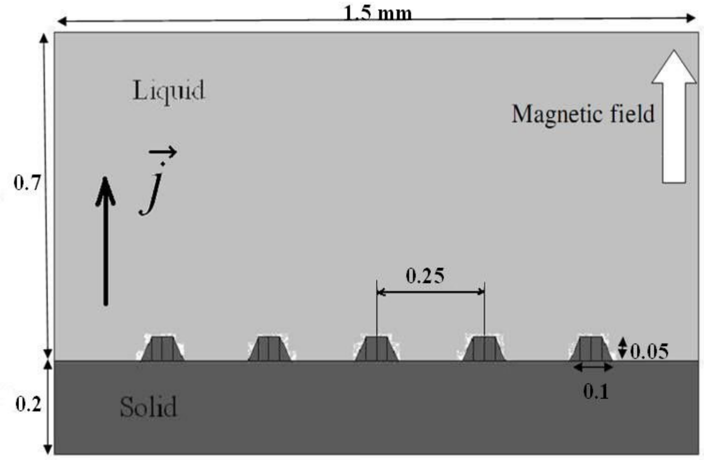

Figure 6.2: Coupe transversale de la géométrie et les dimensions (en mm) utilisés pour la modélisation. Propretés de Pb-Sn alliage sont utilisées (Table 4.1): L=1·10^{-4} m, u=1·10^{-3} m.

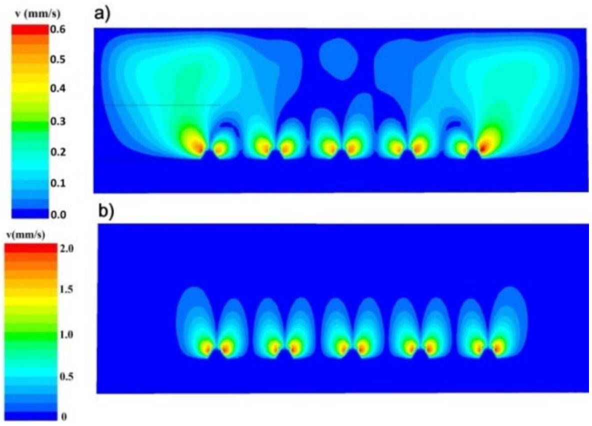

Figure 6.3: distribution de vitesse liquide Calculé provoquée par le champ magnétique axial et le courant électrique (j = 3 • 10^5 A/m^2). Le vitesse à deux valeurs différentes du champ magnétique sont calculée: a) B_z=0.1 T, b) B_z=2 T.

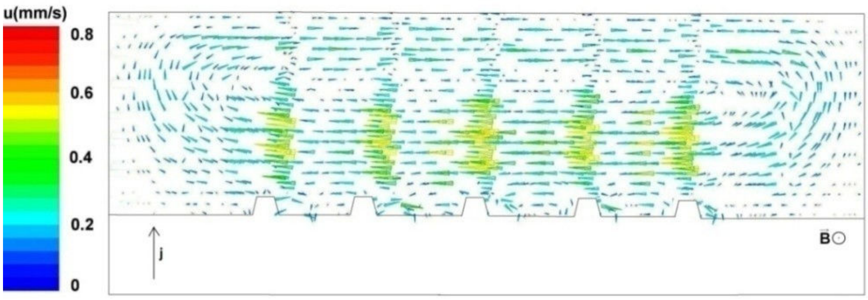

Figure 6.4: Vitesse causé par l'interaction de courant axiale et de champ magnétique transversale. B_x= 0.1 T, j = 0.3 A/mm^2.

6.3. Résultats expérimentaux

Des expériences de solidification sont réalisées avec des échantillons d'alliage binaire Sn-10%wt.Pb.

Les figures 6.5 (vitesse de tirage de 10 $\mu m/s$, champ magnétique axial, courant continu) et 6.6 (vitesse de tirage de 10 $\mu m/s$ et 2 $\mu m/s$ sans et avec champ magnétique axial, courant alternatif 50 Hz)sont des macrographies d'échantillons produits.

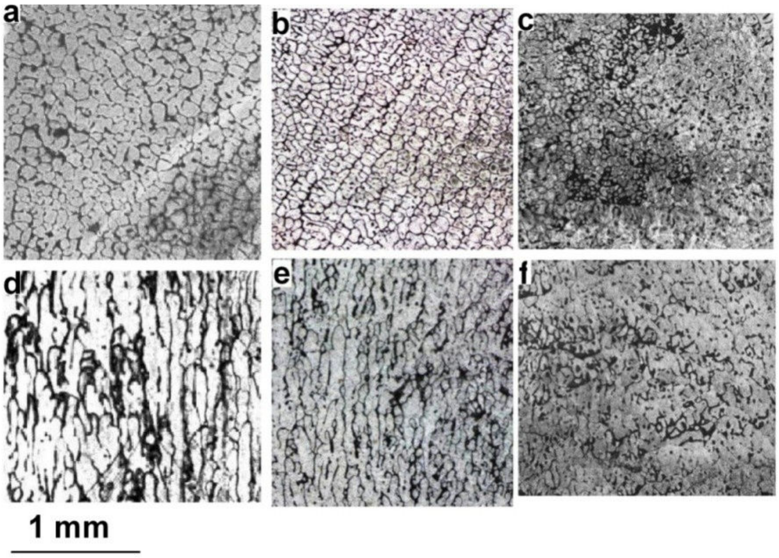

Figure 6.5: Structure d'alliage Sn-10%wt.Pb solidification directionnelle à v = 10 µm/s. Horizontales et verticales sections transversales sont représentées pour les cas suivants: absence de champ (a,d), avec 0.4 T champ axial (b,e), avec 0.4 T champ axial et 1 A/mm^2 courant axial (c, f).

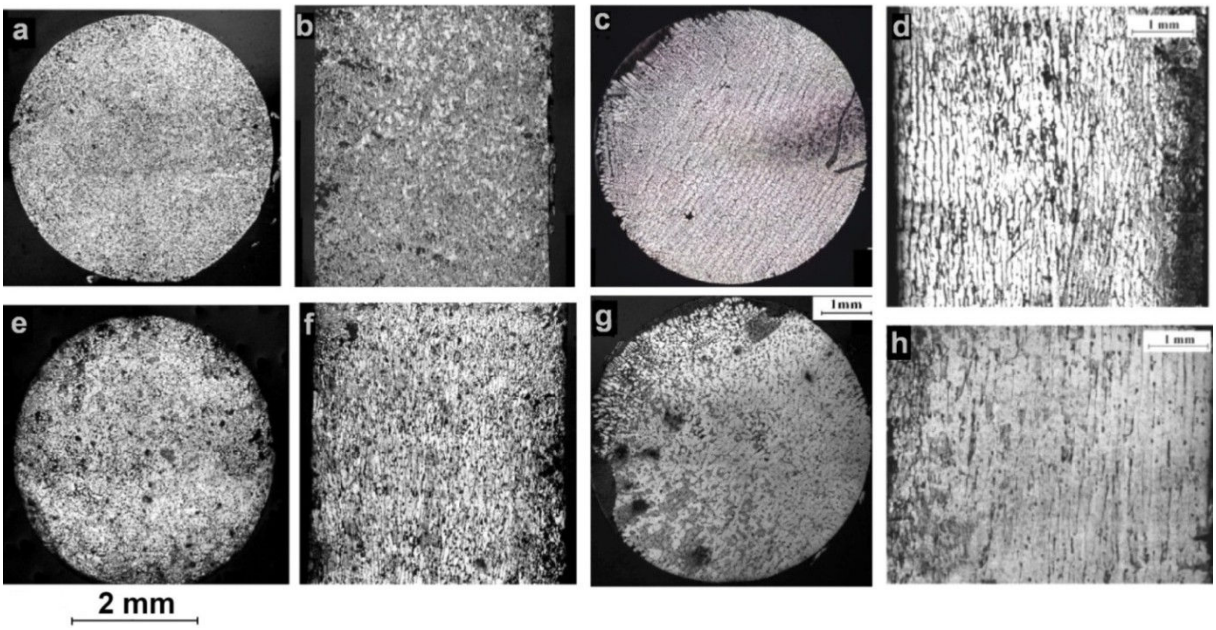

Figure 6.6: Structure de l'alliage Sn-10%. wt.Pb solidification directionnelle avec appliquée courant AC de 50 Hz (1 A/mm^2) et 0.4 T champ magnétique axiale: a, b) 10 µm/s, e, f) 2 µm/s. La structure dans des conditions similaires sans champ et de courant: c,d) 10 µm/s, g, h) 2 µm/s.

6.4. Conclusions

L'application d'une différence de potentiel aux extrémités de l'échantillon en cours de solidification permet de créer des forces électromagnétiques semblables à celles engendrées par l'effet thermoélectrique. Toutefois, dans le cas présent, il est beaucoup plus aisé de contrôler l'intensité et la direction de l'écoulement.

Les résultats expérimentaux sur un alliage Sn-10%wt.Pb montrent que l'application, d'un courant DC axial d'intensité 1 A/mm^2 joint à un champ magnétique axial de $0.4\ T$

- conduit à un raffinage des grains et à un raccourcissement de la zone colonnaire,
- n'engendre pas de macroségrégation

Ces effets sont attribués à la modification des écoulements au voisinage des dendrites.

Lorsque le courant appliqué est alternatif, les forces de Lorentz présentent deux parties

- une partie continue qui amortit l'écoulement
- et une partie oscillante à la même fréquence que le courant appliqué susceptible de produire des vibrations mécaniques.

7. Solidification sous champ magnétique tournant lentement

7.1. Introduction

Dans ce chapitre, un champ magnétique transverse tournant très lentement est appliqué à l'échantillon en cours de solidification directionnelle (figure 7.1).Dans cette configuration, la direction principale de l'écoulement engendré par effet thermoélectrique change au cours du temps engendrant des modifications visibles de macrostructures.

En fonction de la vitesse de rotation deux régimes principaux ont été obtenus :

- Une vitesse de rotation du champ est très lente, l'écoulement le temps de se développer dans toute la zone liquide de l'échantillon,
- Tandis qu'une vitesse plus rapide engendre un écoulement localisé dans l'espace interdendritique.

Le champ des vitesses engendrées dans un cylindre par un champ magnétique tournant a été l'objet de plusieurs articles (L. M. Witkowsky, 1998), (Yu. M. Gelfgat, 1993), (P. A. Davidson, 2001)). Les nombres sans dimension attachés à ce type d'écoulement sont le nombre de Hartman Ha, le paramètre d'interaction N et le nombre de Reynolds magnétique Rm bâti sur la vitesse de rotation du champ magnétique. En utilisant la présente géométrie ($R = 3mm$) et les valeurs des propriétés physiques attachées à l'alliage Sn-10%wt.Pb, nous trouvons :

$$Ha = 42\,;\ N = 2500\,; Rm = 7 \cdot 10^{-7}$$

Cette combinaison de paramètres est significative d'un écoulement en rotation solide avec un profil de vitesse azimutale telle que :

$$u_\theta = \frac{\Omega r}{(1 + 4/Ha)} \tag{7.1}$$

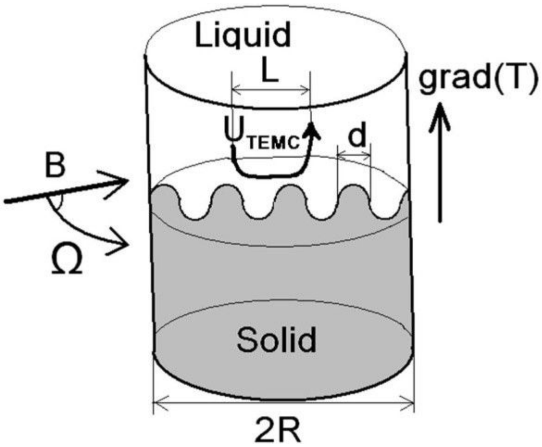

Figure 7.1: Vue schématique de TEMC causé par la rotation du champ magnétique transversale.

Nous pouvons estimer le temps nécessaire à la mise ne place d'une recirculation de taille caractéristique la taille du creuset : $T = \frac{2 \cdot \pi \cdot R}{u_{TEMC}} = 188\ s$

Tandis que le temps nécessaire au développement d'une recirculation de taille égal à 5 fois l'espace inter-dendritique d, est égal à : $T = \frac{10 \cdot \pi \cdot d}{u_{TEMC}} = 31s$

Ici l'ordre de grandeur de u_{TEMC} est donné par l'équation 4.5.

Ces ordres de grandeur, le temps minimal de révolution du champ nécessaire pour obtenir des macroségrégations de taille égale à celle du creuset est de $188\ s$.

7.2. Résultats expérimentaux

La figure 7.2. représente des macrographies de sections longitudinale et transverse d'échantillon élaborer sous champ magnétique tournant à différentes vitesses T (s) pour différentes vitesses de tirage v (m/s). Les temps de révolution sont choisis pour que l'écoulement puisse de développer à l'échelle du creuset. Sur les sections longitudinales, nous observons des structures de solidification spiralées (figures 7.2.d., e, f).

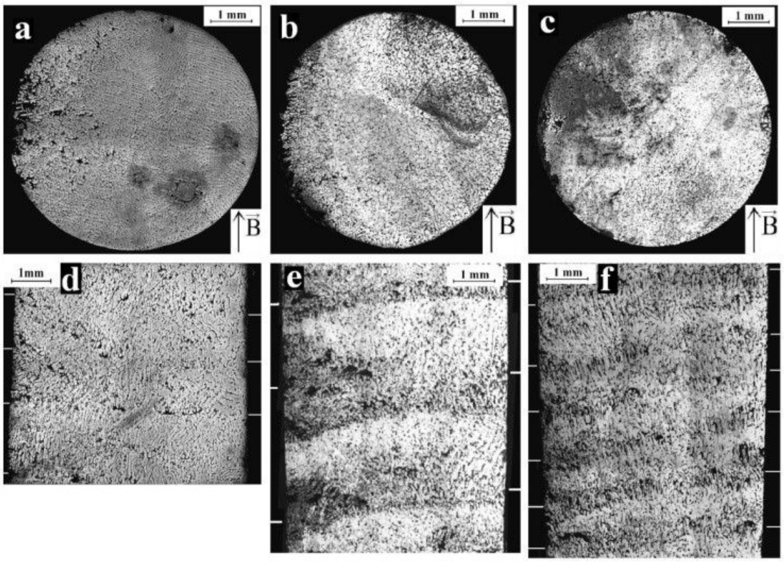

Figure 7.2: Des sections horizontales et verticales de l'alliage Sn-10%wt.Pb à solidification directionnelle sous champ magnétique tournant. a, d) *v*=10 µm/s, *B*=0.4 T, *T*=150 s; b,e) *v*=5 µm/s, *B*=0.4 T, *T*=600 s; c,f) *v*=2 µm/s, *B*=0.4 T, *T*=600 s.

Les macroscopies portées sur les figures 7.3. sont celles d'échantillons élaborés avec une vitesse de rotation du champ magnétique plus rapide. Sur ces images aucune macroségrégation n'apparait, mais l'espacement interdendritique primaire est fortement réduit. Par exemple, cet espacement passe de 125 μm sans champ à 83 μm avec un champ présentant un temps de révolution égal à $30s$.

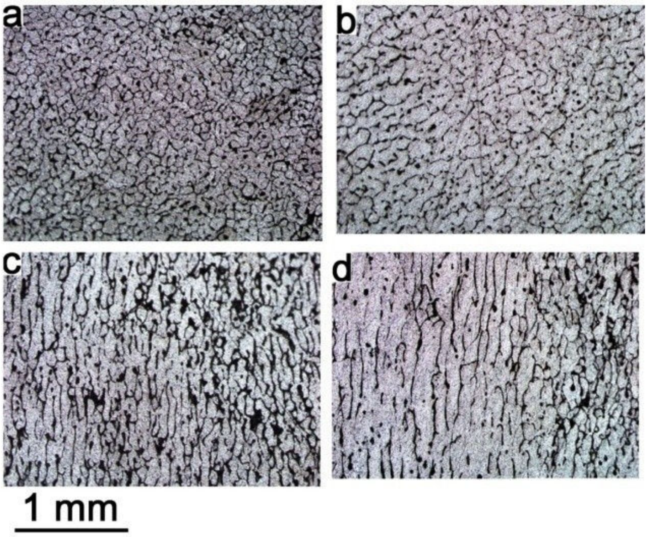

Figure 7.3: Alliage Sn-10%wt.Pb à solidification directionnelle à *v*=3 µm/s. Avec un champ magnétique transversal rotatif (*B*=0.4 T, *T*=30 s); a- une section transversale, c-section longitudinale; Sans champ magnétique; d-section transversale , d-section longitudinale. ($\lambda_{a,c}$=83 µm et $\lambda_{b,d}$=125 µm).

7.3. Conclusion

La configuration de champ magnétique étudiée dans ce chapitre permet d'évaluer expérimentalement la vitesse TEMC. Pour cela, nous devons comparer les effets du lent brassage électromagnétique et l'effet thermoélectrique. Il existe une vitesse de rotation critique pour laquelle ces deux effets s'équilibrent. Dans nos expériences, cette vitesse est trouvée égale à $0.18\ mm/s$. Cet ordre de grandeur est similaire à celui issu de l'équation 4.5.

Nous avons vu dans le chapitre 5 qu'un champ magnétique statique influence les écoulements dans le creuset à l'échelle de ce dernier engendrant des macroségrégations. Ces macroségrégations sont sous forme de spirales pour une rotation du champ lente (dans notre cas $T > 150\ s$) dont la périodicité est égale à celle du champ, tandis qu'une rotation suffisamment rapide de ce champ supprime toute macroségrégation.

8. Conclusions et perspectives

La solidification est un processus complexe faisant intervenir différents phénomènes physiques fortement couplés. Dans certaines circonstances et pour certains alliages, certains de ces phénomènes peuvent être favorisés. C'est le cas dans ce travail où nous avons cherché à mettre en évidence les effets des forces électromagnétiques dues à l'effet thermoélectrique ou à un effet similaire obtenu par l'application d'une différence de potentiel à l'échantillon en cours de solidification.

Etant donné leur nombre, nous n'avons pas pu explorer tous les paramètres de contrôle de la solidification. Néanmoins des résultats intéressants ont pu être mis en évidence.

Dans le futur et à des fins de comparaisons avec des simulations numériques, une analyse quantitative des écoulements lors de la solidification pourra être réalisée grâce à des traceurs et sous rayon X, pour différentes vitesses de tirage et différents gradients de température.

Nous avons montré expérimentalement :

- que les échantillons solidifiés sous champ magnétique tournant à vitesse très lente présentaient des structures de solidification de forme hélicoïdale
- que cette structure permettait une quantification des effets thermoélectriques
- que lorsque les effets de brassage électromagnétique et thermoélectrique présentaient le même ordre de grandeur un affinage des structures de solidification était observé.

Il serait intéressant de reprendre ces expériences avec un autre alliage ou une autre composition de Sn-Pb avec d’autres vitesses de tirage et de rotation du champ magnétique.

Les expériences mettant en œuvre un champ magnétique horizontal et une différence de potentiel appliquée pourraient être adaptées avec profit de la façon suivante : l’électrode plongerait dans la zone liquide jusqu’au voisinage de l’interface de solidification permettant un contrôle de la convection forcée directement à l’interface de solidification.

Enfin, pour compléter les expériences suggérées ci-dessous, nous pensons qu’il est nécessaire de simuler numériquement et avec précision tous les phénomènes physiques mis en jeu lors de la solidification sous champ magnétique ainsi que leur couplage.

Thermoelectric current and magnetic field interaction Influence on the structure of binary metallic alloys

1. Introduction

1.1. Structure of the thesis

During this work influence of applied magnetic field on the structure of metallic alloys is investigated experimentally and theoretically. Mainly work is focused to the investigation of thermoelectromagnetic convection (TEMC) in liquid melt during solidification of metallic alloys and study of its impact on the microstructure and macrostructure of solidified samples. This phenomenon is investigated experimentally, theoretically and numerically during the work. Theoretical results are used to interpret the experimental results and to estimate optional experimental parameters. For better understanding of physical processes during solidification, numerical simulations of thermoelectric current and TEMC at the solid-liquid interface is carried out using FLUENT and COMSOL software. Thesis is divided in following chapters:

1. **Introduction.** In this chapter main physical principles and origin of thermoelectric convection during solidification of metallic alloys are explained. Short theoretical background, scientific novelty of the work and author contribution is explained. Main hypothesis and results are shortly summarized.
2. **Theoretical background.** Short introduction to main disciplines of physics playing role during solidification is given and their connection to microscale and macroscale processes during solidification of metallic alloys is explained.
3. **Thermoelectric property measurements.** Due to lack of reliable and detailed thermoelectric property experimental data available, one of the first stages of this work is to measure absolute thermoelectric power of the alloys which will be used in the experiments of this work. Description of experimental setup for absolute thermoelectric power (ATP) measurements in solid and liquid states is given in this chapter. ATP property measurements as a function of temperature and composition of Sn-Pb and Sn-Bi alloys are presented in this chapter. These data are necessary for analysis of TEMC and its influence on the structure, and will be used in future work. Summary of ATP data available in literature is also given.
4. **Theoretical analysis and numerical simulation of TEMC.** Literature review on thermoelectric boundary problems and theoretical works dedicated to this thematic are given in this chapter. Theoretical analysis of thermoelectromagnetic convection is presented in this chapter. Estimations of significance of TEMC in various cases is carried out, optimal parameters to achieve

maximum TEMC efficiency is estimated. Also numerical simulation results of thermoelectric current and flow in various geometries and magnetic field configurations are presented in this chapter. Necessary evaluations for further experimental work are estimated here.

5. **Solidification under static magnetic field**. Literature review on previous experimental works on the solidification under static magnetic fields is given in this chapter. In this area extensive experimental work has been carried out with many alloys and different magnetic field strengths, however complete theoretical interpretation of results does not exist. Directional solidification results of Sn-Pb and Sn-Bi alloys carried out as a part of this thesis, is given in this chapter. Alloys are directionally solidified under axial or transverse magnetic field (up to 0.5 T) at various growth velocities (0.5-20 μm/s). Results obtained during direct observation of directional solidification under static magnetic field performed in European Synchrotron radiation Facility (ESRF) is presented and explained in this chapter.

6. **Combination of TEMC and applied electric current.** In this chapter applied magnetic field is combined with electromagnetic interactions caused by applied electric current through the solidification interface during solidification. This allows us to compare two different convection effects and to determine the parameters which are unknown. Hypothesis that this kind of electromagnetic interaction causes similar convection pattern than TEMC has been analytically explored and experimentally tested. Thus this interaction of applied electric current and magnetic field could potentially allow to promote or suppress the consequences of TEMC or to create TEMC-like flow in the materials where TEMC is not observed. Following interactions have been used:

- Axial direct electric current and axial or transverse static magnetic field.
- Axial alternating electric current (50 Hz) and axial or transverse magnetic field.

7. **Solidification under slowly rotating magnetic field.** Transverse magnetic field is slowly rotated around the crucible during directional solidification. Depending on the field rotation velocity/growth velocity ratio different interactions on the structure can be achieved. If field rotation is slower than growth velocity then helical macrosegregation pattern within the ingot can be achieved. Whereas at faster field rotation, if characteristic velocities of TEMC and electromagnetic stirring caused by field rotation are of comparable order of magnitude, no macrosegregation is observed but grain sizing and structure is altered by combination of these two effects. Combined action of two different effects also allows us to indirectly estimate characteristics of TEMC. Different cases have been analysed theoretically and experimentally verified in this chapter. Comparison between theoretical estimations and experimental results is given.

8. **Conclusions and future work.** In this chapter general conclusions of the work are given. Main concerns and critical points noticed during the work are listed and described. Future

perspective research directions and possible parameter combinations where it would be worth to collect extra experimental data are described.

1.2. Introduction

It is known that circumstances during solidification of metallic alloy can significantly alter its physical properties. Historically lots of relations between material treatment and conditions during solidification and physical properties have been found empirically. For instance, properties of many metals or metallic alloys depend on cooling rate of the melt during solidification and heat extraction direction. Cooling rate can be changed in wide range and this allows to obtain the same material with different hardness and ductility, and other properties. Along with the development of modern science correlation between circumstances of solidification and microstructure of the material were revealed and theories to describe the phenomena have been created. Nevertheless, in solidification science there are still many things described only by empirical laws and trends. Melt convection influence on the solidification structure is only one example.

Solidification of metallic alloy is an extremely complicated multiphysical process where numerous physical processes take part and influence each other by different ways. Structure of the metal or alloy is also significantly affected by energy and solute transport in the liquid melt at the vicinity of the solidification interface during solidification process. In general, when regular cells are forming at relatively low rates, they grow perpendicular to the liquid-solid interface regardless of crystal orientation. When the growth rate is increased crystallography effects begin to exert an influence and the cell growth direction deviates toward the preferred crystallographic growth direction. Simultaneously the cross section of the cell generally begins to deviate from its previously circular geometry owing to the effects of crystallography. In this case it is called dendritic crystallization, which is the most common type of solidification of metallic alloys in practical metallurgy. Various kinds of dendrite morphologies are known today.

Dendrite spacing and morphology can be affected by many parameters, main of which are growth velocity, cooling rate, temperature gradient and liquid melt flow near the solidification front during solidification. This work is focused on research of effects caused by magnetic field induced melt flow analysis and its influence on the dendrite growth and solidified material structure. Melt flow can be created by various mechanisms, like composition inhomogenities, temperature inhomogenities, presence of electric or magnetic fields, ultrasound and others. Dendrite sizes and growth direction, and velocity are very sensitive to solidification conditions. It is now known that these microscale processes are responsible for material structure and eventually its properties. It is clear that in case of dendritic solidification we cannot assume solidification front to be sharp transition between solid and liquid, because solid phase dendrite array and free solid nuclei, surrounded by liquid phase exists between them. This region is called the mushy zone. Liquid phase motion (convection) in the mushy zone has important role on the formation of metal structure.

Application of magnetic field can be additional mechanism to affect and create convection in the liquid melt and mushy zone of metallic alloy. Main mechanism is the interaction of temperature gradient caused electric current and applied magnetic field interaction caused TEMC. This thesis is focused on the theoretical, numerical and experimental investigation of the consequences of the TEMC on the structure of metallic alloys. From the basic physics it is known that if conducting media is moving in the magnetic field, motion induced electric current interacting with the same magnetic field will create force opposite to motion direction, thus damping the fluid motion. In recent years, it has been conclusively experimentally proven that this kind of influence can significantly alter dendrite structure and macrosegregation of some alloys.

1.3. Main hypotheses to investigate and objectives of the work

Main objective of this thesis is to analyse and verify the possible aspects of magnetic field influence on the solidification of binary metallic alloys. Following hypothesis are investigated and verified experimentally and theoretically during this work:

- Applied magnetic field during directional solidification may cause macrosegregation and changes in dendrite spacing.
- Transverse static magnetic field causes significant macrosegregation, which is greater at low growth velocities.
- Similar melt flow pattern than TEMC near the solidification front can be induced by applied electric current and magnetic field interaction.
- Slowly rotating magnetic field (stirring effect is of comparable order of magnitude with TEMC) causes time-varying TEMC flow. As a result quality of structure can be improved or helical macrosegregation pattern can be achieved.

1.4. Main results

Main results obtained during this work are:

- Experimental setup for absolute thermoelectric power measurements in solid and liquid metallic alloys has been developed and tested by measuring thermoelectric power of Sn-Pb alloy in wide temperature and concentration range.
- Sn-10%wt.Pb alloy was directionally solidified under static (up to 0.5 T) magnetic field at various growth velocities. It is proven that at low growth velocities transverse magnetic field

causes significant macrosegregation. Axial magnetic field does not have significant influence on the structure. This is explained by the fact that axial field causes convection at local scale (comparable to dendrite spacing).

- Applied direct and alternating electric current through the solidification interface during directional solidification causes grain refining. Hypothesis about significant macrosegregation caused by axial DC current and transverse magnetic field is not confirmed.
- Slowly rotating transverse magnetic field creates 3D helical macrosegregation pattern within the ingot. Stirring caused by field rotation is slower than TEMC.
- It is experimentally proven, that if electromagnetic stirring caused by magnetic field rotation is of comparable intensity with TEMC, then structure is refined and more homogeneous than without magnetic field or with static field.

1.5. Author contribution

As a part of this thesis, experimental work is done to study the influence on the structure of alloys by applied magnetic field with different directions and magnitudes. In this work low temperature alloys (Sn-Pb and Sn-Bi) are used for investigation of magnetic field on the micro and macro structures of binary alloys. These alloys have been widely used for directional solidification experiments aimed at investigation of structure dependence on various growth parameters and solidification conditions. Directional solidification experiments are done in Bridgman setup at controlled solidification velocity. Directional solidification experiments in Bridgman setup are done with various alloys: Sn-10%wt.Pb, Sn-20%wt.Bi. Experiments are done with static transverse or axial magnetic field, and slowly rotating magnetic field. In these experiments magnetic field is created by permanent magnet system. Moderate magnetic field values up to 0.5 T are used.

Also experiments combining magnetic field and applied electric current through the solidification interface are done. Electric current interacts with magnetic field and create similar flow pattern in the melt than TEMC. These similarities are experimentally and theoretically analysed in this work.

Directional solidification under slowly rotating transverse magnetic field is done as well. In this case direction of thermoelectromagnetic convection is varying in time and thus structure of alloy is affected in different way than in case of static field. Choosing higher magnetic field rotating velocity it is possible to combine the effect of thermoelectromagnetic convection and stirring of liquid phase by rotating magnetic field. Obtained experimental results show that with this method it is possible to achieve homogeneous and fine grained structure and prevent component segregation.

Experimental setup used in the experiments described in this thesis has been designed and built specifically for this purpose as a part of this work by the author of the thesis. Permanent magnet arrangement has been used to achieve up to 0.5 T high magnetic fields, which can be changed from axial to transverse direction and also can be rotated by programmable step-motor around the crucible. This solution simplifies the experiment and allows conducting long-term experiments more effective.

Experimental setup to measure absolute thermoelectric power (ATP) of liquid metallic alloys has been designed and built by the author. ATP of Sn-Pb alloys has been measured in wide temperature and composition range. Results of these measurements are used to quantify expected TEMC in following work.

Numerical modelling of TEMC around the solid phase dendrite array and at the interface between two media has been done by the author using FLUENT and COMSOL software. Precise modelling of thermoelectric boundary condition description at the solid-liquid interface has been done. Order of magnitude estimations of thermoelectromagnetic current and convection velocity have been carried out, comparing the relation between convection intensity and properties of the media and characteristic grain size and component segregation along the cross section of the sample.

Main experimental and theoretical results of the work has been summarized in several publications written by the author of theses, and has been published in internationally reviewed journals and reported in international and local conferences (see section 9.1).

1.6. Scientific novelty

Aim of the thesis is to experimentally demonstrate the possibilities to affect the solidified structure of binary or multicomponent metallic alloys by means of TEMC. Experimental part of this work is measurements of absolute thermoelectromagnetic power of alloys in solid and liquid state and directional solidification experiments of Sn-Pb and Sn-Bi alloys. Measurements of absolute thermoelectric power of an alloy in such a wide temperature and composition range were done for the first time. Directional solidification under axial and transverse static magnetic field is done showing the influence on the macrosegregation caused by magnetic field. Component distribution along the cross section of the sample is measured by scanning electron microscopy, this method is more accurate than analysis of micrographs. It is shown that applied transverse magnetic field (0.3-0.5 T) causes significant macrosegregation at slow pulling velocities (below 10 μm/s). Dendrite spacing as a function of growth velocity and applied magnetic field has been measured and compared by other experimental results and theoretical models.

Combined action of thermoelectromagnetic convection and magnetic field interaction with applied electric current through the solidification front, has been studied by using both DC and 50 Hz AC current. Heuristic idea about similarities between TEMC and electromagnetic convection has been analysed and experimentally and numerically validated.

Influence of the slowly rotating transverse magnetic field on the structure of an alloy during directional solidification has been studied. This approach creates time varying convection pattern in the liquid melt. Rotation of the magnetic field has been chosen to be slow enough that electromagnetic stirring by field rotation is comparable to thermoelectromagnetic convection. In this case 3D helical macrosegregation can be achieved which is a new interesting result. Significance of the macrosegregation depends on field rotation and solidification velocity. By studying such combined action characteristic velocity of TEMC has been evaluated from experimental results by finding the threshold value of field rotation velocity where TEMC and electromagnetic stirring is in balance. This threshold allows estimating TEMC intensity from experimental results by novel approach.

As a part of this work are solidification experiments in European Synchrotron Facility in Grenoble. In these experiments solidification of Sn-Pb, Al-Cu and Al-Si alloys under moderate magnetic field (0.08-0.2 T) has been investigated by filming the process with high energy X-rays. From these experiments some useful data about flow character in the vicinity of solidification front and dendrite fragmentation due to Lorentz force was obtained. Experimental estimation of TEMC magnitude and influence on dendrite growth direction and morphology was obtained in these experiments.

2. Theoretical background

2.1. Thermoelectric effects

In general, gradient of some quantity induces a density of flux. For instance gradient of potential induces current flow and gradient of temperature induces heat flow. But also gradient of temperature can induce current flow and gradient of potential can induce heat flow. These are called thermoelectric effects. Thermoelectric effect is a conversion of thermal gradient into potential difference or vice versa. This effect was discovered in 1821 by Estonian-German physicist Thomas Johann Seebeck. Seebeck effect has been exploited in thermocouples where voltage generated by the pair of materials is measured and later recalculated to temperature. Inverse effect also exists, namely current flow through the contact place between two materials can cause heat emission or absorption. This is called Peltier effect and was discovered in 1834 by French physicist Jean Charles Peltier. Peltier effect is used in thermoelectric cooling or heating devices. Absolute thermoelectric power (ATP) is the intrinsic property of each metal or metallic alloy. It depends on temperature and internal stresses, and composition in case of an alloy. Absolute thermoelectric power is defined as voltage on the ends of an open conductor if the temperature difference between its ends is 1 K. For most of the metals values of ATP lay between -20 μV/K and 20 μV/K. Exceptions is Li and Co which has ATP up to +30 μV/K. However for some semiconductors ATP can reach even few hundred μV/K (Zide, et al. 2005). In practice, differential thermoelectric power is used more often. It characterizes a pair of materials with ATPs of S_A and S_B, and is defined as difference between them.

$$P = S_A - S_B \tag{2.1}$$

Thermoelectric voltage then can be calculated as a multiplication of differential thermoelectric power and temperature difference between the hot and cold ends of the thermocouple. If ATP temperature dependence is taken into account, then thermoelectric voltage can be calculated by applying second Kirchhoff law to the circuit consisting of two conductors.

$$V = \int_{T_1}^{T_2} (S_B(T) - S_A(T))dT \tag{2.2}$$

Where T_1 and T_2 is cold end and hot end temperatures and V is voltage generated by the thermocouple. In continuous media, if temperature gradient is applied, additional electric field is generated by thermoelectric effect, which in some particular cases can result as a thermoelectric current circulation.

Relation describing the electric current flow in the continuous media is Ohm's law (2.3). Thus electric current in the media can be also caused by temperature gradient; law can be generalized by including thermoelectric term.

$$\frac{\vec{j}}{\sigma} = \vec{E} + \vec{u} \times \vec{B} - S\nabla T \tag{2.3}$$

When a current is flowing through a junction composed of two materials, then heat is absorbed in one side of the junction and is released at the other side. Amount of heat transported by the current in this way is proportional to the electric current and if the current is reversed then also direction of heat transport reverses. Peltier heat per unit junction cross section can be calculated as shown in equation (2.4).

$$Q = \left(\Pi_B - \Pi_A\right) jt \tag{2.4}$$

Where Π_A and Π_B are corresponding Peltier coefficients. This effect can be explained by the fact that in different materials charge carrying electrons have different mean energy. When electron moves from materials where it has highest energy to lowest the energy difference is dissipated as lattice thermal energy. This is called positive Peltier effect, if current is reversed then thermal energy is absorbed and junction is cooled by the current flow (negative Peltier effect). It was observed by English physicist Lord Kelvin (William Thomson) in 1855 that heating or cooling also takes place inside of a current carrying conductor subjected to temperature gradient. Any current carrying conductor with a temperature difference between two points either absorbs or emits heat, depending on the material. If a current density j is passed through a homogeneous conductor, the heat production q per unit volume is:

$$q = j^2 / \sigma - \mu j \theta \tag{2.5}$$

Where μ is called Thomson coefficient and θ is temperature gradient. First term is Joule heating, while second is Thomson term describing heat release or absorption in the material due to charge carrier energy temperature dependence within the conductor.

Thomson coefficient, Peltier coefficient and absolute thermoelectric power are related by Thomson relations.

$$\mu = T\frac{dS}{dT} \tag{2.6}$$

$$\Pi = ST \tag{2.7}$$

2.2. Thermoelectric magnetohydrodynamics

The term thermoelelectric magnetohydrodynamics was introduced by Shercliff (J. Shercliff 1979) in the seventies of 20th century. He developed the idea that thermoelectric current in the presence of magnetic field can cause stirring or pumping of liquid conducting media. He also presented the order of magnitude estimation for a practical magnitude of TEMC velocity, showing that velocity which can be reached in the liquid lithium under high temperature gradient which can be reached in fusion reactors ($grad(T)\approx 10$ K/mm, B=1 T, S_{Li}=25 μV/K) can reach up to 25 cm/s. This principle was exploited by developing thermoelectric pumps, which were also used in practice for cooling of space ships nuclear reactors. In these pumps flow is driven by the temperature difference between the heater and cooler. If heat source is reactor itself, then positive feedback exists and the higher is reactor temperature, the higher is flow velocity in cooling circuit and cooling is more effective (Polzin 2007).

TEMC in the liquid phase has been created by thermoelectric current, driven by Seebeck voltage at the contact surface between two different materials, and applied magnetic field interaction causing Lorentz force

$$\vec{F} = \vec{j}\times\vec{B} \tag{2.8}$$

Thermoelectric current in liquid media can be expressed from Ohm’s law (2.3). Melt motion is described by Navier-Stokes equation:

$$\rho\left(\frac{\partial\vec{u}}{\partial t} + \vec{u}\cdot\nabla\vec{u}\right) = -\nabla p + \mu\nabla^2\vec{u} + \vec{j}\times\vec{B} \tag{2.9}$$

By substituting current density from equation (2.3) into equation (2.9) we get the following equation:

$$\rho\left(\frac{\partial\vec{u}}{\partial t}+\vec{u}\cdot\nabla\vec{u}\right)=-\nabla p+\mu\nabla^2\vec{u}+\sigma\left(\vec{u}\times\vec{B}\times\vec{B}-S\nabla T\times\vec{B}\right) \tag{2.10}$$

Applied magnetic field introduces two new terms in the Navier-Stokes equation. Term $\sigma S\nabla T\times\vec{B}$ is thermoelectric term, which creates thermoelectromagnetic convection in the melt. Whereas term $\sigma\vec{u}\times\vec{B}\times\vec{B}$ is magnetohydrodynamic braking force which is created by the conducting fluid motion in magnetic field, this force always acts opposite to the fluid velocity. As we see, thermoelectric force is proportional to magnetic field while MHD braking force is proportional to B square. This means that at low magnetic field values thermoelectric force is dominant, but as B increases eventually braking force grows faster and finally exceeds thermoelectric force and further increase of magnetic field reduces the convection intensity. This effect has been exploited to damp unwanted natural convection (Davoust, et al. 1997). From here, an important conclusion can be made: Thermoelectromagnetic convection intensity has a maximum at certain magnetic field value when thermoelectric and braking forces are in balance.

2.3. Solidification of binary alloys

Solidification of an alloy is a very complex multiphysical process where many physical phenomena take place simultaneously. There are many different alloys and composites used in technology today, which are produced by different methods. Simplest case is two component or binary alloy, but even for binary alloy many different aspects may influence the final solidified structure of alloy, like cooling rate, heat extraction direction, gravity field and liquid phase flow near the solidification interface (Phillips 2004). Classical binary alloy phase diagram is given in Figure 2.1

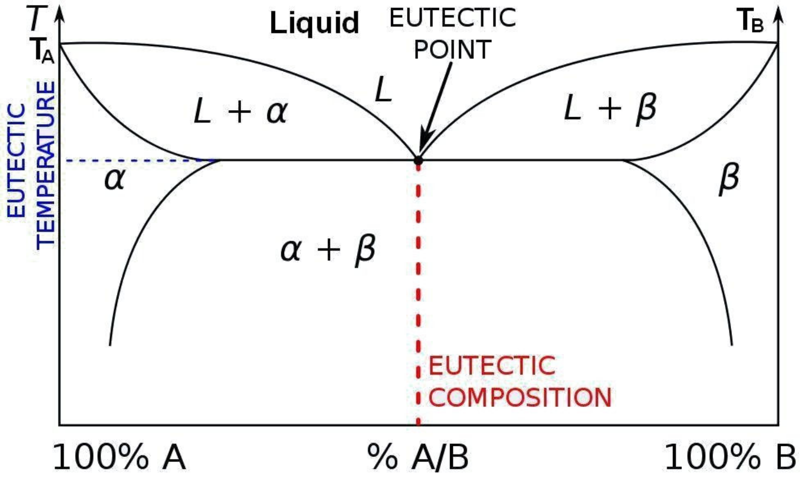

Figure 2.1: Two component alloy phase diagram

Phase diagram describes melting temperature and solidification regime ,and composition of alloy consisting of A and B components. Following regions can be distinguished in phase diagram:

Table 2.1: Different regions in phase diagram

Region	Explanation
α	Solid phase. Trace of component B is fully dissolved in component A.
β	Solid phase. Trace of component A is fully dissolved in component B.
L+α	Mixture of solid α phase and liquid melt.
L+β	Mixture of solid β phase and liquid melt.
Liquid	Fully liquid alloy.
α+β	Solid alloy consisting of regions of both phases α and β. Several possible morphologies exist.

Alloy with A concentration lower than eutectic is called hypoeutectic alloy, while if A concentration is higher than eutectic then it is hypereutectic alloy. At eutectic composition melting temperature is lowest (Eutectic temperature) and at this concentration alloy melts and solidifies similar as a pure metal without forming solid-liquid mixture. At x axis of phase diagram usually mass fraction or atomic fraction in percents are putted. Depending on alloy properties and solidification conditions, four typical solidification structures of eutectic alloys can be distinguished as listed in Figure 2.2.

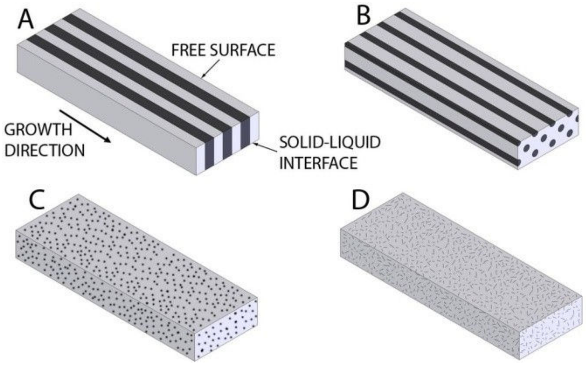

Figure 2.2: Typical eutectic structures: A) lamellar; B) rod-like; C) globular; D) acicular (Phillips 2004)

For alloys with different than eutectic composition columnar and equiaxed solidification regimes can be distinguished. Columnar structure is forming if heat is extracted directionally-columns are forming in the direction of heat extraction. While equiaxed structure is obtained during solidification of undercooled liquid, when solidification nuclei start to grow symmetrically in the volume on the liquid melt without preferred direction. If we look at the ingot structure solidified in the crucible, then both regions can be distinguished in most cases, columnar crust and equiaxed structure in the volume. This is actual problem in metallurgy because structure is not homogeneous, thus several methods have been developed how to control columnar-equiaxed transition (CET) and avoid crust formation during crucible solidification shown in Figure 2.3. Besides heat extraction direction and rate, which are hard to control in real industrial process, transition between these two structures are mostly determined by the liquid melt convection. Various methods has been developed how to control this flow and modify CET (Kurz, Bezencon and Gaumnn 2001), (Kurz and Fisher, Fundamentals of Solidification 1984).

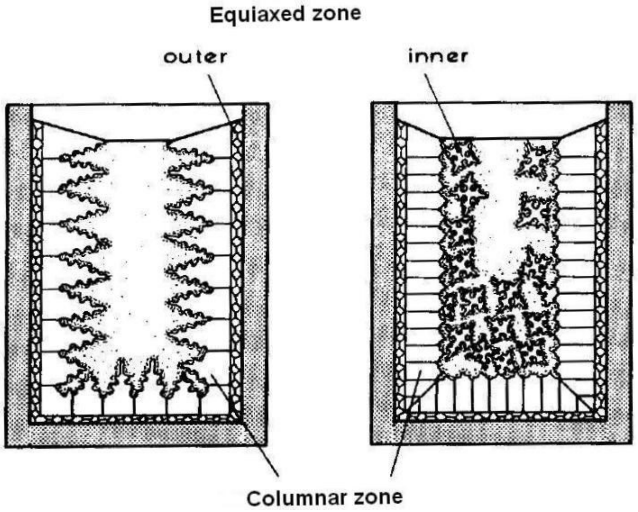

Figure 2.3: Columnar and equiaxed regions in crucible solidification (Kurz and Fisher 1984)

All pure metals at solid state have certain crystalline lattice while in liquid state only near order exists. Dendrite morphology and structure of solidified alloy is largely defined by lattice type. Fourteen different three dimension lattice types exist (Kittel 1996). Metals used in the experimental part of this work have following crystalline structures: lead has face centered cubic structure, bismuth has rhombohedral structure. Tin can exist in four allotropic structures α, β, γ, σ. Two latter allotropes appear for pure tin at temperature above 161 ^{o}C and under high pressure. Most common two allotropes are α or gray tin which have diamond cubic crystal structure and β or white tin which has tetragonal structure. For pure tin α-β transformation temperature is 13.2 ^{o}C but even small quantities of impurities can significantly lower the transition temperature or even transformation may not occur at all.

In solid and liquid phases electrons have different motion properties thus during solidification or melting, electron transport properties (electrical conductivity, heat conductivity, absolute thermoelectric power) may change with a jump. Atoms in crystalline lattice have smaller energy than in liquid, thus during solidification latent heat of fusion is released. This heat can play significant role is some cases causing local remelting of solid due to this extra heat. This mainly occurs if solidification is rapid and large amount of heat is released in short time (usually during solidification of undercooled liquid). In this case latent heat can cause remelting of solid. Latent heat of lead is 23 J/g and of tin 60 J/g (Brandes and Brook 1992). During slow directional solidification this heat source does not play any significant role.

During dendritic solidification of binary alloy local change of composition takes place. Growing dendrite or nucleus more likely attracts atoms of one component than the other. This is characterized by the partition coefficient *k* which shows the ratio between newly solidified solid phase and liquid phase.

$$k = \frac{C_S}{C_L} \tag{2.11}$$

This ratio defines normal gradient of solute concentration at the solidification front as

$$\left(\frac{dC}{dx}\right) = -\frac{v}{D} C_l (1-k) \tag{2.12}$$

Where C_l is nominal concentration, D is diffusion coefficient, v is solidification velocity. In uniformly undercooled melt solidification starts with spontaneous formation of small solid nuclei which then continues to grow. In practice most common is heterogeneous nucleation when nucleation starts from solid impurity or oxide particles in the liquid or from crucible walls. In this case nucleation activation threshold can be significantly lower and much smaller undercooling of liquid is possible. Small nucleus continues to grow if certain undercooling is reached or if it can overcome energy threshold necessary for further nucleation, which is called critical activation energy.

$$\Delta G_n = \left(\frac{16\pi}{3}\right)\left(\frac{\sigma^3}{\Delta g^2}\right) \cdot f(\vartheta) \tag{2.13}$$

Where σ is solid-liquid interface energy and Δg is differential Gibbs free energy between solid and liquid per unit volume. Gibbs free energy (also free enthalpy) is thermodynamical potential of the system characterizing systems energy at constant temperature and pressure, ϑ is wetting angle between melt and solid particle or crucible wall and it is the main parameter determining possible undercooling. Function *f(ϑ)* may vary from 0 (complete wetting), which means that any undercooling of melt will trigger nucleation to 1, which corresponds to homogeneous nucleation. If nucleation starts it continues exponentially under saturation is reached, nucleation rate is given by following expression:

$$I = I_0 \cdot \exp\left(\frac{\Delta G_n + \Delta G_d}{k_b T}\right) \tag{2.14}$$

Where I_0 is constant determined by heat extraction rate and other circumstances, ΔG_n is activation energy given by equation (2.13) and ΔG_d is activation energy for atom transfer from solid to liquid phase.

2.4. Directional solidification

Experimental work of this thesis is aimed to determine the effects on crystalline structure caused by forced convection in the melt and mushy zone. Directional solidification is a particular kind of solidification when solidification front moves in one direction remaining parallel to itself over time. This kind of solidification with strictly controlled parameters as temperature gradient and growth velocity, is widely used for experimental study in solidification science. Directional solidification is usually done in Bridgman setup which is also used in a photovoltaic and electronic silicone growth (renewable-energy-concepts 2012). This method allows us to know the crucial parameters of the system at all time, thus such relation as grain structure and sizing dependence on growth velocity and other scan be experimentally validated. Directional solidification at various velocities will be performed to develop and validate numerical models and theoretical estimations.

In the directional solidification, initial position is assumed to be flat solid–liquid interface from which solidification continues. In case of binary alloy at the solidification front will always exist regions with different compositions, temperatures or curvatures. All these parameters contribute to the fact that one component will be attracted while other is rejected. This difference will cause perturbations on the solidification front, development of which will define front shape and formation of grains, columns or lamellas.

Temperature at which solidification occurs at each point is dependent on various factors and can be expressed as described by equation (2.15) (A. Kao 2010).

$$T_i = T_0 - \frac{\Gamma}{L} T_0 \kappa - m_L (C_0 - C_i) - \frac{\nu}{\mu(\theta, \kappa)} \tag{2.15}$$

Where T_0 and C_0 are nominal melting temperature and concentration, C_i is local concentration. Second term represents additional undercooling due to front curvature (κ- mean local curvature, Γ-surface stiffness), third term represents contribution in melting temperature change caused by composition inhomogenity (m_L is liquidus slope (Line between solid and liquid in Figure 2.1), fourth term accounts for the kinetic effects due to solidification front motion with velocity ν ($\mu(\theta,\kappa)$ is coefficient showing the kinetic mobility). From equation (2.15) it can be seen that in directional solidification tip of the dendrite grows faster (T_i is lower) than the flat place at the solidification front mainly because of contribution of curvature term.

If parameters of solidification and properties of alloys are known it is possible to predict characteristic primary dendrite arm spacing or interlamellar distance during directional solidification. In ideal directional solidification characteristic distance is defined by equilibrium of capillary and diffusion effects. Characteristic planar front perturbation wavelength can be found by taking geometric mean of a diffusion length and capillary length.

$$\lambda_i = 2\pi\sqrt{\frac{D\Gamma}{v\Delta T_0}} \tag{2.16}$$

By taking into account mutual partition and diffusion, following expression can be derived to describe primary dendrite arm spacing during directional solidification (Kurz and Fisher, Fundamentals of Solidification 1984).

$$\lambda = \frac{4.3(\Delta T_0 D\Gamma)^{0.25}}{k^{0.25}v^{0.25}\sqrt{\theta}} \tag{2.17}$$

Front stability is dependent on many parameters during solidification main of which are temperature gradient, concentration gradient at the front and growth velocity. Due to composition profile at the solidification front described by equation (2.11), near the solidification front liquid region may exist where actual temperature is lower than equilibrium solidification temperature. Such zone is in metastable state and may lead to front instabilities. If this zone exists it is called constitutional undercooling. Condition for liquid above solidification front to become constitutionally undercooled is:

$$\nabla T < m \cdot \nabla C \tag{2.18}$$

Unstable growth of the constitutionally undercooled front will take place if temperature gradient due to heat flow dT_q/dz is smaller than liquid us temperature gradient dT_l/dz in liquid at solidification interface, front is stable if opposite (Figure 2.4).

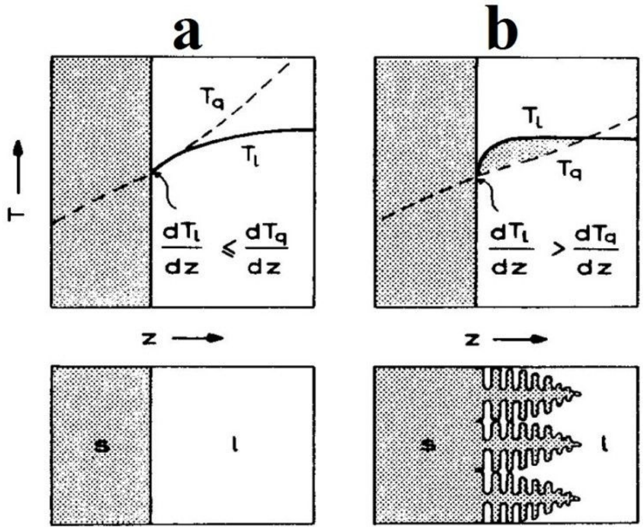

Figure 2.4: Constitutional undercooling at solidification interface: a) stable growth; b) unstable (dendritic growth). (Kurz and Fisher, Fundamentals of Solidification 1984)

2.5. Role of convection during directional solidification

If any kind of liquid melt convection is present then solidification structure and spacing can be radically different than predicted by equation (2.17) which was developed by analyzing fully diffusive solidification regime. Convection in the melt can be caused by mechanical stirring or various electromagnetic methods (forced convection). But there is also convection which inevitably appears in the melt due to thermal expansion of the melt (thermal convection) (Muller, Neumann and Weber 1984) and composition inhomogenity (thermosolutal convection) (Seifert, Reinshaus and Bachran 1998). These convections are caused by temperature and composition caused density inhomogenities of liquid melt, resulting in buoyancy driven flow. Significance of natural convection is characterized by Grashof number (2.19) which shows the ratio between buoyant and viscous forces. Buoyancy force in case of a two component alloy is created by thermal and solutal expansion. Rayleigh number (2.20) which compares the convective and conductive heat transfer mechanisms.

$$Gr = \frac{gL^3\rho^2}{\mu^2}\left(\beta\Delta T + \beta_C\Delta c\right) \tag{2.19}$$

$$Ra = Gr \cdot \Pr \tag{2.20}$$

Where L is characteristic length and ΔT temperature difference along this length, $\alpha=\lambda/\rho c_p$ is thermal diffusivity, $Pr=\mu/\alpha\rho$ is Prandtl number, Δc is composition difference over length L and β_C is concentration expansion coefficient. Thermosolutal and thermal convections can be analysed separately by introducing thermosolutal and expansion Rayleigh and Grashof numbers characterizing solely the contribution by one of these effects. In case of directional solidification temperature effects are usually of considerable importance because of high temperature gradient.

There are several works dealing with the research of thermal and thermosolutal convection influence on the solidification structure (Wettlaufer, Worster and Huppert 1997), (Szekely and Chhabra 1970) these works qualitatively agree that presence of convection during directional solidification reduces dendrite spacing. In directional solidification primary dendrite spacing is changed by convection according to relation (2.11) if w is melt flow velocity entering the mushy zone, v is growth velocity and λ_0 is primary dendrite spacing at purely diffusive solidification.

$$\lambda = \frac{\lambda_0}{\sqrt{1+w/v}} \tag{2.21}$$

In some cases convection in the melt is unwanted. One of the methods to reduce convection is application of strong magnetic field which damps the macroscale convection (Prescott and Incropera 1993), (Vives and Perry 1987), (Li, Noeppel, et al. 2009). To eliminate these types of convection completely, experiments are even done in microgravity during parabolic flight (Dupouy, Camel and Favier 1989).

2.6. Thermoelectromagnetic convection

At the solidification interface most of the metals and metallic alloys have jump of absolute thermoelectric power. Temperature gradient is usually present at the solidification front. These conditions mean that at the solidification front thermoelectric current circulation may appear. By applying external magnetic field, Lorentz force appears and forced convection of the liquid phase in the vicinity of the solidification front can be introduced (TEMC). In case of multicomponent alloy convection takes part in the solute and heat transport in the mushy zone and in the liquid part of the ingot, which later affects the structure of the alloy. It is shown that macrostructure and microstructure can be affected by this mechanism (Li, Ren, et al. 2012). Influence of TEMC on the structure of an alloy is usually studied during directional solidification of an alloy in Bridgman apparatus (Lehmann, Camel and Bolcato 1998), (Garandet and Alboussiere 1999) or similar.

First publications on the effect of liquid phase motion in static field appeared in the second half of twentieth century when semiconductor production became an actual problem (L. Gorbunov 1987). The idea of influencing the interdendritic convection by magnetic field during solidification is relatively new and was introduced by Moreau and Lehmann (Lehmann, Camel and Bolcato 1998) in the nineties. Temperature gradient at the solidification front can be quite high thus even with moderate magnetic field quite strong convection can be reached. Solute and energy transport due to this convection may then affect macrosegregation, cell and dendrite morphology and even solidification front shape. This type of convection and its influence on the dendrite growth, macrosegregation and interface morphology will be analysed in more detail in following chapters of this thesis.

3. Thermoelectric property measurements

3.1. Introduction

To maximize the magnetic field influence on the structure of the alloy in Bridgman directional solidification setup, choice of appropriate alloy is important point. Absolute thermoelectric power (ATP) is the intrinsic property of each pure metal or alloy. ATP depends on electron structure and lattice type of metal. In monocrystalline material ATP is a tensor (Gasser 2008), (A. Marwaha 1967). It also may be significantly dependent on lattice defects, impurities, even for small concentrations, and on internal stresses and temperature. Due to these reasons, there are difficulties to accurately measure this property for an alloy with certain composition. Usually in literature ATP for tempered polycristalline material is given. It is important to know these properties as a function of temperature and composition in both solid and liquid state for an accurate prediction of thermoelectric phenomenon during solidification, including TEMC in liquid metals. In this chapter measurement setup for ATP measurements is described and ATP of different Sn-Pb alloys was measured as a part of this work. For Sn-Pb alloys ATP were measured in wide temperature and composition range. This is an important step for the further work for the result interpretation and more accurate order of magnitude analysis of TEMC during directional solidification.

3.2. Theoretical background

Multiple theories to calculate ATP values theoretically have been developed, but none of them seems to be reliable to predict the ATP precise enough, even for pure metals (Gasser 2008). In recent years due to development of the computing technique, it is possible to calculate structure factor and pseudopotential form factor of the crystalline lattice more accurate, which are needed to calculate theoretical values of ATP of a metal in polycrystalline state, according to Ziman (Khalouk, Chaib and Gasser 2009) theory, the most common theory used to describe ATP theoretically. This theory correlates ATP with other electronic transport properties, like resistivity and heat conductivity, in solid and liquid metals, and according to this theory, in crude approximation, ATP is proportional to the derivative of resistivity versus temperature. There are some research done which confirms this relationship for some metals and alloys. According to this theory ATP of all polyvalent metals should be negative, and increasing by absolute value with temperature.

ATP can be theoretically explained from electron theory similar like thermal and electrical conductivities. Electric current carried by one electron can be calculated as evf_k, amount of heat transported by electron can be found as $(E_k - \mu_e)vf_k$. To obtain heat and current flux carried by all electrons in conductor one must add up contribution from all electrons within the observed volume. Here f_k is form factor, v is electron velocity, k is Boltzman constant, E is Fermi energy, ρ is resistivity, e is electron charge, q is volume charge density.

$$J = q\int vf_k \frac{dV_k}{4\pi^3} \tag{3.1}$$

$$Q = q\int (E_k - \mu_e)vf_k \frac{dV_k}{4\pi^3} \tag{3.2}$$

ATP can be expressed as

$$S(E) = \frac{\pi^2 k^2 T}{3eE}\left|\frac{\partial \ln E(\rho)}{\partial \ln(E)}\right| \tag{3.3}$$

If ATP and electrical resistivity are known for liquid metal then heat conductivity can be calculated by using Wiedemann-Franz law (Graf, Yip and Sauls 1996). It has been shown this law is valid for most of the liquid metals with sufficient accuracy. This is quite important aspect because heat conductivity should be measured in static fluid, but temperature gradient necessary to measure it creates unwanted convective heat transfer (Gasser 2008).

During solid-liquid transition and allotropic phase transformations, jump of absolute thermoelectric power occurs, which can be explained in the following way. In solids, an electron cloud of each ion in the crystalline lattice is affected by the electric field of its neighbour atoms. In liquid sate no crystalline structure exists and electron transport conditions are different, leading to different electronic transport properties, ATP among them (Favier, et al. 1996). In liquid state there are no theories predicting ATP theoretically thus experimental measurements is the only way to get to know these quantities.

Another point of importance of measuring ATP in solid and liquid states is because during solidification of metallic alloy thermoelectric current circulation may appear in the vicinity of solidification front. Particularly important is to know the different ATP between solid and liquid states at the melting temperature as a function of composition of an alloy, because thermoelectric current is created by this difference.

Values of ATP given in literature are given for tempered, polycrystalline metal, where no internal stresses are present. However in different sources those data for the same metals varies significantly, especially for liquid metals. This dispersion can be related to the variety of used measurement techniques, which produces different systematic errors. Indicative ATP-temperature dependence for various metals is given by Shercliff (J. Shercliff 1979). One of the widest summaries of thermoelectric properties of various metals and some most popular thermoelectric alloys can be found in Handbook of Physical quantities (Grigoriev and Melnikov 1991). Nevertheless data for each individual material is still fragmentary, especially for liquid state. Because of difficulties to measure ATP, in the literature usually relative thermoelectric voltage is given versus reference material with known ATP. Before 1990 when international temperature standard was changed, reference material usually was lead, but in new temperature scale International Temperature Scale 90 (ITS90) reference material is tungsten (ITS90 2000).

ATP for lead and tin has been measured by Cusack in solid and liquid state (Cusack and Kendall 1958), (Marwaha and Cusack, The absolute thermoelectric power of liquid metals 1965). In these articles ATP of different liquid metals, pure Sn and Pb among them, is measured and result is given in form $S=a+b\cdot T$. ATP of Sn-Pb alloys as a function of concentration at room temperature has been measured by Pascore (Pascore 1976). Measurements of Sn and few other metals are done by Bath (Bath and Kleim 1979). Alloy which can generate large electric current at the interface during solidification must have good electrical conductivity in solid and liquid phases and high differential thermoelectric power between solid and liquid phases at melting temperature. Figure of merit Z is a quantity which is widely used to characterize material efficiency for thermoelectric heating and cooling elements.

$$Z = \frac{\sigma \cdot S^2}{\lambda} \tag{3.4}$$

Force density which generates liquid phase motion due to thermoelectric current and magnetic field interaction is $\sigma S \vec{\nabla} T \times \vec{B}$. The motion intensity is proportional to electric conductivity and absolute thermoelectric power, and temperature gradient. To maintain sufficient temperature gradient with certain heat flux material should be with low heat conductivity. In our case optional quantity to compare in order to find optimal alloy for solidification experiments under moderate magnetic field is ratio Z_{TE} (also called thermoelectric figure of merit), which has dimension of [A/W] and which shows the material ability to generate current when certain heat flux is applied. Summary of properties of some pure metals and their figures of merit is given in Table 3.1.

$$Z_{TE} = \frac{\sigma \cdot \Delta S}{\lambda} \tag{3.5}$$

Table 3.1: Comparison of thermoelectric figure of merit of some pure metals

	S(μV/K) Solid state at T_m	S(μV/K) Liquid state at T_m	Electric conductivity $\sigma\cdot 10^6$ [Sim/m]	Thermal conductivity λ [W/K·m]	Figure of merit ($\sigma S^2/\lambda$) $Z\cdot 10^{-6}$	TE figure of merit $\sigma\Delta S/\lambda$ [A/W]	Melting temperature T_m (C^0)
Al	-2.1	-3	35	237	0.65	0.13	660
Cu	7.4	—	57	390	8.00	—	1085
Pb	-2.4	-3.4	4.8	33	0.84	0.15	328
Li	15	20	10.8	85	28.59	0.64	180.5
Sn	-1.8	-0.6	8.7	67	0.42	0.16	232
Na	-9	-9	20.1	142	11.47	0.00	98
K	-16	-13	13.9	102	34.89	0.41	63.4
Hg	-3.5	-3.5	1.04	8.3	1.53	0.00	-39
Bi	-2	-0.7	0.78	8	0.05	0.13	271.5
Ga	-0.2	-0.4	3.7	41	0.01	0.02	30
In	-1.4	-1	11.9	82	0.15	0.06	314
Sb	-0.4	0	2.4	24.4	0.02	0.04	631

Data summarized in Table 3.1 are extracted from the references mentioned in text above and (Brandes and Brook 1992). However knowledge of ATP of each component does not allow predicting ATP of an alloy. ATP data of alloys is quite fragmentary or absent at all. Summary shows that lithium and potassium have the highest TE figure of merit. However solidification experiments with these metals are complicated and does not have large practical interest. In this chapter ATP of Sn-Pb alloy will be measured as a function if temperature and composition to deduce the optimal concentration which will be used in further solidification experiments.

3.3. Experimental setup for ATP measurements

An experimental setup (Figure 3.1) was designed to allow measuring ATP continuously in both solid and liquid states in temperature range from room temperature to 600 ^{0}C. Alloys at right compositions, are prepared using high purity lead and tin (99,99%). Quartz tubes with inner diameter of 4 mm, wall thickness of 1 mm, and length of 120 mm are filled with these alloys. After tubes are cooled to room temperature, a pair of 0.2 mm diameter copper and constantan electrodes is soldered with the same alloy to the each end of the tube. Copper-constantan electrode pair is chosen to form a T-type thermocouple, for which ITS-90 voltage-temperature and vice versa relations are known with high accuracy (National Institute of Standards 2010). If cold end of the thermocouple is at 0 ^{0}C temperature, and thermoelectric signal U is measured, then temperature T can be found according to equation (3.6).

$$T = \sum_{n=0}^{6} b_n \cdot U^n \tag{3.6}$$

where b_n are coefficients given by tables for certain temperature intervals.

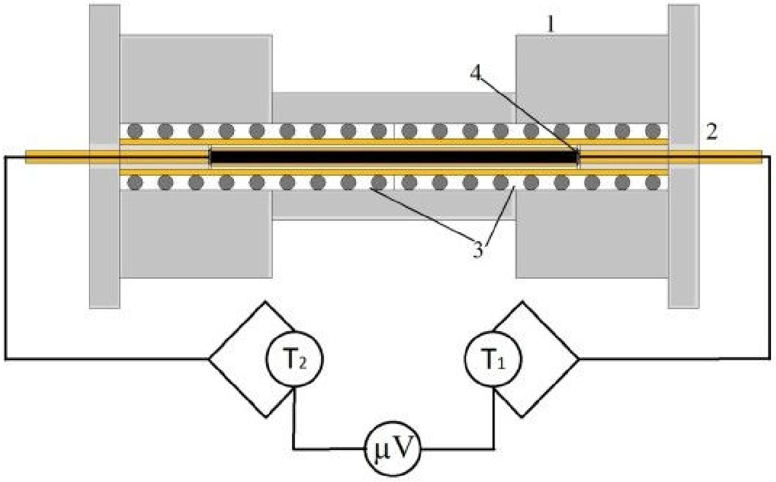

Figure 3.1: ATP measurement setup (1-thermal insulation, 2-two channel alumina tube with copper and constantan electrodes, 3- kanthal electric heaters, 4-ceramic sealing and electrode contacts at the end of the tube)

Ends are then sealed with high temperature resistant zirconium silicate based ceramics. In order to prevent tube breaking due to thermal expansion of the metal, small holes are left in the sealing. Heating is performed by two kanthal electric heaters, allowing to control temperature difference between both ends of the sample. Extra thermal insulation is added at the ends of the heaters to compensate heat losses through the ends of the tube, and, more important, to reduce temperature gradient in these regions where the contact between electrodes and metal is taking place. This reduces the error if the electric contacts between metal and both electrodes are not exactly in the same point. To calculate ATP, temperatures of both ends of the tube are measured by T-type thermocouples, thermoelectric signal generated by the sample metal is calculated by measuring signal between copper electrodes and then subtracting the signals generated by electrodes.

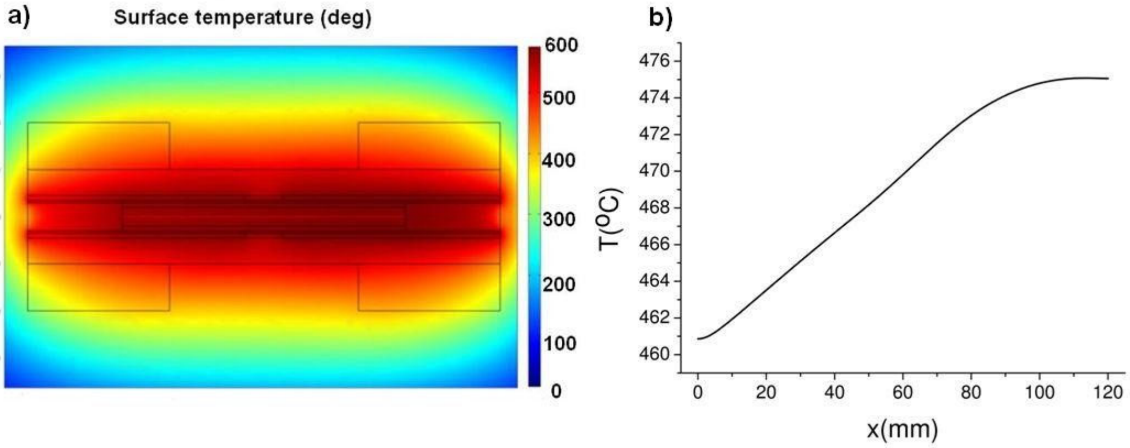

Figure 3.2: a) Calculated temperature distribution along the cross section of the experimental setup the setup; b) Temperature profile along the axis of the sample

ATP is defined as:

$$S = \frac{\partial V_0}{\partial T} \tag{3.7}$$

where V_0 is the signal between ends of the open circuit of the metal if ends are at different temperatures. Measured signal in our setup, V is a sum of signal generated by the sample metal V_0 and signals generated by both copper electrodes. By applying second Kirchhoff law to the circuit consisting of copper electrodes and sample metal, we get:

$$V = \int_{T_0}^{T_2} S_{Cu}(T)dT + \int_{T_2}^{T_1} S(T)dT + \int_{T_1}^{T_0} S_{Cu}(T)dT \tag{3.8}$$

where S_{Cu} and T_0 is ATP of copper and cold end temperature of electrodes respectively. Assumption is made that ATP of sample does not change significantly within the temperature interval from T_1 to T_2. Therefore, ATP of the sample metal S is then calculated as:

$$S = \frac{V - \int_{T_1}^{T_2} S_{Cu}(t)dt}{T_1 - T_2} \tag{3.9}$$

In this work following absolute thermoelectric power of copper is used (Grigoriev and Melnikov 1991), (Brandes and Brook 1992)

$$S_{Cu} = 1.684 + 0.00507 \cdot T \quad (3.10)$$

We note that using equation (3.9) leads to the average sample ATP between T_1 and T_2, attributed to the temperature value $(T_1+T_2)/2$. To verify the performance and accuracy of our experimental setup, we first measured the ATP of pure lead and tin and compared our results with data available in literature (Cusack and Kendall 1958), (Marwaha and Cusack 1965), (J. Shercliff 1979), (Pascore 1976). Three measurement sessions were done with pure lead and tin. Measurements are performed either when $T_1>T_2$ and $T_2>T_1$. Points are recorded at quasi-stationary state to avoid errors due to response time of measuring devices.

3.4. Measurement procedure and main difficulties

Sn-Pb alloy is chosen to be measured because this alloy is widely used for solidification research and model experiments in liquid phase convection research. In this work ATP of pure Sn and Pb is measured in wide temperature interval from room temperature to 600 °C. Following composition alloys has been measured: Pb-20wt.%Sn, Pb-40wt.%Sn, Pb-60wt.%Sn and Pb-80wt.%Sn. Measurements are done by gradual heating and cooling as well. During such measurements moving from liquid state to solid, undercooling of liquid was observed when measured ATP suggests that alloy is still liquid at the temperature under melting temperature. Reading of signals has been done in continuous regime at different heating or cooling rates within the range 1-20 K/min to determine the effects of thermal inertia on the results. For the reference some points are measured in static situation when thermal equilibrium is established. Experimental results with high heating and cooling rate exhibit much larger difference between measurements done during heating or cooling, thus they will be eliminated in future processing and presentation of experimental results. This discrepancy of results measured in dynamic regime may arise because of the delay of the nanovoltmeter.

Necessary heater power to achieve 600 °C is approximately 50 W for each heater. Increasing or decreasing heating power of one or both heaters allows to change temperature and temperature difference between the ends of the sample. Before making measurement in steady state, heater powers are kept constant for at least 5 minutes.

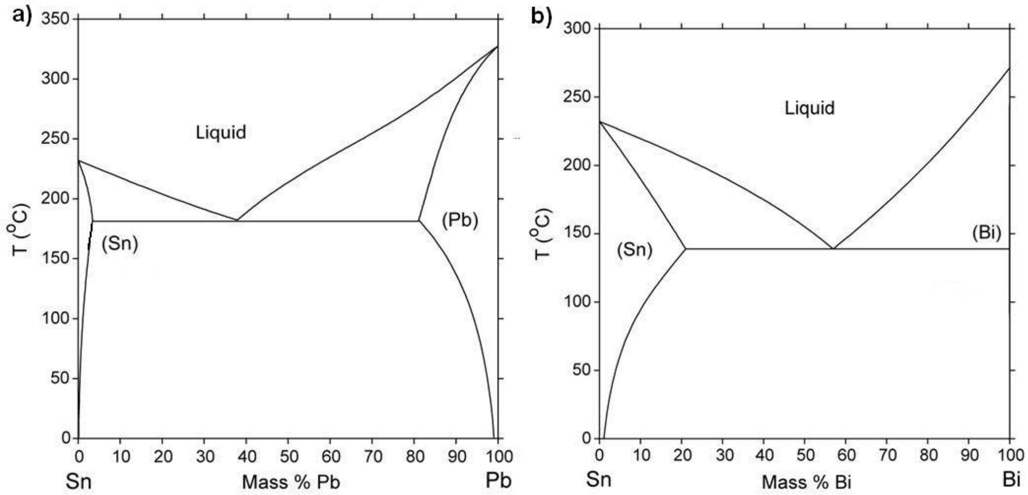

Figure 3.3: Phase diagram of Sn-Pb (a) and (b) Sn-Bi alloys (NIST 1998)

Accuracy of the microvoltmeters used in temperature measurements is 2 μV, and accuracy of nanovoltmeter is 100 nV. From here we can calculate the total error of ATP calculated from equation (3.9).

$$\Delta S = \frac{1}{(T_2 - T_1)^2} \sqrt{((V - \int_{T1}^{T2} S_{Cu} dT) \cdot \Delta T)^2 + \left((T_2 - T_1)\Delta V\right)^2} \qquad (3.11)$$

ΔT=0.1 K is temperature measurement accuracy, ΔV=0.1 μV is voltage measuring accuracy. This calculation give us the maximal total error of ATP of 0.1 μV/K. Additional error can be introduced if the contact between both electrodes of thermocouple and sample metal are in slightly different locations. Error due to this reason can be estimated using assumption that distance between contact places is 0.5 mm, which is reasonable if the diameter of each electrode is 0.2 mm. We get temperature measurement error of 0.1 K at each end of the sample, which may introduce up to 0.05 μV/K additional errors in result. The total accuracy of the results presented results is expected to be smaller than 0.15 μV/K which is reasonable compared with data available for solid metals. But as mentioned before reliable data for liquid metals are quite scarce, and the present work is a definitive improvement compared with available results.

ATP is very sensitive to other factors, whose impact on results is difficult to estimate. Thus we cannot be sure that our measurement results will agree with real values within this error range. Tempered copper and constantan thermocouples used in these experiments were calibrated before measurements from room temperature to 800 K, and agreed with (National Institute of Standards 2010) within the range of errors. Variation of ATP of metals due to deformations is relatively low, but it increases rapidly when threshold of plastic deformations is reached. For copper this threshold is about $1 \cdot 10^8$ Pa (Brandes and Brook 1992), leading to a critical force for the 0.2 mm diameter wire equal to 2.8 N. Thus electrodes after tempering should be handled very carefully not to exceed this value.

Other potential uncertainty sources might be oxidation, impurities of ceramics particles and reaction between electrodes and sample metal at high temperatures, and natural convection which may appear in the tube when measurements in liquid state are being done. Nevertheless according to the basic theoretical concepts of ATP these factors should not affect the results. However we cannot be sure they have no influence on the results at all, and it is assumed additional error due to them is expected to be smaller than to those analysed before.

3.5. Experimental results

ATP of pure Sn and Pb has been measured (Figure 3.4) Sn-Pb alloy has been measured for following concentrations: Pb-20wt.%Sn, Pb-40wt.%Sn, Pb-60wt.%Sn and Pb-80wt.%Sn from room temperature to 600 ^{0}C.

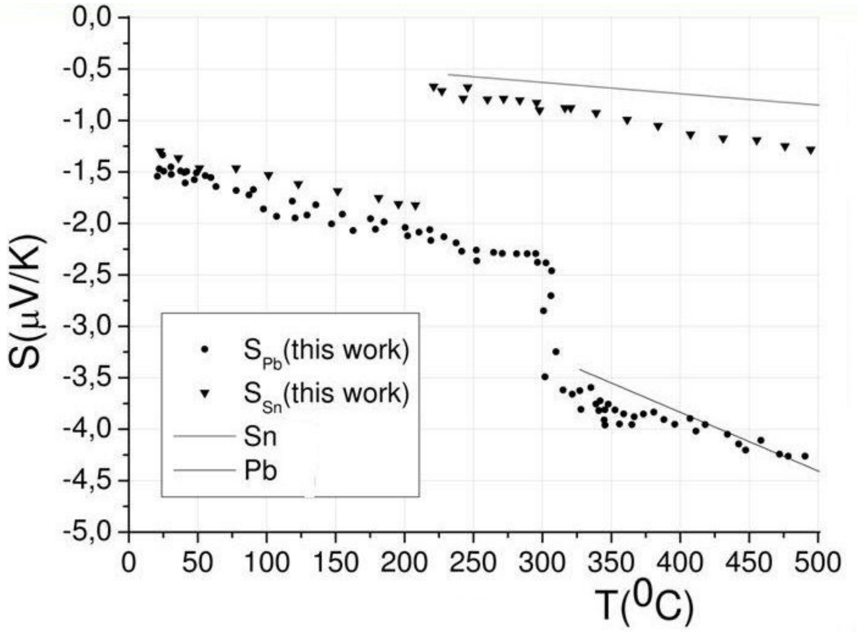

Figure 3.4: ATP of pure lead and tin. Experimental results of this work (dots and triangles) compared with (Cusack and Kendall 1958) (solid lines)

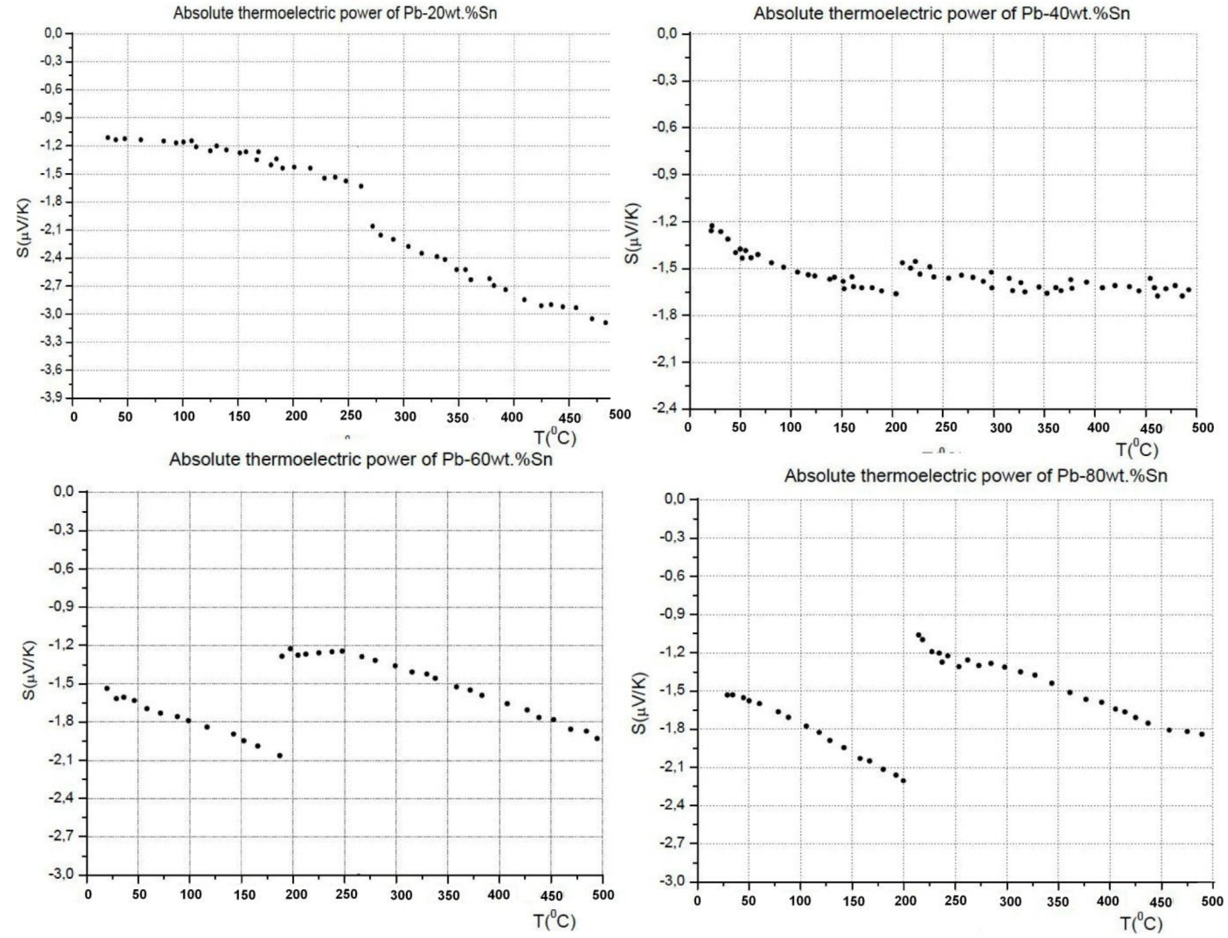

Figure 3.5: ATP of Sn-20%wt.Pb, Sn-40%.wt.Pb, Sn-60%wt.Pb, Sn-80%wt.Pb

Figure 3.4 shows that ATP of pure tin has positive jump during melting, while for pure lead it is negative. In both cases ATP increase with temperature by absolute value as predicted by equation (3.3). Figure 3.5 shows how ATP jump changes sign as Sn content in the alloy is increased. Concentration at which there is no jump of ATP during solidification or melting can be seen from Figure 3.6 and it is at concentration Pb-35%wt.Sn. Sn-Pb alloy is widely used for soldering of electronics and in many cases thermoelectric signals there are unwanted. In such applications solder with this composition could be used. ATP of liquid tin and lead has been measured and calculated according to various models by Chaib (Chaib 1987). Experimental results are in good agreement with this work while theoretical models give inaccurate results in most cases.

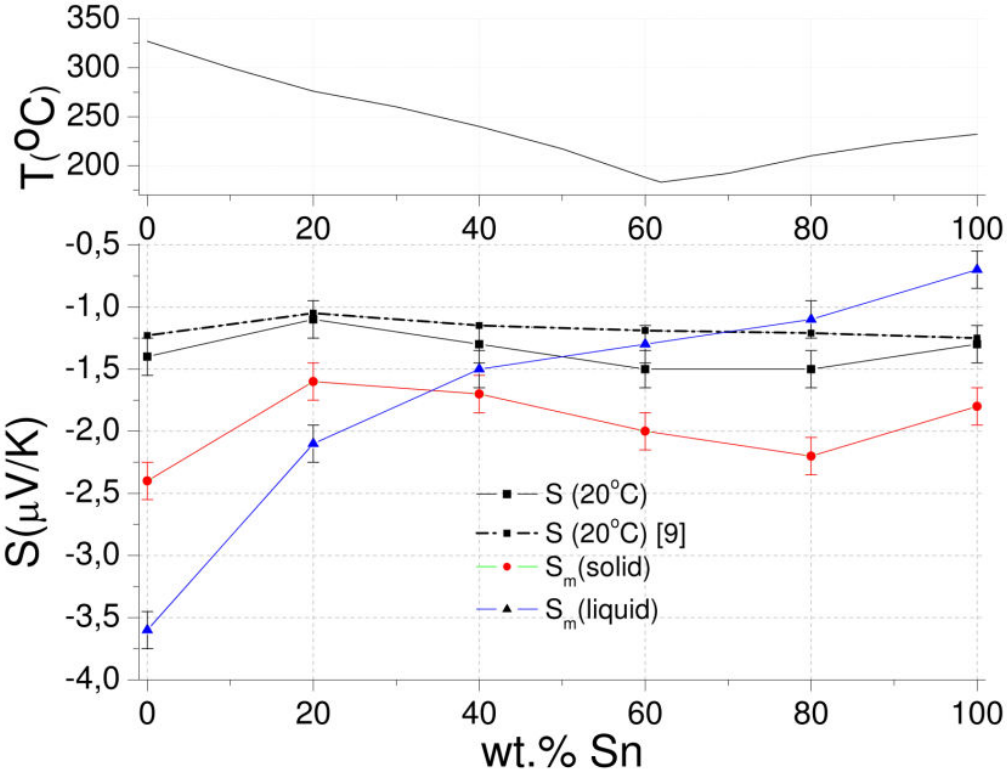

Figure 3.6: Measured ATP for different Pb-Sn alloys: squares-20 °C, circles-at melting temperature in solid state, triangles-at melting temperature in liquid state, dashed line- 20 °C (Pascore 1976). Black line above indicates the melting temperature as a function of Sn fraction

Table 3.2: Linear relationship between ATP and temperature for various Pb-Sn compositions (From Figure 3.4 and Figure 3.5)

Alloy (melting point)	Solid		Liquid	
	A (μV/K)	B·10^3 (μV/K^2)	A (μV/K)	B·10^3 (μV/K^2)
Sn (232 °C)	-1.25	-2.36	-0.18	-2.24
Pb-80wt.%Sn (210 °C)	-1.42	-3.68	-0.52	-2.76
Pb-60wt.%Sn (185 °C)	-1.44	-3.03	-0.95	-1.90
Pb-40wt.%Sn (241 °C)	-1.26	-1.82	-1.32	-0.77
Pb-20wt.%Sn (270 °C)	-1.06	-2.00	-0.93	-4.35
Pb (327 °C)	-1.36	-1.95	-2.27	-4.05

Results show that at liquid state, pure lead is much more impurity sensitive than pure tin. Measured ATP-temperature dependence for Pb, Sn and its alloys seems to be close to linear in solid and liquid states within the range of error. Linear approximation is done for each alloy separately in solid and liquid state according to equation (3.12). Coefficients of linear function are given in Table 3.2.

$$S[\mu V/K] = A + B \cdot T[^\circ C] \tag{3.12}$$

3.6. Conclusions

In order to choose optimal concentration for the planned solidification experiments, ATP of Sn-Pb alloy has been measured as a function of temperature and composition. Measurement setup for ATP measurements of metallic alloys in solid and liquid state has been developed and measurements have been made. Although high accuracy nanovoltmeters were used during measurements, precision of the results is ±0.15 μV/K due to experimental difficulties and many side factors. However the main result of the task is fulfilled and ATP jump during phase transition, which is the key parameter defining thermoelectric effect strength during solidification, has been measured.

Temperature difference of about 2-10 K is maintained between the ends of the sample, the problems emerge when sample is partially melted. In this case measured result is not accurate and is dependent on liquid/solid ratio within experimental tube. Nevertheless ATP at melting temperature can be obtained by extrapolating the measurement results obtained in purely solid or liquid phase. Close to melting point several measurement sessions were repeated with minimal temperature difference.

In the measurements described in these chapter it was found out that certain concentrations of Sn-Pb alloys has a significant ATP difference (around 1 μV/K) between solid and liquid phases at melting temperature. This is important aspect indicating that effect on the melt flow and solidification structure by applied magnetic field can be expected.

Sn-10%wt.Pb was chosen to be main alloy for further solidification experiments. This alloy has ATP change during solidification of 1 μV/K and does not change significantly with concentration close to nominal composition as shown in Figure 3.5, and it has low melting point (220 ^{0}C). Structure of directionally solidified Sn-Pb alloys has been studied by Cadirli (Cadirli and Gunduz 2000). Structure of alloy with this concentration is cellular, formed of tin grains with lead rich fraction between them.

4. Theoretical analysis and numerical simulation of TEMC

4.1. Introduction

In this chapter a simplified solution of Navier-Stokes equation will be given to estimate characteristic TEMC velocity for various cases, using order of magnitude analysis. These results are taken into account when choosing experimental parameters and alloys for directional solidification experiments. These estimations show that maximum TEMC intensity in interdendritic region is reached at quite low magnetic field values, which can be easily reached by permanent magnets or with ordinary electromagnets. Detailed analysis of thermoelectric boundary problem is given in this chapter summarizing various approximations used to describe the thermoelectric current flow at the interface between two different media. For quantitative order of magnitude analysis of TE current and convection, physical properties of Sn-10%wt.Pb alloy will be used in order to ease interpretation of experimental results in further work.

Numerical modelling nowadays is a powerful and widely used tool for quantitative research of many physical processes. It is used in industry and in academic science as well. Increase of available computing power in last few decades gives a chance to accurately simulate complicated, three dimensional processes like fluid flows and electromagnetic problems. In many cases, numerical simulation can replace experimental test or help to optimize planned experimental setup, thus making significant time and cost savings. The most popular numerical simulation software packages are Comsol, ANSYS CFX, Fluent, OpenFoam, FEMM. In this chapter results of numerical modelling of thermoelectric current and thermoelectromagnetic convection in various cases are presented. Detailed thermoelectric current flow simulations at the interface between two different media have been done by numerically solving the potential and current continuity problem at the interface between two media. This algorithm was developed in Fluent by using user defined functions. Calculation of thermoelectromagnetic flow in simple geometry with fixed dendrite mesh surrounded by liquid phase has been done. Applied electric current and magnetic field interaction has been numerically simulated in similar fashion, results of this simulation is given in chapter 6. In this case it was found that by increasing magnetic field value, characteristic convection velocity is reduced due to MHD braking which agrees well with theoretical predictions.

4.2. Literature review

Besides experimental works on solidification under magnetic field, there are some theoretical works dedicated to describe and analyse TEMC in the liquid melt near the solidification interface and its expected impacts on the structure of solidified alloy. One of the first works about magnetic field influence on solidification were done in Institute of Physics University of Latvia by Gorbunov (L. Gorbunov 1987), (Gorbunov and Lyumkis 1990). In this work he derives the simple expression for thermoelectric current density and force acting on liquid melt, and introduces dimensionless number describe the intensity of thermoelectromagnetic motion of liquid phase flow compared to viscous forces.

$$Te = \frac{\sigma \Delta S \theta B L^3}{\rho v^2} \tag{4.1}$$

Detailed analysis of TEMC intensity and its impact on the solute transport in the mushy zone is done by Lehmann (Lehmann, Moreau and Camel 1998) by analysing applied magnetic field influence on the solute and energy transport in horizontal directional solidification setup. In this work thermoelectric current and force density is analytically evaluated. Value obtained for current density is of order of magnitude of 10^4 A/m^2 . In this work dendrite spacing during directional solidification is analysed as a function of introduced forced convection intensity caused by applied transverse magnetic field. It is concluded that forced convection has small influence on the dendrite size at well established convective regime. However differences of the structure of directionally solidified Cu-Ag and Al-Cu alloys with and without magnetic field are experimentally demonstrated.

Crystal growth was numerically simulated by Lan (Lan 2004). Numerical simulation of TE current distribution in liquid phase around solidified nucleus is done by Kao (Kao and Pericleous 2012) , (Kao and Pericleous 2012). In his work dendritic growth under static magnetic field is analysed. Thermoelectric current and flow are calculated, modifications of crystal growth caused by applied magnetic field is numerically simulated. Thermoelectric current numerical simulation at the fixed solidification front is done by Xi Li (Li, Fautrelle and Ren, et al. 2009) showing the qualitative current density distribution at the arbitrarily shaped static interface. In these works it is shown that in case of dendritic solidification TE current flows from tip to root of the dendrite or opposite.

4.3. Analytical estimate of TEMC

Conditions necessary to achieve high TEMC intensity during solidification, are high differential thermoelectric power between solid and liquid phases at melting temperature, high temperature gradient along the solidification front, good electrical conductivity of both media, and non smooth solidification front shape. Ability of a pair of materials to produce thermoelectric current if certain heat flux is applied is characterized by thermoelectric figure of merit according to equation (3.5).

From Table 4.1 it can be found that figure of merit for pair of solid and liquid Sn-10%wt.Pb is equal to 0.09 A/W, which is comparable to the values of Z_{TE} of the other alloys used to experimentally study TEMC, like Al-4.5%wt.Cu (Z_{TE}=0.04 A/W) (X. F. Li 2007) or Sn-0.5%at.Bi (Z_{TE}=0.08 A/W) (Favier, et al. 1996).

Electric current flow in the continuous media is governed by generalized Ohm's law shown by equation (2.3). Thermoelectric term gives contribution into electric field if temperature gradient is present in the material, and may be a cause for thermoelectric current at the interface. If ATP is dependent only of temperature in homogeneous continuous media, then no TE current flow will appear. In this case *grad(S)* and *grad(T)* are always parallel, whereas necessary condition for the current to appear is that their cross product is nonzero. Let us look at the situation when no magnetic field is present and *E* is irrotational. If we apply curl operator to the Ohm's law in this case we get following equation.

$$curl(\vec{j}/\sigma) = -grad(S) \times grad(T) \tag{4.2}$$

This condition can be satisfied if *S* is function of the composition in binary or multicomponent alloy. But the strongest thermoelectric current may appear at the interface between two media with different ATP's. In such case *grad(S)* is always directed perpendicularly to the interface from one material to another. Thus *grad(T)* must have a component which is parallel to the interface. This criteria is usually met in dendritic directional solidification. If significant macrosegregation appears during solidification of binary alloy, then TE current can also originate in the volume of inhomogeneous solid or liquid as a consequence of *S* dependence on concentration.

Table 4.1: Physical properties of Sn-10%wt.Pb alloy used in estimations. Physical properties are given for melting temperature (T_m=220 ^{0}C)

Name	Symbol	Value	Unit
Density (s)	ρ_s	7100	kg/m^3
Density (l)	ρ	6974	kg/m^3
Electric conductivity (s)	σ_s	$4\cdot10^6$	S/m
Electric conductivity (l)	σ	$2\cdot10^6$	S/m
Dynamic viscosity (l)	μ	0.0021	Pa·s
Thermal conductivity(s)	λ_s	55	W/m·K
Thermal conductivity(l)	λ	30	W/m·K
Absolute thermoelectric power (s)[1]	S_s	$-2\cdot10^{-6}$	V/K

Absolute thermoelectric power (l)[1]	S	$-1\cdot10^{-6}$	V/K
Differential thermo electric power	P	$1\cdot10^{-6}$	V/K
Heat capacity	c_p	130	J/kg·K
Temperature gradient at the interface	θ	8000	K/m
Volumetric thermal expansion (l)[2]	β	$6.9\cdot10^{-5}$	1/K
Mass diffusivity (l)	D	$4\cdot10^{-9}$	m^2/s
Free fall acceleration	g	9.8	m/s^2
Partition coefficient[3]	k	0.1	
Solidification interval	ΔT_0	30	K
Gibbs-Thomson coefficient[3]	Γ	$0.5\cdot10^{-7}$	m·K
Liquidus slope	m	1	%/K
s-solid, l-liquid 1- (Kaldre, Fautrelle, et al. 2010), 2- (Brandes and Brook 1992), 3- (Lehmann, Camel and Bolcato 1998)			

Let us look at the arbitrarily shaped solidification front with characteristic spacing of primary dendrite arms of d. In case of a non smooth solidification front, tangential temperature gradient component exists at the solidification front, thus criteria for thermoelectric current to appear are met. Thermoelectric current will flow from the tip to the root of dendrite arm, or vice versa if differential thermoelectric power is negative (Yesilyurt, et al. 1999). In our case P is positive and temperature gradient is directed from liquid to solid, thus current in the liquid will flow from tip to the root of the dendrite arm, which is parallel to growth direction. Calculated current distribution is shown in Figure 4.1. At solidification front normal current component is conserved while tangential currents are different in both media. Thermoelectric current boundary condition at the solid-liquid interface is given by Shercliff (J. Shercliff 1979).

$$\frac{j_s}{\sigma_s}-\frac{j}{\sigma}+\tau\frac{\partial j_n}{\partial l}+u_t B_n=P\theta \tag{4.3}$$

Where j and j_s are tangential current densities in the liquid and solid regions close to the front, σ and σ_s are electrical conductivities of liquid and solid media, u_t is tangential velocity of liquid phase close to the front, but outside the viscous boundary layer, B_n is normal component of applied magnetic field induction and τ is contact resistance, which in further evaluation will be neglected. This can be done because normally wetting between liquid melt and same solid at melting temperature is complete, thus there are no sources of additional electric resistance at the interface between solid and liquid zones.

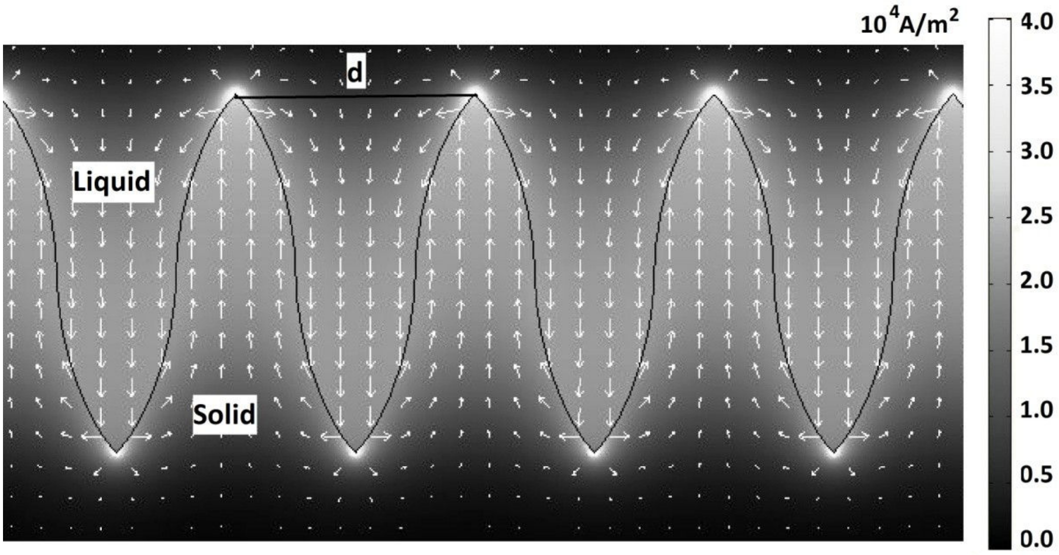

Figure 4.1: Thermoelectric current distribution at the 2D dendritic solidification front. Calculation is done for Sn-10%wt.Pb alloy (*d*=100 µm, *h*=200 µm)

In experimental study of TEMC typically static magnetic field is applied either in axial or transverse direction with respect to growth direction. With applied magnetic field convection of liquid phase is induced by Lorentz force which is the cross product and TE current as given by equation (2.8). Quantitative current flow and TE force directions are shown in Figure 4.2. Axial magnetic field induces liquid melt rotation around each axial dendrite arm while transverse field causes macroscopic flow as a result of summation of contributions of all dendrite arms.

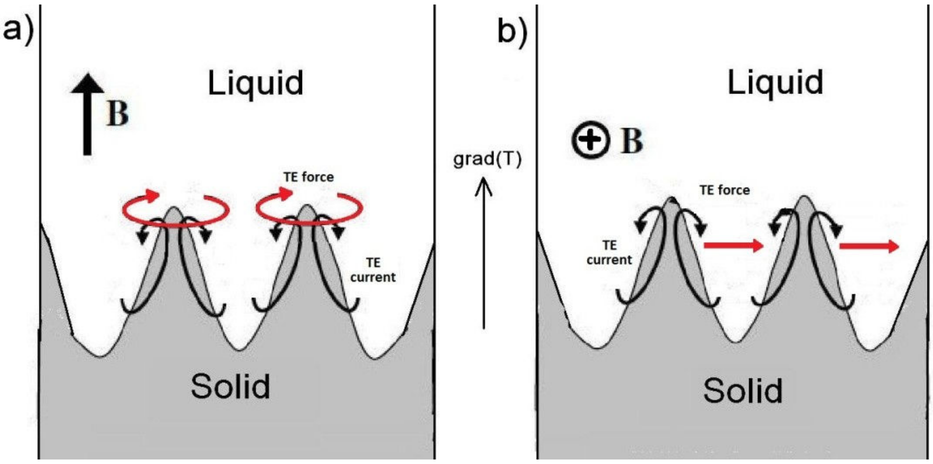

Figure 4.2: Schematic TEMC patterns at the dendritic solidification interface: a) under axial magnetic field; b) under transverse magnetic field

If no magnetic field is applied then thermoelectric voltage is the only source of current and its density order of magnitude near the solidification interface can be estimated simply from Ohm’s law applying it to the small circuit at the solidification interface.

$$j = c\sigma P\theta \tag{4.4}$$

Where c is coefficient which characterize the current loop shape at the solidification interface. It depends on the current path length in each media and ratio of electric conductivities between solid and liquid phases (Kaldre, Fautrelle, et al. 2010) as shown by equation (4.5)

$$c = \frac{1}{1 + \frac{\sigma_l d_l}{\sigma_s d_s}} \tag{4.5}$$

In following evaluation it is assumed that solidification front shape is symmetric between solid and liquid phase $d_l = d_s$, which suggest value of c equal to 0.66 which will be used in following TEMC order of magnitude estimation. By inserting the parameters from Table 4.1 into equation (4.4) we get current density value of $1.5 \cdot 10^4$ A/m^2 which agree well with estimations given by Lehmann (Lehmann, Moreau and Camel 1998) and numerically calculated and shown in Figure 4.1.

If magnetic field is applied, Lorentz force appears, and motion of liquid phase is induced. In this case situation becomes more complicated because fluid motion introduces viscous and electromagnetic induction forces. Liquid phase motion is governed by Navier-Stokes equation:

$$\rho\left(\frac{\partial \vec{u}}{\partial t} + \vec{u} \cdot \nabla \vec{u}\right) = -\nabla p + \mu \nabla^2 \vec{u} + \rho \vec{g} \beta \vec{\theta} L + \vec{j} \times \vec{B} \tag{4.6}$$

TEMC velocity order of magnitude at dendrite scale $L=d$ can be estimated by solving simplified Navier-Stokes equation where derivatives is replaced by ratios of characteristic quantities. In order to do so it is useful to introduce some dimensionless groups to characterize the ratios between different force terms. These groups are commonly used in magnetohydrodynamics to estimate which effect has to be taken into account and which can be neglected at each particular situation. Number to characterize the importance of Lorentz force by comparison with the viscous friction is Hartman number. Ratio between Lorentz and viscous force densities is then Ha^2

$$Ha = BL\sqrt{\frac{c\sigma}{\mu}} \tag{4.7}$$

Ratio between inertial force and viscous force is characterized by Reynolds number.

$$\mathrm{Re} = \frac{\rho u L}{\mu} \tag{4.8}$$

Number to characterize Lorentz force by comparison with inertia is magnetic interaction parameter N (Davidson 2001).

$$N = \frac{c\sigma B^2 L}{\rho u} \tag{4.9}$$

Buoyant force ratio to Lorentz force can be characterized by the following dimensionless group:

$$Bu = \frac{\rho\beta g L}{c\sigma P B} \tag{4.10}$$

TEMC velocity order of magnitude at the solidification front is estimated in (Kaldre, Fautrelle, et al. 2010), (Yesilyurt, et al. 1999). It can reach up to few mm/s if the characteristic dendrite arm spacing is of order of magnitude of 0.1 mm. However, real effective velocity is expected to be smaller due to crucible and mushy zone limitations. Inserting values from Table 4.1, and assuming characteristic length L equal to primary dendrite spacing d=0.1 mm and velocity u=1 mm/s for Re and N estimation we get Re=0.4, Ha^2=1, N=3, Bu=$1\cdot10^{-3}$. These numbers are calculated for the dendrite order of magnitude length scale, but in many cases different length scales can exist simultaneously causing TEMC of different scales and magnitudes (Figure 4.3). To investigate phenomena at the scale of crucible or secondary dendrite arms, different length scales have to be chosen and the ratios between forces will be different. From the estimations of dimensionless numbers, we may see that at a primary dendrite length scale, melt motion is determined by the Lorentz force, inertia and viscous force, while buoyant force can be neglected in further evaluation. In fact for a given situation contribution of inertial term is also relatively small but inertial term will be kept in further evaluation because this will allow us to obtain a solution which will be applicable also for other length scales. Inertial force plays a larger role at crucible size TEMC which can be caused by convex solidification front for example. Different length scales which are present in directional solidification are shown in Figure 4.3. Three main length scales which has to be distinguished in most cases are primary dendrite scale, secondary dendrite scale and crucible scale.

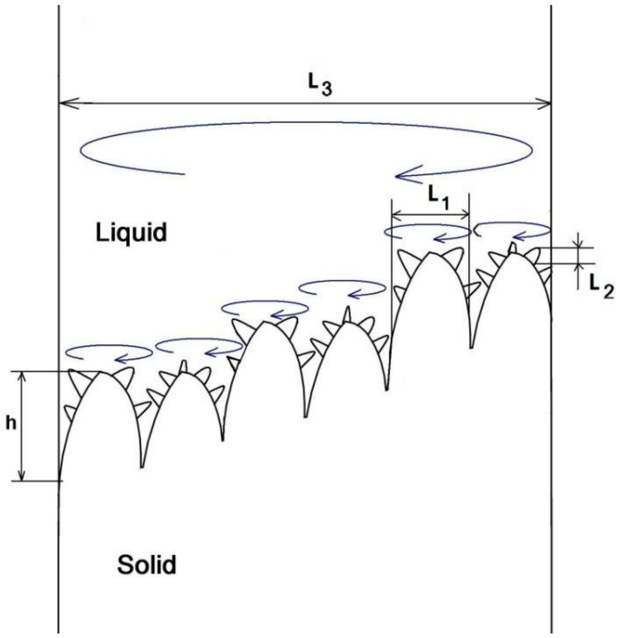

Figure 4.3: Sketch of the solidification front showing various length scales and corresponding convection patterns (L_1-primary dendrite spacing, L_2-secondary dendrite spacing, L_3-crucible scale, *h*-characteristic primary dendrite longitudinal size)

For the order of magnitude estimation equation in stationary case, equation (4.6) is simplified by replacing derivatives by simple ratios of characteristic values, thus $\nabla\vec{u}$ becomes *u/L* and $\nabla^2\vec{u}$ becomes u/L^2. Current density is substituted from Ohms law equation (2.3).

$$\rho\frac{u^2}{L}+\mu\frac{u}{L^2}+c\sigma\ (uB^2-P\theta B)=0 \tag{4.11}$$

Solution of square equation (4.11) gives following expression for TEMC velocity order of magnitude:

$$u=\frac{\left(\sqrt{\left(c\sigma\ LB^2+\frac{\mu}{L}\right)^2+4\rho cP\theta B\sigma L}-\left(c\sigma LB^2+\frac{\mu}{L}\right)\right)}{2\rho} \tag{4.12}$$

Thus due to replacing derivatives with ratios in Navier-Stokes equation signs are lost, only the minus sign after square root in equation (4.12) give physically valid result. Solution eq. (4.12) shows that TEMC velocity has maximum at certain magnetic field strength, and further increase of magnetic field will decrease convection velocity due to MHD braking effect (Davidson 2001) which is proportional to magnetic field square while thermoelectric motion driving force is proportional to first order of *B* (Kaldre, Fautrelle, et al. 2010), (X. F. Li 2007). Relation between TEMC characteristic velocity and applied magnetic field induction for slowly directionally solidified Sn-10%wt.Pb alloy with 8 K/mm temperature gradient is given in Figure 4.4. For a given alloy and experimental parameters (Table 4.1) theoretical maximum TEMC intensity is reached at a magnetic field of 0.5 T.

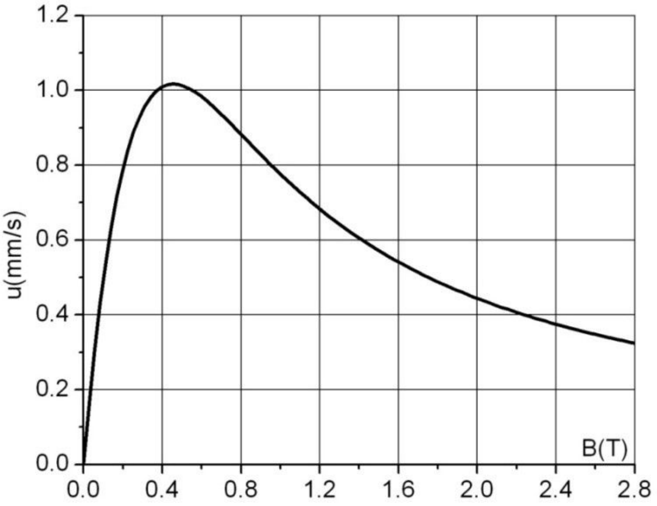

Figure 4.4: Characteristic velocity of thermoelectromagnetic convection velocity in dendrite scale (L=100 μm) in a Sn-10wt.Pb alloy as a function of applied magnetic field U_{max}=1 mm/s, B_{max}=0.5 T

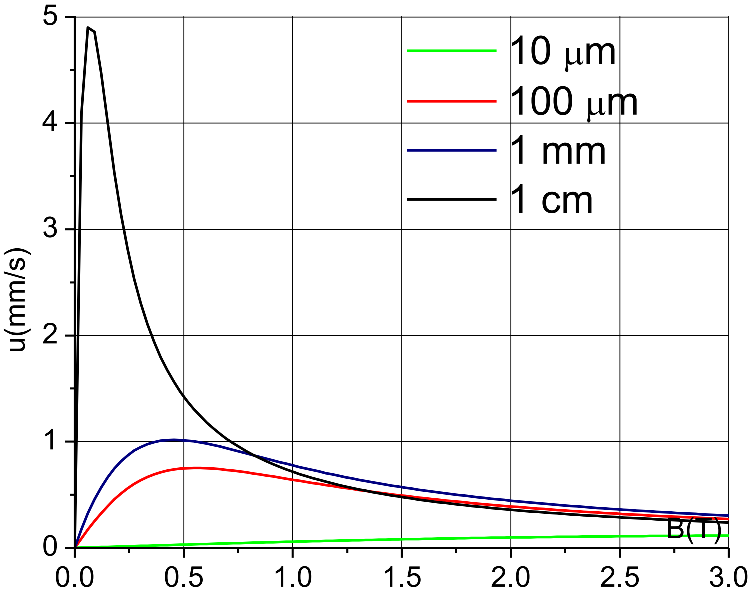

Figure 4.5: TEMC velocity order of magnitude at four different length scales (properties of Sn-wt.10%.Pb are used)

Figure 4.5 compares characteristic velocity evaluation given by equation (4.12) at four different length scales. It shows that maximum velocity is reached at different magnetic field values at each length. For crucible scale (R=3 mm) velocity maximum is reached at very low magnetic field (≈0.2 T) while for secondary dendrite length scale, which is typically of 10^{-5} m, velocity is linearly growing till high magnetic field values (up to 5 T).

4.4. TEMC contribution in energy and solute transport

To better understand the influence TEMC flow might have on energy and solute transport at each length scale it is useful to introduce some additional criteria to compare diffusion and convection heat transfer mechanisms. General energy transport is described by heat transport equation.

$$\frac{\partial T}{\partial t} + u \cdot grad(T) = \alpha \cdot \nabla^2 T \tag{4.13}$$

Where α is thermal diffusivity $\lambda/\rho c_p$. To characterize the significance of TEMC in energy transport dimensionless number describing the ratio between conductive and convective heat transfer times is introduced, which is called Peclet number. Characteristic convection time can be calculated as

$$T_{conv} = \frac{L}{u} \tag{4.14}$$

Whereas conduction time is calculated as

$$T_{Cond} = \frac{L^2 \rho c_p}{\lambda} \tag{4.15}$$

Ratio of these two times is Peclet number showing the ratio between convective and conductive heat transfer mechanisms.

$$Pe = \frac{T_{Cond}}{T_{Conv}} = \frac{Lu\rho c_p}{\lambda} \tag{4.16}$$

If the flow is non stationary due to solidification front evolution over time or magnetic field or crucible motion, then parameter characterizing this unsteadiness should be defined. Energy transport time oscillations is characterized by Strouhal number. The Strouhal Number represents a measure of the ratio of inertial forces due to the unsteadiness of the flow or local acceleration to the inertial forces due to changes in velocity from one point to another in the flow field.

$$Sh = \frac{\omega L}{u} \tag{4.17}$$

Where ω is characteristic oscillation frequency. Heat transfer equation (4.13) can then be written in dimensionless form using dimensionless velocity $u_d=P\theta/B$ and defined dimensionless numbers.

$$Sh\frac{\partial T}{\partial t} + u_d \cdot grad(T) = \frac{1}{Pe} \cdot \nabla^2 T \tag{4.18}$$

Solute transport equation can be written in similar form than heat transfer equation

$$\frac{\partial C}{\partial t} + u \cdot grad(C) = D \cdot \nabla^2 C \tag{4.19}$$

Similar solute transport dimensionless numbers can be introduced and equation can be written in dimensionless form just like energy transport equation. Mass diffusion Peclet number is

$$Pe_C = \frac{Lu}{D} \tag{4.20}$$

Table 4.2: Maximum TEMC velocity and Peclet number for different length scales.

Characteristic size L (mm)	U_{max}(mm/s)	B_{max}(T)	Pe	Pe_C
0.01	0.12	4	0.000036	0.3
0.1	1	0.5	0.003	25
1	3.7	0.15	0.111	925
10	7.2	0.07	2.16	18000

Table 4.2 it can be seen that at small length scales TEMC conduction heat transfer is much stronger than convection, thus it is expected that influence of TEMC on the energy transport is greater at larger length scales. Since D of metals is of order of magnitude of 10^{-9} m^2/s, in liquid metals even small convection easily overcomes mass diffusion, and thus we may say that TEMC and other convection mechanisms has influence on solute redistribution at all length scales. Mass diffusion is comparable with TEMC only at very small length scale below 10^{-5} m, which is typically secondary

dendrite arm spacing for some alloys (Guofa, Pu and Songyan 2009). This is in agreement with the fact mentioned by other authors that it is very difficult to achieve fully diffusive solidification regime in metals (Lehmann, Moreau and Camel 1998), (Favier, et al. 1996).

4.5. Thermoelectric boundary problem between two media

If we look at the open circuit consisting of two different metals as shown in Figure 4.6, thermo EMF generated in the circuit can be calculated from Kirchhoff's law according to equation (4.21).

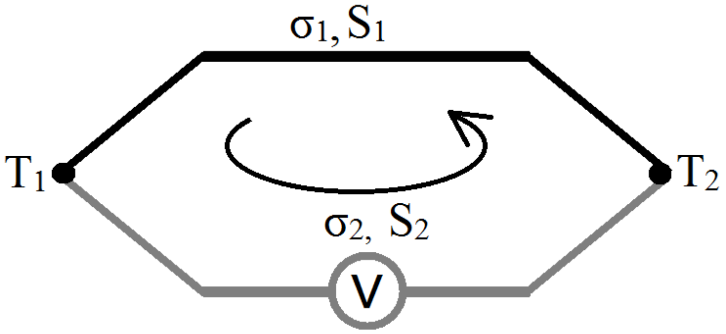

Figure 4.6: Schematic drawing of circuit made of two different conductors

$$\varepsilon_T = \int_{T_1}^{T_2} S_2(T) \cdot dT + \int_{T_2}^{T_1} S_1(T) \cdot dT \tag{4.21}$$

If S is constant in temperature interval between T_1 and T_2 inside each material, then voltage can be calculated simply as shown by equation (4.22).

$$\varepsilon_T = \int_{T_1}^{T_2} (S_2 - S_1) \cdot dT = \Delta S \cdot \Delta T \tag{4.22}$$

If the circuit is closed, then current flow exists in the circuit. In this case situation is different because current density must be conserved at the contact points. This condition cannot be achieved if potential is fixed as given in equation (4.22). Here the discrepancy appears, because current through the interface modifies potential distribution in the circuit, compared with the case with open circuit without current flow.

In continuous media the principle is similar, and solution for a potential and current distribution at the boundary is complicated. At the interface between two media with different ATPs and electrical conductivities, potential profile is created due to thermoelectric effect if tangential temperature gradient is present. Electric current normal component and electric potential continuity has to be fulfilled at the interface. According to Ohm's law electric potential in the domain can be calculated assuming that electric current flow does not affect potential field and ignoring induced electric current.

$$\varphi = S \cdot T \tag{4.23}$$

At the interface between two media thus potential drop is achieved, which is approximate boundary condition.

$$\Delta\varphi = \Delta S \cdot T \tag{4.24}$$

Accurate thermoelectric process on the boundary between two media is not clearly described yet. Different approaches and approximations are used in various works described in the literature to solve potential and electric current at the boundary and within both domains.

Moving fluid element along the solid wall is analysed by J.A. Shercliff (J. Shercliff 1979). Boundary condition given in his work by equation (4.2) relates tangential current densities in both media. Practically this is second Kirchhoff's law applied for the small circuit at the interface as shown in Figure 4.7.

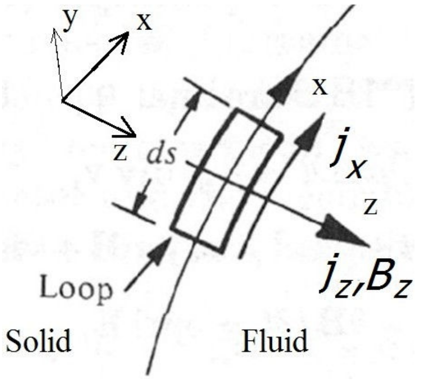

Figure 4.7: Schematics of moving fluid element along the solid wall (J. Shercliff 1979)

If no magnetic field is applied, fluid is at rest (or boundary between two solids), and contact resistance is neglected then boundary condition given by equation (4.3) can be written as:

$$\frac{j_{xw}}{\sigma_w} - \frac{j_x}{\sigma} = P\frac{\partial T}{\partial x} \tag{4.25}$$

Where index *w* means the quantity within the wall. As we will see in further results in section 4.6, this is only true if normal current to boundary is negligible compared with tangential current. Such representation does not fully describe the boundary condition at the interface in general case when current circulates from one media to another, and normal current component is of the same order of magnitude as tangential for particular geometries.

Different approach has been used by Kao (Kao and Pericleous 2011, september 8-13), (A. Kao 2010). Prescribed electric potential profile is given for the interface between two media. Normal derivative of the electric potential is conserved at the boundary. Constant thermoelectric potential difference $\Delta S \cdot T$ is applied at the boundary. Current flow is calculated separately for two domains with the same electric conductivities. For each domain total potential drop is divided by two, and gauge potential is added or subtracted.

$$\begin{aligned} \psi_1 &= +\frac{1}{2}\Delta ST + \psi_E^i(T) \\ \psi_2 &= -\frac{1}{2}\Delta ST + \psi_E^i(T) \end{aligned} \tag{4.26}$$

To avoid singularity at the boundary, finite thickness of interface is defined and electric potential changes linearly in this layer.

In ref. (Kurenkova, Zienicke and Thess 2001) boundary equation for tangential currents is given in the following way.

$$\frac{1}{\sigma_w}\frac{\partial j_{wz}}{\partial z} - \frac{1}{\sigma_l}\frac{\partial j_{lz}}{\partial z} = P\left(\frac{\partial^2 T}{\partial x^2} + \frac{\partial^2 T}{\partial y^2}\right) \tag{4.27}$$

In ref. (Chen, Rosendahl and Condra 2011) numerical simulation of current distribution and temperature field in thermoelectric generators is done. Thermoelectric voltage equation in the grid cell is given as equation (4.28).The same is applied to the neighbouring cells at the interface. This condition can be applied for two cells at the interface-one in each media. Applying this equation for tangential component and then subtracting equations of both cells, we get the same Shercliff boundary condition given by equation (4.25).

$$\nabla V = -S(T)\nabla T - \frac{j}{\sigma(T)} \tag{4.28}$$

Ref. (Zhang, et al. 2009) describes the model experiment to demonstrate and quantify TEMC in macroscale, TEMC values measured with ultrasound probe are compared with numerical simulation. Experimental setup consisting of liquid GaInSn pool with copper walls and nickel bottom is used. Wall resistance is neglected, thus boundary condition is only an approximation which cannot be used in different geometry or material properties. Ohm's law is used to estimate electric current in the liquid metal by assuming electric current to be uniform along the cross section of the pool.

$$I = \frac{\Delta S \cdot \Delta T}{R_1 + R_2} \tag{4.29}$$

Here R_1 and R_2 stands for integral electrical resistances of liquid pool and copper walls. This is simplified approach where it is assumed that current flowing through the interface does not affect the TE potential distribution.

Potential profile along the interface between two different conductors will be analysed for the situation depicted in Figure 4.8. In this approximation where tangential current density is much larger than normal and voltage is not affected by current flow through the interface, solution can be found analytically. This approximation can be used in some practical cases to find thermoelectric current and potential distribution. Let us choose a pair of different materials connected by ideal conductors of different temperatures at the ends.

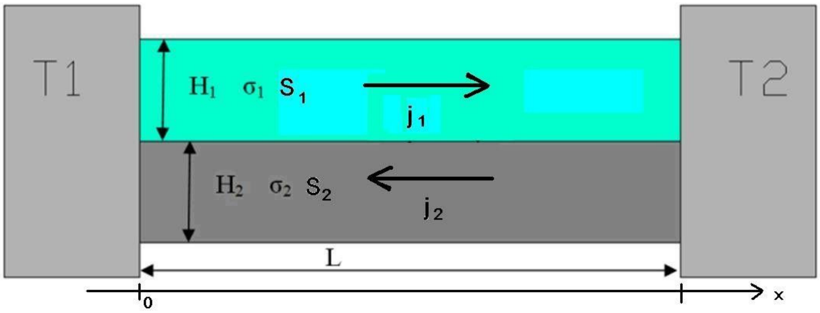

Figure 4.8: Thermoelectric current flow near the boundary of pair of different conductors with applied temperature gradient

Temperature gradient is constant and parallel to the interface $\theta=(T_2-T_1)/L$ in this case. Kirchhoff's law can be written for the current circuit. Thermoelectric voltages is balanced by the voltage drop due to current flow in the media.

$$S_1(T_1 - T_2) + S_2(T_2 - T_1) = \frac{j_1 L}{\sigma_1} - \frac{j_2 L}{\sigma_2} \tag{4.30}$$

Integral current has to be equal in both media, thus current continuity can be written as

$$j_1 H_1 = -j_2 H_2 \tag{4.31}$$

Current densities in both media can be expressed from equation (4.30) and equation (4.31), and using *c* defined by equation (4.5).

$$j_1 = c\sigma_1 P\theta \qquad j_2 = -\frac{H_1}{H_2} c\sigma_1 P\theta \tag{4.32}$$

Then electric field intensity parallel to interface can be calculated from Ohm's law eq. (2.3)

$$E_1 = c \cdot P\theta + S_1\theta \qquad E_2 = -\frac{H_1\sigma_1}{H_2\sigma_2} c \cdot P\theta + S_2\theta \tag{4.33}$$

Remembering the definition of *c* form equation (4.5) it can be shown that electric field intensities at both sides of the boundary are equal. Thus electric field along the interface is constant, electric potential in the domains can be found as $\varphi = E \cdot x$. This approach can be applied to any small volume element at the interface. In fact this is just another approach how to derive Shercliff boundary condition equation (4.25) describing current flow along the boundary between two media.

4.6. Electric boundary condition mathematical modelling

Boundary condition given by equation (4.24) is an approximation, which can be used quite accurately to calculate thermoelectric current distribution if electric conductivities of materials are not very different and geometry is symmetric or close to symmetric (current paths in both media are of similar length). This approximation is convenient to use if the aim of numerical simulation is only qualitatively find the thermoelectric current flow distribution. Simplest numerical approach is to divide this potential drop at the interface inversely proportional to the electric conductivities, and to calculate current density for each domain separately. In this case boundary condition for each domain is temperature dependant electric potential as shown in equation (4.34).

$$\begin{aligned} \varphi_1 &= PT \cdot \frac{\sigma_2}{\sigma_1 + \sigma_2} \\ \varphi_2 &= -PT \cdot \frac{\sigma_1}{\sigma_1 + \sigma_2} \end{aligned} \tag{4.34}$$

Accurate solution may be obtained if potential profile is not fixed as temperature function at the interface, but current and potential distribution in both domains are found numerically by iterative steps in order to satisfy potential and current continuity at the interface.

Two dimensional problem is solved for temperature, potential and electric current. Geometry for this numerical simulation is chosen to be similar to directional solidification cell used in experiments done in European Synchrotron Radiation Facility in Grenoble. These experiments were intended to in-situ observation of dendritic solidification of binary metallic alloys under magnetic field. Alloy is filled into 200 µm thin cell which is 6 mm wide and 40 mm long, this cell is then melted by small furnace, and then slowly solidified by gradually reducing the heater power of the furnace. Experimental results of these experiment are analysed in section 5.6. It is assumed in the model that liquid and solid regions are separated by inclined solidification front (Figure 4.9). Such geometry is close to the realistic situation observed in the experiments. Inclined solidification front is caused by temperature and composition inhomogenities and natural convection, and heat transported macroscopically by TEMC of the liquid phase.

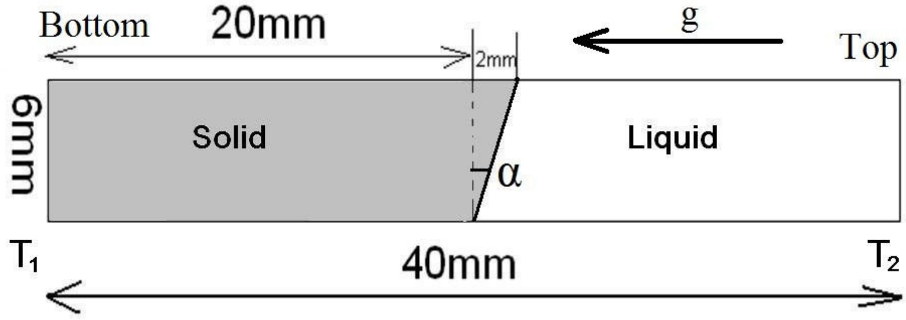

Figure 4.9: Geometry of experimental cell used in numerical simulation

Constant temperature difference of $T_2 - T_1$=120 K is applied between top and bottom walls of the experimental cell, while side walls are assumed to be thermally insulating. Temperature distribution is calculated by solving Fourier's law. Calculated temperature distribution is then used as input data for electric problem. Potential and normal current conservation at the interface must be fulfilled.

$$\begin{aligned} U_1 &= U_2 \\ (\vec{j}_1 \cdot \vec{n}_1) &= (\vec{j}_2 \cdot \vec{n}_2) \end{aligned} \tag{4.35}$$

Electric current in both domains is calculated as shown by equation (4.36). As can be seen electric current consists of two components, caused by electric potential gradient and temperature gradient. In case of applied magnetic field solution is more complicated because of additional current source created by induced magnetic field and MHD damping term.

$$\vec{j} = -\sigma\nabla U - \sigma S\nabla T \tag{4.36}$$

FLUENT solves general transport equation (4.37). This equation for quantity *Ψ* is given in the following form (cfd-online 2006)

$$\frac{\partial \rho\psi}{\partial t} + \nabla \cdot (\rho\vec{u}\,\psi) = \nabla \cdot (\Gamma\nabla\,\psi) + S_{\psi} \tag{4.37}$$

Where ρ is density, Γ is diffusion coefficient, S_{ψ} is a source term. Terms in the left side are transient and convective terms accounting for the accumulation of *Ψ* and transport due to velocity of flow, while diffusion and source terms in the right side accounts for diffusive *Ψ* transport due to gradient of quantity and source or leak. For a stationary situation when fluid is at rest equation (4.37) takes form:

$$\nabla(\Gamma\nabla\,\psi) = -S_{\Psi} \tag{4.38}$$

For a given problem we must solve general transport equation for electric potential caused by one source term in equation (4.39). In this model it is assumed *grad(S)*=0 in the bulk of the both media, thus also source term vanishes there. Whereas at the interface S and σ change with a jump, thus source term is only present at the interface.

$$\nabla(\sigma\nabla U) = \nabla(-\sigma S\nabla T) \tag{4.39}$$

Mesh used to model this problem consists of 25000 quadrilateral cells. Double precision solver is used (12 digits) to ensure sufficient accuracy for potential calculation, which is measured in µV. At the interface derivatives of quantities are calculated, and discretization is done to find corresponding transport equation for given problem for FLUENT to solve. Discretization is done as shown in the Figure 4.10. By using special functions to acquire values at the edges of the cells or in the centre of the cells. By using these quantities, transport equation can then be modified to equation (4.40).

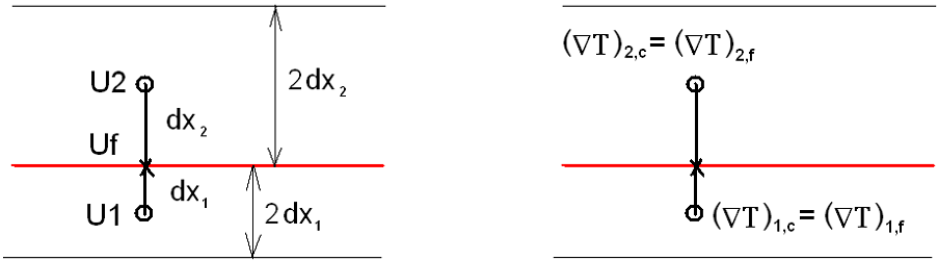

Figure 4.10: Illustration of the discretization of a derivative at the boundary

$$-\sigma_1 \frac{U_f - U_1}{dx_1} - \sigma_1 S_1 \nabla T_1 = -\sigma_2 \frac{U_2 - U_f}{dx_2} - \sigma_2 S_2 \nabla T_2 \tag{4.40}$$

From this equation and potential continuity follows that electric potential at the interface must satisfy following equation (4.41). Solution of this equation is found numerically.

$$U_f = \frac{\sigma_1 S_1 \nabla T_1 - \sigma_2 S_2 \nabla T_2 - \sigma_1 U_1 / dx_1 - \sigma_2 U_2 / dx_2}{\sigma_1 / dx_1 + \sigma_2 / dx_2} \tag{4.41}$$

Numerical model for potential and electric current distribution in this two domain system is solved for Al-3%wt.Cu alloy with properties as shown in Table 4.3.

Table 4.3: Physical properties of Al-3%wt.Cu alloy used in model

Property	**solid**	**liquid**	**unit**
Electric conductivity	$1.38\cdot10^{7}$	$0.38\cdot10^{7}$	Sim/m
Thermal conductivity	200	100	W/mK
Density	2700	2400	Kg/m^3
Absolute thermoelectric power	$1.1\cdot10^{-6}$	$0.1\cdot10^{-6}$	V/K
Dynamic viscosity		0.0024	Pa·s

First step of the model is calculation of temperature and temperature gradient components which by numerically solving temperature equation.

$$\nabla(\lambda \nabla T) = 0 \tag{4.42}$$

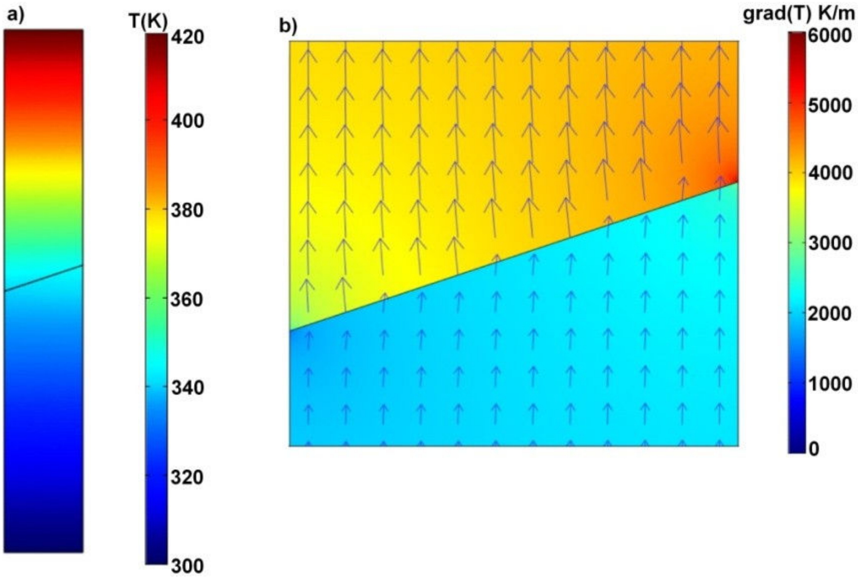

Figure 4.11: a) Calculated temperature in the experimental cell; b) temperature gradient distribution near the interface

Temperature gradient components are calculated, and potential is calculated according to satisfy equation (4.41).

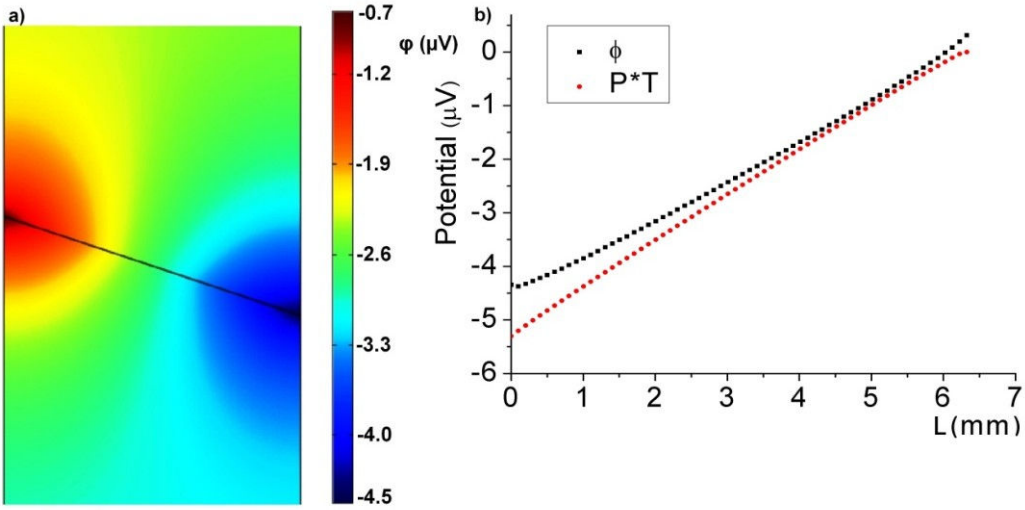

Figure 4.12: a) Calculated electric potential near the interface φ (μV); b) comparison between actual potential profile along the interface compared with approximation $\Delta\varphi=P\cdot T$

Figure 4.12 shows that difference between exact solution of potential profile along the interface versus approximation ($\Delta\varphi=P\cdot T$) in this geometry is small thus approximation can be used for qualitative current distribution calculation with good accuracy. Simple model of current and potential distribution at the interface between liquid and solid Al-3%wt.Cu alloy using this boundary condition compared with exact solution is shown in Figure 4.13.

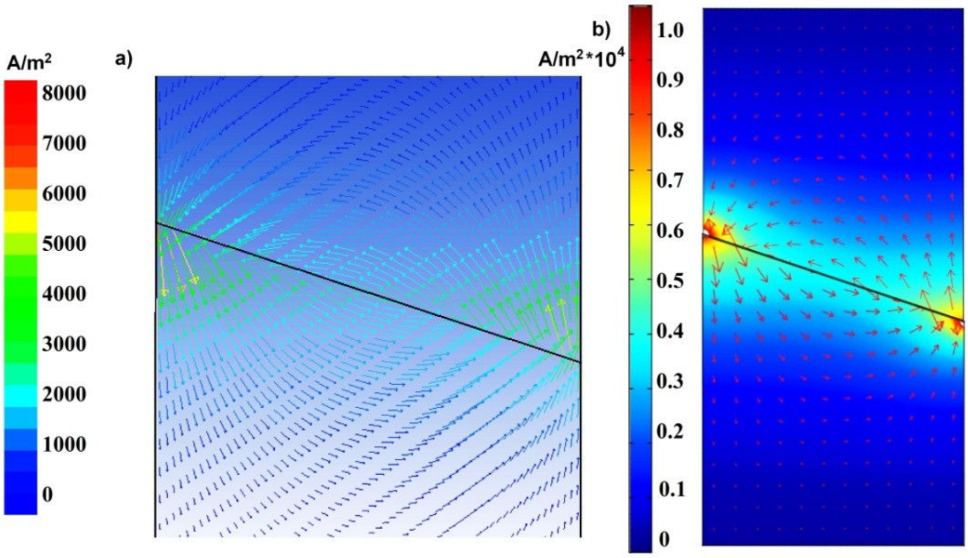

Figure 4.13: Calculated thermoelectric current near the interface; a) Exact solution; b) approximation with fixed potential at the interface $\Delta\varphi = P \cdot T$

Calculated current density can be compared with estimation obtained by equation (4.34). Figure 4.13 shows that current distribution calculated exactly and with approximation are quite similar and maximum difference is about 15%. Biggest difference is at the sides of the cell where current magnitude is greatest. It seems logical because larger electric current is capable to affect potential stronger. From these results also follows that characteristic thickness of current layer in both media is equal. By using parameters from the Table 4.3 and assuming θ=3000 K/m like used in experiments, estimation according to equations (4.4) and (4.5) gives c=0.22 and $j \approx$ 9000 A/m^2. This current density value is very close to maximum values of current in both cases which confirms the significance of dimensionless group c as a electric current limiting factor.

Solution can be used to validate the accuracy of boundary condition given by Shercliff (J. Shercliff 1979). This boundary condition (eq.(4.25)) for a given situation (without magnetic field and neglecting contact resistance) can be written as:

$$\frac{j_s}{\sigma_s} - \frac{j}{\sigma} = P\theta \sin\alpha \tag{4.43}$$

Where j is tangential current density near the interface in the liquid domain while j_s in the solid and σ and σ_s are corresponding electrical conductivities, $\theta \cdot \sin\alpha$ is interface parallel temperature gradient component. Normal and tangential current components at the interface can be expressed from current density components j_x and j_y calculated by FLUENT via equation (4.44).

$$\begin{aligned} j_{\perp} &= j_y \cos\alpha + j_x \sin\alpha \\ j_{\angle} &= j_x \cos\alpha - j_y \sin\alpha \end{aligned} \tag{4.44}$$

Current continuity at the interface can be verified by comparing normal current through the boundary from both domains (Figure 4.14). Current continuity is fulfilled within the range of numerical error (±0.1 %), which can be explained by finite cell size and rounding of numbers.

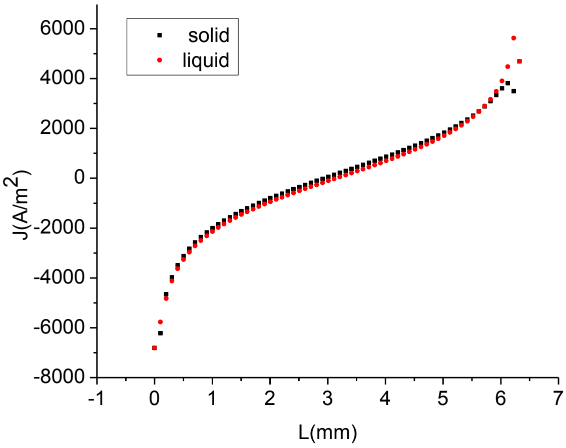

Figure 4.14: Normal electric current through the interface. Black line-current exiting from solid domain, red line-current entering into liquid domain

Whereas tangential current components are different in both sides of the interface because of different electrical conductivities.

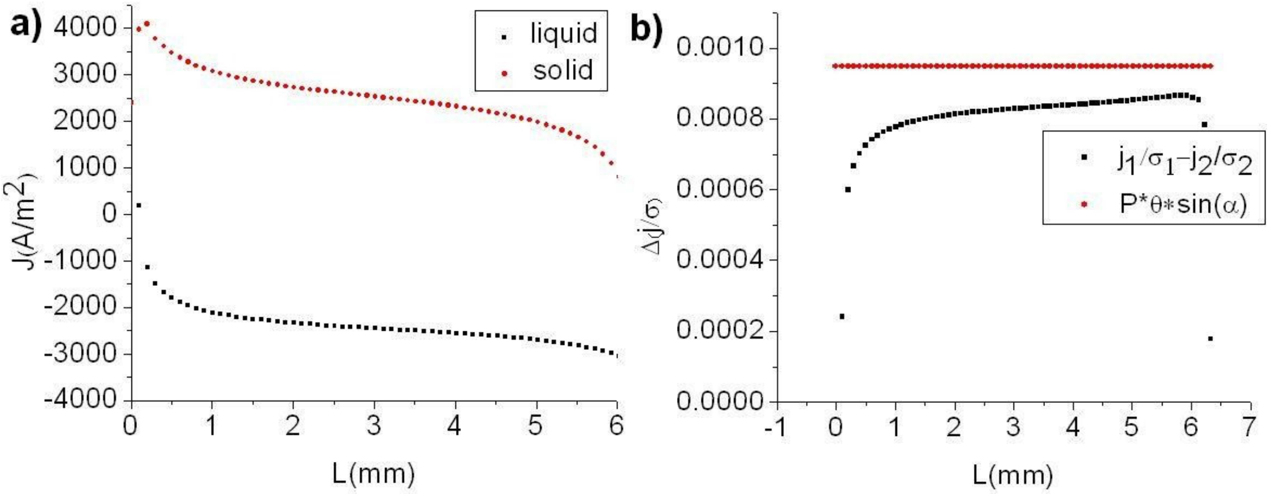

Figure 4.15: a) Comparison of tangential current along the interface; b) numerically calculated comparison of right and left sides of boundary condition given by equation (4.43)

As analysed before, boundary condition given by equation (4.43) is obviously not fulfilled in case where normal current exists through the boundary. Figure 4.15(b) compares left and right sides of the equation (4.43), and it can be seen that difference is about 15% which is acceptable for order of magnitude estimation and qualitative analysis of electric current distribution. Figure 4.15(a) shows tangential current densities along the interface in both domains showing that in solid domain current density is higher. This means that current path is not symmetric in both domains. Main difficulties to use precise algorithm are large computing power which would be necessary to solve more complex or 3D problem and complexity to write algorithm for different solidification interface shape.

4.7. TEMC flow modelling

In this section two numerical models are described to illustrate TEMC flow caused by axial and transverse magnetic fields and to verify flow velocity dependence on magnetic field described in chapter 3, and to numerically test the accuracy of analytical order of magnitude estimations.

Electric current interacts with applied magnetic field, creating liquid phase flow. Modelling of TEMC flow is more complicated task because there are several physical effects which act simultaneously and affect each other. To overcome these difficulties usually various approximations have been used where some feedbacks are neglected. In this model we use prescribed interface and neglect the fact that liquid phase flow distorts temperature field and can affect solidification front shape, thus affecting potential distribution. In our case Peclet number is small thus this factor does not cause large difference. Flow is calculated in the same geometry used previously for electric current calculation. Magnetic field is imposed perpendicular to sample plane parallel to z axis. Magnetic field values are chosen to be 0.08 T and 0.2 T which are actual values which are used in performed and planned experiments. Lorentz force components are calculated as:

$$\vec{F} = \vec{j} \times \vec{B} = \begin{pmatrix} j_x & j_y & j_z \\ 0 & 0 & B \\ \vec{i} & \vec{j} & \vec{k} \end{pmatrix} = j_y B\vec{i} - j_x B\vec{j} \tag{4.45}$$

Using parameters from Table 4.3 and d=3 mm, θ=3 K/mm, c=0.22 we get following TE pressure and force in experimental cell shown in Figure 4.9 caused by TE current and magnetic field interaction is shown in Figure 4.16. It can be seen that Lorentz force acts only close to the interface and is directed towards solid region, thus approximation by balancing force order of magnitudes in infinite media is not accurate in this case.

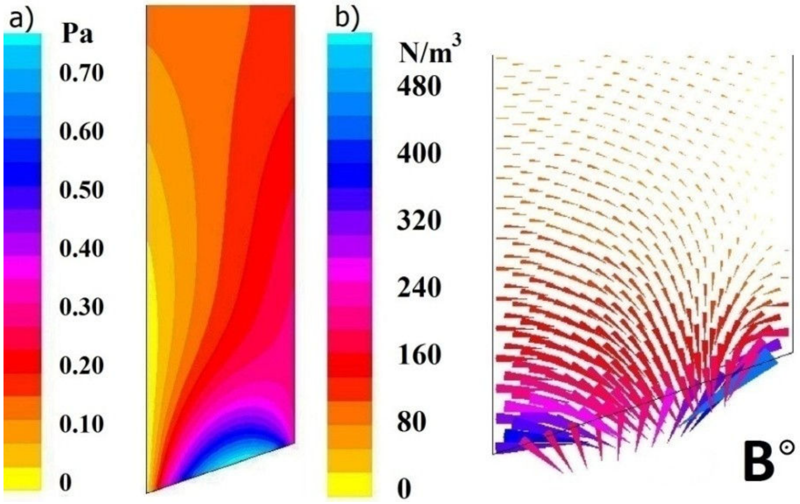

Figure 4.16: Calculated pressure (a) and Lorentz force (b) distribution in the liquid part of experimental cell caused by 0.08 T magnetic field

To numerically verify the velocity dependence on magnetic field at axial and transverse field orientation, 3D numerical model is developed to calculate TEMC flow around solid material needle surrounded by liquid metal. Needle represents single dendrite arm and liquid metal represents melt surrounding it. Parameters and geometry for numerical model are chosen based on experimental facility built in Institute of Physics University of Latvia. This experiment was intended to demonstrate TEMC in macroscopic scale and to verify TEMC pattern under axial and transverse magnetic field. Experiment is done in axisymmetric volume as shown in Figure 4.17. Material of the central needle is cobalt, which has one of the highest ATP at among metals (A. Bojarevics 2003). Liquid phase is represented by GaInSn alloy which is liquid at room temperature (T_m=10 ^{o}C).

Table 4.4: Physical properties of Cobalt and GaInSn (GaInSn properties 1982) used in numerical simulation

Property	**Cobalt**	**GaInSn**
Electrical conductivity [S/m]	$1.6 \cdot 10^7$	$3.6 \cdot 10^6$
Thermal conductivity [W/m·K]	100	35
ATP [µV/K]	-46	-0.4
Surface tension [mN/m]		$607.6\text{-}0.25 \cdot T$
Volumetric thermal expansion [1/K]		$6{,}92 \cdot 10^{-5}$
Density [kg/m^3]		$6492.12\text{-}0.44 \cdot T$
Viscosity [Pa·s]		0.0022

Heat flow is applied to the bottom of the cobalt needle while heat is removed through the water cooled side walls. Input data for the model is wall temperatures which were measured with thermocouples. Temperature of water cooled wall T_0=17 ^{o}C and at the bottom of cobalt needle is

T_1=50 °C. Thermoelectric current is driven by temperature gradient at the interface between cobalt and GaInSn.

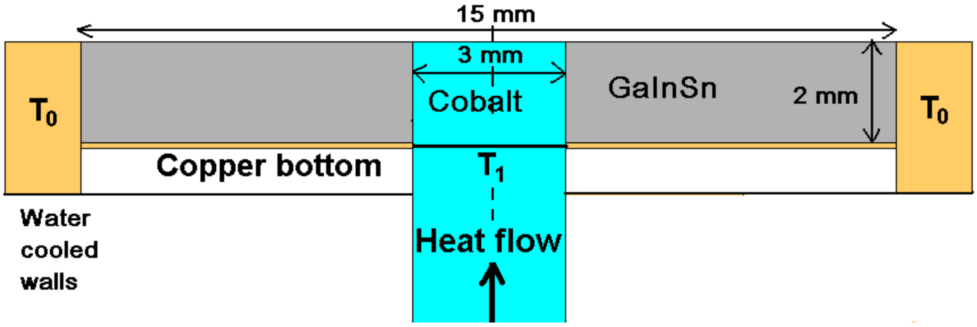

Figure 4.17: Modelling geometry and dimensions

Flow calculations with applied axial and transverse magnetic field of various magnitudes are done. Maximum velocity is plotted versus magnetic field in Figure 4.22, comparing numerical results and theoretical velocity estimation given by equation (4.12). Contribution in the flow by natural convection is numerically estimated. This model allows to numerically verify the hypothesis posed in section 4.3 about different flow patterns in cases with axial and transverse magnetic field shown in Figure 4.2. These modelling results also allows us to verify the hypothesis that motion velocity is reduced by increase of magnetic field after critical field value is exceeded.

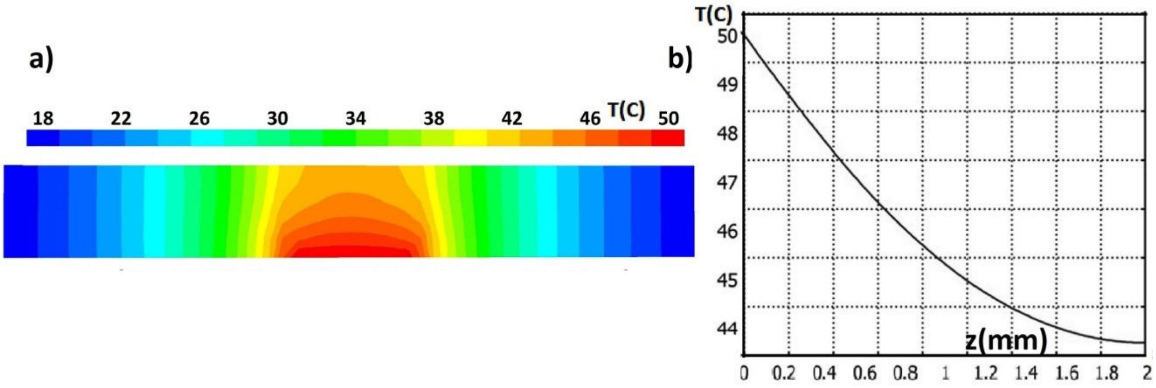

Figure 4.18: a) Temperature distribution in experimental setup; b) Temperature profile along the Cobalt-GaInSn interface

Figure 4.18(b) shows that temperature gradient along the interface between cobalt and GaInSn is approximately 3 K/mm. Electric potential difference between top of the needle and bottom can be estimated as multiplication of total temperature drop and differential thermoelectric power. Equation (4.24) gives $\Delta\varphi$=168 μV, and characteristic current density estimated form equation (4.4) gives value of $3 \cdot 10^5$ A/m^2. Figure 4.19 shows the numerically calculated electric current density. Numerically calculated maximum current density near the interface is $8 \cdot 10^5$ A/m^2.

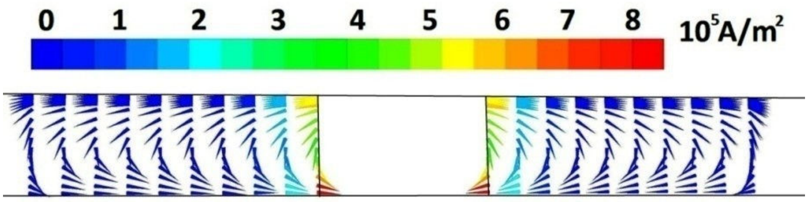

Figure 4.19: Thermoelectric current distribution in liquid domain

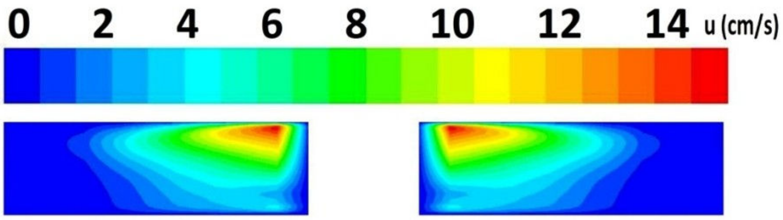

Figure 4.20: Azimuthal velocity component with applied axial magnetic field B_z=0.2 T

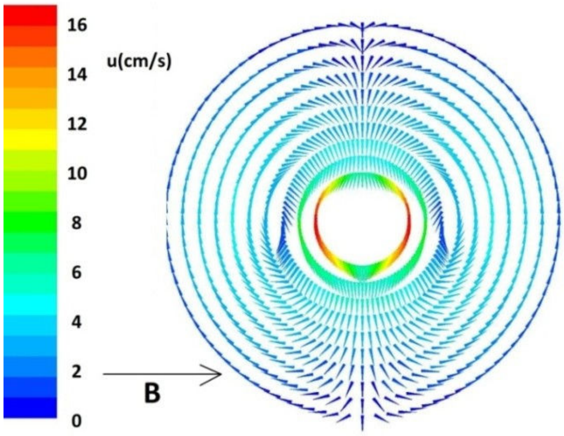

Figure 4.21: Velocity at the middle depth of the pool under B_x=0.2 T transverse magnetic field

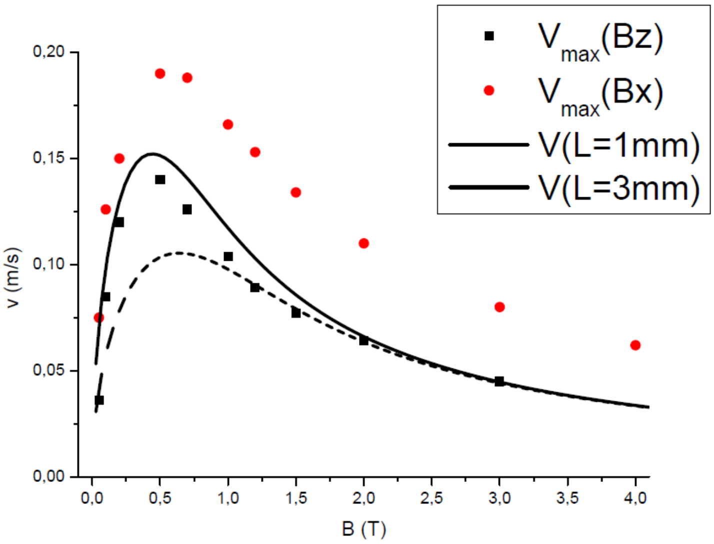

Figure 4.22: Comparison between analytical order of magnitude estimations and numerical solution

Flow is calculated in laminar approximation, no slip conditions for surface and walls is used. Figure 4.20 and Figure 4.21 show that calculated TEMC flow patterns caused by axial and transverse magnetic field qualitatively agrees with theoretical predictions. Axial field causes liquid rotation around dendrite arm. Transverse magnetic field in given confined volume creates two vortices as liquid is pumped perpendicular to magnetic field direction near the needle and returns along the sides of the volume. In case of solidification, force on the liquid acts in very thin layer (comparable to dendrite characteristic length) above the interface and flow closes through the bulk of the liquid or near the crucible walls.

Figure 4.22 compares analytical velocity estimation calculated according to equation (4.12) with numerically calculated maximum velocity. Theoretical curves at two different characteristic lengths (d=1 mm and d=3 mm) are given. Maximum velocity caused by transverse field is greater than by axial field because transverse field causes much greater local force density near the dendrite arm.

Other forces which may have influence on the flow are thermal convection caused by thermal expansion of the liquid metal and Marangoni force caused by surface tension dependence on temperature. Thermal convection was calculated numerically by using quantities from Table 4.4.

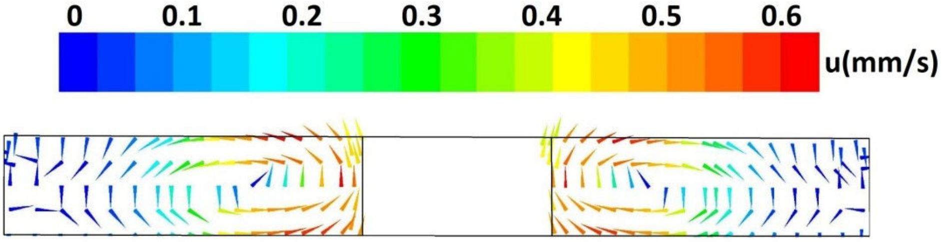

Figure 4.23: Numerically calculate natural convection velocity

At the nonisothermal free surface force and fluid motion may appear because surface tension of liquid is a function of temperature leading to different force density distribution at the surface. Marangoni stress can drive significant convection on the surface of liquid metals as shown by (Bojarevics and Pericleous 2009) where Marangoni flow on the surface of levitated droplet is numerically calculated. In many real cases this motion is suppressed by oxide layer which inevitably forms at the surface unless experiment is done in deep vacuum or in the atmosphere of inert gas to prevent evaporation. Marangoni convection was calculated numerically for given setup assuming top surface to be free liquid metal surface. Numerical simulation result is shown in Figure 4.24. It can be seen that significant velocity is reached at the surface while inside the volume of the liquid velocity is much smaller.

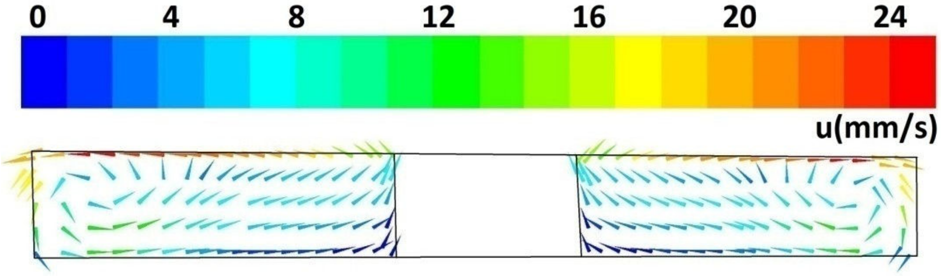

Figure 4.24: Numerically calculated Marangoni flow velocity. Ignoring the effects caused by surface oxidation

4.8. Thermoelectric effects on the free particle

During solidification, in the mushy zone solid particles of various sizes are floating in the liquid phase. These particles are either solidified nuclei or broken dendrite fragments, or impurity particles. If particle is surrounded by liquid which has different ATP, then thermoelectric current circulation around the particle appears if temperature gradient is present. In the presence of magnetic field, Lorentz force acts on the particle and on the liquid surrounding it. This force can cause particle motion in liquid or particle rotation. Deeper evaluation of this effect would allow to quantify and measure TEMC itself or to estimate thermoelectric properties of the materials because in many cases flow velocity and distribution can only be determined by measuring the velocities of tracer particles moving along with the flow. This section is devoted to analysis of solid conducting particle surrounded by conducting liquid. Influence of TE effects of particle are analysed. During solidification experiment with in-situ filming of dendrite growth and flow with X-rays, such particles are observed.

Spherical solid conducting particle in the liquid phase is chosen as a simple model to be analysed in this section. Solid and liquid material properties form Table 4.3 is used to analytically estimate and numerically simulate characteristic values of this problem. TE potential, electric current and pressure calculation around particle in an axisymmetric case are done. Particle with diameter of 1 mm is chosen for numerical model and analytical calculations.

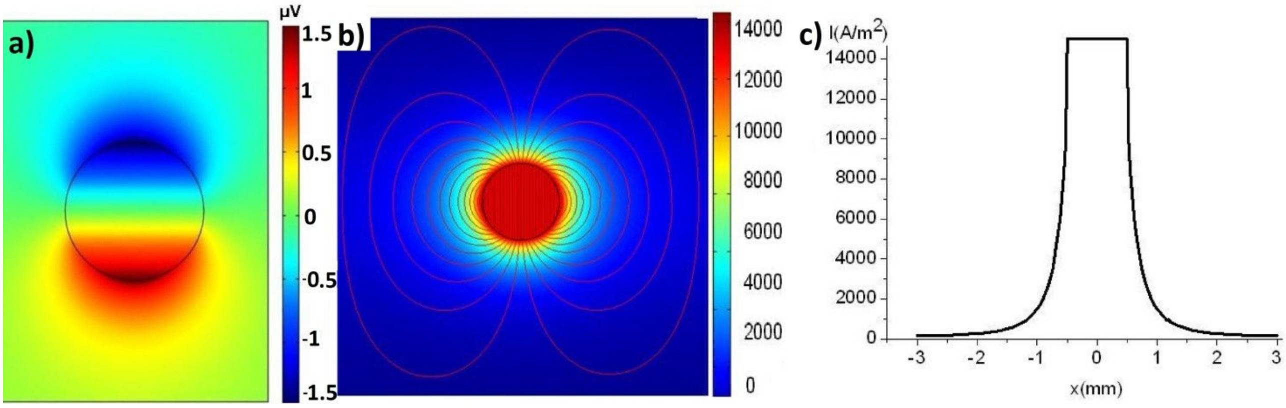

Figure 4.25: Numerical simulation of solid particle floating in liquid melt: a) Electric potential; b) Electric current streamlines and magnitude; c) Electric current density magnitude along *x* axis

Figure 4.25 shows that inside the spherical particle electric current density is almost uniform while outside the sphere it decreases rapidly with the distance away from the sphere as shown in figure. If magnetic field is applied then Lorentz force acts on the particle and in the surrounding liquid as well. Applied transverse field will drag the particle to one side perpendicular to magnetic field. Particle velocity can be estimated by applying Stokes law describing sphere motion in viscous fluid. Sphere is moving to the right side of the picture in a given case. Drag force due to fluid viscosity can be found as $4\pi\mu Ru$ while resistance force due momentum particle gives to surrounding liquid is $2\pi\mu Ru$ in case if liquid is at rest and no other forces are present. Current density within the particle can be estimated from equation (4.4). This estimation gives value of $8\cdot 10^3$ A/m^2 (c=1/3 in this case). Which is close to value obtained by numerical simulation (j=1.3$\cdot 10^4$ A/m^2). If applied magnetic field is 0.08 T then velocity of particle can be calculated by balancing integral force on the particle caused by Lorentz force and Stokes drag force according to equation (4.46), which gives particle velocity of 20 mm/s (4.47) which is quite large value indicating that effect of the particle and dendrite fragmentation by magnetic field may be significant.

$$F = (j \times B)\frac{4}{3}\pi R^3 = 6\pi\mu Ru \tag{4.46}$$

$$u = \frac{2c\sigma P\theta BR^2}{9\mu} \tag{4.47}$$

Where σ is average conductivity of solid and liquid phases $(\sigma_S+\sigma_L)/2$. However velocity expression get from equation (4.47) is an approximation because TE force action on the liquid surrounding particle is not taken into account. Similar approximation is used by Wang obtaining formula with slightly different c and averaged σ term (Wang, et al. 2012). TE force acting on the fluid modifies pressure field around particle, thus drag force in this case is different than calculated according to Stokes law. Pressure created by TE force is shown in Figure 4.26(a). This pressure creates liquid motion around particle which slows down the particle motion in opposite direction. TEMC velocity around particle caused by 0.08 T magnetic field is shown in Figure 4.26(b). Results show that near the particle velocity of fluid is opposite to particle motion caused by Lorentz force on the particle. Magnitude of this velocity is approximately 1.7 mm/s. Thus due to pressure redistribution in case of spherical particle velocity is reduced by this value.

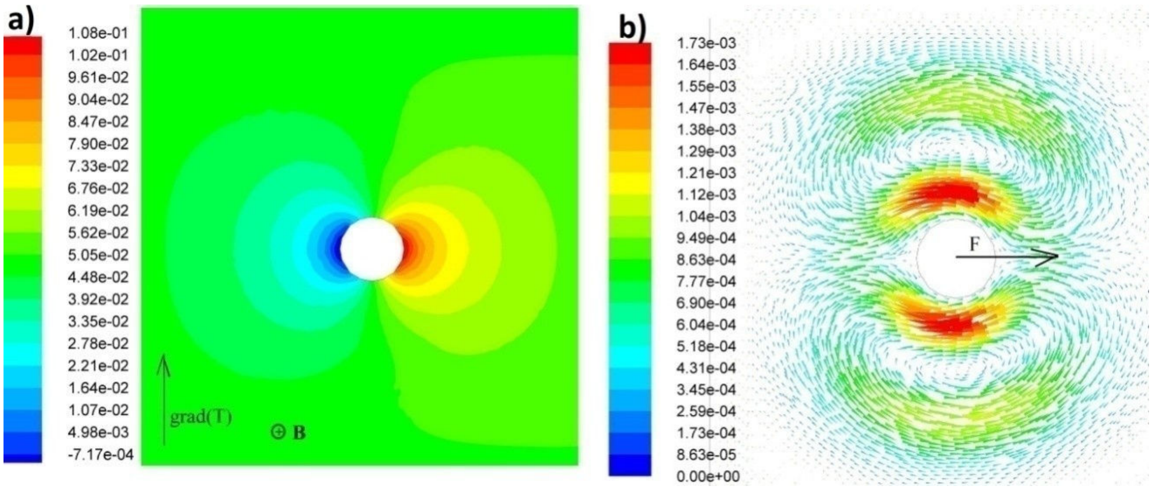

Figure 4.26: a) electromagnetic pressure distribution in the liquid caused by 0.08 T transverse magnetic field; b) TEMC flow around 1 mm diameter particle

Particle in this case acts similar as dipole-current lines exit from the top of the particle and returns through the bottom of particle as shown in Figure 4.25(b). From here it can be concluded that current density (and pressure) magnitude decrease proportionally to $1/x^3$ with the distance away from the particle. This idea is tested and confirmed in Figure 4.27 where current magnitude from the numerical model is fitted with this function and agreement is perfect.

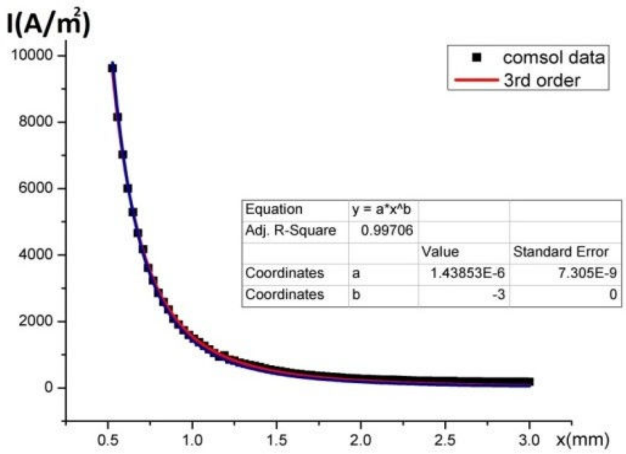

Equation	y = a*x^b		
Adj. R-Square	0.99706		
		Value	Standard Error
Coordinates	a	1.43853E-6	7.305E-9
Coordinates	b	-3	0

Figure 4.27: Current density magnitude as a function of the distance from sphere surface. Numerical data fitted with the function $I=a/x^3$

This result allows us to estimate particle velocity decrease due to TE pressure field in fluid in general case. If electric current density in liquid decreases as $1/x^3$ and near the surface current density magnitude is similar as in solid, as confirmed by simulation results, than particle velocity is reduced by approximately $u/8$.

4.9. Conclusions

Analytical order of magnitude estimations carried out in this chapter give some interesting points about static magnetic field influence on the melt motion characteristics near the solidification front in case of dendritic solidification. It was confirmed that TEMC intensity increases until certain magnetic field value is reached and further increase of field reduces TEMC because of MHD braking force which becomes dominant over TE forces after this threshold. Analysis of these phenomena at different length scales revealed the fact that critical field at which TEMC is highest, is strongly dependant of characteristic scale of structure which causes TEMC flow. In case of convex or slope solidification front shape, crucible size flow can appear. Critical field values for this flow can be as low as 0.3 T as demonstrated by the numerical model in section 4.7. As the characteristic size is reduced to primary and secondary dendrite arms, critical magnetic field increases. These values can significantly vary depending on properties of the material. In real solidification various different length scales are present, thus magnetic field strength has to be chosen based on these calculations and knowing at which scale we want to influence the melt flow in the crucible. In section 4.3 velocity magnitude as a function of magnetic field at various length scales are calculated for Sn-10%wt.Pb alloy. In further experimental work, our main interest is to investigate TEMC influence on the primary dendrite morphology and size. Based on this order of magnitude analysis, maximum TEMC at this scale (100-200 μm) is reached at magnetic field intensity of 0.5 T. In directional solidification experiments presented in next chapters magnetic field of 0.3-0.5 T will be used, which is sufficient to reach maximum flow in the scale of crucible size and primary dendrite size.

Numerical simulations of various geometries and length scales given in this chapter qualitatively confirms previous assumptions about flow characteristics under axial and transverse magnetic fields. TEMC intensity dependence on magnetic field strength was also numerically verified in section 4.7 and good agreement between estimation and simulation, regarding velocity order of magnitude, is demonstrated. Meanwhile it was shown that not always it is possible to correctly chose constant c and characteristic length d to acquire agreement between estimation and numerical results. As shown in section 4.6 geometry can significantly limit the flow velocity in some cases. Numerical simulation of the TE effects on the spherical particle floating in liquid melt is performed. Current density in the particle and in the surrounding liquid is calculated, particle motion velocity is estimated, showing that particle motion velocity is proportional to particle size square. TE current density magnitude around particle decreases as $1/x^3$ with the distance away from particle. Thus results indicate that TE induced motion and force on the larger particles is greater than on smaller particles.

Thermoelectric boundary calculation algorithm was derived and tested in this chapter in sections 4.5 and 4.6. It can be concluded that precise calculation with this approach is rather complex and requires lots of computer resources even in relatively simple 2D geometry. It was also demonstrated that in most of the practical cases approximation can be use with acceptable accuracy. Approximate condition produces greatest error at the places on interface where normal electric current density is higher as shown by the Figure 4.15.

Analytical and numerical results and estimations of TE quantities obtained in this chapter will be used to interpret the experimental results in the following chapters and to choose optional experimental parameters to achieve expected effect. Derived expressions which allows to estimate TEMC parameters will be used to estimate corresponding quantities during experiments. Obtained values will be verified by the ones extracted from experimental results. Thus many physical effects acts on the melt flow simultaneously, it is important to correctly estimate relative ratios between them depending on characteristic scale and material properties. Main dimensionless ratios are defined and explained in this chapter to ease the comparison of competing physical effects.

5. Solidification under static magnetic field

Influence on the structure of Sn-Pb and Sn-Bi alloys caused by static magnetic field is experimentally investigated in this chapter. Axial or transverse magnetic field is applied during directional solidification at various growth velocities. Literature overview about previous experimental works in this field is given in the first section of the chapter. Sn-10%wt.Pb alloy is used for extended experimental work to investigate grain size and macrosegregation as a function of growth velocity. Influence of the field on grain structure and sizing, and macrosegregation is analysed.

5.1. Literature review

Several experimental works has been done to study static magnetic field impact on the structure of metallic alloys (X. F. Li 2007), (Li Xi 2007), (Lehmann, Camel and Bolcato 1998). Experimental studies are usually done by directional solidification using Bridgman setup or similar where solidification parameters, like solidification velocity and temperature gradient can be controlled. Previous experimental studies have shown that for some alloys influence on the macrostructure and microstructure can be achieved by means of TEMC. Some alloys exhibit significant changes in component distribution and grain morphology within the sample at moderate magnetic field less than 0.5 T (X. F. Li 2007).

It has been shown that TEMC may cause changes in grain structure and dendrite morphology, and spacing (Lehmann, Moreau and Camel 1998), (Khine and Walker 1998). Al-4.5%wt.Cu in presence of static magnetic field exhibits significant changes in solidification front shape and cell morphology as a consequence of TEMC in the mushy zone (Shen, et al. 2011). There are also some theoretical works in this field (Lehmann, Moreau and Camel 1998), (Kaldre, Fautrelle, et al. 2010) showing that thermoelectromagnetic convection intensity is increasing with magnetic field initially, but when critical magnetic field value is reached, further increase of magnetic field reduces the effect due to counteraction by induced magnetic field. This relation is also confirmed by experimental results (X. F. Li 2007) showing that at very high axial magnetic field influence on the structure is weak due to strong MHD braking of any flow perpendicular to magnetic field. Although in Al-Cu alloy strong axial magnetic field leads to formation of ring like structure which is likely the result of damped radial component of natural convection. Influence of high magnetic field on columnar to equiaxed transition and column morphology at various magnetic field values has been experimentally studied by Li (Li, Fautrelle and Zaidat, et al. 2010).

This area is also on the scope of interest in the field of semiconductor crystal growth. Semiconductor materials have metallic conductivity at liquid state and high temperature, they usually have high absolute thermoelectric power (Yesilyurt, et al. 1999). Applied magnetic field may drive a significant melt circulation due to TEMC, and thus may be the way to improve the material structure (Kaldre, Fautrelle, et al. 2010), (Gorbunov and Lyumkis 1990) by refining grains and reducing inclusions. Many works has also been devoted to the analysis of the influence of applied magnetic field on the melt flow caused by natural or electromagnetic convection. Influence of magnetic field on the structure and macrosegregation during semiconductor growth has been studied by Yesilyurt (Yestilyurt, et al. 2004) and Series (Series and Hurle 1991).

Research of TEMC influence on the liquid phase flow and dendrite morphology during solidification has been performed by X-ray imaging of thin samples to visualize the effects of melt flow and dendrite growth caused by applied magnetic field (Mathiesen and Arnberg 2006), (Yasuda, Ohnakaa, et al. 2004). Attempts to numerically simulate TEMC and its influence of crystal morphology has also been done (Kao A. 2008), (Yesilyurt, et al. 1999), and results qualitatively agree with experimental observations. TEMC influence on macrosegregation has been numerically and theoretically studied (Samanta and Zabaras 2006). In this work applied magnetic field and its gradient influence on component distribution has been analysed. Nevertheless it is difficult to directly relate convection pattern and intensity with changes of the cellular or dendritic structure of the solidified alloy. In most cases only qualitative trend how TEMC influences segregation or dendrite spacing can be deduced.

5.2. Experimental setup and procedure

High purity tin, lead and bismuth (99.99%) is used to prepare Sn-10%wt.Pb and Sn-20%wt.Bi alloy, which is then casted into the alumina799 crucible (*L*=110mm, *ID*=6mm, *OD*=10mm). Samples are then remelted and solidified under intense magnetic stirring to ensure good homogeneity of initial samples. The samples are directionally solidified in a Bridgman setup at controlled growth velocities from 0.5 μm/s to 20 μm/s. Upper part of the sample is melted by the furnace around the crucible while bottom part is kept solid by water cooled copper ring. Furnace and water cooled ring are stationary while crucible is lowered by programmable pulling system. Solidification front is always located between heater and cooler at the same location, thus actual solidification velocity is assumed to be equal to the pulling velocity of the crucible.

Various cross sections of solidified samples are examined by optical microscopy. For optical microscopy analysis samples are polished to 1 μm surface roughness and then chemically etched. To visualize the cellular structure of the alloy, pretreatment with the 10% aqueous HCl solution were done to remove oxide layer. Samples were then etched with 4% nitric acid ethanol solution. This reagent darkens the lead rich fraction while tin matrix remains light, revealing cellular structure and qualitative component distribution over the cross section of the sample (Brandes and Brook 1992). Quantitative component distribution along the diameter of the sample is measured by scanning electron microscopy.

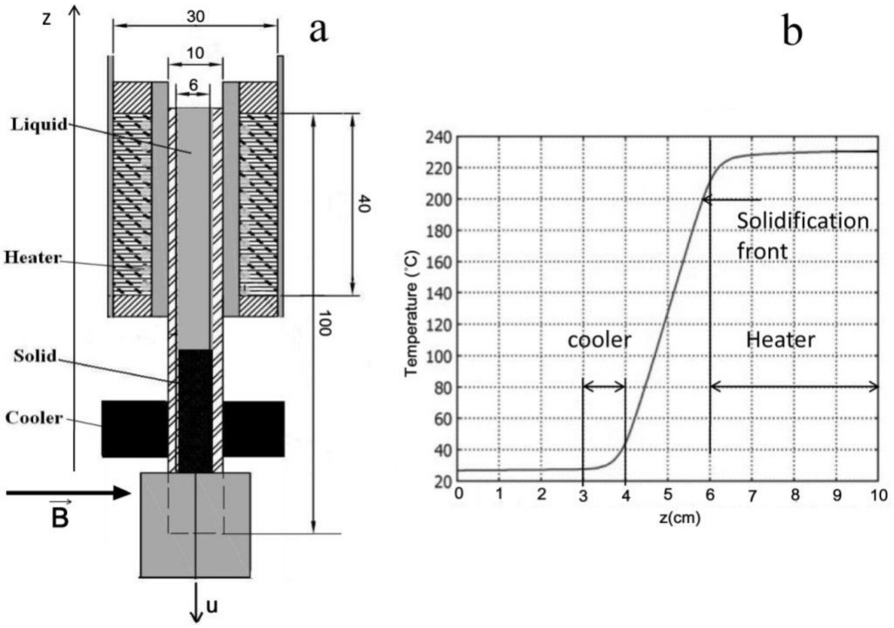

Figure 5.1: Directional solidification setup: a) cross section of the setup; b) temperature distribution along the axis of the setup

Magnet system is assembled from six rectangular permanent magnets (four 51x51x25AA mm and two 58x110x20AA mm). Magnets are put on the 20 mm thick steel plate to concentrate the magnetic field. Distance between surfaces of the magnets is 4 cm. Sample is located in the centre between magnets where magnetic flux density is highest and reaches 0.47 T as was measured with gaussmeter and calculated analytically (Schroeter 2013). Magnetic field induction can be adjusted by changing the distance between magnets. Advantages of permanent magnet system compared to electromagnets are that such system does not require energy to sustain magnetic field, which is especially important during long solidification experiments with low growth velocity. This magnetic system can be easily changed from axial to transverse magnetic field by turning the system. Magnetic field can be rotated by electric motor (0.01-3 rev/min) to investigate the influence of the slowly rotating magnetic field, which will be done in chapter 7. This is simpler than to design special coil system to achieve rotating magnetic field by electromagnets. However the main disadvantage of using permanent magnets is high inhomogenity of magnetic field between the magnets and limited magnetic flux density which can be achieved. This problem can be overcome by using more magnets and different arrangement of magnets. However in these experiments diameter of the sample is only 6 mm and it can be assumed the field is homogeneous along the sample diameter (Figure 5.3).

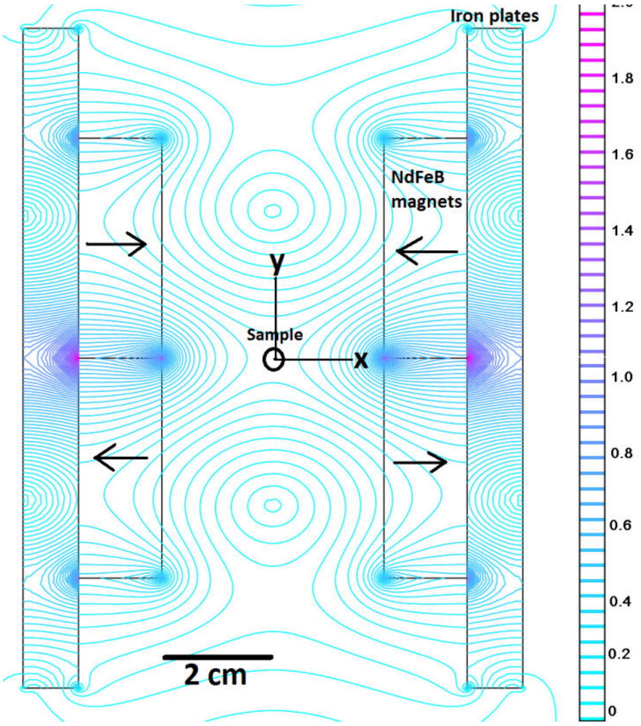

Figure 5.2: Sketch of magnet system (view from above) with magnetic field isolines calculated with Femm (Meeker 2011)

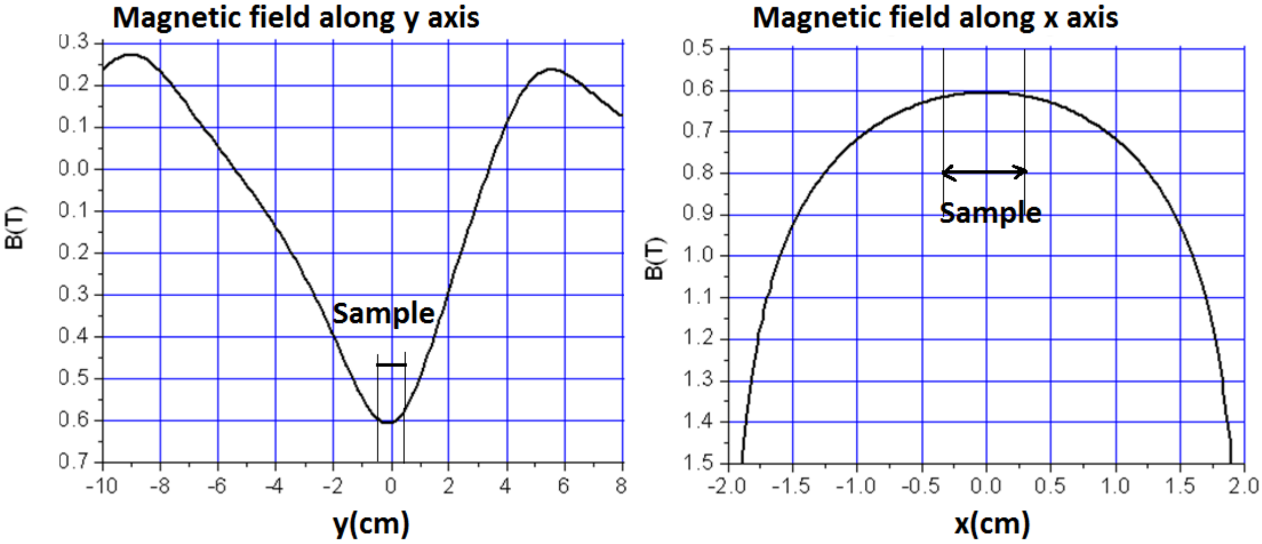

Figure 5.3: Magnetic field in the magnetic system along x and y axis

Figure 5.2 shows the magnetic field distribution in the magnetic system. Maximum magnetic field in the steel plates is 1.7 T which is saturation magnetization of steel. Ideal infinite magnetic plate beneath magnet doubles its effective height thus increasing its magnetic field. Here it is almost reached because we can see that virtually no magnetic field goes through the steel plates. Magnetic field inhomogenity along x and y axis is shown in Figure 5.3 field is maximum at the sample but as we can see inhomogenity is quite high. Force inhomogenity due to magnetic field inhomogenity can be estimated as shown in equations (5.1) and (5.2)

$$\Delta f = f(B+\Delta B) - f(B) \tag{5.1}$$

$$\begin{aligned}
&f = jxB = \sigma\left(uB^2 - P\theta B\right)\\
&\Delta f = \sigma\left(u(B+\Delta B)^2 - P\theta(B+\Delta B) - uB^2 + P\theta B\right) = \sigma \cdot \Delta B \cdot \left(2uB - P\theta\right)\\
&\frac{\Delta f}{f} = \frac{\Delta B}{B}\left(\frac{2uB - P\theta}{uB - P\theta}\right)\\
&\frac{\Delta f}{f} \approx \frac{\Delta B}{B}
\end{aligned} \tag{5.2}$$

Where ΔB is field variation along the distance of crucible diameter, and Δf is force density difference along the crucible diameter caused by this variation. Result means that with our experiment parameters, additional force caused by the field inhomogenity is proportional to the field inhomogenity itself. From equation (5.2) can be calculated $\Delta f/f$=20mT/500mT=4%. This is relatively small difference and will have little effect on the overall convection pattern, thus it can be assumed that they will not cause any changes in structure of an alloy.

5.3. Solidification under static axial magnetic field

Static magnetic field interacts with thermoelectric currents at the solidification interface and creates liquid phase convection at the vicinity of the solidification interface. Stationary TEMC flow is forming in the liquid part of the sample above solidification front. This flow plays a role in heat and mass transfer thus affecting structure of the alloy. Magnetic field also produces a fluid motion damping force due to induced electric field and magnetic field interaction. For each alloy and solidification parameters combination there is a certain field value at which the thermoelectric and MHD braking forces are in balance and maximum TEMC intensity is reached.

Axial magnetic field does not create macroscopic flow in the size of the crucible, but creates a local convection around each dendrite arm as shown in Figure 4.2(a). In this case no macrosegregation is observed but there is influence on microstructure due to TEMC and motion damping effects in the direction perpendicular to magnetic field. Local melt rotation around primary dendrite arms creates effective convection in the local scale thus main effects can be expected to the grain structure and inclusions.

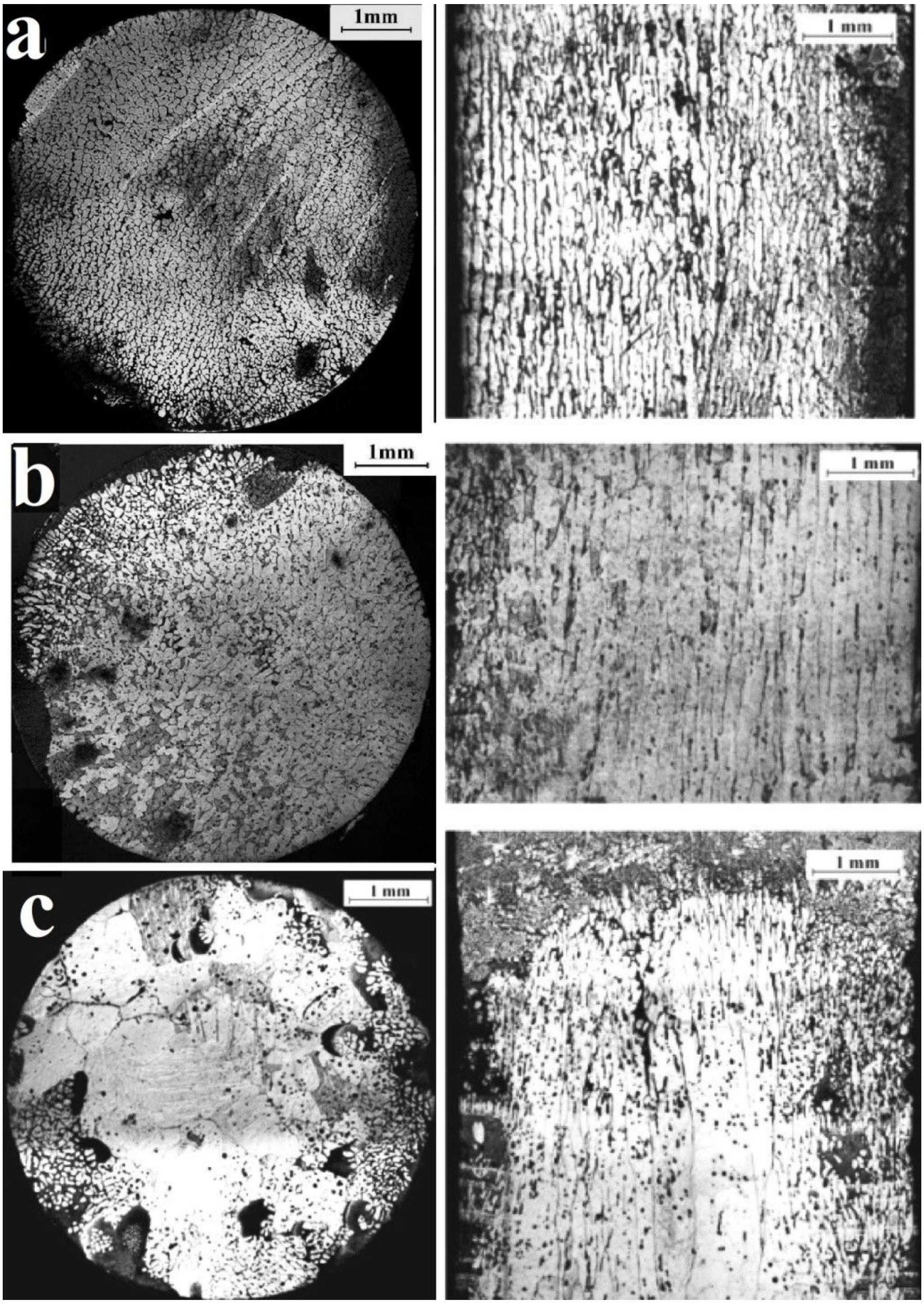

Figure 5.4: Directionally solidified Sn-10%wt.Pb alloy; a) 10 μm/s, b) 2 μm/s, c) 0.5 μm/s

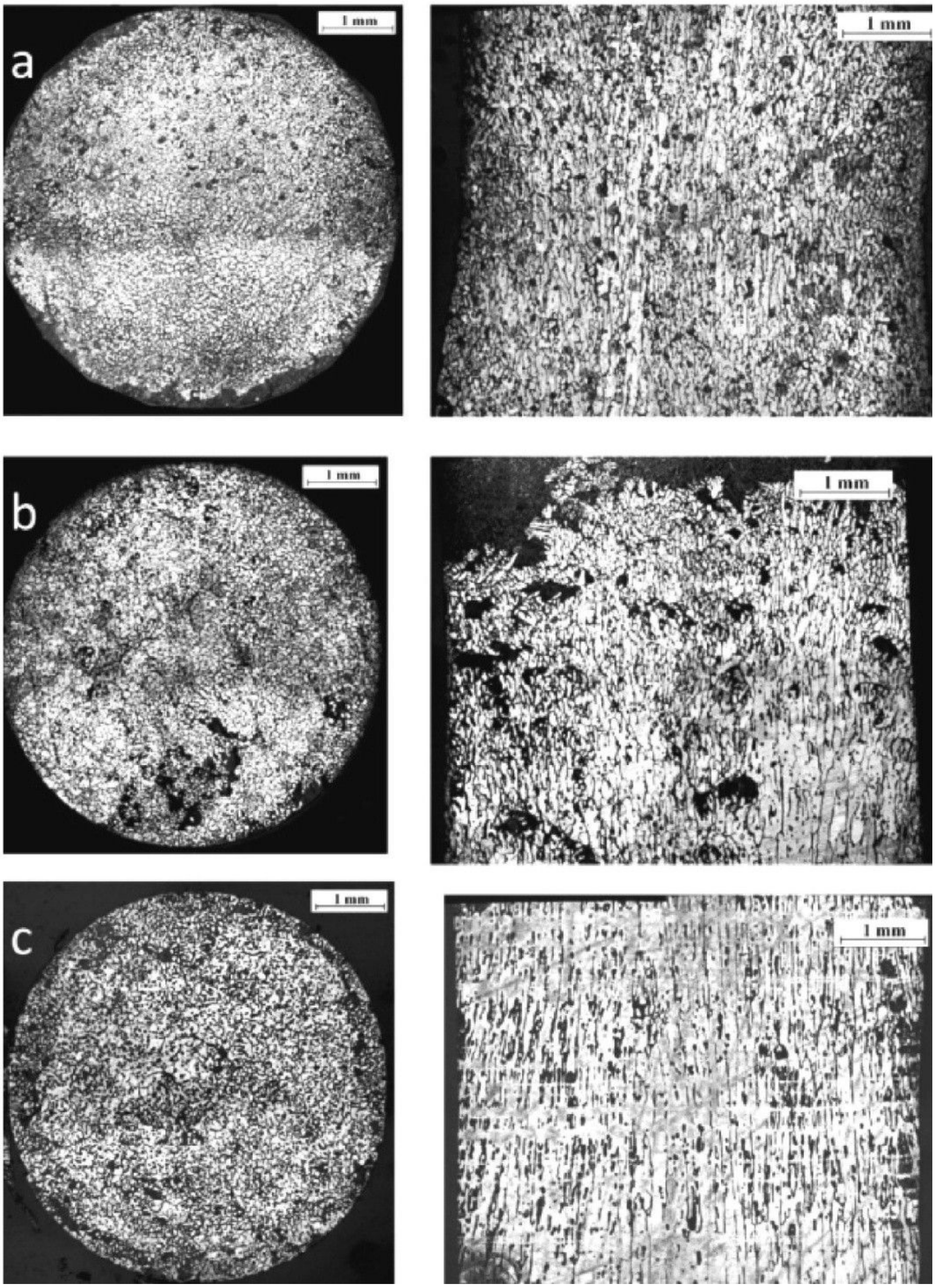

Figure 5.5: Directionally solidified Sn-10%wt.Pb alloy under 0.4 T axial magnetic field; a) 10 μm/s, b) 2 μm/s, c) 0.5 μm/s

As can be seen from Figure 5.4 and Figure 5.5, static axial magnetic field does not have influence on macosegregation a growth velocities 2 μm/s and 10 μm/s while at 0.5 μm/s structure is severely different. This influence is most likely caused by MHD braking and thermosolutal, and natural convection. At small pulling velocities differences of the structure is significant due to these reasons. Without magnetic field grains are large and lead rich β phase inclusions (dark regions in micrographs), are concentrated in the sides of the crucible. With axial magnetic field these radial flows are damped by magnetic field and fine grained homogeneous structure is forming as seen in the Figure 5.5(c).

Microstructure is affected in all cases. Grain size is affected by applied magnetic field and as can be seen from longitudinal cross sections of the Figure 5.4 and Figure 5.5, also column length in longitudinal cross section is significantly reduced as shown in Figure. 5.6 and Figure 5.7. Difference in grain spacing is much larger at growth velocity 10 µm/s.

Detailed analysis of characteristic grain size change as a function of applied magnetic field and growth velocity is given in section 5.5.

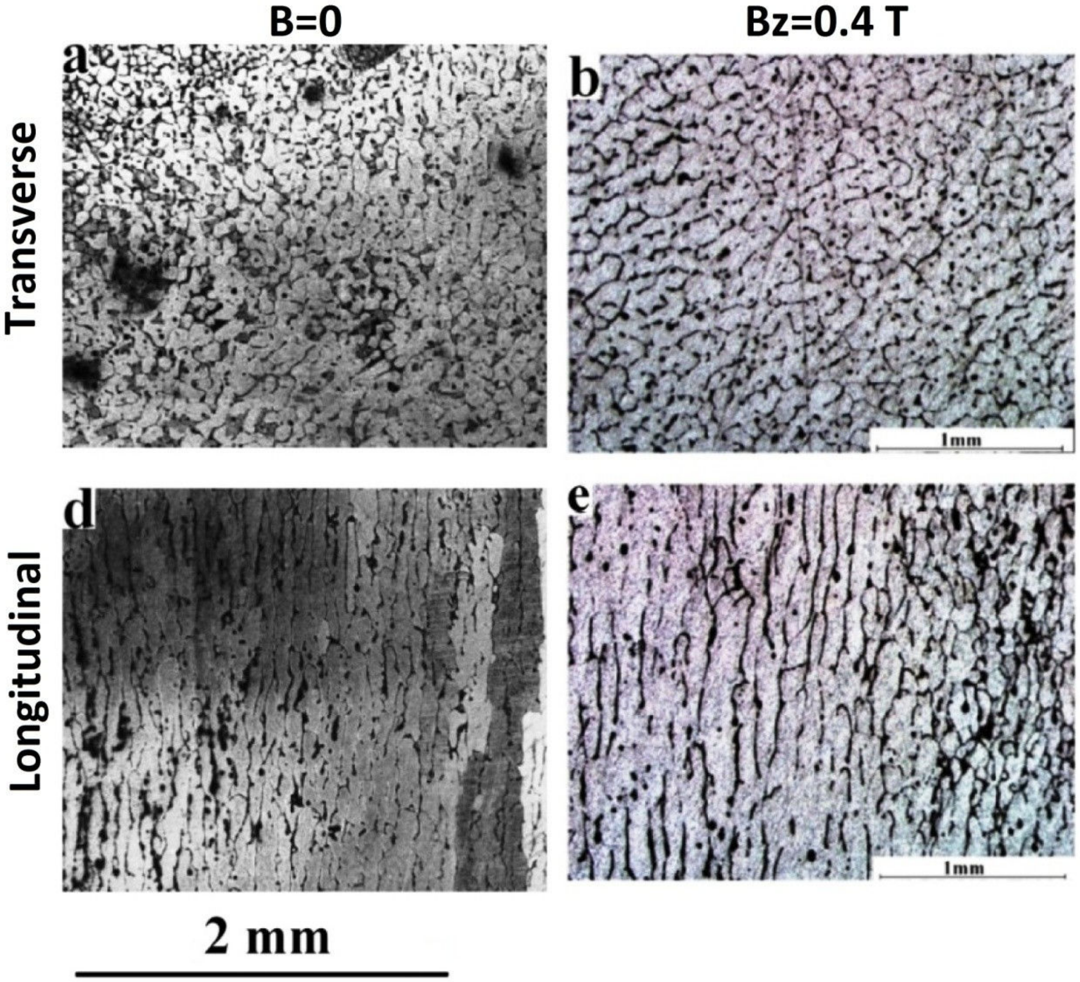

Figure. 5.6: Structure of directionally solidified Sn-10%wt.Pb alloy at *v*=2 µm/s: a,d) without field; b,e) with 0.4 T axial field

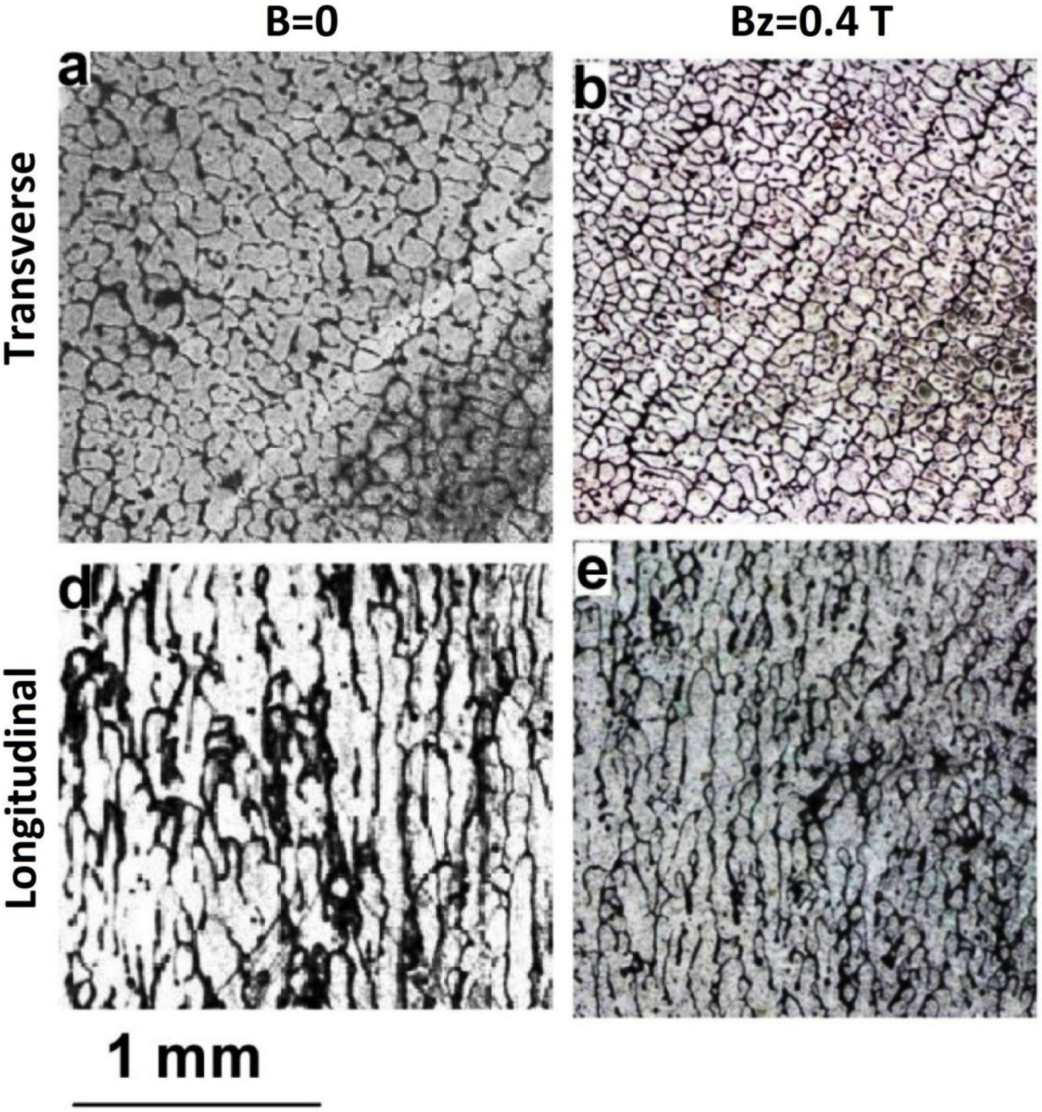

Figure 5.7: Structure of directionally solidified Sn-10%wt.Pb alloy at v=10 µm/s: a,d) without field; b,e) with 0.4 T axial magnetic field

Anisotropy seen in Figure 5.7(b) might be caused by magnetic field or temperature inhomogenity in the crucible. As mentioned before even small field asymmetry may result as a melt flow in the crucible scale. According to theoretical description TEMC flow in case of axial magnetic field is small vortices in primary dendrite scale.

5.4. Static transverse magnetic field

Static transverse magnetic field creates TEMC flow perpendicular to magnetic field according to numerical models and theoretical analysis. Flows from all dendrite arms add up and cause macroscopic flow at the size of a crucible. It is expected for this flow to cause macrosegregation along the cross section of the sample perpendicular to magnetic field as shown in Figure 5.8. TEMC flow is driven by Lorentz force in thin region above dendrite mesh and within the mushy zone.

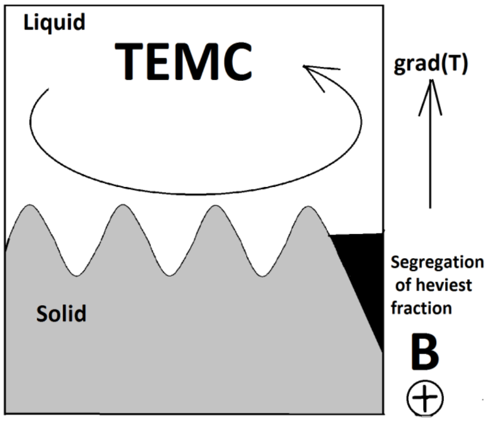

Figure 5.8: Schematic illustration of TEMC caused by transverse magnetic field and heaviest fraction macrosegregation formation as a result of this flow

Structure of directionally solidified Sn-10%wt.Pb alloy at various growth velocities under 0.4 T transverse magnetic field compared to corresponding structure without magnetic field is shown in Figure 5.4 and Figure 5.9. Experimental results confirm the previously mentioned hypothesis that transverse magnetic field creates macrosegregation at the crucible scale. In the pictures dark regions represent β phase (Sn-80.8%wt.Pb) and light regions are α phase (Sn-2.5%wt.Pb).

Optical microscopy of etched samples actually does not reveal quantitative component distribution but only gives qualitative distribution. Pb rich fraction is concentrated at the left side perpendicular to magnetic field direction as shown in Figure 5.9. At lower growth velocities due to TEMC relatively large Pb rich β phase and eutectic regions are forming in the left side of the cross section of the sample. These inclusions are forming when sufficiently high concentration of Pb is reached. At very low growth velocity of 0.5 µm/s large tin grains are forming in the middle part of the ingot while lead rich fraction is located close to the walls of the crucible. This could be the consequences of the thermosolutal and thermal convections due to radial temperature differences and of the fact that heat is input in the sample and removed from the sides, causing radial temperature gradient.

Figure 5.10 compares directionally solidified Sn-20%wt.Bi alloy with 0.4 T static transverse field and without field. Although the grain morphology of this alloy is different from Sn-Pb, it exhibits the same macrosegregation of Bi in the direction perpendicular to magnetic field. However this result can only be used as an example to demonstrate that magnetic field has similar effect on various alloys, detailed analysis would require more experimental data at different growth velocities. More detailed analysis will be done on grain spacing of Sn-10%wt.Pb alloy which are solidified at various velocities with and without magnetic field.

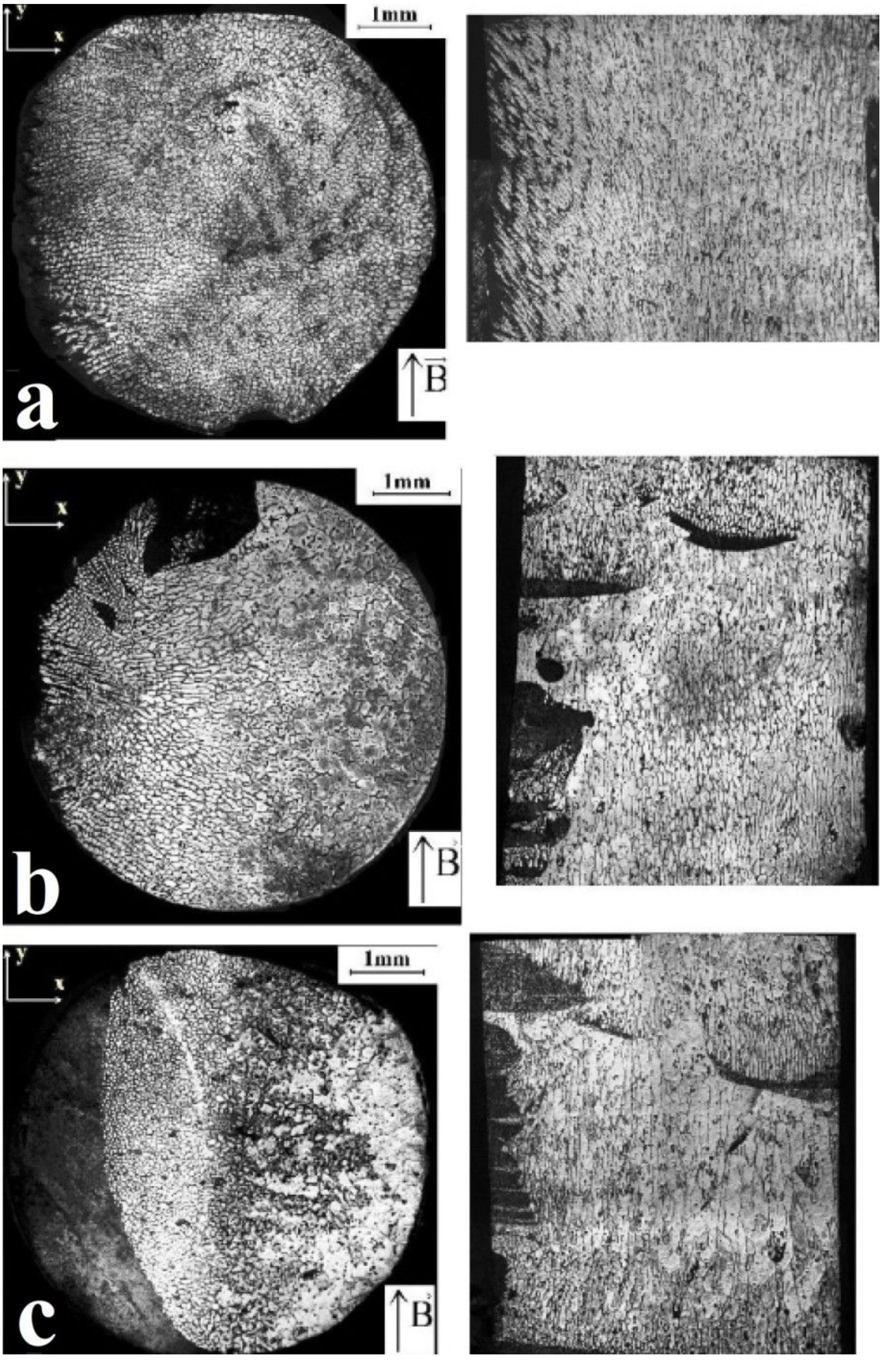

Figure 5.9: Directionally solidified Sn-10%wt.Pb under 0.4 T transverse magnetic field: a) 10 μm/s; b) 2 μm/s; c) 0.5 μm/s

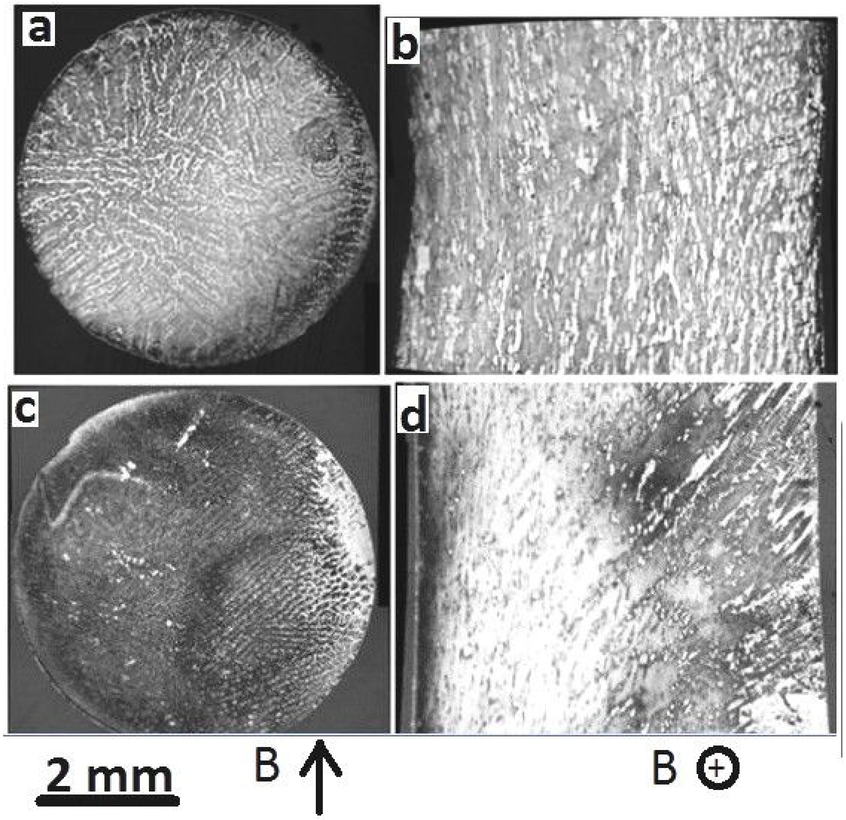

Figure 5.10: Directionally solidified Sn-20%wt.Bi alloy at 10μm/s: a,b) without field; c,d) solidified under 0.4 T transverse magnetic field

Figure 5.11 shows the transition region from cellular to eutectic structure. Eutectic structure is forming when certain composition proportion is reached. In eutectic region it is still possible to distinguish separate components at great magnification, but eutectic solidification is different from solidification of alloy with different concentration. Eutectic structure is also affected by magnetic field as studied by Li (Xi, Ren and Fautrelle 2006).

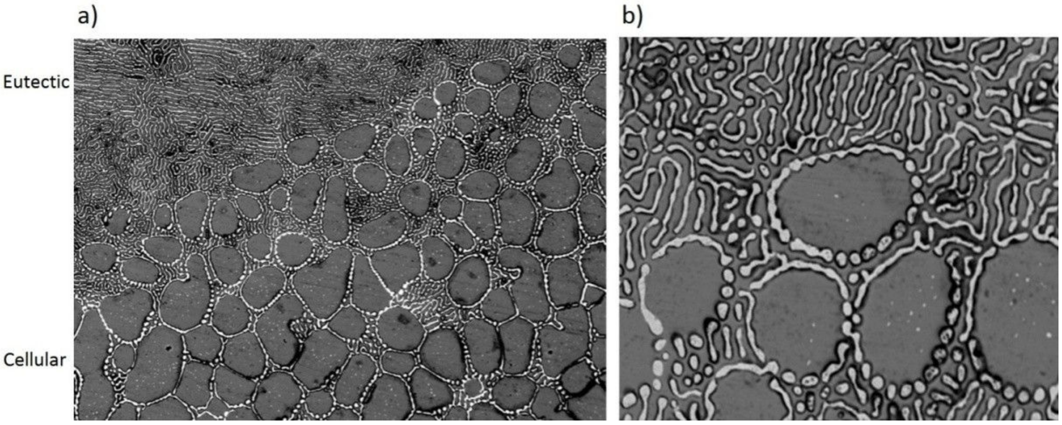

Figure 5.11: SEM pictures of Sn-10%wt.Pb alloy (dark regions- β (Sn-80.8%wt.Pb), light regions-α (Sn-2.5%wt.Pb)). Region where transition from cellular to eutectic structure takes place is shown here from Figure 5.9(c): a) magnification 500×; b) magnification 2000×

5.5. Result analysis

In this section detailed analysis of primary dendrite spacing as a function of applied magnetic field will be carried out. Obtained results will be compared to analytical relations describing the characteristic dendrite size as a function of forced convection intensity. Figure 5.12 illustrates the differences in longitudinal structure of the Sn-10%wt.Pb alloy solidified at the same velocity, but under different influences of magnetic field. Illustration shows significant difference in dendrite spacing and column length. Concentration and sizing of inclusions are also different in each case.

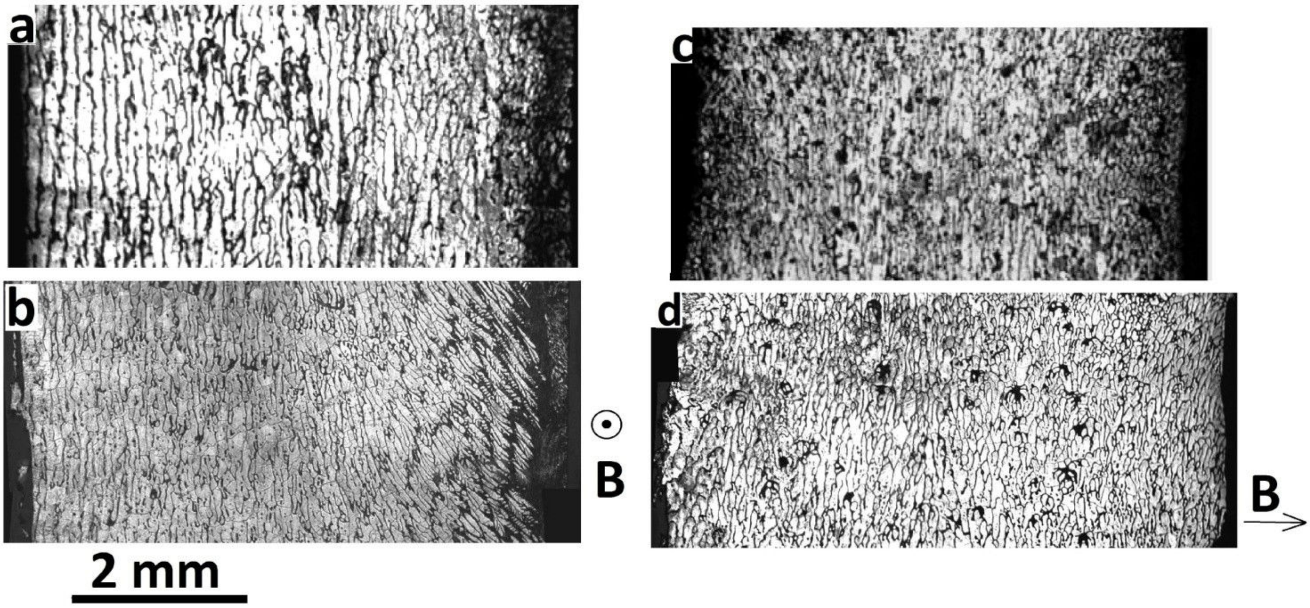

Figure 5.12: Longitudinal structure of directionally solidified Sn-10%wt.Pb alloy at 10 µm/s: a) without magnetic field; b) perpendicular to transverse magnetic field; c) under 0.4 T axial magnetic field; d) parallel to transverse magnetic field

Based on obtained results, columnar to equiaxed transition (CET) can be analysed and critical transition growth velocity can be estimated. CET and its control is an important field of interest of solidification science (Li, Ma and Song, et al. 2009), (Eckert, et al. 2005). Columnar to equiaxed transition depends mainly on temperature gradient and growth velocity, but also on material properties. CET threshold is described by Hunt diagram showing CET value at certain temperature gradient and growth velocity. Diagram for Sn-10%wt.Pb alloy is given in Figure 5.13. Threshold velocity can be found according to equation (5.3) (Hunt 1984).

$$\theta = 0.617 \cdot n^{1/3} \cdot \sqrt{\frac{vC_0}{A}} \left(1 - \left(\sqrt{\frac{A \cdot \Delta T_n^2}{vC_0}} \right)^3 \right) \tag{5.3}$$

where n is nuclei density in the melt, A is empirical constant characterizing each alloy, ΔT_n is difference between liquidus temperature and nucleation temperature. Here n is chosen based on grain sizing in the solidified samples which are typically few hundred micrometers $n=d^{-3}$, A is estimated to be 10^{-5} m%/sK^2, ΔT_n is assumed to be equal to 1 K.

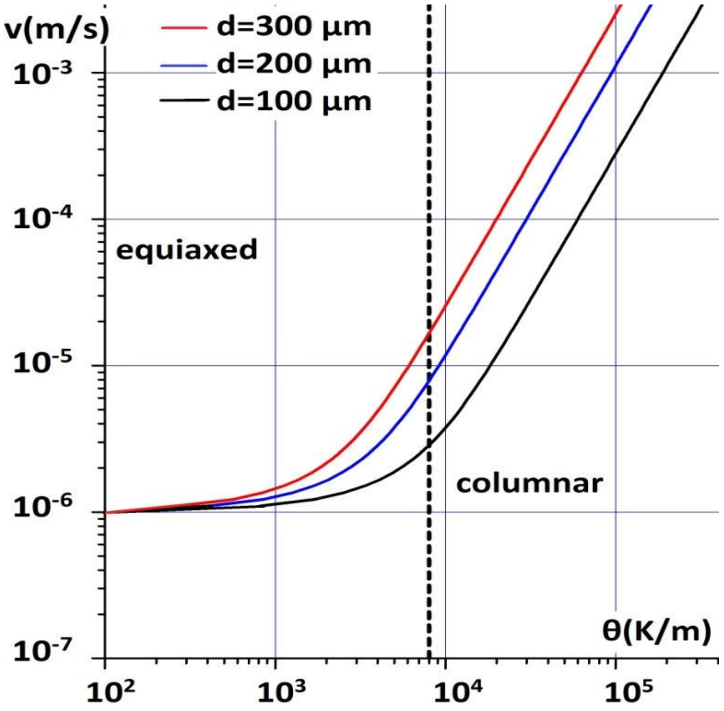

Figure 5.13: Hunt diagram for directionally solidifies Sn-10%wt.Pb, describing columnar to equiaxed threshold at three different nuclei sizes

Expression for critical velocity from columnar to equiaxed transition is given also by Kurz &Fisher (Kurz and Fisher, Fundamentals of Solidification 1984). If inequality given by equation (5.4) is fulfilled then structure is columnar otherwise it is dendritic.

$$\theta > mvC_0 \frac{(1-k)}{D} \tag{5.4}$$

where v is solidification velocity, D is diffusion coefficient, C_0 is nominal concentration, k is partition coefficient, m is liquidus slope, θ is temperature gradient. For directionally solidified Sn-10%wt.Pb corresponding values are given in Table 4.1. We get critical growth velocity of 3.5 µm/s which agrees well with the value predicted by Hunt model. This critical velocity can be modified by forced convection (TEMC in this case).

Directional solidification experiments under 0.4 T static transverse magnetic field show that structure of the Sn-10%wt.Pb alloy is affected by magnetic field. In this case at all three solidification velocities, structure is columnar but characteristic column length reduces as TEMC influence increases.

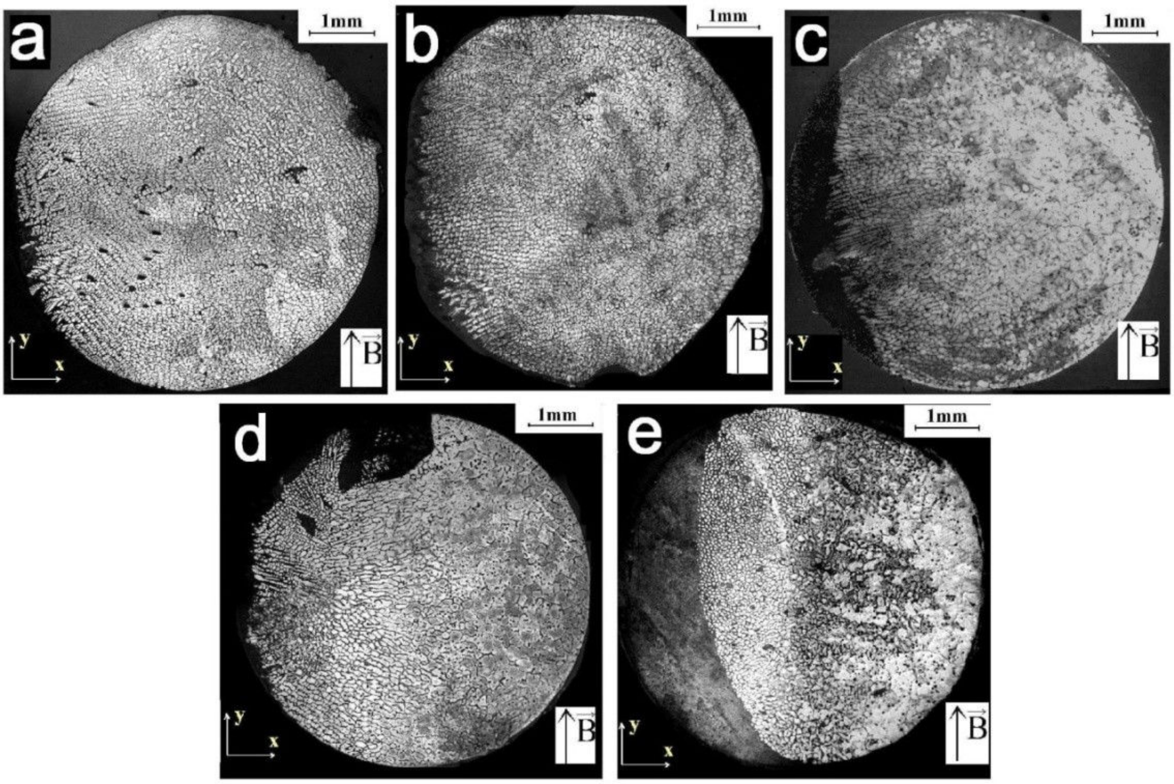

Figure 5.14: Comparison of structure of Sn-10%wt.Pb alloy solidified under 0.4 T transverse magnetic field: a) 20μm/s; b) 10 μm/s; c) 5 μm/s; d) 2 μm/s; e) 0.5 μm/s

In directional solidification lower growth velocity means larger dendrite spacing and larger grain size of an alloy. Directional solidification at various growth velocities, compositions and temperature gradients is experimentally analysed by (Cadirli and Gunduz 2000). In this work experimental results were compared model given by with (Kurz and Fisher 1984) as shown in equation (5.5). Model gives larger values than obtained in experiment. Comparison between experimental results obtained in our work and theoretical expression given by equation (5.5) is shown in Figure 5.15. Data from Table 4.1 is use in the calculation of characteristic dendrite spacing. Agreement of experimental results and theoretical model without magnetic field are more accurate than with applied magnetic field. With applied magnetic field experimental results are smaller than predicted by theory.

$$\lambda_0 = 4.3\left(\frac{D\Gamma\Delta T_0}{v}k\right)^{0.25}\left(\frac{1}{\theta}\right)^{0.5} \tag{5.5}$$

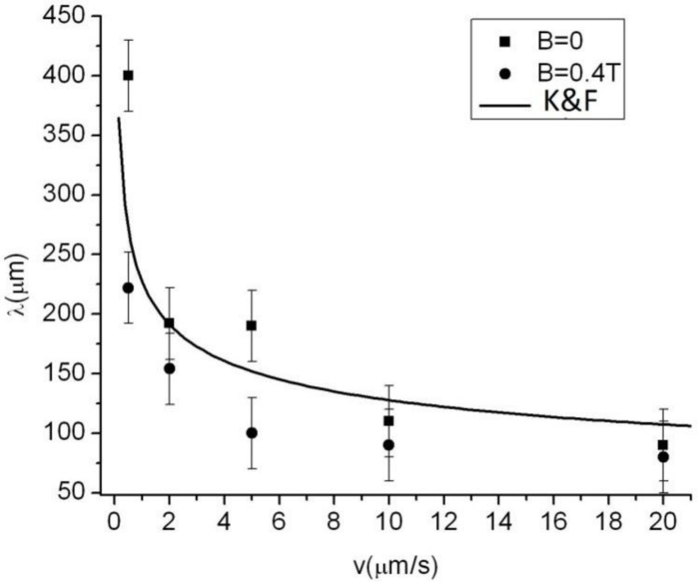

Figure 5.15: Comparison between experimental and theoretical primary dendrite spacing of directionally solidified Sn-10%wt.Pb alloy as a function of growth velocity without magnetic field and with 0.4 T magnetic field

Characteristic grain sizes is measured by counting the number of grains crossed by diameter parallel to magnetic field. In this way, grain size under forced convection influence in obtained which are not strongly affected by macrosegregation in the field perpendicular direction (Figure 5.14).

Table 5.1: Measured characteristic dendrite spacing at different growth velocities without magnetic field and under 0.4 T transverse field.

***v* (μm/s)**	**λ (μm) B=0**	**λ (μm) *B*=0.4 T**
0.5	400	222
2	192	154
5	190	100
10	110	90
20	90	80

Micrographs indicate only approximate component distribution along the cross section of the sample, thus in order to measure actual Pb concentration along the diameter of the samples solidified under transverse magnetic field at various solidification velocities as shown in Figure 5.14, different measurement method has to be used. We chose to measure composition distribution with scanning electron microscope (SEM). Quadrant backscattered electron (QBSE) detector is used to photograph the sample (Goldstein, et al. 2003). Back scattered electrons are beam electrons which are elastically reflected by the sample. Their energies are strongly dependent on atomic number of the atom from which they are reflected. By processing these signals from four detectors located around the sample, local composition at certain point can be measured. In this case, if picture is taken by this detector then composition is directly proportional to the gray level in the picture as shown in Figure 5.16. Composition distribution profile is obtained by plotting gray level as a function of coordinate. Result is then averaged and fitted with exponent function (eq. (5.6)) as shown in Figure 5.17. It was measured that light regions in QBSE picture corresponds to tin solution in lead (α phase Sn-80.8%wt.Pb) and dark corresponds to lead solution in tin (β phase Sn-2.5%wt.Pb) .

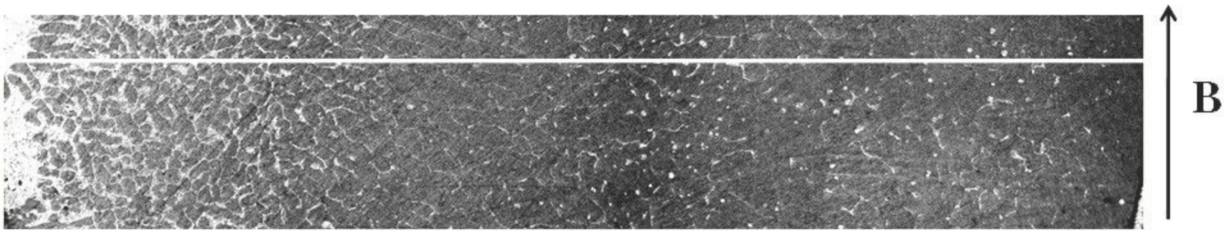

Figure 5.16: Electron microscope QBSE image of sample cross section; Light: Sn solution in Pb (Sn-80.8%wt.Pb) α; Dark: Pb solution in Sn (Sn-2.5%wt.Pb) β

Measured composition profile is fitted with exponent function

$$C = C_0 + C_1 \cdot \exp(-x / C_2) \tag{5.6}$$

where C_0, C_1, C_2 are constants. This analysis and the obtained results summarized in Figure 5.17 shows that averaged component distribution is close to exponential. This is an interesting outcome because if we look at the one dimensional convection-diffusion exercise (Thermal-Fluids Central 2010), (Wesseling 2001), it also gives exponential component distribution with coefficients depending on diffusion/convection ratio (since Peclet number *Pe=uL/D*). Convection-Diffusion equation is given in the form

$$\varphi = \varphi_0 - (\varphi_L - \varphi_o)\left(\frac{\exp(ux/D) - 1}{\exp(uL/D) - 1}\right) \tag{5.7}$$

where φ_0 is concentration at the one end (*x=0*), φ_L is concentration at the other end (*x=L*), φ is concentration at the coordinate *x* and *u* is convection velocity.

Matching equation (5.6) and equation (5.7) characteristic diffusion velocity *u* can be estimated from these considerations. Found values summarized in Table 5.2 are very small. Equation (5.7) describes the equilibrium concentration profile which is reached in infinitively long time as a result of steady convection and diffusion between the fixed concentrations at the both sides.

Peclet numbers suggest that convective and diffusive mass transports are of comparable order of magnitude in this case. In case of directional solidification time for concentration profile to form is limited by the growth velocity and convection should be dominant over molecular diffusion which is very slow process whose characteristic time can be estimated form equation (5.8). We obtain $t \approx 5$ h, while characteristic convection time given by equation (4.14) is much faster.

$$t = \frac{l^2}{2D} \tag{5.8}$$

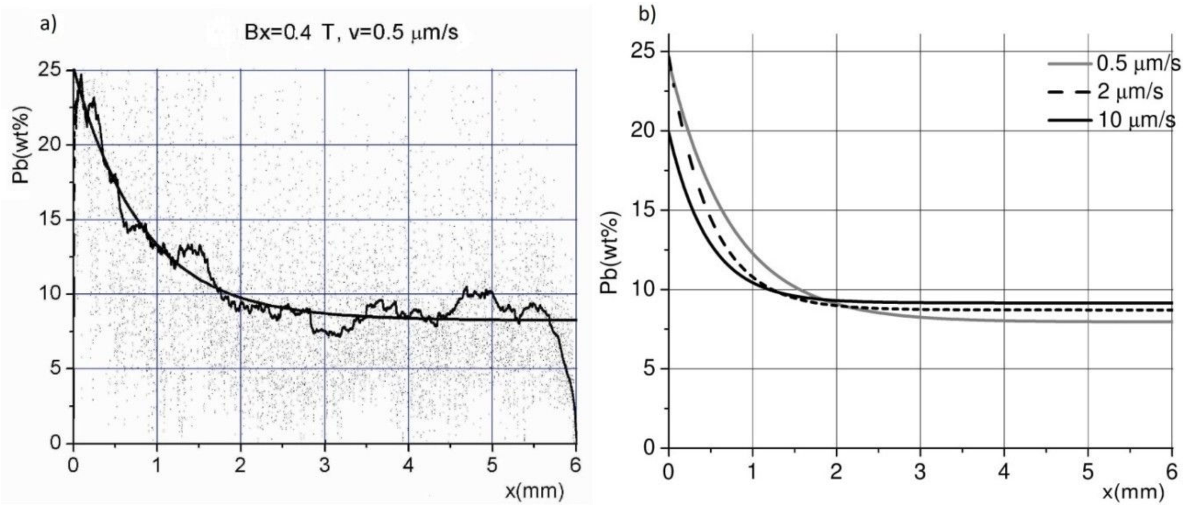

Figure 5.17: SEM composition measurements: a) Pb content along cross section of the sample at growth velocity 0.5 μm/s. Experimental points, averaged distribution and exponential fit with equation (5.6); b) Pb content in directionally solidified Sn-10%wt.Pb alloy as a function of coordinate at three different solidification velocities

Table 5.2: Coefficients of exponential fit and results of one dimensional convection-diffusion problem (equation (5.7))

v (μm/s)	C_0 (%)	C_1(%)	C_2	φ_0 (%)	φ_L (%)	u (μm/s)	d (μm)	$Pe=ud/D$	$Pe=uL/D$
0.5	7.95	16.4	0.75	8	25	1.3	222	0.29	7.8
2	8.71	15.94	0.49	8.5	24	2	154	0.32	12
10	9.15	10.74	0.47	9	20	2.2	90	0.20	13.2

u- calculated convection velocity from equation. (5.7), *d*- measured grain size, mutual diffusion coefficient $D=1\cdot10^{-9}$ m^2/s (Anusionwu, Madu and Orji 2009)

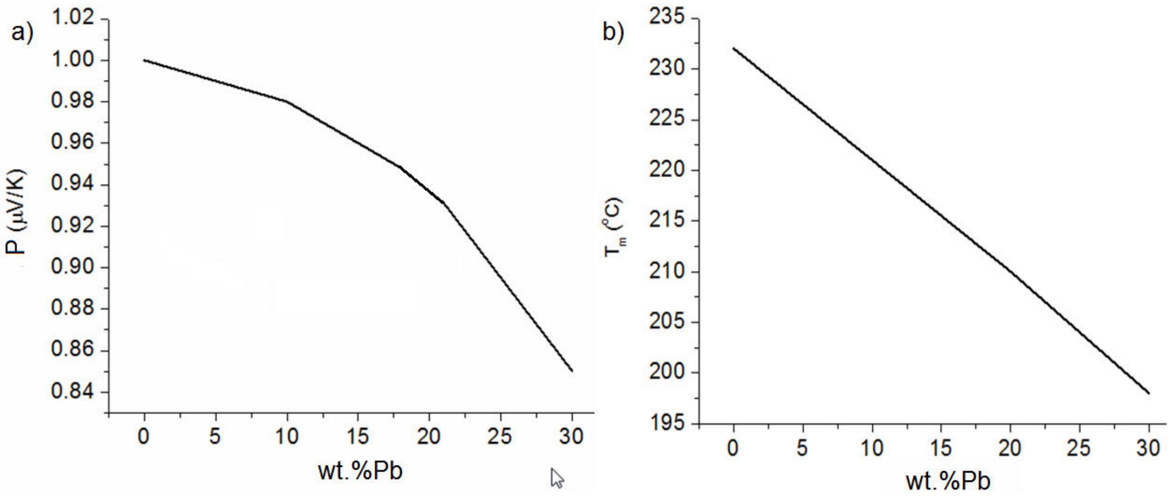

Figure 5.18: Differential thermoelectric power and melting temperature as a function of Pb concentration (Kaldre, Fautrelle, et al. 2010)

As shown in Figure 5.17(b), Pb concentration along the cross section of the sample varies from 8% to 25 %. Differential thermoelectric power of Sn-Pb alloys are measured in chapter 3. Dependence of melting temperature and differential thermoelectric power between solid and liquid phase are shown in Figure 5.18. Melting temperature variation along the diameter of the sample may result as a slope solidification front, if temperature gradient is vertical. *P* variation results as a difference of TE force density along the sample, however in this case the difference is only less than 10% within the concentration range from 8% to 25 %, and will have relatively small effect on overall TEMC flow. Slope solidification front may cause crucible scale TEMC flow, such situation is analysed in section 4.6. Characteristic TEMC intensity of Sn-10%wt.Pb alloy at different length scales is shown in Figure 4.5. At 0.4 T magnetic field crucible scale flow is significantly damped by magnetic field. In 3D cylindrical container flow pattern would be similar. In case of directional solidification under transverse magnetic field this flow is oriented in the same direction as TEMC flow caused by primary dendrite arms as depicted in Figure 4.2(b).

5.6. ESRF in-situ observation solidification experiment

Directional solidification experiments of Al-4%wt.Cu, Al-7%wt.Si and Sn-3%wt.Pb alloy were carried out in European Synchrotron Radiation Facility (ESRF) in Grenoble by the international group of scientists from Latvia, France and China. Expected results from these experiments are to determine the TEMC velocity by measuring the particle and broken dendrite fragment motion velocity and observation of changes caused by TEMC on the dendrite growth and morphology.

5.6.1. Experimental facility

Solidification in thin experimental cell is filmed with high energy and coherence X-rays to visualize the processes during solidification of a binary alloys. Aim of the solidification observation with X-rays is to visualize the differences in dendrite growth and liquid phase flow without and with applied magnetic field. Recent developments of technology allows performing in situ observation of solidification process which can give new insights in the processes taking place near the solidification interface and interdendritic region. Real solidification observation gives an opportunity to directly observe dendrite growth and liquid phase motion affected by effects of applied magnetic field. It is also important to acquire experimental data to compare with theoretical estimations and numerical models presented in previous chapters.

Experimental setup consists of a furnace with a windows for incoming and outgoing X-ray beam, which is placed inside a vacuum chamber. Sample with thickness of 150-500 μm is casted into the ample and placed into the furnace. Length and width of the sample are correspondingly 40 mm and 6 mm. Estimated temperature gradient at the solidification interface is approximately 3 K/mm based on the temperature measurements at the top and bottom of the sample. Power of the furnace is gradually decreased and sample is solidified. Solidification sessions with and without magnetic field are performed with each alloy. Growth velocity is controlled by cooling rates, ranging from 0.1 K/min to 2 K/min.

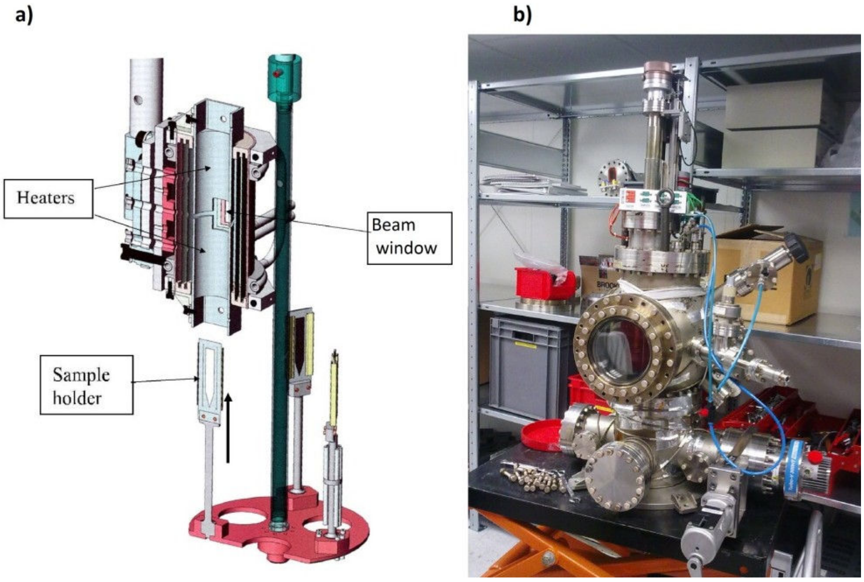

Figure 5.19: a) Schematic drawing of experimental furnace; b) Photo of experimental vacuum chamber built by IM2NP

Experiments with solidification under 0.08 T magnetic field has been done using single NdFeB cube magnet with 50 mm edge. For higher magnetic field values permanent magnet system is designed to create magnetic field in ESRF experiment as shown in Figure 5.20(a). Due to limitations of space available in the vacuum chamber, optimal design was chosen in order to achieve sufficiently high magnetic field. Magnet system is assembled from 3 pieces of NdFeB magnets. Modelling of magnetic field distribution in the furnace is calculated with Comsol to evaluate the net magnetic field and its gradient on the sample. It was found that maximum magnetic field at the centre of the furnace, where sample is located is about 0.2 T.

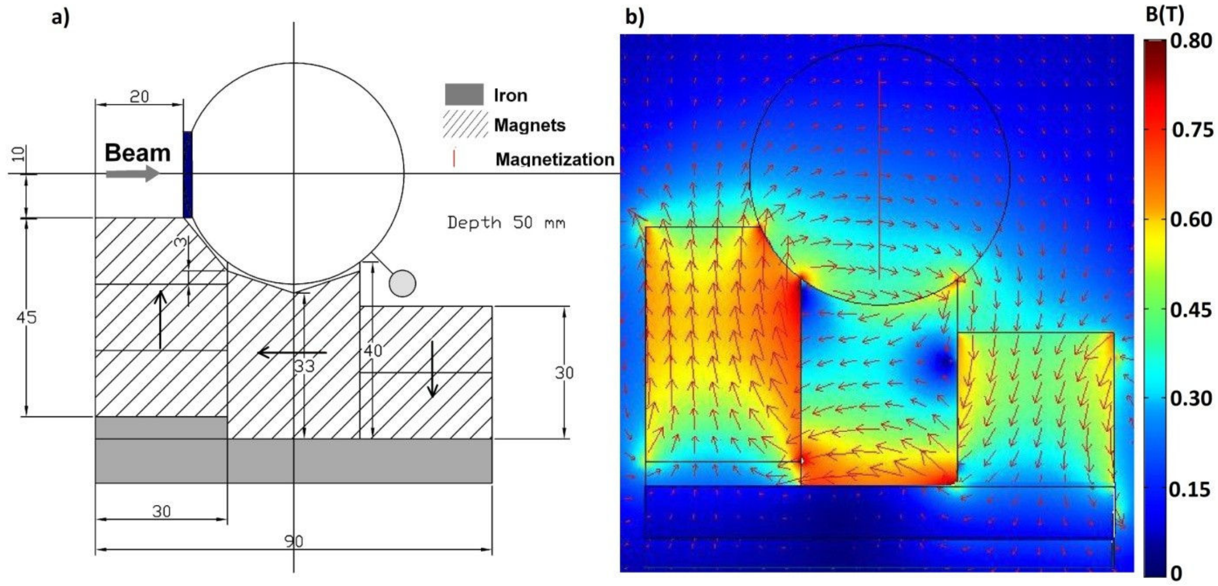

Figure 5.20: Permanent magnet magnetic system for solidification experiments under magnetic field. a) Sketch of magnet arrangement; b) Numerical simulation of field distribution

According to the TEMC theoretical estimation, given in section 4.3, such magnetic field and temperature gradient can cause considerable convection which might have visible effects on the structure of dendrite growth and melt flow in the experimental cell. Thus these experiments are done in 200 μm thin experimental ample, which is comparable to viscous layer thickness, Hele-Shaw flow approximation has to be applied to compare these results with estimations and numerical models. In this case thickness is comparable with dendrite sizing, thus viscous damping is mainly defined by cell thickness which is characteristic size in equation (4.12) in this case, giving velocity of 0.3 mm/s at 0.08 T magnetic field and 0.5 mm/s at 0.2 T magnetic field for Sn-3%wt.Pb alloy.

5.6.2. Experimental results

In the first series of experiments solidifications under 0.08 T magnetic field at cooling rates 0.1 K/min, 0.5 K/min and 1 K/min are done . Results are analysed in this section comparing dendrite growth direction and spacing without and with applied magnetic field. Characteristics of motion and velocity of free solid particles in liquid melt caused by applied magnetic field has been experimentally measured and compared to analytical and numerical simulation results.

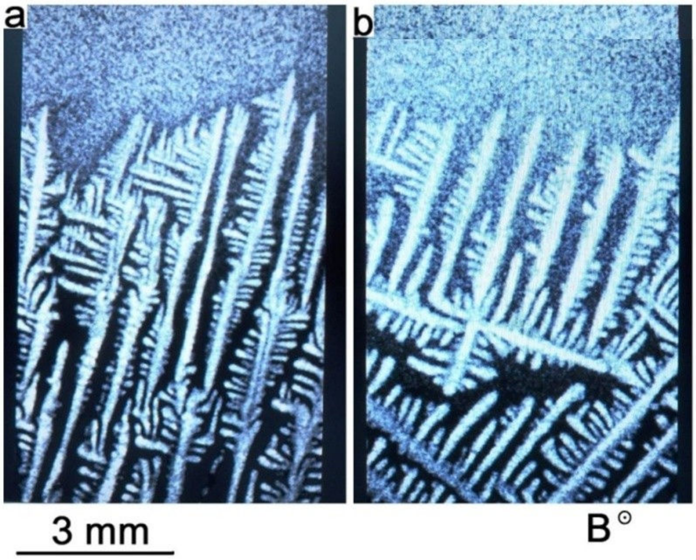

Figure 5.21: Dendrite structure of solidified Sn-3%wt.Pb (cooling rate 0.1 K/min): a) Without magnetic field; b) With 0.08 T magnetic field

Figure 5.21 compares dendrite structure during solidification without and with applied magnetic field. It can be seen that without magnetic field dendrite growth direction is mainly determined by heat extraction direction from the crucible, while with magnetic field dendrite growth direction is modified, and due to the effect of liquid melt convection, preferred growth direction is less distinct and characteristic column length is shortened. This conclusion agrees with previous experimental results presented in section 5.5 showing that CET is promoted by applied magnetic field.

During solidification of Al-4%wt.Cu dendrite braking was observed. Broken dendrite particles were carried away by the Thermoelectric forces. From this observation particle velocity caused by thermoelectric effect is estimated. From equation (4.47) follows that velocity is proportional to particle size square, thus larger particles move faster than smaller. This is confirmed by experimental observations during filming solidification process with X-rays (Wang, et al. 2012).

Figure 5.22 shows magnified view of a gap in interdendritic mesh at two successive time moments. Solid particle in liquid is indicated by white arrows. Experimentally measured 60 μm size particle velocity is 0.3 mm/7 s=44 μm/s. From equation (4.47) analytical velocity value is calculated 64 μm/s by taking R=30 μm and c=1/3. Thus it may be concluded that theoretical model gives fairly accurate particle velocity estimation. Differences might emerge due to assumptions made during derivation of analytical expression, calculation of c and because of the use of Stokes drag formula which describes spherical particle in laminar approximation.

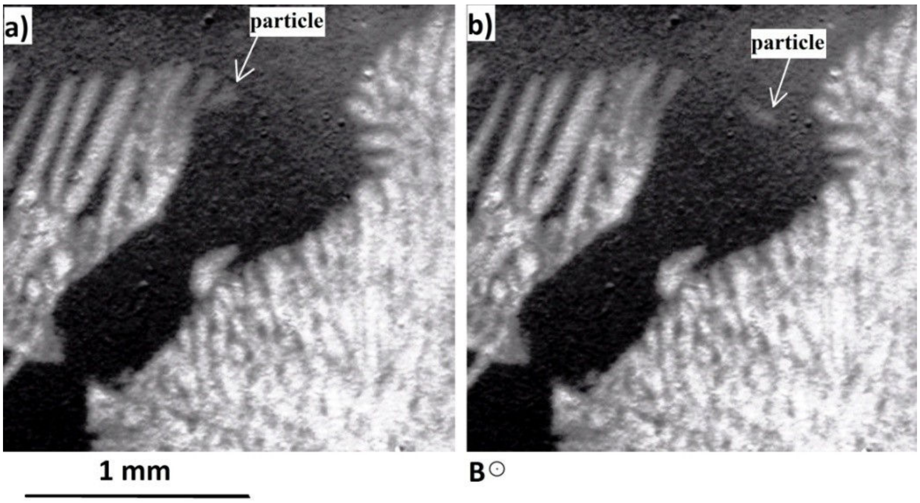

Figure 5.22: Magnified region during directional solidification of Al-4wt%Cu alloy under 0.08 T magnetic field (cooling rate 0.5 K/min): a) *t*=0; b) *t*=7 s

Qualitatively different solidification interface shape and dendrite growth direction was observed. Changes in solidification front shape can be explained due to TEMC flow in the scale of a crucible. At the beginning difference between highest and lowest points of planar solidification front is larger and eventually decreases until this difference becomes very small. This observation is contrary to observations made during solidification of same alloy without magnetic field (Bogno, et al. 2011) where solidification front perturbations show tendency to grow over time. This difference can be attributed to influence of applied magnetic field and TEMC flow which transports heat along the solidification interface.

5.7. Conclusions

Influence of magnetic field applied during directional solidification of binary metallic alloy on macrosegregation and dendrite morphology and spacing are demonstrated in various experiments described in this chapter. Experimental results are compared with numerical models and analytical calculations. Overall agreement of results are good and in most cases experimental observations can be interpreted in relation with numerical and analytical results. Nevertheless significant disagreement between estimated TEMC characteristic velocity and effective convection velocities calculated from relation describing grain spacing in usage of convection-diffusion equation (5.7), is observed. Effective convection velocities estimated by these indirect methods turned out to be two orders of magnitude smaller than TEMC velocity estimation (eq.(4.12)). This can be explained by several reasons. Thermoelectric current is circulating at a very small distance from the solidification front, thus also the force density decreases rapidly along the distance from solidification front thus local velocity near the front can be much larger than effective convection velocity at crucible scale in the bulk of the melt. This was also confirmed by numerical simulations of TE current and force calculations in section 4.7. Formation of structure is caused by composition distribution in mushy zone and in the region very close to solidification interface where effective velocity can differ significantly from the TEMC velocity outside the mushy zone. Thus velocity estimation obtained from solution of convection-diffusion exercise and analysis of grain sizes in convective regime refers to oriented velocity in the mushy zone, while velocity deduced from approximate solution of Navier-Stokes equation and analysis of threshold velocity obtained by analyzing superimposed TEMC and magnetic stirring (given in chapter 7) gives velocity in the volume of the liquid part of the sample.

Solidification of Sn-10%wt.Pb under 0.4 T axial magnetic field showed little effect on grain size and microstructure of alloy. However significant changes in dendrite spacing is observed if alloy is directionally solidified with very low solidification velocity, which is presumably the consequence of damped natural convection by magnetic field.

Solidification of Sn-10%wt.Pb alloy under transverse magnetic field showed macrosegregation in the field perpendicular direction. Macrosegregation significance is larger at lower solidification velocity. Measured primary dendrite spacing agrees well with analytical Kurz&Fisher model and other experimental works. It is shown that dendrite spacing and component segregation can be altered by TEMC caused by moderate magnetic field (0.4 T in these experiments). Component segregation profile is measured by backscattered electron detector in section 5.5 and approximated with exponent function as expected according to theory.

Impact of the transverse magnetic field on the solidification front shape and dendrite morphology were observed in experiments with X-ray in-situ observation of solidification. Experimentally measured solidification interface shape and free particle motion in liquid phase are compared with numerical simulation results and analytical relations. Analytical and experimental particle velocities show good agreement, while solidification front with magnetic field behaves differently than without.

Nevertheless correlation between convection intensity and microstructure morphology is not clear yet, and only in some cases it is possible to qualitatively predict the way how the solute flow will affect structure of the alloy. Main side factors affecting experimental results are melt flow due to natural and thermosolutal convection, and magnetic field and temperature inhomogenity. These reasons and characteristics of described phenomena itself makes it difficult to achieve precise match between measured experimental results and theoretical quantities. Relations and trends described and verified in this chapter might not be valid for all alloys due to their specific properties and behaviour, but based on literature review of previous experimental works, results are not contradictory and seems applicable for most of binary alloys.

6. Combination of TEMC and electric current

In this chapter, solidification with superimposed static magnetic field and electric current through the solidification front is investigated. Interaction between current and magnetic field causes additional force term in Navier-Stokes equation thus flow field in the liquid melt is affected. Influence on the directional solidification process and its outcome caused by magnetic field and direct or alternating electric current is experimentally and analytically studied.

6.1. Introduction

By combining action of TEMC with other sources of forced convection on the metallic alloy during solidification, it is possible to vary the significance of total forced convection and see how it affects the structure of an alloy. In such a way we can estimate the intensity of TEMC, by comparing it with another convection whose magnitude is better known. This comparison of two simultaneous effects allows us to experimentally deduce the TEMC characteristics and to compare them with the ones obtained from experimental results in chapter 5 and theoretically estimated from various models in chapter 4.

Applied electric current through the solidification interface interacts with magnetic field and liquid phase convection is created. In this chapter similarities between electromagnetic convection caused in this way and TEMC will be analysed. Main focus will be devoted to analysis of axial magnetic field and same direction electric current. In this case force distribution at the solidification interface is similar than thermoelectric force, but in this case its magnitude can be easily varied by changing electric current magnitude. Inside the volume of solid and liquid parts of crucible with metallic sample, force is zero, while at the interface it is different because of different electric conductivities of solid and liquid phases. If interface is not flat, then due to this reason current density component in the plane perpendicular to axis of the sample appears. Transverse magnetic field and axial current will also be experimentally investigated and numerically simulated. This case is more complicated because Lorentz force density is present in all fluid volume, causing intensive flow in the crucible if magnetic field is not homogeneous in the liquid part of the sample. This cause problems to do experiment to analyse solely the effects of melt flow on the structure of an alloy. However numerical simulation suggests that if sample is placed in a confined crucible and homogeneous field, then melt flow pattern caused by electric current and magnetic field interaction is also similar to TEMC caused by transverse magnetic field, and this effect can be used to enhance or suppress the effects of TEMC.

6.2. Literature review

In literature the most described is the influence of alternating current on the solidification structure. Influence of current pulses and alternating current through the solidification interface during directional solidification has been widely studied experimentally and its influence on structure refining and homogenization is demonstrated. Modifications of CET caused by electric current pulse has been investigated in ref. (Li, Ma and Changjiang, et al. 2009). It was shown that applied electric current pulses change structure from columnar to equiaxed during solidification of bearing steel, and homogeneity of structure is improved. Alternating current influence on primary dendrite spacing has been theoretically analysed by Ma (Ma, Zheng and Larson 2004). In this work different frequency and direction is analysed and time-varying convection caused by applied current has been numerically modelled in each case. Current pulse effects on structure refining of pure aluminium is studied in ref. (Liaoa, et al. 2007). In this work several effects introduced by current are analysed. It is concluded that the main mechanism causing significant changes in structure is that pulse current makes solidified nuclei fall off the wall, thus promoting the multiplication of crystal nuclei leading to structure refining. Pulsed current and alternating current influence on the interface shape and primary dendrite spacing has been studied by Song (Song, et al. 2011). It is experimentally demonstrated that current can delay planar/cellular transition and primary dendrite spacing is reduced. Similar work with Sn-0.9%wt.Cu is done by Brush (Brush and Grugel 1997) also showing the refining effect of current pulses parallel to growth direction. Tensile strength of ZA27 (zinc-aluminium) alloy solidified under electric current and without has been measured in ref. (Gaoa, et al. 2002). It is concluded that various pulse current refines material structure and increases tensile strength. Alternating electric current (50 Hz) on the directional solidification of Al-4.5wt%Cu under axial magnetic field has been experimentally investigated by Xi Li (Li, Ren and Fautrelle 2008). Obtained results demonstrate the grain refining effect by electric current and magnetic field interaction, and columnar to equiaxed transition is delayed for a given alloy. Influence of superimposed static magnetic field and alternating electric current on the orientation of the crystalline grains of Sn-Pb alloys has been studied and its validity to modify crystal orientation is shown experimentally by doing X-ray diffraction of the solidified samples (Usui, Iwai and Asai 2006).

Direct electric current flow through the solidification interface has different effect. There are very few studies about direct current influence on structure. One of the works showing the influence of steady electromagnetic force on the structure of metallic alloy is done by Vives (Vives

1997). Here different types of interaction are analysed and structure refining effects caused by different current magnitudes are compared. Expected influence of direct electric current and parallel magnetic field on the melt convection has been analysed in (Vives 1986). In these works also possibility to artificially achieve microgravity conditions by balancing gravity with electromagnetic force is analysed. It is concluded that steady electromagnetic force allows to partially balance gravity thus affecting natural and thermosolutal convection in the melt.

6.3. Influence of direct current

If direct electric current is applied through the solidification front, then current component which is perpendicular to the magnetic field interacts with magnetic field and additional melt convection is caused by this force. Electrical conductivities of solid and liquid phases can be very different for metals and metallic alloys as shown in Figure 6.1, thus at the dendritic solidification interface electric current redistribution takes place and if magnetic field is parallel to electric current in the bulk of the liquid, then at the dendritic solidification interface, significant perpendicular current density component may appear.

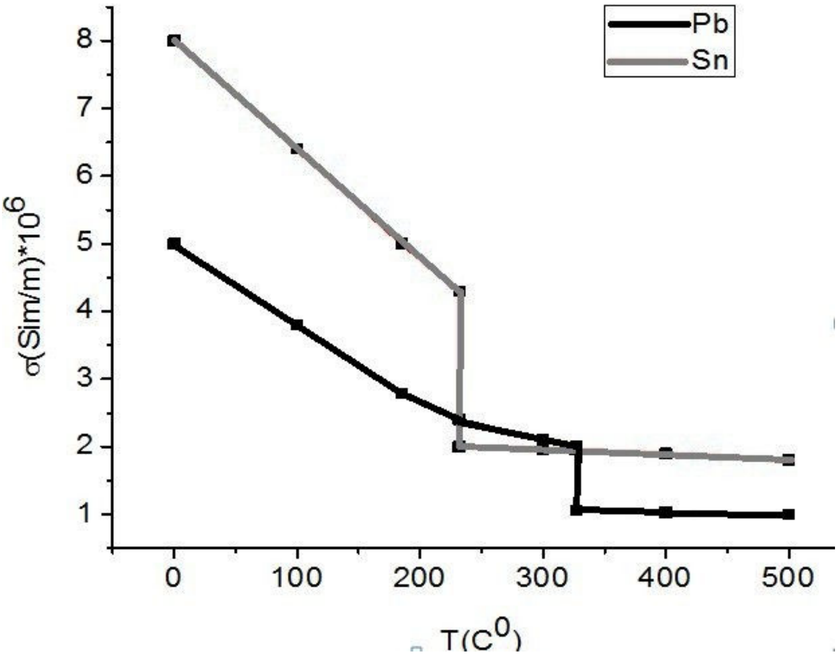

Figure 6.1: Electric conductivity of lead and tin as a function of temperature in solid and liquid state (Grigoriev and Melnikov 1991)

In case with applied electric current, additional term has to be introduced in Navier-Stokes equation, which describes Lorentz force caused by current and magnetic field interaction. Similarly than in section 4.3, Navier-Stokes equation can be simplified to estimate characteristic convection velocity order of magnitude. Electric current density component, which is perpendicular to magnetic field, depends on ratio of electric conductivities of alloy at solid and liquid states, and ratio between vertical and horizontal structure lengths as illustrated in Figure 6.3. Expression relating these quantities is given by equation (6.1), which is only valid if conductivities and sizes are of the same order of magnitudes.

$$j_{\perp} = j\left(1-\frac{\sigma}{\sigma_s}\right)\frac{h}{d} \tag{6.1}$$

For order of magnitude estimation, Navier-Stokes equation can be rewritten similarly as in case without electric current:

$$\rho\frac{u^2}{d}+\mu\frac{u}{d^2}+c\sigma\ (uB^2-P\theta B)+\left(1-\frac{\sigma}{\sigma_S}\right)\frac{h}{d}jB=0 \tag{6.2}$$

where j is electric current density far from the solidification front, σ_S and σ are electric conductivities in solid and liquid states, and h and d are vertical and horizontal characteristic size. Solution of this equation is:

$$u=\frac{\left(\sqrt{\left(c\sigma\ dB^2+\frac{\mu}{d}\right)^2+4\rho cBd\left(\sigma P\theta+J\left(1-\frac{\sigma}{\sigma_S}\right)\frac{h}{d}\right)}-\left(c\sigma dB^2+\frac{\mu}{d}\right)\right)}{2\rho} \tag{6.3}$$

Convection velocity order of magnitude caused by axial magnetic field and parallel electric current through the solidification interface is shown in Figure 6.2. In this estimation properties of Sn-10%wt.Pb given in Table 4.1 are used. Two cases are analysed here: electric current parallel to the magnetic field and opposite. We can see that if electric current is opposite to the field at certain current value TEMC is compensated by electromagnetic convection. For a given case the current density necessary to achieve this regime is around 5000 A/m^2 (from Figure 6.2) or 0.14 A for the sample of 3 mm radius as used in experiments of this work, which is relatively low value. Negative velocity in Figure 6.2, if electric current and magnetic field are opposite means that in this case electromagnetic force causes convection opposite to TEMC.

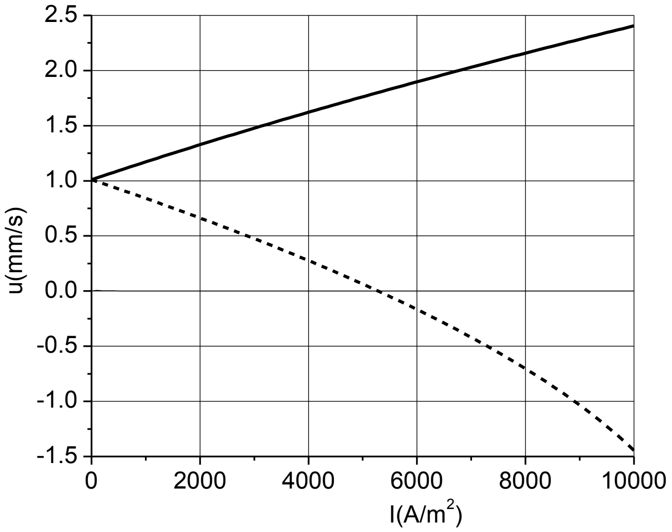

Figure 6.2: Convection velocity order of magnitude as a function of applied current density through the solidification front. In this calculation B=0.4 T and d=0.1 mm: solid line-magnetic field and electric current are parallel, dashed line-opposite

If conduction current flows through the interface between two different media, then some additional physical effects emerge. Let us list these effects and estimate the significance of each effect by using parameters from Table 4.1 and maximum current density used in present experiments (1 A/mm^2). Joule heat density within the sample can be calculated as

$$q = \frac{j^2}{\sigma} \qquad (6.4)$$

Which gives q=0.5 W/cm^3 in liquid phase and q=0.25 W/cm^3 in solid phase leading to net power of approximately 1 W within the 10 cm long and 6 mm diameter sample. This power is much smaller than power applied to the sample to melt it and to maintain temperature gradient at the solidification front, which is 40-60 W. Joule heating caused by thermoelectric current ($\approx 10^4$ A/m^2) is much smaller and is only present in small region near to the solidification front so it can be neglected.

Heat is also absorbed or released if current is passing through the media with temperature gradient due to Thompson effect. Thompson heat can be explained by the fact that charge carriers have higher mean energy in the region with higher temperature which causes heat redistribution. Thompson heat is released if hot end of the metal is at higher electric potential for most of the metals, but some exceptions exists. Thompson heat density can be expressed as:

$$q_T = -jT\frac{dS}{dx} \tag{6.5}$$

Thermoelectric power temperature derivative close to melting temperature is $-2\cdot10^{-9}$ V/K^2 in solid phase and $-4\cdot10^{-9}$ V/K^2 for liquid (Kaldre, Fautrelle, et al. 2010) Which gives approximate value for the region close to the solidification front of about 15 mW/cm^3.

Other thermoelectric effect is Peltier effect, which is caused due to different internal potentials between two media. Peltier heat is released or absorbed at the interface if electric current is flowing through the interface between two media. Peltier heat release or absorption per unit interface area can be calculated as

$$q_P = -jT(S_2 - S_1) \tag{6.6}$$

For a given case Peltier heat density is about 50 mW/cm^2 which is also small heat source and do not have any measurable effect on total temperature field.

Due to significant differences of electrical conductivities at the solid-liquid interface current is redistributed. If axial magnetic field is applied there is no Lorentz force in the bulk of the liquid.

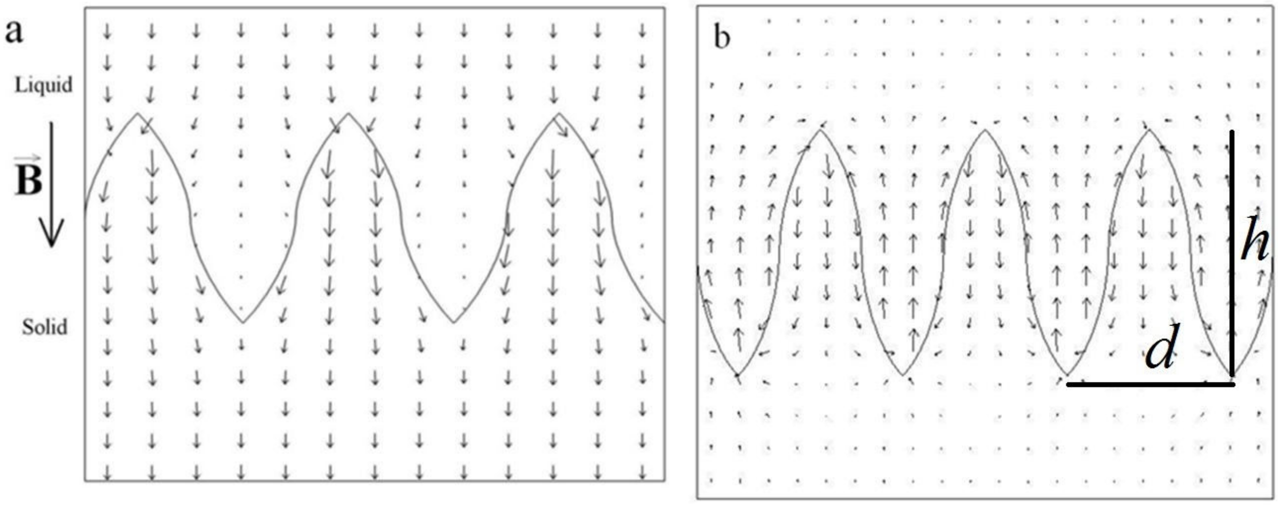

Figure 6.3: a) Current distribution at the interface between two media with different conductivities; b) Current component when axial current in the bulk liquid is subtracted. Properties from Table 4.1

Arbitrary dendritic solidification front between solid and liquid states with different electrical conductivities is depicted in Figure 6.3. In fact we can subtract uniform axial current component far from the interface from total current in the crucible because this component does not create any force. This is done in Figure 6.3(b) where the current distribution which is obtained if averaged current density far from the solidification front is subtracted from total current density showed in

Figure 6.3(a). As a result we get current circulation from root to tip of the dendrite arms (or opposite if current direction is reversed) which is qualitatively similar to thermoelectric current distribution (Kaldre, Fautrelle, et al. 2010), (X. F. Li 2007). As a consequence of this, liquid phase convection and eventually the influence on the structure of the alloy by these two mechanisms should be similar.

6.4. Modelling of convection caused by field and applied electric current

Numerical simulations of liquid phase convection caused by applied electric current and magnetic field are carried out. Two cases are analysed: magnetic field and electric current are both applied parallel to growth direction and electric current parallel to growth direction and perpendicular magnetic field. In the first case in the liquid bulk force density is equal to zero, but, similar like TEMC force appears only at the solidification interface. Whereas in the second case in the bulk of the liquid magnetic field and electric current are perpendicular, thus constant volume force acts on the liquid melt and solid phase. However this force only causes steady pressure gradient and is not a source of liquid motion. At the dendritic solidification interface electric current is redistributed as a consequence of the fact that solid dendrite arms has significantly larger electrical conductivity than liquid melt. Due to this reason in the interdendritic region the current density is smaller in the liquid then far from the interface and macroscopic flow of the liquid melt may appear.

Numerical models has been developed to verify the idea that this flow is similar like TEMC caused by transverse magnetic field. Three dimensional model is created and calculations are performed for various magnetic field values and electric current density values. Properties of Sn-10%wt.Pb alloy (Table 4.1) are used in numerical simulation. Current densities of up to 1 A/mm^2 combined with axial or transverse magnetic field are applied to the sample. Thus parameters used in numerical simulation match the experimental work done as a part of this research. Solidification interface shape and sizing are chosen to be close to realistic sizing of Sn-Pb alloys solidified at slow growth velocities (around 10 μm/s). Solidification geometry is shown in Figure 6.4.

Aims of this model are to verify theoretical predictions on flow characteristics and magnitudes, and to investigate the influence of TE force, electromagnetic force and magnetohydrodynamic damping effects on the melt flow. Three dimensional mathematical modelling of the liquid phase flow around an array of 5x5 solid phase dendrite arms has been done. Current density is evenly distributed over the cross section area of the sample. Also modelling of one solid phase body surrounded by liquid phase is done. It is found out that shape of the dendrite arm do not have significant influence on the current distribution and convection intensity magnitude, but characteristic size is most important parameter which defines flow intensity.

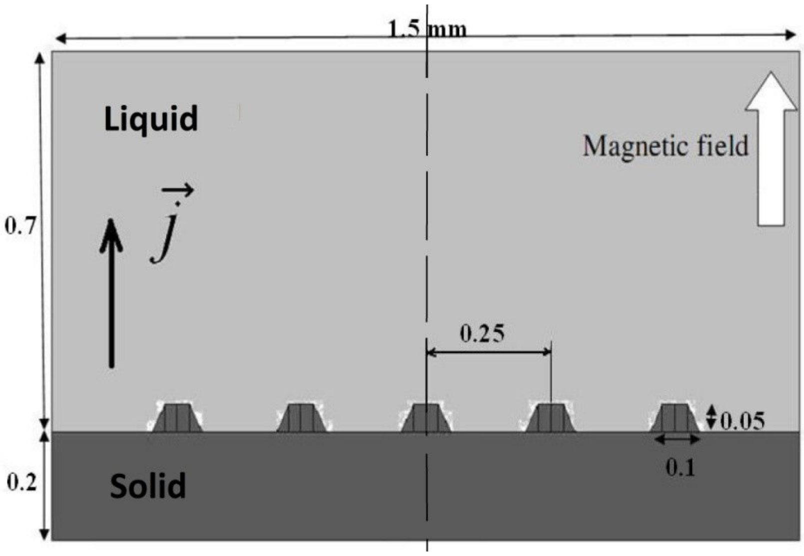

Figure 6.4: Longitudinal cross section of the geometry and dimensions (in mm) used for the modelling. Realistic dendrite size for Pb-Sn alloy is chosen ($d=1\cdot10^{-4}$ m, $u\approx1\cdot10^{-3}$ m)

Since Reynolds number is small ($Re=\rho ud/\mu=0.3$) in this case, laminar flow approximation is used for flow calculation. Model is developed by using FLUENT MHD module by numerically solving current density from Ohms law, magnetic field is calculated according to induction equation (eq.(6.7)) and flow is calculated by Navier-Stokes equation. In this calculation mesh consisting of 900000 tetrahedral cells is used.

$$\frac{\partial\vec{B}}{\partial t}+(\vec{u}\cdot\nabla)\vec{B}=\frac{1}{\mu\sigma}\nabla^2\vec{B}+(\vec{B}\cdot\nabla)\vec{u} \tag{6.7}$$

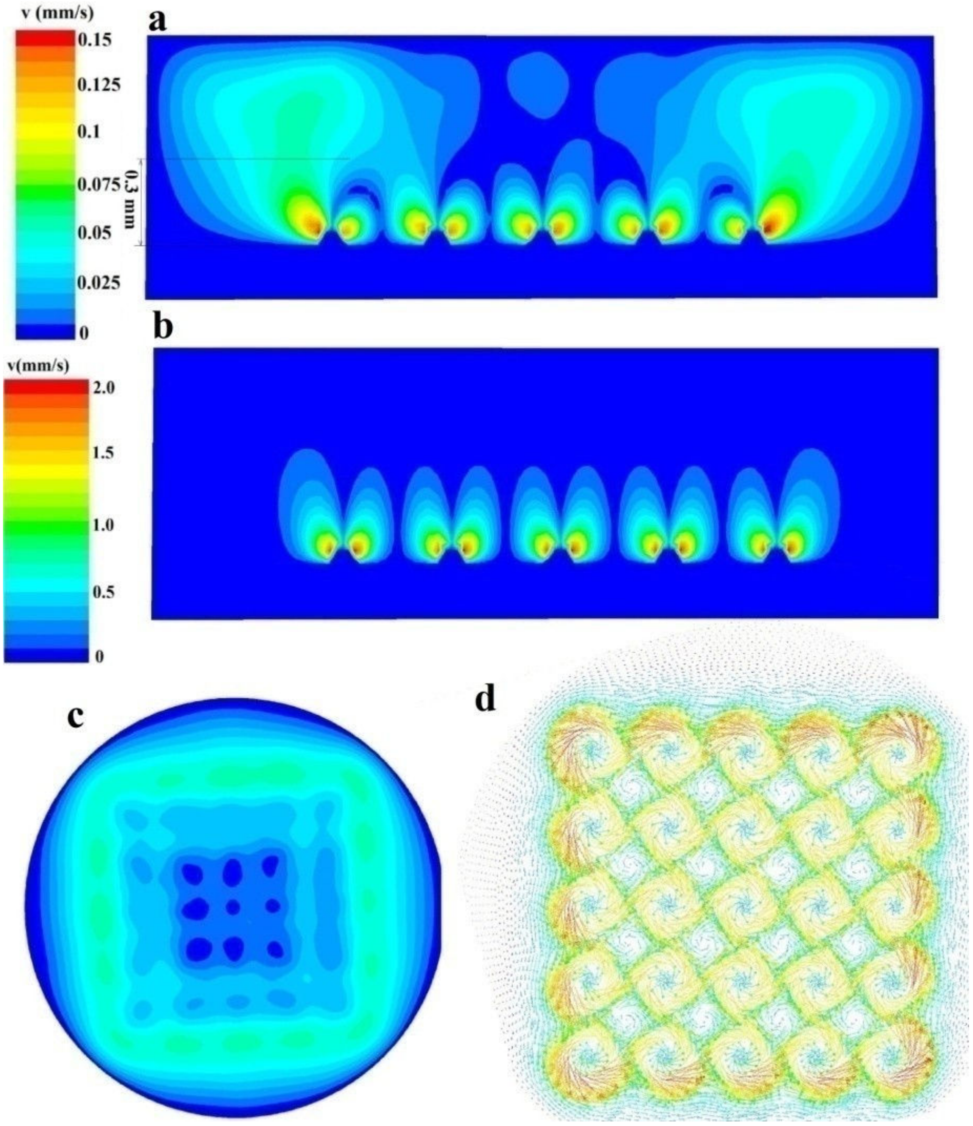

Figure 6.5: Calculated liquid phase velocity distribution caused by axial magnetic field and electric current ($j=3\cdot10^5$ A/m^2). Azimuthal velocity at diameter cross section: a) B_z=0.1 T; b) B_z=2 T. Velocity field 0.3 mm above solidification front: c) B_z=0.1 T; d) B_z=2 T

Numerical simulation results are shown in Figure 6.5 which compares the velocity field at two different magnetic field values 0.1 T and 2 T. At higher magnetic field values, velocity is more concentrated in the close vicinity of the solidification front due to MHD braking force, which limits the formation of large scale flow. Figure 6.5(c and d) shows that 0.1 T magnetic field causes crucible size flow above solidification front, while at 2 T flow in the bulk liquid is much smaller as estimated in Figure 4.5. This result qualitatively agrees with previous theoretical predictions. It also shows that this kind of interaction causes only local convection whose scale is comparable to dendrite size thus no crucible-scale flow and macrosegregation are not expected in this case.

Velocities calculated according to equation (6.3) as function of applied electric current density are shown in Figure 6.6. Predicted velocity order of magnitude estimation are about 40 % larger than maximum values obtained in numerical simulation. This difference can be explained by approximations made during derivation of analytical expression.

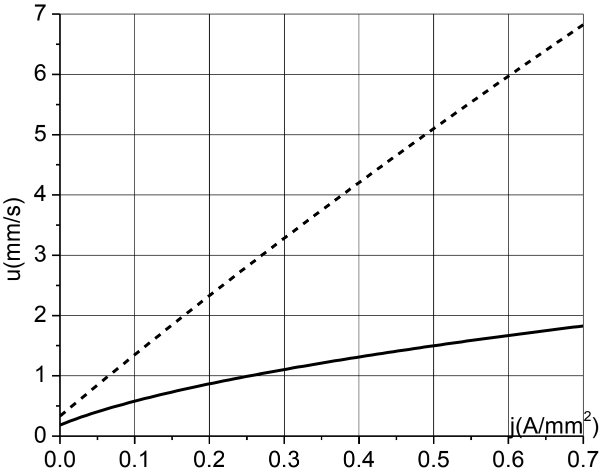

Figure 6.6: Velocity order of magnitude according to equation (6.3). Dashed line-B_z=2 T, Solid line-B_z=0.1 T

If transverse magnetic field is applied then situation is different, and an asymmetric crucible scale flow emerges as a net flow from all dendrite arms. Numerical model using the same geometry as in previous model is made to calculate liquid melt flow induced by axial electric current and transverse magnetic field. In this model we chose top surface to be closed, thus surface deformation caused by electromagnetic force in the liquid domain does not cause additional pressure.

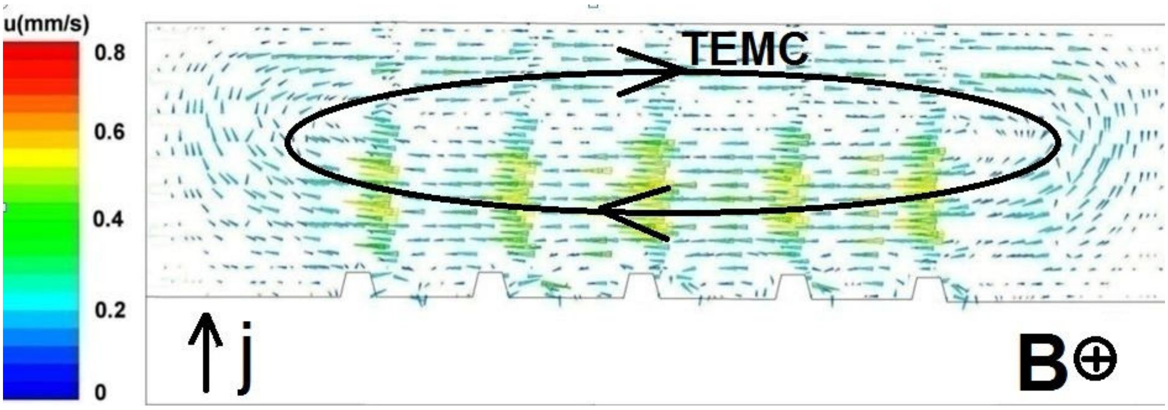

Figure 6.7: Calculated flow velocity caused by axial current and transverse magnetic field interaction, at field perpendicular cross section. B_x=0.1 T, j=0.3 A/mm^2

Cross section along the diameter perpendicular to magnetic field direction is shown in Figure 6.7. Results show that flow of the size of the crucible is created by adding up the contributions from all dendrite arms. In this case qualitative flow pattern is similar for both cases with applied 0.1 T and 2 T magnetic fields. Maximum velocity magnitudes are 0.7 mm/s at 0.1 T magnetic field and 3.5 mm/s at 2 T magnetic field. These velocity values are higher than it is possible to achieve by TEMC only for the Sn-Pb alloy as estimated analytically in chapter 4.

6.5. Experimental results with DC current and magnetic field

Directional solidification experiments of Sn-10%wt.Pb are carried out by using the same directional solidification setup described in section 5.2, but equipped with option to add current electrodes at the bottom of the solid part and top of the liquid part. 3 mm diameter stainless steel electrodes are used for current input. Aim of these experiments are to investigate the influence of electric current and static magnetic field on the microstructure of binary metallic alloy and macrosegregation. Comparisons with results obtained at the same experimental conditions without magnetic field and with static magnetic field but no electric current are done. In the experiments current density value 1 A/mm^2 has been used, which is two orders of magnitude higher than estimated TE current. Aim of these experiments is to demonstrate the consequences of convection caused by current redistribution at the solidification interface. Influence on the structure of binary Sn-Pb alloy by this interaction is qualitatively compared with consequences of TEMC.

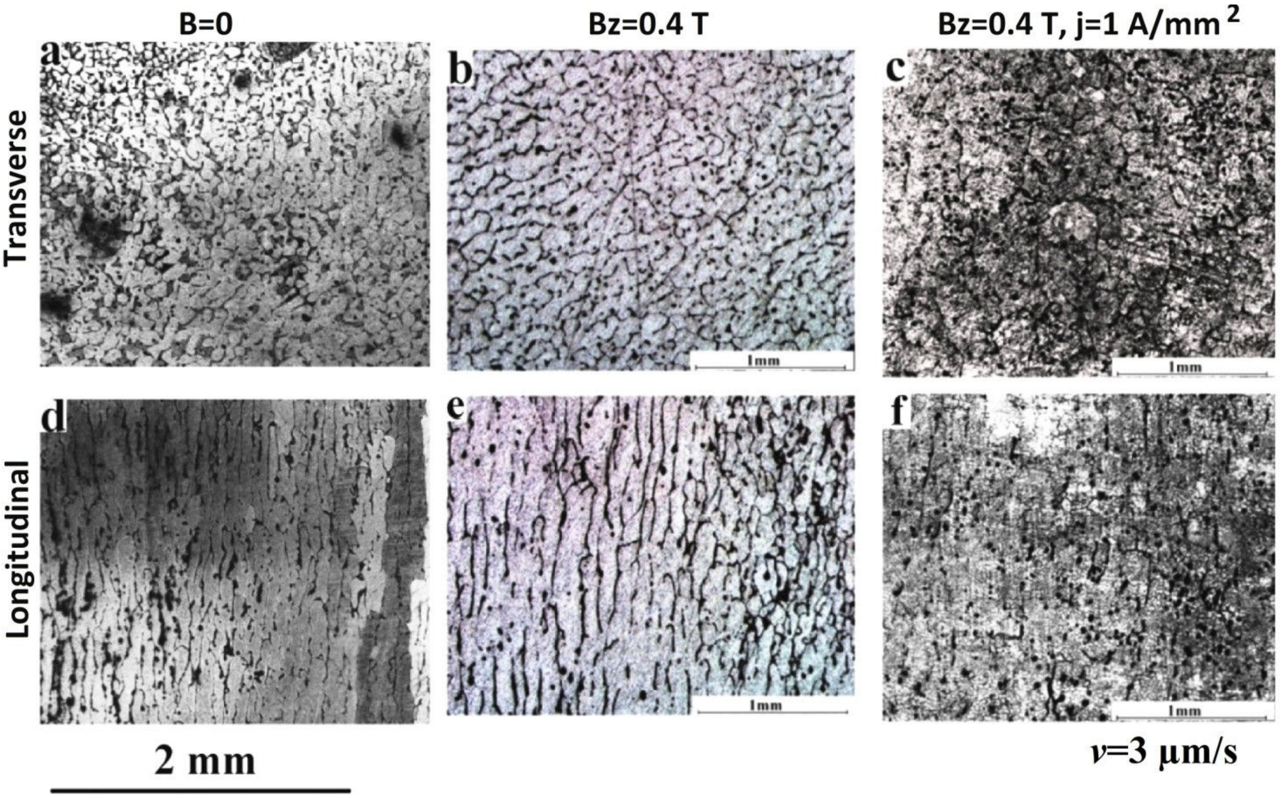

Figure 6.8: Structure of directionally solidified Sn-10%wt.Pb alloy at *v*=3 μm/s: a,d) without field; b,e) with 0.4 T axial field; c,f) with 0.4 T axial field and 1 A/mm^2 axial current

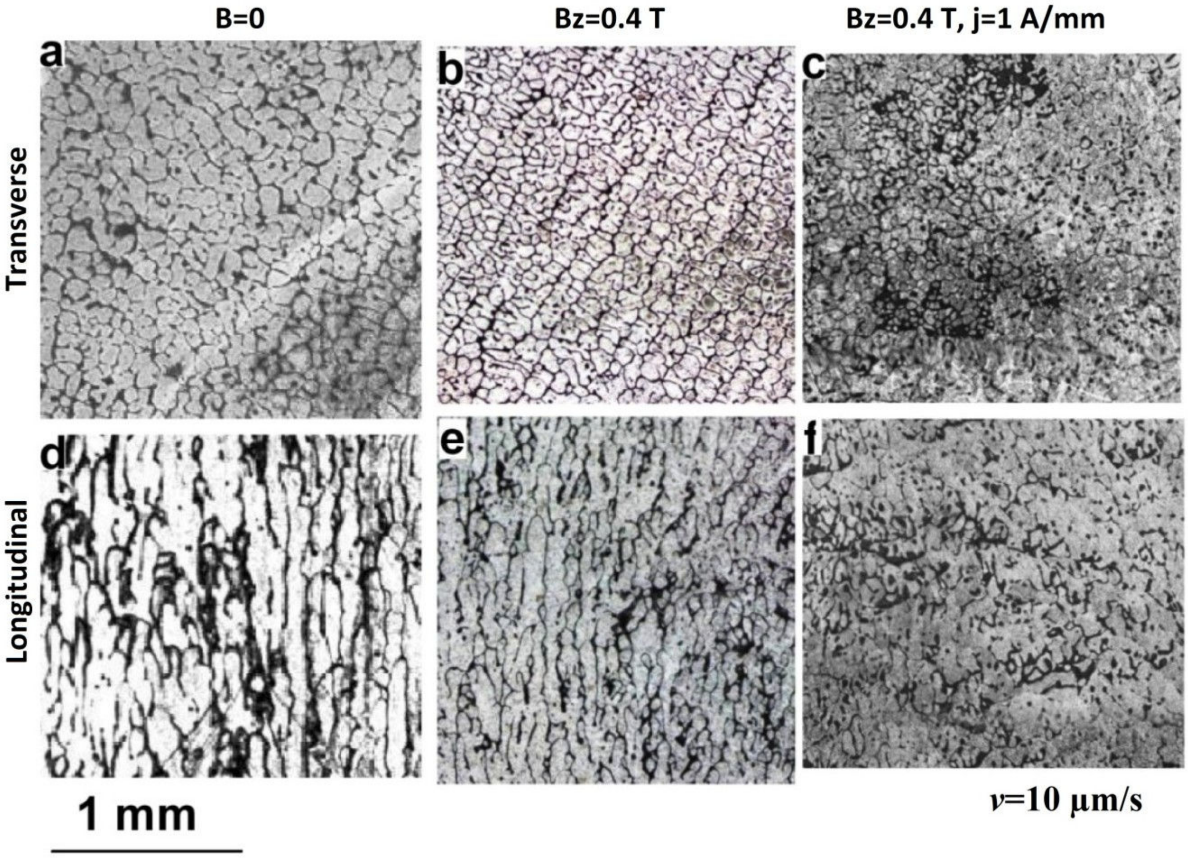

Figure 6.9: Structure of directionally solidified Sn-10%wt.Pb alloy at *v*=10 µm/s: a,d) without field; b,e) with 0.4 T axial field; c,f) with 0.4 T axial field and 1 A/mm^2 axial current

Solidification structure with axial magnetic field and axial current does not show any macrosegregation along the cross section of the sample. In Figure 6.8 and Figure 6.9 microstructures of horizontal and vertical sections at two different growth velocities 3 µm/s and 10 µm/s, are compared for three cases (without magnetic field, with axial 0.4 T magnetic field, with axial 0.4 T magnetic field and applied axial electric current *j*=1 A/mm^2) . Experimental results show that electric current has some influences on the microstructure. Grain structure is reduced due to presence of electromagnetic convection in comparison with case with static magnetic field without current, but difference is relatively small. This result agrees with previously mentioned conclusion that well established convection has small influence on the grain size. Main difference can be seen between the longitudinal cross sections (e) and (f) in pictures Figure 6.8 and Figure 6.9. Lead rich columns are slightly shorter and columnar structure is less distinct in case with applied electric current. This observation indicates that despite axial electric current causes only local convection, it obviously influences columnar to equiaxed transition (CET). Figure 6.9 (f) shows that structure of directionally solidified Sn-10%wt.Pb alloy at 10 µm/s with magnetic field and electric current is difficult to define between columnar and equiaxed, while without magnetic field and with 0.4 T static field only it is columnar (Figure 6.9 (d)and (e)). This means that intensive local convection around dendrite arms caused by electric current decreases CET critical velocity.

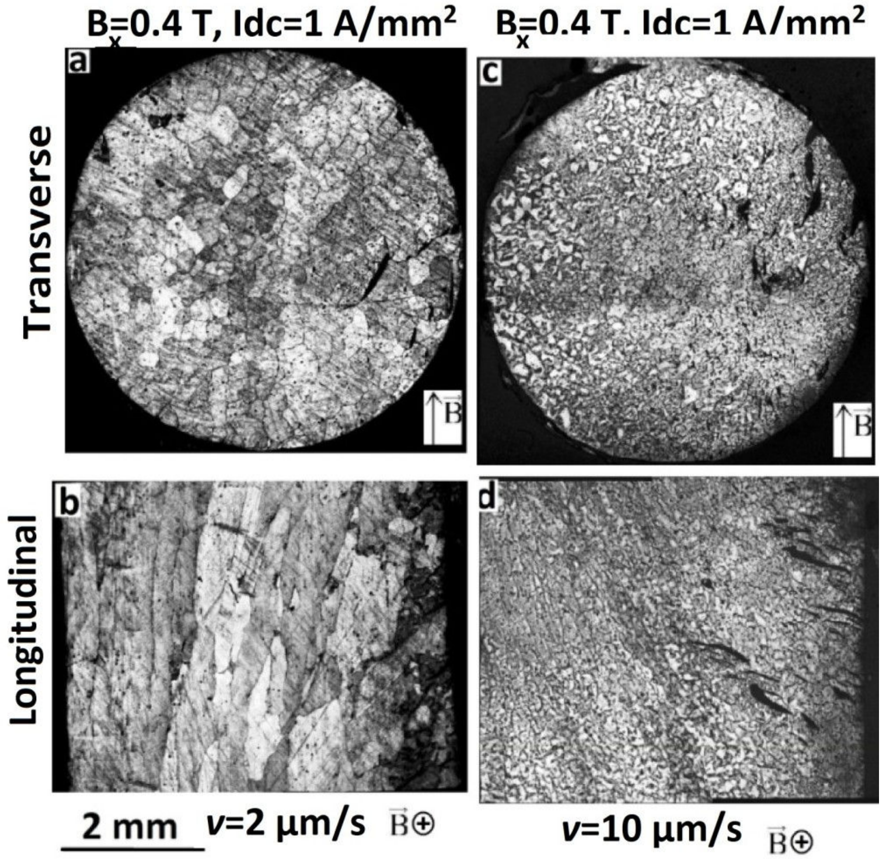

Figure 6.10: Directionally solidified Sn-10%wt.Pb alloy with 0.4 T transverse magnetic field and axial DC current 1 A/mm^2: a,b) *v*=2 µm/s, *λ*=270 µm; c,d) *v*=10 µm/s, *λ*=150 µm

Structure of directionally solidified Sn-10%wt.Pb alloy under 0.4 T transverse magnetic field and axial electric current 1 A/mm^2 through the sample are shown in Figure 6.10. Results show that macrosegregation perpendicular to magnetic field direction is observed but it is less distinct than with static transverse magnetic field. Cellular structure with characteristic cell spacing of 270 µm at 2 µm/s and 150 µm at 10 µm/s growth velocity is observed. Measured cell spacing is slightly larger than in case without magnetic field or with static magnetic field (Figure 5.15), which is an unexpected result. This result might be the consequences of surface covering lid instead of free surface in previous experiments or Joule heating inhomogenities within the sample.

6.6. Influence of alternating current

Similar solidification experiments are done by using static magnetic field and 50 Hz alternating electric current combination. Applied alternating current and axial magnetic field cause time varying force. AC also causes induced magnetic field and induced current in the sample. Induced current and magnetic field values for cylindrical conductor are given by Ma (Ma, Zheng and

Larson 2004). In this work complex expressions for induced azimuthal current and magnetic field as a functions of radial position are given. By calculating amplitudes with our experimental parameters (j=$1\cdot10^6$ A/m^2, R=3 mm, σ=$2\cdot10^6$ sim/m) we get B_A =2 mT and j_A=3100 A/m^2. Magnetic field is not significantly perturbed by induced field while induced current is only one order of magnitude smaller than TE current magnitude. Alternating current density in the cylindrical conductor is not uniform because of skin effect. Current density as a function of radial position can be expressed as

$$j = j_0 e^{-r/\delta} \tag{6.8}$$

where r is distance from crucible wall, j_0 is current density at near the wall, δ is skin layer thickness, which is equal to the distance at which from the wall current density decreases e times compared to the one near the wall. Skin layer thickness for the cylindrical wire can be calculated

$$\delta = \sqrt{\frac{1}{\sigma\pi f \mu\mu_0}} \tag{6.9}$$

For 50 Hz calculated skin depth in the Sn-Pb alloy is 3.6 cm. During experiments average current density of 1 A/mm^2 were applied to the 6 mm diameter sample. As a consequence of skin effect current density is the middle of the sample is 9% smaller than near the wall and local Joule heat density is 18% higher near the wall. This results as a higher force density near the walls thus in this case, melt convection is affected. Inhomogeneous heating and TE force distribution may result a curved solid-liquid interface shape compared to flat one in directional solidification without current. Interface shape changes caused by current pulses and AC current are analysed in refs. (Li, Regel and Wilcox 2001), (Lie, Walker and Riahi 1990). Curved interface shape may result in crucible scale TEMC because in this case crucible size becomes a characteristic length in equation (4.12) and as shown in Figure 4.3.

In Figure 6.11 horizontal and vertical cross sections of directionally solidified Sn-10%wt.Pb alloy are compared in both cases with applied magnetic field and alternating electric current and without. Central parts of the same cross sections are shown in Figure 6.12 to demonstrate the differences in microstructure. It can be seen that effect of electromagnetic force has different effects on the structure at 2 μm/s and 10 μm/s growth velocities. At growth velocity of 2 μm/s it can be seen from both pictures that without magnetic field structure is columnar and with magnetic field and AC electric current columnar structure is much less visible. Solidification structures without magnetic field and with a axial magnetic field (Figure 5.4 and Figure 5.5) showed columnar structure. Thus we may conclude that AC current promotes CET and allows us to achieve equiaxed structure at lower growth velocities.

Radial macrosegregation is caused by natural convection and temperature inhomogenities in the crucible. This can be seen as dark, lead rich regions near the side of the sample in Figure 6.11(c) and (g) and also are present in case of static magnetic field (Figure 5.5). In corresponding cross sections solidified with AC current and magnetic field (a and e) segregation near the walls is prevented. This fact can be explained with previously mentioned fact that AC current and magnetic field interaction causes crucible size flow, which transports the solute more effective in radial direction.

In case of axial magnetic field as used in these experiments, interacts with this current and radial direction oscillating force is obtained, which might have influence of solute transport. It is known that such oscillating force may cause not only small amplitude oscillations but also steady large scale flow, this effect is known as steady streaming effect (Ilin 2011), (Otto, Riegel and Voth 2008). In these works effect is numerically simulated and also experimentally measured by ultrasound particle velocimetry. Steady streaming effect originates from non-linear nature of Navier-Stokes equations, small perturbation can start to grow as a consequence of oscillating force, thus it can be a source of steady melt flow in this case.

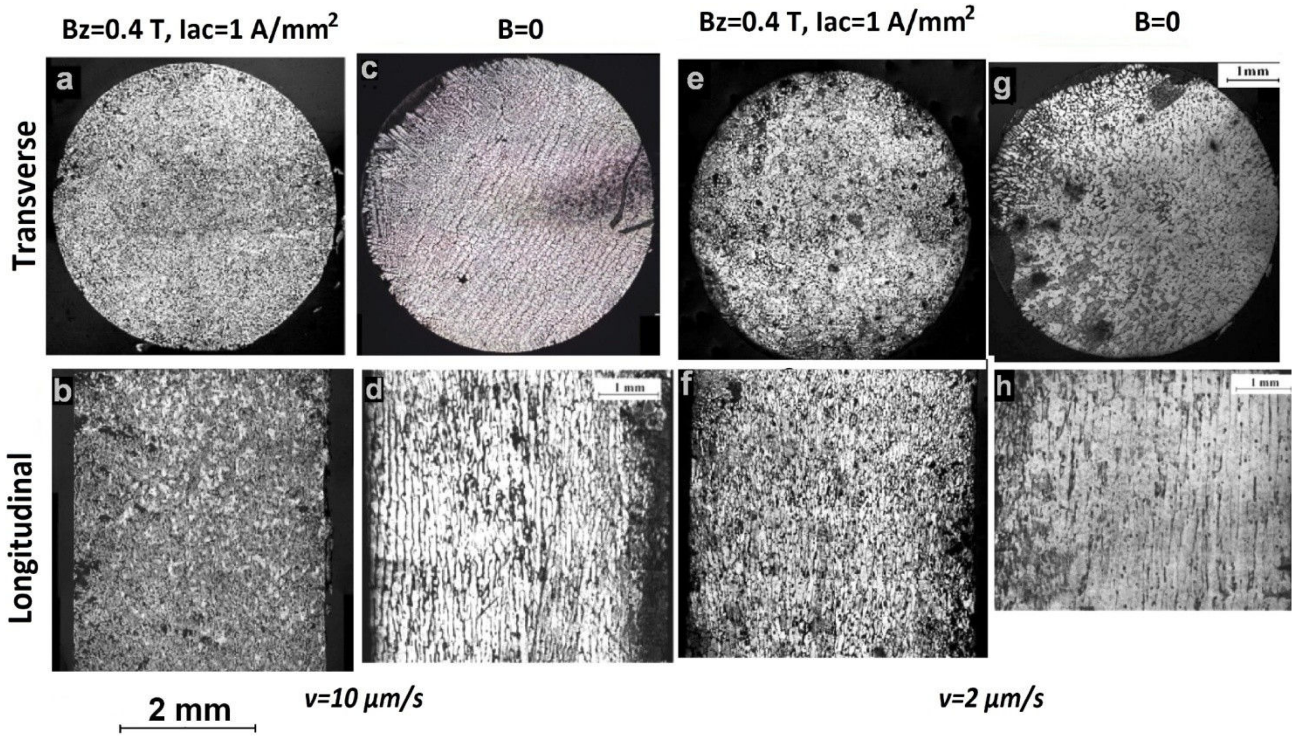

Figure 6.11: Structure of directionally solidified Sn-10%wt.Pb alloy. With applied 50 Hz AC current (1 A/mm^2) and 0.4 T axial magnetic field: a,b) 10 µm/s, e,f) 2 µm/s. Structure in similar conditions without field and current: c,d) 10 µm/s, g,h) 2 µm/s

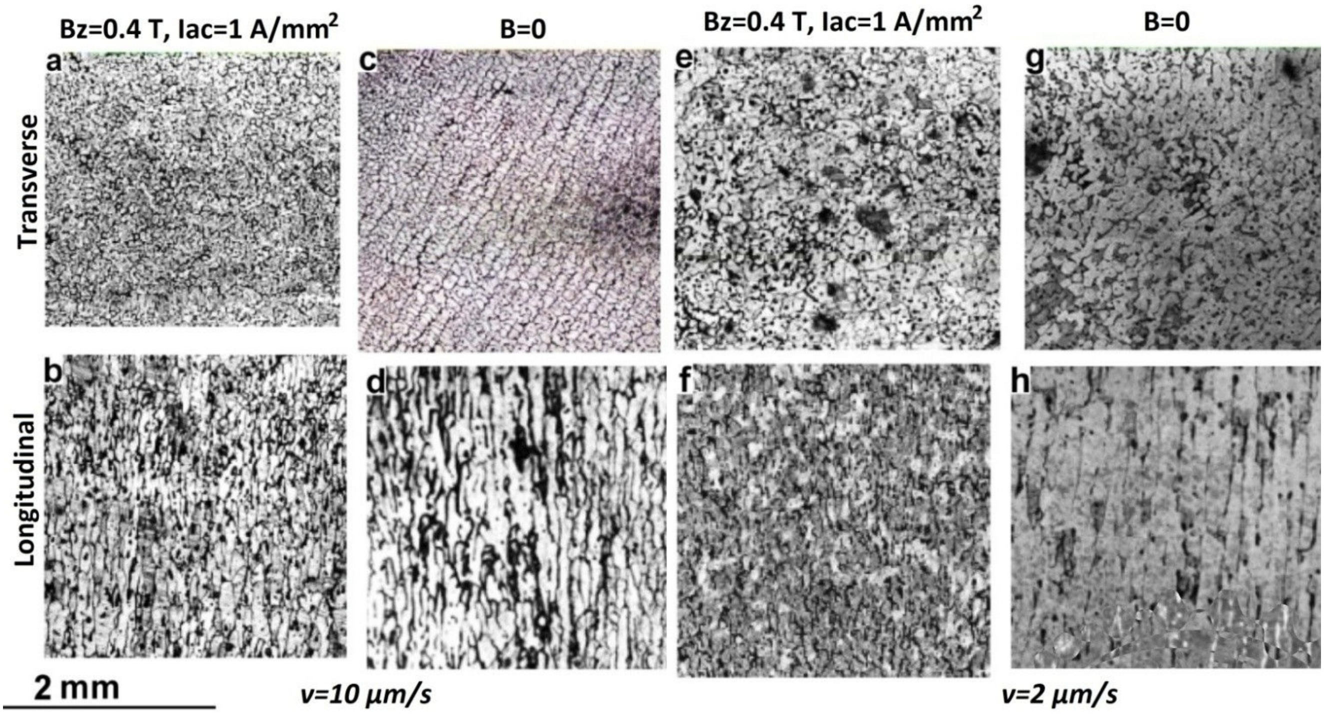

Figure 6.12: Structure of directionally solidified Sn-10%wt.Pb alloy. With applied 50 Hz AC current (1 A/mm^2) and 0.4 T axial magnetic field: a,b) 10 μm/s, e,f) 2 μm/s; Structure in similar conditions without magnetic field and current: c,d) 10 μm/s, g,h) 2 μm/s

This kind of electromagnetic treatment during solidification also has influence on the microstructure (Figure 6.12). Dendrites are significantly fragmented compared to the solidification without field. Characteristic spacing is reduced from 190 μm at 2 μm/s and 125 μm at 10 μm/s to 110 μm and 83 μm correspondingly. Figure 6.12 (a) and (b) also shows that alternating current also promotes the formation of small spherical inclusions which were not present in experiments with static magnetic field. These inclusions are apparently the consequences of current induced electromagnetic and mechanical vibrations which effectively enhance the formation of small spherical eutectic droplets as a consequence of small scale fluid oscillations and steady streaming flow.

6.7. Conclusions

Theoretical estimation and numerical simulation of current distribution and flow pattern at the interface between solid and liquid metals indicate that by this mechanism, in case of dendritic solidification front, is capable to create similar convection than TEMC, but in this case it is more easy to control convection magnitude and direction. This could potentially allow to enhance TEMC effects in materials with weak or zero differential thermoelectric power between solid and liquid phase.

Experimental results show that DC electric current through the boundary during directional solidification has some effect on the structure of Sn-10%wt.Pb alloy. Axial 0.4 T magnetic field and axial electric current 1 A/mm^2 through the solidification interface cause significant grain refining and column shortening effect of microstructure of an alloy. However these results does not allow to deduce actual electromagnetic convection velocity magnitude and distribution at the solidification interface, because, as explained before, local convection at dendrite scale does not affect microstructure significantly. Axial electric current and transverse magnetic field superposition creates macrosegregation perpendicular to magnetic field direction. In this case cellular structure is obtained, and grain size is larger than with static magnetic field alone. This can be explained by Joule heating inhomogenity, and it can also be consequences of flow caused by Lorentz force density inhomogenity within the liquid volume caused by asymmetric current and magnetic field distribution. In this case force density in the liquid is high ($f=j\times B=4\cdot 10^5$ N/m^3), and thus 4 % field difference as estimated by equation (5.2) can drive considerable convection. In this case experimental procedure should be improved because magnetic field should be highly homogeneous, current inputs should be improved to eliminate unwanted sources of melt motion which can overwhelm TEMC.

AC current and static axial magnetic field does not create macrosegregation and decrease grain size, which can be attributed to intense small scale convection around each dendrite arm. Convection characteristics in this case is similar than TEMC but its intensity for used current density should be much higher as shown in Figure 6.2. In case of AC, oscillating force causes mechanical vibrations and flow can be also caused by steady streaming effect. However detailed experimental analysis of this phenomenon requires more experimental capacity to analyse the trends at various growth velocities and current densities and frequencies.

The idea about superimposed electric current and magnetic field is experimentally tested as a part of this work. Obtained experimental results show differences in grain spacing and macrosegregation in both cases with AC and DC electric current. Nevertheless correlation between theoretical predictions and experimental results is difficult to test quantitatively, and it would require more detailed and extensive experimental work. Further experimental sessions by varying electric current value should be done.

7. Solidification under slowly rotating magnetic field

Slowly rotating transverse magnetic field is applied to the sample during directional solidification in the Bridgman setup. In this case the direction of thermoelectromagnetic convection is changing all the time along with the magnetic field, thus the influence on the macrostructure is caused by time averaged convection. Depending on the field rotation velocity several regimes can be obtained

- Field rotation is very slow, thus TEMC can fully develop in the size of the crucible and follow the field direction.
- Field rotation allows TEMC to develop in the scale comparable to the primary dendrite arm spacing.
- Field rotation is fast, and electromagnetic stirring fully suppresses the effects of TEMC.

In this chapter first two cases will be theoretically analysed and experimentally tested. Structure of directionally solidified Sn-10%wt.Pb alloy with various growth rates and under 0.4 T magnetic field with different rotation velocities are analysed.

7.1. Literature review

Usually solidification under rotating magnetic field is studied with fast field rotation velocity (Roplekar 1999), (Kovacs, et al. 2009) where induction effect is dominant, and strong mixing is achieved by moving magnetic field. This treatment has significant influence on grain spacing and radial segregation in the samples. This treatment has been widely used in metallurgy and semiconductor growth (Croll, et al. 1999). Influence of solidification of Pb-85%wt.Sn alloys has been experimentally studied in ref. (Herlach 2004). In this work rotating magnetic field starting from $Ta=2\cdot 10^5$ is used. It is experimentally proven that CET can be significantly modified by rotating field. Microstructure of an alloy was significantly refined in case of $Ta=8\cdot 10^6$. Ta stands for Taylor number characterizing the ratio between centrifugal forces and viscous forces given in equation (7.1). Similar work has been presented in ref. (Xiaohua, et al. 2006). In this work field strength was 450 mT and rotation velocity 100 rad/s. Influence of magnetic field to the temperature profile in the crucible was analysed and micrographs of the structure are taken. Pictures qualitatively confirm that magnetic field refines the dendrite structure and promotes CET. Influence by the rotating magnetic field on temperature and velocity in the liquid melt was measured in this work. It is numerically and experimentally proven that rotating magnetic field can cause significant radial segregation in Al-Si alloy (Noeppel, et al. 2010)

Effect of 50 Hz rotating magnetic field on the microstructure of Al-Si-Mg alloy has been studied by Steinbach (Steinbach and Ratke 2005). In this work characteristic grain sizes are analysed at different growth velocities, and grain sizes with and without forced convection are compared with analytical models.

Combination of rotating and travelling magnetic fields has been also investigated in ref. (Rabiger, et al. 2011). Liquid melt flow pattern and temperature distribution changes with different combinations of travelling and rotating fields are investigated. Solidification experiments of Sn-15%wt.Pb has been done, showing the significant effect of this interaction on microstructure of alloy. These experiments are qualitatively different from experimental work done in this work. As will be shown in further evaluation field rotation has to be very slow to observe combination of TEMC and magnetic stirring and its influence on the structure of an alloy. No literature data about directional solidification under slowly (0.1 Hz and lower) rotating magnetic field were found.

7.2. Experimental setup

High purity tin and lead (99.99%) is used to prepare Sn-10%wt.Pb alloy, which are then casted into the alumina799 crucible (*L*=110mm, *ID*=6mm, *OD*=10mm). Samples are then remelted and solidified under intense magnetic stirring to ensure good homogeneity of initial samples. The samples are directionally solidified in a Bridgman setup at controlled growth velocity and temperature gradient. In these experiments growth velocity within the range from 2 μm/s to 10 μm/s has been used. Temperature gradient at the interface is 8 K/mm in all experimental sessions of this work. Upper part of the sample is melted by the furnace around the crucible while bottom part is kept solid by water cooled copper ring. Furnace and water cooled ring are stationary while crucible is lowered by programmable pulling system. Solidification front is always located between heater and cooler at the same location, thus actual solidification velocity is assumed to be equal to the pulling velocity of the crucible. Magnetic field of 0.4 T is created by permanent magnet system, which can be rotated around the furnace by electric step-motor with range (0.1-10 rev/min). For optical microscopy analysis samples are polished to 1 μm surface roughness and then chemically etched with 4% nitric acid ethanol solution.

7.3. Analytical description

Directional solidification experiments of Sn-Pb and Sn-Bi alloys are done with applied slowly rotating field with rotation period from 30 to 600 s. Solidification velocities are used from 2 μm/s to 10 μm/s. For this solidification velocity range it is reasonable to choose characteristic primary dendrite size *d*=0.1 mm as demonstrated in chapter 5.

To characterize rotating magnetic field influence on the liquid metal motion, Taylor number is introduced. Taylor number characterizes electromagnetic force created by rotating magnetic field to viscous force ratio.

$$Ta = \frac{\sigma \pi f B^2 R^4 \rho}{\mu^2} \tag{7.1}$$

Where *f* is magnetic field rotation frequency. Using parameters from Table 4.1 we can calculate *Ta* for the experiments performed within this work. Field rotation period value used in experiments is 30-600 s, which leads to *Ta*=5000 at 30 s period and 250 at 600 s field rotation, which are low values compared to experimental works mentioned in literature review section, thus characteristic electromagnetic force is of comparable magnitude with viscosity in this case.

Estimation given by equation (4.12) gives the maximum TEMC velocity order of magnitude for Sn-10%wt.Pb of about 1 mm/s at 0.4 T magnetic field, but in reality effective convection velocity is much smaller due to limitations of crucible and mushy zone. Effective convection velocity is estimated based on various interpretations of experimental results of solidification experiments with static magnetic field given in section 5.5. Thus 0.1 mm/s would be an appropriate order of magnitude assumption for TEMC velocity. TEMC flow caused by transverse magnetic field is macroscopic flow loop in magnetic field perpendicular plane, as shown in Figure 4.2. Electromagnetic convection velocity and flow profile in the long liquid metal cylinder is analysed for different parameter combinations by several authors (Witkowski and Marty 1998), (Gelfgat, Gorbunov and Kolevzon 1993), (Davidson 2001). In order to estimate the balance between forces acting on the fluid it is useful to estimate some dimensionless parameters characterizing the flow. In this case three dimensionless numbers, given by equations (7.2), (7.3), (7.4), are sufficient to describe the problem. Hartmann number *Ha* square is the ratio between electromagnetic and viscous forces. Lorentz force versus inertia is characterized by magnetic interaction parameter *N*. To characterize the alternating magnetic field magnetic Reynolds number *Rm* is defined, which shows the significance of induced magnetic field and skin effect.

$$Ha = BR\sqrt{\frac{\sigma}{\mu}} \tag{7.2}$$

$$N = \frac{\sigma B^2 R}{\rho u} \tag{7.3}$$

$$Rm = \mu \sigma u R \tag{7.4}$$

Inserting parameter from Table 4.1 we get *Ha*=42 and *N*=2500 and *Rm*=$7\cdot10^{-7}$. Such parameter combination indicates that rigid body approximation for metal column rotation can be used to estimate rotating field induced velocity in the volume of the crucible:

$$u_\theta = Ar \tag{7.5}$$

Where *A* is constant and *r* is radial coordinate. Similar parameter combination (*Ha*=30, *Rm*=0, high *N*) is numerically simulated by Witkowski (Witkowski and Marty 1998) and result confirms that in the volume is solid-like body rotation which is only limited by viscosity at the walls of the crucible. Electromagnetic torque per unit length is

$$\tau_{EM} = \int_0^R 2\pi\sigma B^2(\Omega r - u_\theta) r^2 dr = 2\pi\sigma B^2(\Omega - A)\int_0^R r^3 dr = \frac{\pi\sigma B^2(\Omega - A)R^4}{2} \tag{7.6}$$

where *Ω* is field rotation angular velocity, *R* is crucible radius. If solid body approximation is used then viscous torque is generated only in viscous boundary layer near the crucible wall. Viscous thickness can be estimated as $\delta = R / Ha$, thus viscous torque can be expressed as follows:

$$\tau_V = 2\pi R^2 \mu \left(\frac{du_\theta}{dr} \right) \approx \frac{2\pi R^2 \mu A R}{\delta} \tag{7.7}$$

By balancing electromagnetic and viscous torques we may express azimuthal velocity caused by rotating magnetic field

$$u_\theta = \frac{\Omega r}{(1 + 4 / Ha)} \tag{7.8}$$

In this case *Ha*=42, then in fact column of fluid rotates as a solid body with the same angular velocity as magnetic field, and velocity is different only in 70 µm thick viscous boundary layer.

Thermoelectromagnetic convection develops in the plane perpendicular to magnetic field. It takes certain time since magnetic field is applied, for TEMC to transport solute and heat in the size of a crucible. If magnetic field is rotating then TEMC has no time to develop in full scale, but it can only develop and transport heat and solute in smaller range *L,* which depend on field rotation velocity (Figure 7.1). Our aim is to choose such magnetic field rotation value that *L* is comparable with characteristic primary dendrite spacing of an alloy *d*. It is expected to achieve improved alloy structure without macrosegregation and to modify cell morphology with this interaction during directional solidification.

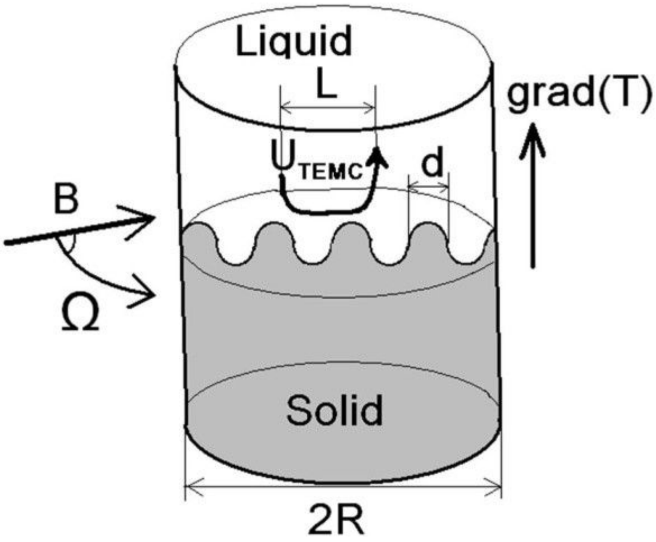

Figure 7.1: Schematic view of TEMC caused by rotating transverse magnetic field

If we wish TEMC mixing zone radius *L* to be equal to $5\cdot d$, then characteristic field rotation velocity can be estimated by finding time in which TEMC flow completes one loop with this radius. This consideration gives us $T=10\pi d/u_{TEMC}=31$ s. Whereas field rotation period which allows TEMC to develop in the size of a crucible can be estimated as follows $T=2\pi R/u_{TEMC}=188$ s. These estimations indicate that crucible size macrosegregation caused by TEMC might be observed if field rotation period is slower than 188 s.

7.4. Experimental results

This section is divided into two parts because of qualitatively different effects caused on macrosegregation by slow and faster field rotation velocities. Slow magnetic field with periods 300 s and 600 s causes helical macrosegregation which is interesting result and allows to calibrate TEMC by comparing contributions of TEMC and magnetic stirring. Main effects caused by faster rotating magnetic field with 30 s and 60 s periods, are attributed to time varying TEMC direction. If field rotation is correctly adjusted then mixing effect by TEMC in the scale of few dendrite spacing is created and structure of alloy is improved by reducing cell spacing and reduce β phase inclusion concentration and size.

7.4.1. Slow magnetic field rotation

Magnetic field rotation period is chosen to be larger than estimated value at which TEMC flow can transport solute in the crucible scale (*T*>188 s), thus effect caused by TEMC should be visible as macrosegregation in the crucible scale. Horizontal and vertical cross sections were examined by optical microscopy. Observed structure in Figure 7.2 confirms that component distribution within the ingot is 3D spiral shaped.

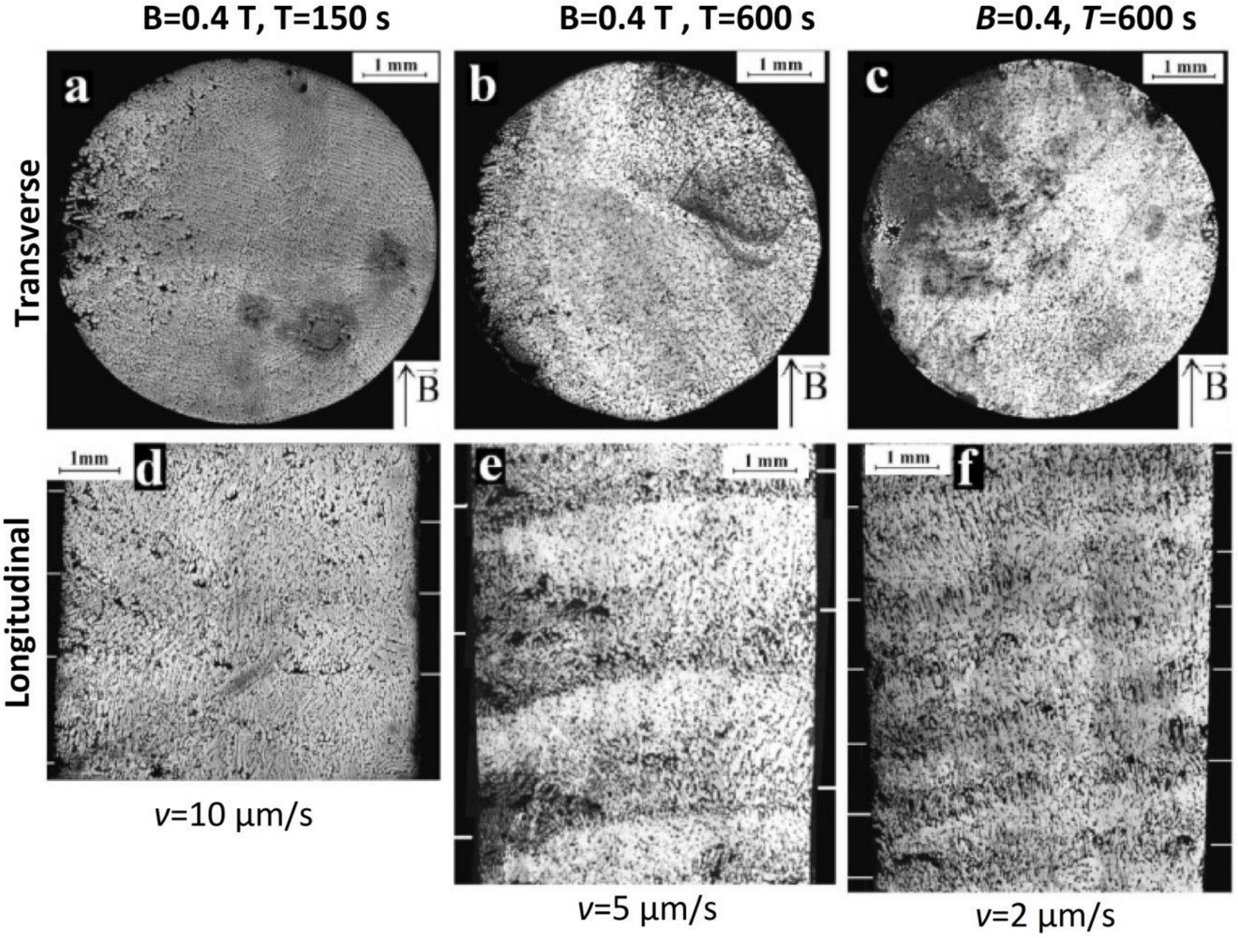

Figure 7.2: Horizontal and vertical cross sections of directionally solidified Sn-10%wt.Pb alloy under slowly rotating magnetic field. a,d) *v*=10 µm/s, *B*=0.4 T, *T*=150 s; b,e) *v*=5 µm/s *B*=0.4 T , *T*=600 s; c,f) *v*=2 µm/s, *B*=0.4 T, *T*=600 s

Regular lead fraction segregation pattern are observed in longitudinal cross sections Figure 7.2(e,f). Spacing of the regularity corresponds to the solidified length during one magnetic field rotation period. At larger solidification velocity and field rotation frequency, component segregation is less distinct than if the velocity is small and field rotation is slow.

TEMC velocity during directional solidification cannot be measured directly, and usually it is only estimated by analyzing the TEMC impact on the structure of an alloy. In this case magnetic field direction is changing all the time and TEMC flow together with it. Thus, these experimental results give us opportunity to estimate actual TEMC intensity at the vicinity of solidification front during directional solidification. By analyzing the results obtained in this study it is possible to deduce the critical field rotation value at which TEMC is exceeded by magnetic stirring due to magnetic field rotation. This result allows to estimate TEMC intensity for given alloy and applied temperature gradient, and compare it with theoretically estimated value. At field rotation period of 150 s, influence of TEMC is still visible (Figure 7.2 (d)). No influence on the structure by TEMC was observed with T=60 s and T=30 s (Figure 7.5 and Figure 7.6). Thus we may conclude that u_{TEMC} must be of the same order as electromagnetic steering velocity, if field rotation period is T≈100..120 s. This corresponds to the stirring flow velocity of 0.18 mm/s, which is a reasonable value and comparable with the theoretical estimation (equation (4.12)) and estimations based on experimental results with static transverse magnetic field presented in section 5.4.

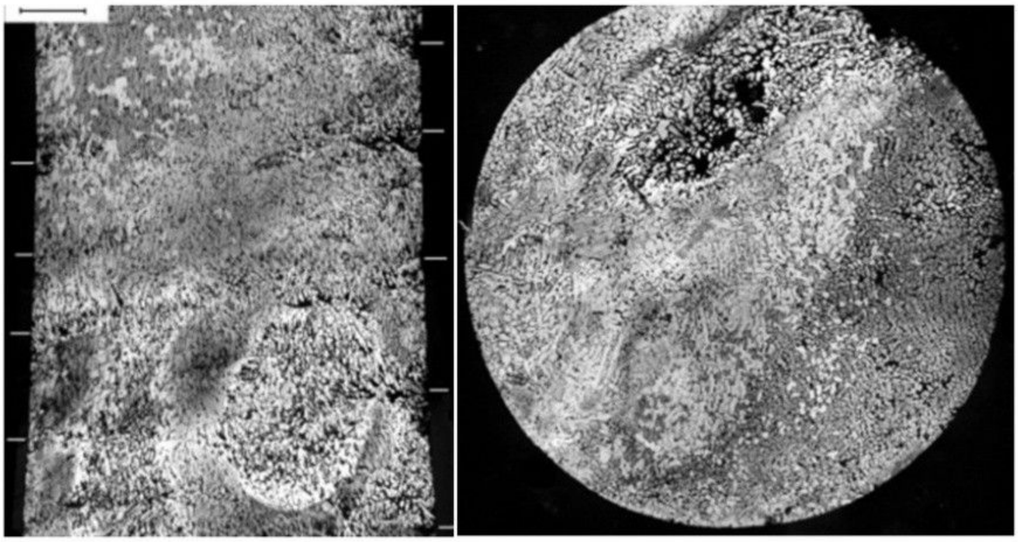

Figure 7.3: Sn-10%wt.Pb solidified at 5 µm/s under rotating transverse magnetic field (B=0.4 T, T=300 s) One field revolution corresponds to 1.5 mm of height

In case of slow magnetic field rotation velocity, measured grain spacing obeys well to this rule, while at faster field rotation spacing is smaller than with static magnetic field because of additional forced convection caused by magnetic stirring.

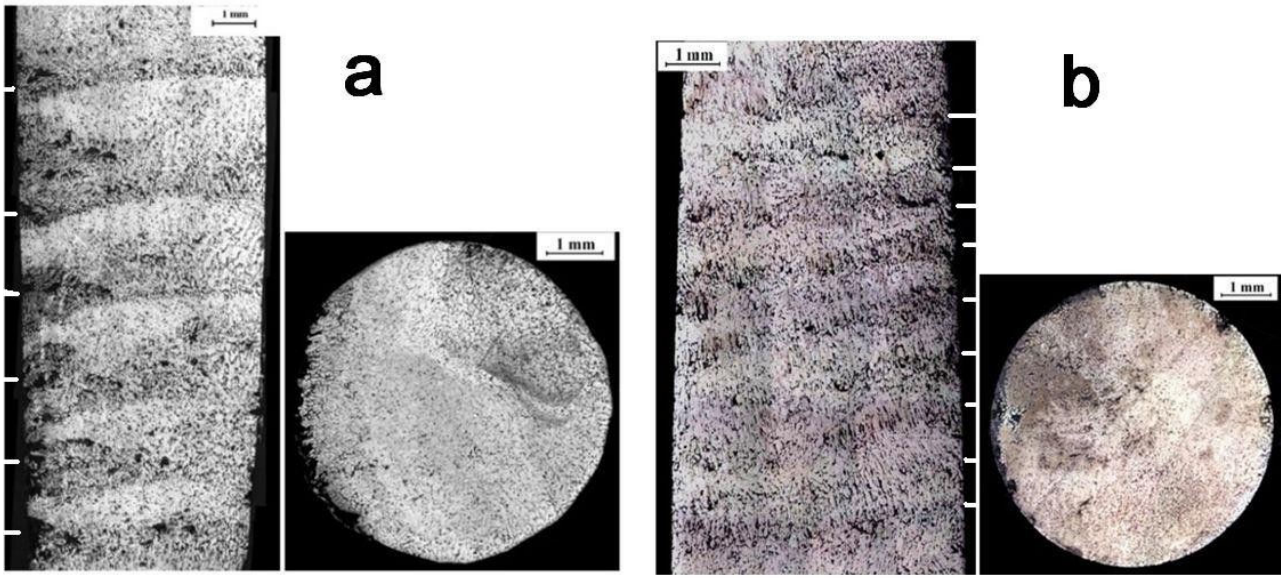

Figure 7.4: a) Sn-10%wt.Pb, *v*=5 µm/s, *B*=0.4 T, *T*=600 s; b) *v*=2 µm/s, *B*=0.4 T, *T*=600 s

From Figure 7.4 it can be seen that in longitudinal cross section macrosegregation pattern is regular and spacing of regularity corresponds to solidified distance during one field rotation period $S=v\cdot T$.

7.4.2. Faster field rotation

Column length is significantly decreased if magnetic field rotation is faster (30-100 s). In this case flow direction changes too fast and macrosegregation in the scale of the crucible is not observed. At such field rotation TEMC velocity is still comparable with magnetic stirring intensity. In the scale of each separate dendrite arm the flow can fully develop while in crucible scale TEMC flow has no time to redistribute melt and energy as magnetic field rotates.

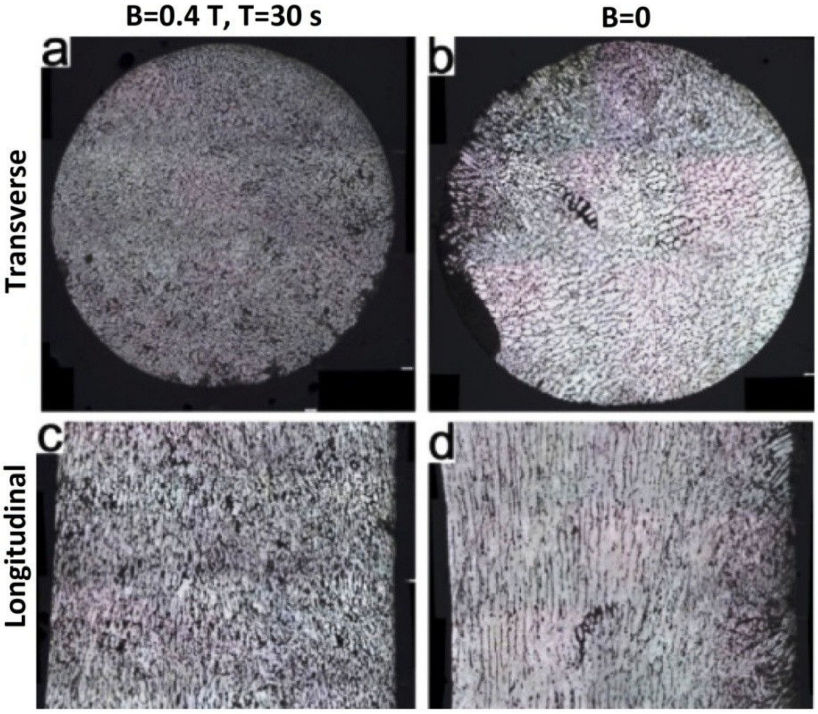

Figure 7.5: Sn-10%wt.Pb solidified at 3 µm/s: a,c) Under rotating transverse magnetic field (B=0.4 T, T=30 s); b,d) Without magnetic field. ($\lambda_{a,c}$=100 and $\lambda_{b,d}$=142 µm)

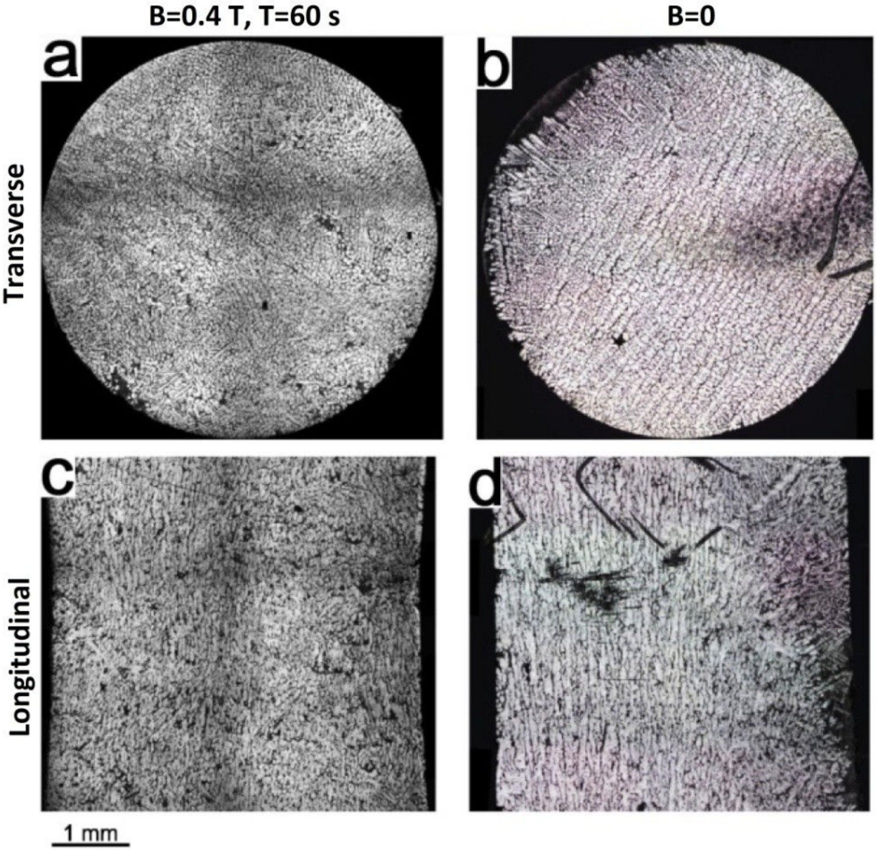

Figure 7.6: Sn-10%wt.Pb solidified at 10 µm/s: a,c) Under rotating transverse magnetic field (B=0.4 T, T=60 s); b,d) Without magnetic field. ($\lambda_{a,c}$=80 and $\lambda_{b,d}$=125 µm)

Two experiments are done with 30 s and 60 s field rotation period. Results do not show macrosegregation and helical structure which would indicate the field rotation is too low.

Figure 7.7 shows optical micrographs of directionally solidified Sn-10%wt.Pb alloy without magnetic field and under 0.4 T rotating transverse magnetic field (*T*=30 s). Without magnetic field (b, d) typical solidification structure was achieved similar like given in Ref. (Cadirli and Gunduz 2000) where dendrite spacing of Sn-Pb alloys as a function of solidification velocity and temperature gradient is extensively investigated. Solidification structure with rotating magnetic shown in Figure 7.7 (a,c) field is homogeneous and macrosegregation was not observed. Primary dendrite spacing is significantly reduced due to influence of magnetic field. Primary dendrite spacing is 142 μm without magnetic field and 100 μm with magnetic field.

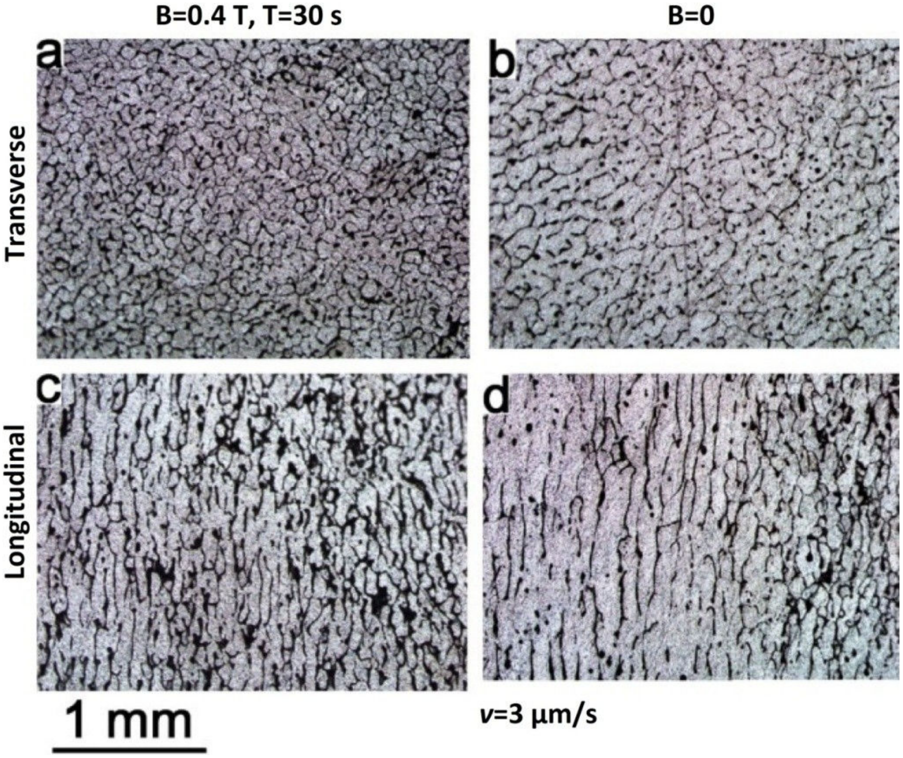

Figure 7.7: Directionally solidified Sn-10%wt.Pb alloy at v=3 μm/s. a,c) With transverse rotating magnetic field (B=0.4 T, T=30s); b,d) Without magnetic field. ($d_{a,c}$=100 and $d_{b,d}$=142 μm)

Rotating magnetic field with period *T*=60 s shows similar effect on the structure compared to case without magnetic field (Figure 7.8). Solidification velocity here is 10 μm/s, which means dendrite spacing is smaller than if solidification is done at 3 μm/s (Figure 7.7) as described by generic law of directional solidification (Lehmann, Moreau and Camel 1998). In presented experiments dendrite spacing is decreased from 125 μm to 80 μm by applied magnetic field. With applied magnetic field columnar structure in much less profound than without magnetic field indicating that also this slow rotating field modifies columnar to equiaxed transition (CET), similar conclusion is done by Eckert (Eckert, et al. 2005).

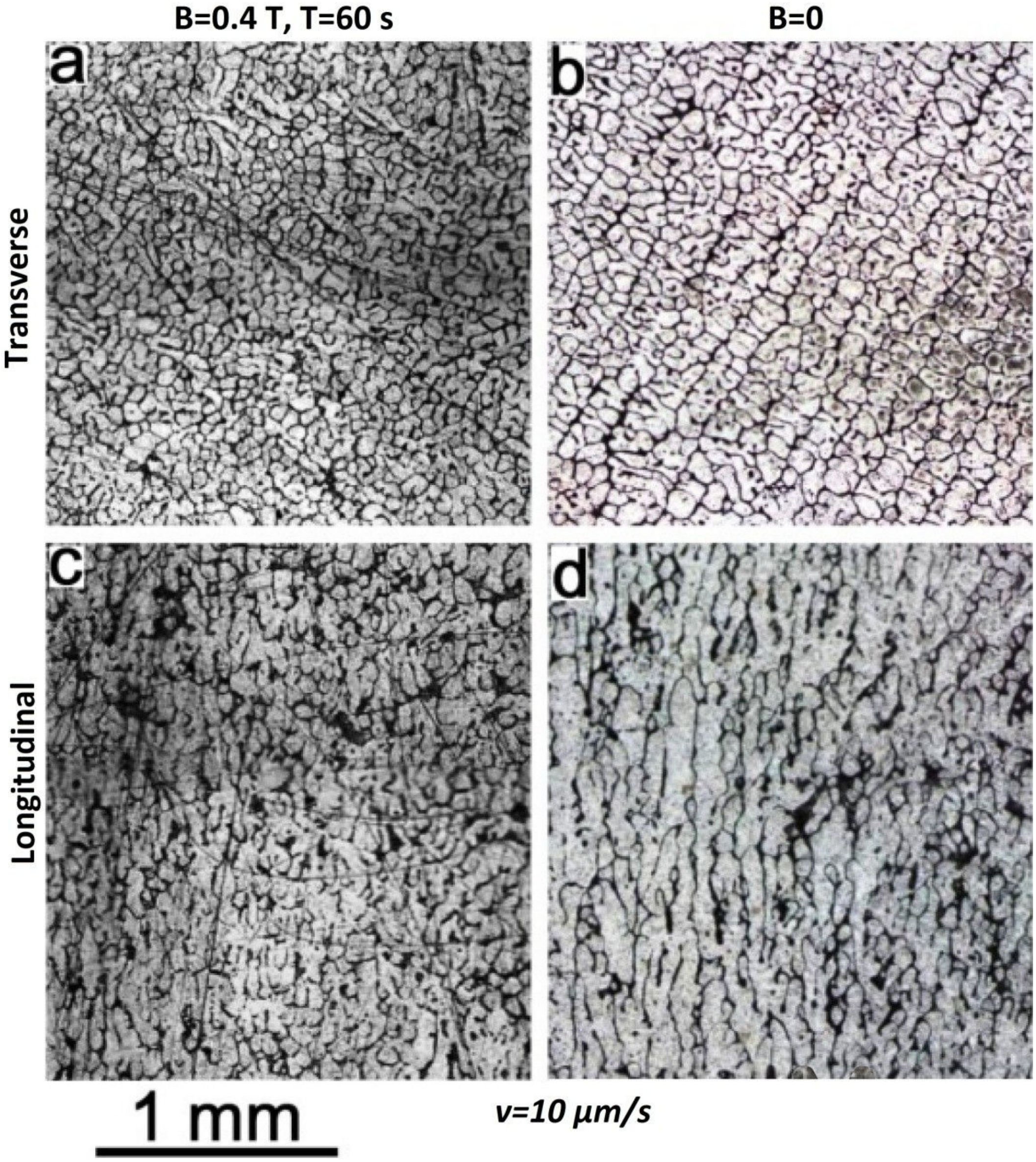

Figure 7.8: Directionally solidified Sn-10%wt.Pb alloy at 10 µm/s. a,c) With transverse rotating magnetic field (*B*=0.4 T, *T*=60s. b,d) Without magnetic field. ($d_{a,c}$=80 and $d_{b,d}$=125 µm)

7.5. Conclusions

Obtained experimental results show that thermoelectromagnetic convection caused by static transverse magnetic field has influence on the macrosegregation on the scale of the crucible. For an alloy Sn-20%wt.Bi this segregation is more profound than for Sn-10%wt.Pb.

Table 7.1: Comparison of directional solidification experiments of Sn-10%wt.Pb alloy under 0.4 T rotating transverse magnetic field (θ=8 K/mm)

Growth velocity v (μm/s)	Magnetic field rotation period T (s)	Characteristic dendrite spacing (μm)	
		B=0.4 T	B=0
2	600	140	192
3	30	100	142
5	600	160	190
5	300	150	190
10	150	90	125
10	60	80	125

All experimental results are summarized in Table 7.1. Characteristic spacing is measured along the two perpendicular diameters of the transverse cross sections. Characteristic size measurements confirm the fact that faster field rotation causes finer grain structure.

In case of rotating magnetic field, characteristic magnetic field rotation period at which electromagnetic stirring is equal with TEMC was estimated to be approximately 150 s for given alloys and experimental configuration. Below this threshold magnetic stirring intensity exceeds thermoelectromagnetic and thus no macrosegregation is observed or it is weak. Whereas experimental results with period of 300 s show clear regular segregation structure with regularity corresponding to growth distance during one magnetic field rotation period (Sn-10%wt.Pb, Sn-20%wt.Bi). As the structure of the ingot must be axially symmetric we may conclude from that distribution of the Bi or Pb rich regions 3D spiral. Segregation intensity, like in experiments with transverse static field, is inversely proportional to pulling velocity. At lower pulling velocity stirring by rotating magnetic field is lower and thermoelectromagnetic convection has more time to develop and follow the field direction.

Influence on the macrosegregation of a directionally solidified Sn-10%wt.Pb alloy, caused by the rotating, transverse magnetic field was observed. If magnetic field rotation is slow enough, 3D spiral shaped component distribution is obtained.

This combination of slow electromagnetic stirring and thermoelectromagnetic convection (TEMC) gives the opportunity to estimate TEMC velocity experimentally by comparing these two effects and finding the critical value at which electromagnetic convection fully eliminates the consequences of TEMC. Estimated TEMC velocity is 0.18 mm/s for crucible scale convection which is reasonable estimation of the same order of magnitude as analytical estimation (eq. (4.12)).

Slowly varying magnetic field can be used to alter the macrosegregation during directional solidification. Unordinary component distribution could be achieved by controlling temperature gradient, field rotation velocity and growth velocity during solidification.

8. Conclusions and future work

8.1. Main conclusions

In this work influence of thermoelectromagnetic convection (TEMC) on the structure of metallic alloys was investigated theoretically and experimentally. Sn-Pb and Sn-Bi alloys were used as a model alloys for experimental work because of their low melting temperature and good thermoelectric figure of merit suggesting that influence on the structure and segregation can be modified with applied magnetic field. One of the problems to accurately describe TEMC phenomena in alloys and chose alloy with optimal properties to achieve intensive TEMC and to demonstrate its influence on the structure is lack of data about thermoelectric properties of alloys in solid and liquid states. Experimental setup for ATP measurements were developed and tested on Sn-Pb and Sn-Bi alloys. Sn-Pb was measured in wide temperature and composition range. It was measured that Sn and Pb has ATP jump during melting in opposite directions, thus at some concentration range differential thermoelectric power between solid and liquid alloy is close to zero. Such alloy will not exhibit any TEMC at the solidification front under applied magnetic field which explains why some authors mention that Sn-Pb alloy shows little effect by applied magnetic field during solidification (Tewary, Shah and Song 1994).

Extensive experimental work was done to investigate influence of static magnetic field on the structure and macrosegregation during directional solidification with various velocities. Sn-Pb and Sn-Bi alloys were directionally solidified at various growth velocities from 0.5 μm/s to 20 μm/s. Influence of static magnetic field on the macrosegregation and microstructure, and columnar to equiaxed transition has been studied. At lower growth velocities influence of magnetic field is greater which can be explained with the fact that TEMC velocity is rather low and in that case TEMC has more time to develop in the size of the crucible. With applied transverse magnetic field macrosegregation along the cross section of the sample takes place. This type of segregation can be well explained by the simple model that TEMC transports solute to one side in the plane perpendicular to magnetic field. At lower growth velocity natural and thermosolutal convection has more influence on the structure. It was analytically shown and numerically confirmed that to achieve maximum flow velocity in the crucible size, quite low magnetic field has to be used. Magnetic field value used in these experiments is 0.4 T, which is close to value at which TEMC is maximum for primary dendrite scale of Sn-Pb alloy.

Axial magnetic field during directional solidification does not create macrosegregation but grain size is reduced and CET is modified by it, and eutectic inclusion concentration in the ingot is reduced. This may be explained by local TEMC at the primary dendrite scale which prevent formation of eutectic inclusions and damped radial flows in the crucible. In strong magnetic field due to this reason ring-like structure was observed (Li, Fautrelle and Ren, et al. 2009). Grain sizing as a function of growth velocity and forced convection caused by applied magnetic field qualitatively agrees with the trend relations given by (Kurz and Fisher, Fundamentals of Solidification 1984).

Influence of the slowly rotating transverse magnetic field has been studied. At low growth and magnetic field rotation velocity interesting results were obtained. 3D spiral component distribution was achieved as a result of TEMC. While higher field rotation showed no such effect, but structure was better (fine grained and without inclusions) than without magnetic field and with static field. Based on these results TEMC velocity can be indirectly estimated by finding threshold field rotation velocity at which TEMC effects in the crucible scale is suppressed by electromagnetic stirring by rotating magnetic field.

It seemed that applied direct electric current through the solidification front combined with magnetic field can induce similar convection of the liquid melt than TEMC. This idea was numerically and experimentally tested in this work. Numerical results showed similar flow patterns. Experiments with DC current and axial magnetic field showed some effect on grain refinement while experiments with transverse field were problematic due to Lorentz force in bulk of the liquid caused by superimposed current and perpendicular magnetic field. Main reason which affected successful experiments in this case was inhomogenity of magnetic field which caused intensive convection, shadowing effects of TEMC. Similarities between such influence and TEMC were not conclusively confirmed.

Experiments by observing solidification of metallic alloys (Sn-Pb, Al-Cu, Al-Si) under magnetic field with X-rays was carried out in European Synchrotron Radiation Facility (ESRF) in Grenoble. These experiments gave an opportunity to directly observe the differences of dendrite growth and liquid phase motion due to magnetic field. Results show differences in dendrite morphology and preferred growth direction caused by applied magnetic field. Obtained results about flow velocity and measured free particle motion are compared with theoretical analysis and numerical simulation results, and seems in agreement with them.

Various numerical simulations are presented in these thesis. As this was mostly experimental work, their aim is only to validate analytical estimations or to help to interpret the experimental results, or to estimate optional experimental parameters to achieve expected physical effects. Numerical modelling of exact TE boundary condition was developed in FLUENT. However because of complexity of this algorithm in most cases approximated solution can be used because difference in most practical cases are small.

8.2. Future work and perspectives

Solidification is a very complex multiphysical process and there are several parallel effects influencing the structure of solidified alloy. In particular circumstances and for each specific alloy different effects can be dominant. In this work TEMC and its combination with electromagnetic force caused by applied electric current and stirring by rotating magnetic field have been studied. Major relations have been studied analytically, numerically and experimentally. Results agree within the order of magnitude. However there are too many experimental parameters which determines solidification, and not all trends can be tested by quantitative series of experimental solidifications.

As a continuation of this work more detailed flow measurements during solidification needs to be done to fully map the TEMC for various cases with different field orientations and solidification front morphology. For quantitative flow analysis and comparison with numerical data direct x-ray solidification observations at various growth velocities and various temperature gradients has to be done. Tracer particles has to be used for better visualization of the flow. Thus direct flow measurements at the real solidification front are difficult due to small sizes of the dendrites, it would be worth to build a scaled up model for flow mapping purposes.

Promising idea about TEMC caused by slowly rotating magnetic field can be developed further by obtaining more experimental results. Helical structure obtained by very slow field rotation is interesting result for quantification of TEMC effects, but more promising for further, deeper investigation is the case when TEMC and stirring is of comparable magnitudes. Results obtained during this work are very promising and further research to deeper analyse this interaction is needed. Detailed experimental session should be done with Sn-Pb and other alloys with different field rotation velocity and growth velocity ratios. Detailed numerical modelling should be done for better estimation of required experimental parameters to better control the range at which TEMC solute transport takes place.

Similar more detailed work can be done for deeper analysis of electric current and magnetic field caused convection on the structure of alloy and macrosegregation. New experimental setup could be developed for research of transverse current and axial magnetic field interaction. To avoid the high force density in whole liquid volume, electrodes could be injected in the melt in specific places close to solidification interface. Such experiments would also allow to perform experiments for description of forced convection influence on solidification in general.

To precisely simulate all physical effects taking place during solidification under magnetic field, complex numerical models can be build based on the experimental and analytical results of this work. Full problem numerical simulation would be very complex due to many parallel physical effects and different feedbacks among them.

- Thermal problem
- electric problem
- liquid flow
- MHD effects due to magnetic field
- solidification of multicomponent alloy
- solute and energy transport

Effects listed above have feedbacks with each other thus all quantities has to be recalculated each iteration. Solution of such problem would require large computing power and specialization in numerical simulations because model has to be done in 3D with fine cell size to correctly describe all different length scales which contribute to the overall physical problem.

Results obtained by direct observation of solidification by X-rays proves the efficiency of this method to investigate dendrite growth during solidification and to analyze melt flow near the solidification front. In experiments described in this work, main drawbacks of are that solidification is done in thin sample holder, thus effects of 3D melt flow cannot be analysed with this setup. 3D analysis can be done by tomography by filming simultaneously from various angles and later combining obtained results. Better visualizing of flow at various magnetic field values should be done to quantitatively analyse dendrite growth as a function of melt flow intensity.

9. Appendix

9.1. Publication produced by this research work

SCI Journals

1. I. Kaldre, Y. Fautrelle, J. Etay, A. Bojarevics, L. Buligins. "Investigation of liquid phase motion generated by the thermoelectric current and magnetic field interaction." *Magnetohydrodynamics*, 2010: Vol. 46, No. 4, pp. 371-380.

2. I. Kaldre, Y. Fautrelle, J. Etay, A. Bojarevics, L. Buligins. "Absolute thermoelectric power of Pb-Sn alloys." *Modern Physics letters B*, 2011: Vol. 25, Iss. 10, pp. 731-738.

3. J. Wang, Y. Fautrelle, Z. Ren , X. Li, H. Nguyen-Thi, N. Mangelinck-Noel, G. Salloum Abou Jaoude, Y. Zhong, I. Kaldre, A. Bojarevics, L. Buligins. "Modification of liquid/solid interface shape in directionally solidifying Al–Cu alloys by a transverse magnetic field." *Journal of materials science*, 2013: Vol. 48, Iss. 1, pp. 213-219.

4. I. Kaldre, A. Bojarevics, Y. Fautrelle, J. Etay and L. Buligins. "Current and magnetic field interaction influence on liquid phase convection." *Magnetohydrodynamics*, 2012: Vol. 48, No. 2, pp. 399-406.

5. J. Wang, Y. Fautrelle, Z. Ren , X. Li, H. Nguyen-Thi, N. Mangelinck-Noel, G. Salloum Abou Jaoude, Y. Zhong, I. Kaldre, A. Bojarevics, L. Buligins. "Thermoelectric magnetic force acting on the solid during directionl solidification under static magnetic field." *Applied physics letters*, 2012: Vol. 101, Iss. 25, 251904.

6. I. Kaldre, Y. Fautrelle, J. Etay, A. Bojarevics, L. Buligins. "Thermoelectric current and magnetic field interaction influence on the structure of directionally solidified Sn-10%wt.Pb alloy." *Journal of Alloys and Compounds*, 2013: Vol. 571, pp. 50-55.

Conference proceedings

1. I. Kaldre, Y. Fautrelle, J. Etay, A. Bojarevics, L. Buligins. "Influence of the slowly rotating transverse magnetic field on the solidification of metallic alloys." *Journal of Iron and steel research international*, 2012: Vol.19. pp. 373-377.

2. J. Wang, Z. Ren, Y. Fautrelle, X. Li, H. Nguyen-Thi, N. Mangelinck-Noel, G. Salloum Abou Jaoude, Y. Zhong, I. Kaldre, A. Bojarevics, L. Buligins. "In-situ analyzing the Influence of Thermoelectromagnetic Convection on the Nucleation ahead of the Advancing Interface during Directional Solidification." *Journal of Iron and steel research international*, 2012: Vol. 19. pp. 381-386.

Conference reports

1. A. Bojarevics, I. Kaldre, Yu. Gelfgat, Y. Fautrelle. "A Sensor for Continuous Measurements of the Absolute Thermoelectric Power of Liquid Metal during Turbulent Non-Isothermal Mixing or Segregation of Multi-Component Melts." PAMIR 2008 conference proceedings, Gieres, France ,September 2008.

2. I. Kaldre, Y. Fautrelle, J. Etay, A. Bojarevics, L. Buligins. "Thermoelectric current and magnetic field interaction influence in the motion of liquid metal." PAMIR 2011 proceedings, Borgo, France, September 2011.

3. I. Kaldre, Y. Fautrelle, J. Etay, A. Bojarevics, L. Buligins. "Investigation of Liquid Phase Motion Generated by the thermoelectric Current and Magnetic Field Interaction." Modelling for materials processing. Riga, Latvia, September 2010.

4. I. Kaldre, A. Bojarēvičs, L. Buligins, K. Kundziņš. "Influence of thermoelectromagnetic convection on macrosegregation of binary alloys." 70th conference of University of Latvia, Riga, Latvia, February 2012.

5. I. Kaldre, Y. Fautrelle, J. Etay, A. Bojarevics, L. Buligins "Influence of the slowly rotating transverse magnetic field on the solidification of metallic alloys." 7th international EPM conference, Beijing, China, October 2012.

6. I. Kaldre, L. Buligins, A. Bojarēvičs. "Rotating magnetic field influence on the solidification of metallic alloys." 71st conference of University of Latvia, Riga, Latvia, January 2013.

9.2. Pictures of experimental results

In this appendix pictures of directional solidification results are presented. All the experiments are done with 6 mm diameter cylindrical samples and temperature gradient of 8 K/mm at the solidification front. Detailed description of experimental setup is given in section 5.2.

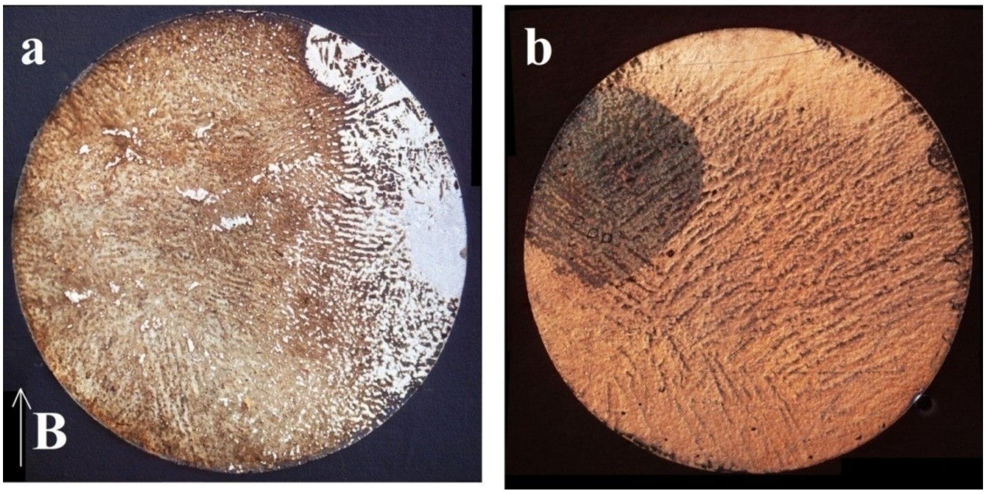

Figure 9.1: Directionally solidified Sn-20%wt.Bi at 5 µm/s (θ=8 K/mm); a) with 0.4 T transverse magnetic field ; b) without magnetic field

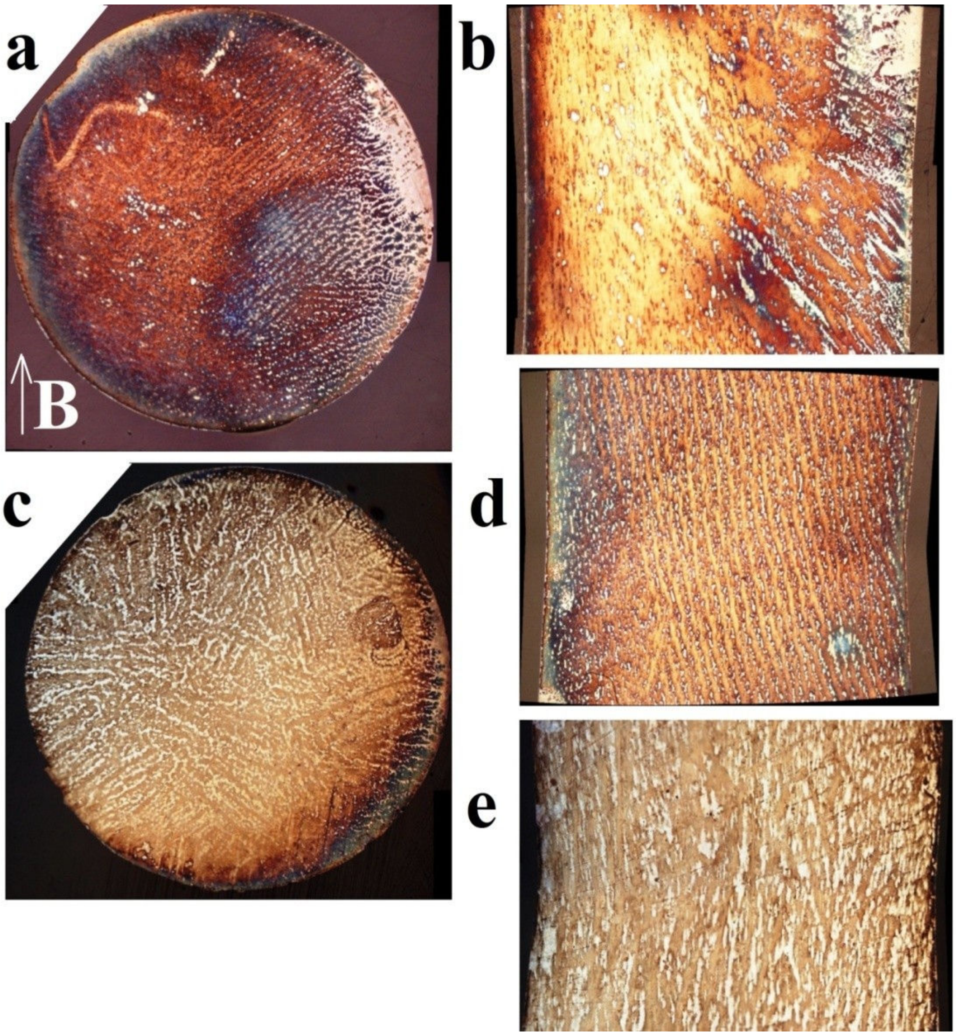

Figure 9.2: Directionally solidified Sn-20%wt.Bi at 10 µm/s (θ=8 K/mm); a,b,d) with 0.4 T transverse magnetic field ; c,e) without magnetic field

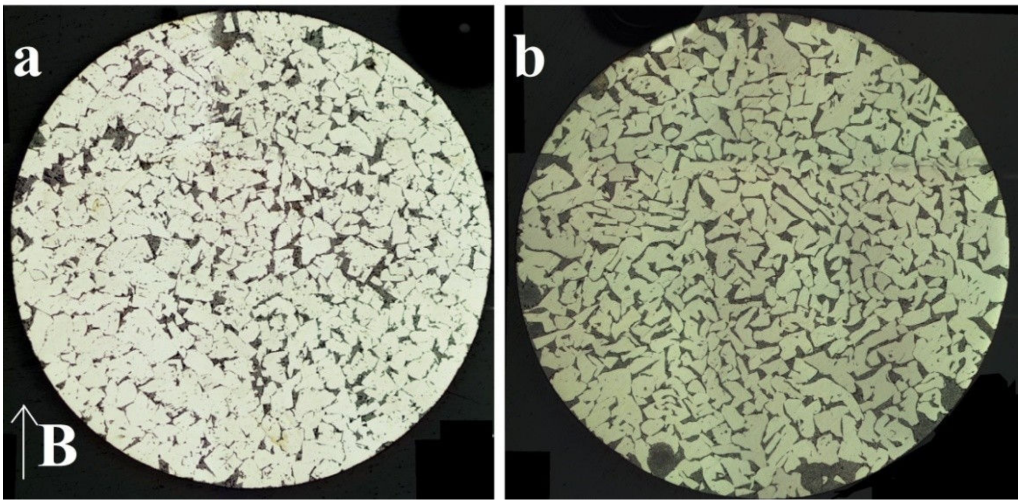

Figure 9.3: Directionally solidified Sn-90%wt.Bi at 10 µm/s, θ=8 K/mm: a) With transverse magnetic field B=0.4 T; b) Without magnetic field

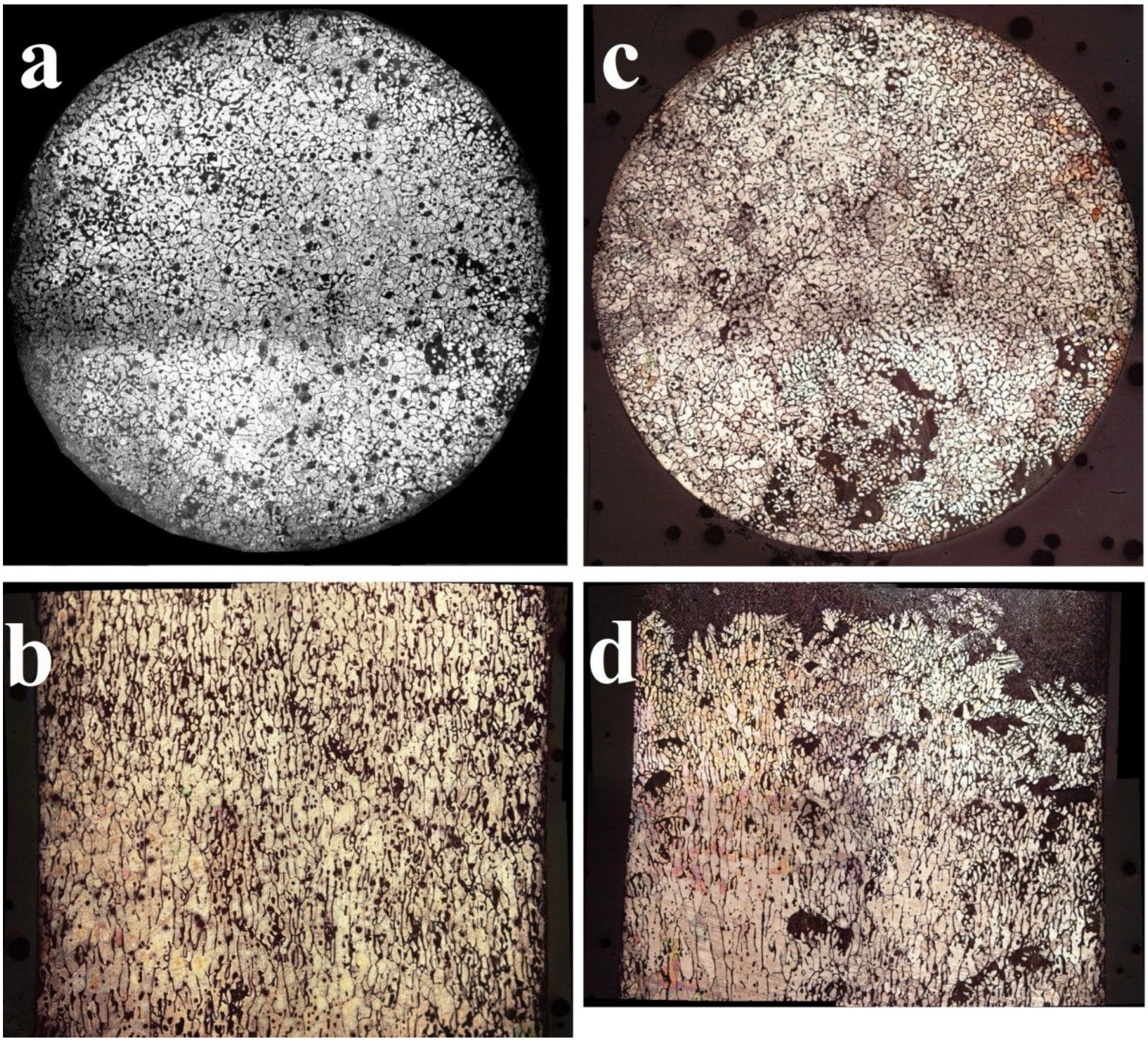

Figure 9.4: Directionally solidified Sn-10%wt.Pb alloy at 2 µm/s: a,b) With axial magnetic field B=0.4 T and electric current j=1 A/mm^2; c,d) With magnetic field but without current

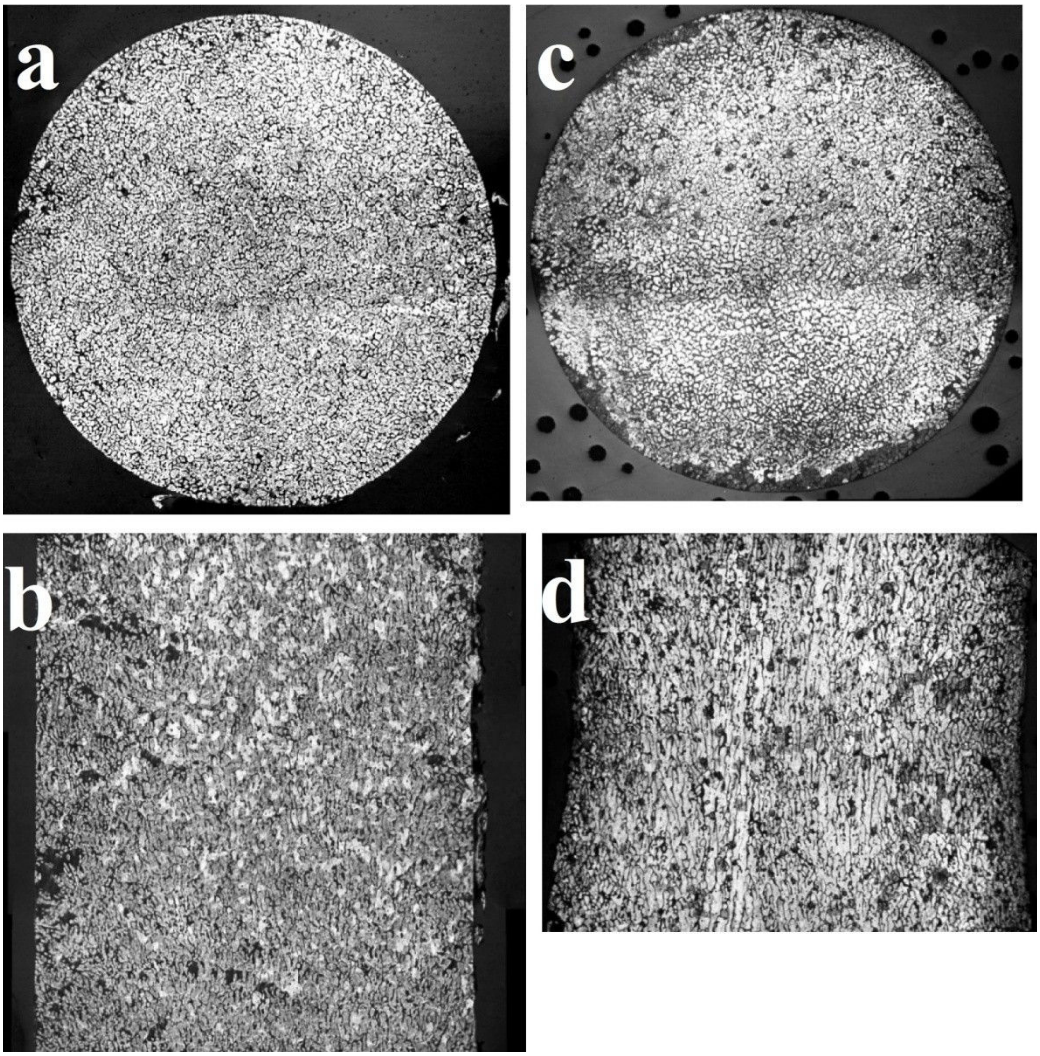

Figure 9.5: Directionally solidified Sn-10%wt.Pb alloy at 10 μm/s: a,b) With axial magnetic field B=0.4 T and alternating electric current j=1 A/mm^2, f=50 Hz; c,d) With magnetic field but without current

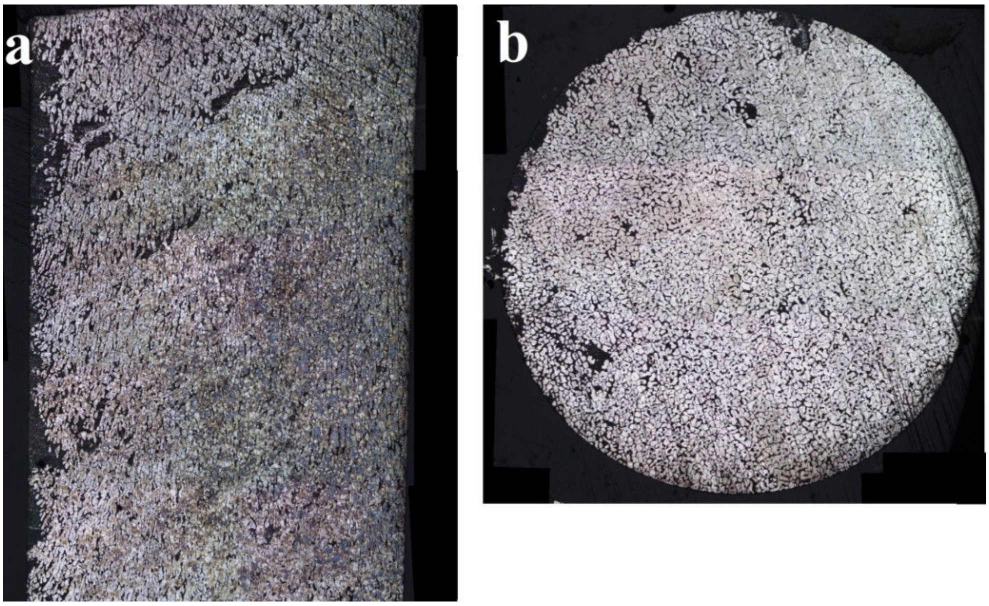

Figure 9.6: Directionally solidified Sn-10%wt.Pb alloy solidified at v=2 μm/s under rotating transverse magnetic field (B=0.4 T, T=150 s)

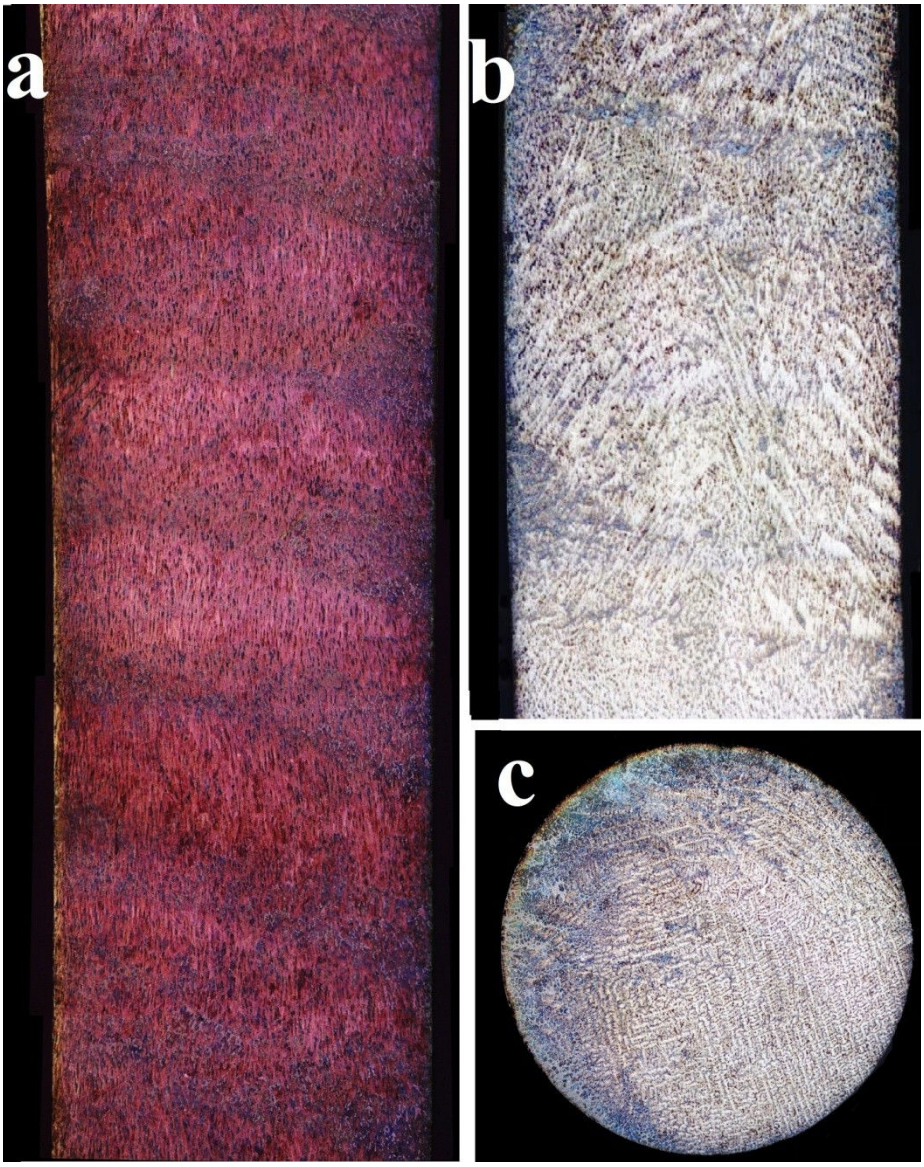

Figure 9.7: Directionally solidified Sn-20%wt.Bi under 0.4 T rotating magnetic field: a) v=10 μm/s, T=300 s; b,c) v=30 μm/s, T=300 s

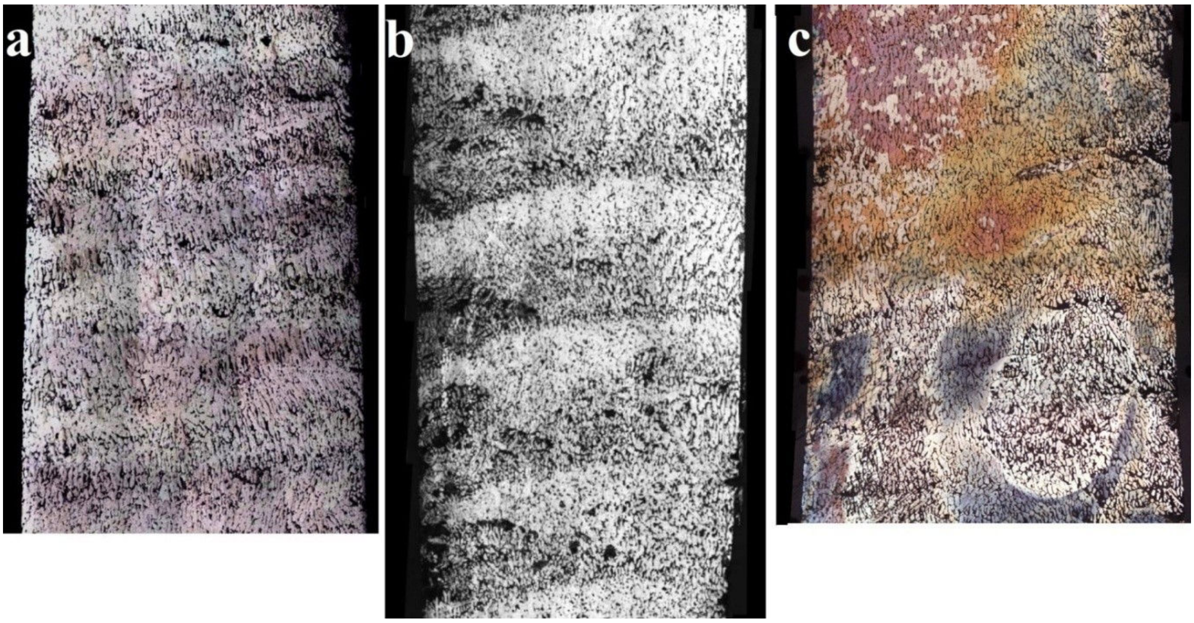

Figure 9.8: Directionally solidified Sn-10%wt.Pb under 0.4 T rotating transverse magnetic field: a) *v*=2 µm/s, *T*=600 s; b) *v*=5µm/s, *T*=600 s; c) *v*=5 µm/s, *T*=300 s

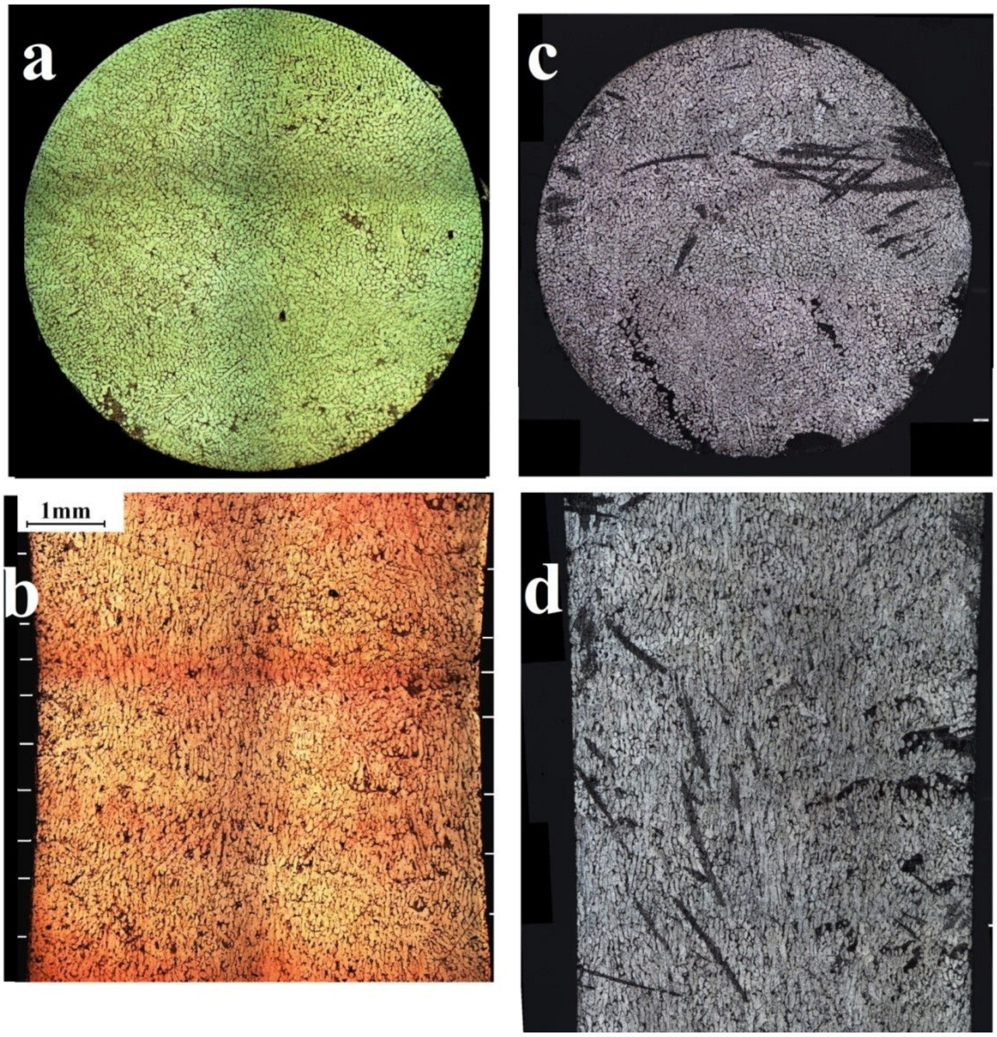

Figure 9.9: Directionally solidified Sn-10%wt.Pb alloy under rotating 0.4 T transverse magnetic field: a,b) *v*=10 µm/s, *T*=60 s; c,d) *v*=5 µm/s, *T*=60 s

Bibliography

1. Anusionwu, B.C, C.A Madu, and C.E Orji. "Theoretical studies of mutual diffusivities and surface properties in Cd-Ga liquid alloys." *Pramana-journal of physics*, 2009: Vol. 72, No. 6, pp. 951-967.

2. Bath, A, and R Kleim. "Apparatus for thermoelectric power measurements on metals an alloys in the liquid state. Application to antimony and cadmium antimony alloys." *Physics Abstracts*, 1979: Vol.14, pp. 595-601.

3. Bogno, A, et al. "In situ analysis of the influence of convection during the initial transient of planar solidification." *Jornal of crystal growth*, 2011: Vol. 318, Iss. 1, pp. 1134-1138.

4. Bojarevics, A. "Experimentl model to investigate the thermoelectromagnetic convection in uniform axial magnetic field." Riga, 2003.

5. Bojarevics, V, and K Pericleous. "Levitated droplet oscillations: Effect of internal flow." *Magnetohydrodynamics*, 2009: Vol. 45, No. 3, pp. 475-485.

6. Brandes, E.A, and G.B Brook. *Smithells metals reference book.* Butterworth Heinemann, 1992.

7. Brush, L.N, and R.N Grugel. "The effect of an electric current on rod-eutectic solidification in Sn-0.9 wt.% Cu alloys." *Materials science and Engineering: A*, 1997: Vol. 238, Iss.1, pp. 176-181.

8. Cadirli, E, and M Gunduz. "The directional solidification of Pb-Sn alloys." *Journal of materials science*, 2000: Vol. 35., pp. 3837-3848.

9. *cfd-online.* 2006. www.cfd-online.com/Wiki/Generic_scalar_transport_equation.

10. Chaib, C. "Contribution a l'etude des proprietes electriques d'alliages metalliques liquides metal noble-polyvalent metal de transition-polyvalent." Thesis, Grenoble, 1987.

11. Chen, M, L.A Rosendahl, and T Condra. "A thee dimensional numerical model of the thermoelectric generators in fluid power systems." *International Journal of Heat and Mass Transfer*, 2011: Vol. 54, pp. 345-355.

12. Croll, A, P Dold, T Kaiser, F Szofran, and K.W Benz. "The influence of static and rotating magnetic fields on heat and mass transfer in silicon floating zones." *Journal of the Electrochemical Society*, 1999: Vol. 146, No. 6, pp. 2270-2275.

13. Cusack, N, and P Kendall. "The absolute scale of thermoelectric power at high temperature." *Proceedings of the physical society*, 1958: Vol. 72, No. 5.

14. Davidson, P.A. *An introduction to Magnetohydrodynamics.* New York: Cambridge University Press, 2001.

15. Davoust, L, F Bertrand, R Moreau, P Tanguy, and R Bolcato. "Recent results on MHD damped convection in the horizontal Brigman configuration." *Magnetohydrodynamics*, 1997, 33 ed.

16. Dupouy, M.D, D Camel, and J.J Favier. "Natural convection in directional dendritic solidification of metallic alloys—I. Macroscopic effects." *Acta Metallurgica*, 1989: Vol.37, Iss.4, pp.1143-1157.

17. Eckert, S, B Willers, P.A Nikrityuk, K Eckert, U Michel, and G Zouhar. "Application of a rotating field during directional solidification of Pb-Sn alloy. Consequences of CET." *Materials science and engineering A*, 2005: Vol.413-414, pp.211-216.

18. Favier, J.J, P Lehmann, J.P Garandet, B Drevet, and F Herbillon. "On the measurements of thermophysical properties during planar front solidification of an Sn-Bi alloy in microgravity: Results of the mephisto-USMP1 Experiments." *Acta materialia*, 1996: Vol. 44, No. 12, pp. 4899-4907.

19. *GaInSn properties.* Moscow: Rare metal institute of soviet union, 1982.

20. Gaoa, M, G.H Hea, F Yanga, J.D Guoa, Z.X Yuanc, and B.L Zhoua. "Effect of electric current pulse on tensile strength and elongation of casting ZA27 alloy." *Materials science and Engineering:A*, 2002: Vol. 337, Iss.1-2, pp. 110-114.

21. Garandet, J.P, and T Alboussiere. "Bridgman growth." *Progress in crystal growth and characterization of materials*, 1999: pp. 73-132.

22. Gasser, J.G. "Understanding the resistivity and absolute thermoelectric power of disordered metals and alloys." *Journal of Physics of Condensed matter*, 2008: Vol. 20, pp.14.

23. Gelfgat, Yu M, L.A Gorbunov, and V Kolevzon. "Liquid metal flow in a finite length cylinder with a rotating magnetic field." *Experiments in Fluids*, 1993: Vol. 15, pp. 411-416.

24. Goldstein, J, D.E Newbury, D.C Joy, C.E Lyman, E Echlin, and E Lifshin. *Scanning Electron Microscopy and X-ray Microanalysis.* New York: Springer, 2003.

25. Gorbunov, L.A, and E.D Lyumkis. "Unique features encountered in the influence exerted by thermoelectromagnetic convection on melt hydrodynamics in the process of monocrystal growth by the czochralski method in a magnetic field." *Magnetohydrodynamics*, 1990, No.2 ed.

26. Gorbunov, L.A. "Effect of thermoelectromagnetic convection on the production of bulk single crystals consisting of semiconductor melts in a constant magnetic field." *Magnetohydrodynamics*, 1987: No. 4, pp. 65-69.

27. Graf, M.J, S.K Yip, and J.A Sauls. "Electronic thermal conductivity and the Wiedemann-Franz law for unconventional superconductors." *Phys. Rev. B 53, 15147–15161*, 1996: Vol.53, pp. 15147-15161.

28. Grigoriev, I.C, and E.Z Melnikov. *Handbook of Physical quantities.* Moscow: pp. 559-567, 1991.

29. Guofa, M, X Pu, and Z Songyan. “Effect of solidification condition on secondary dendrite arm spacing on the A357 alloy under counter-pressure casting.” *Journal of Wuhan university*, 2009: Vol. 24, Iss. 1, pp. 119-122.

30. Herlach, D. *Solidification and Crystallization.* London: Willey, 2004.

31. Hunt, J.D. *Materials science and engineering*, 1984: Vol. 65, pp. 75.

32. Ilin, K. *Steady streaming in a channel with permeable walls.* York: University of York, 2011.

33. *ITS90.* 2000. www.its-90.com/.

34. Kaldre, I, Y Fautrelle, J Etay, A Bojarevics, and L Buligins. "Absolute thermoelectric power of Sn-Pb alloy." *Modern Physics Letters B* 25, no. 10, pp.731-738 (2010): Vol. 25, Nr. 10, pp. 731-739.

35. Kaldre, I, Y Fautrelle, J Etay, A Bojarevics, and L Buligins. "Investigation of liquid phase motion generated by the thermoelectric current and magnetic field interaction." *Magnetohydrodynamics*, 2010: Vol. 46, No. 4, pp. 371-380.

36. Kao A., Pericleous K., Patel M.K., Voller V. “The effects of magnetic fields on crystal growth.” *Pamir conference.* Gierres, France, 2008.

37. Kao, A, and K Pericleous. "A Multiscale method for Thermoelectric MHD in Dendritic Solidification." *Journal of iron and steel research international* (Journal of Iron and Steel Research Interanational) 1, no. pp.317-321 (2012): Vol. 19, pp. 317-321.

38. Kao, A, and K Pericleous. "The effect of secondary arm growth on thermoelectric magnetohydrodynamics." *Magnetohydrodynamics*, Vol. 48, No.2 2012: Vol.48, No.2, pp. 361-370.

39. Kao, A, and K Pericleous. *The Effect of Secondary Arm Growth on Thermoelectric Magnetohydrodynamics.* Borgo, Corsica: 8th Pamir conference, 2011, september 8-13.

40. Kao, A. *Thermoelectric magnetohydrodynamics in dendritic solidification.* dissertation, London: Greenwich University, 2010.

41. Kao, Andrew. “Thermoelectric mgnetohydrodynamics in dendritic solidification.” *Thesis.* London, August 2010.

42. Khalouk, K, C Chaib, and J.G Gasser. "Electrical and thermal conductivities and Seebeck coefficient of liquid copper-bismuth alloys." *Philosophical Magazine & Philosophical Magazine Letters*, 2009: Vol. 89, pp. 249-262.

43. Khine, Y.Y, and J.S Walker. "Thermoelectric magnetohydrodynamic effect during Bridgman semiconductor crystal growth with a uniform axial magnetic field." *Journal of Crystal Growth*, 1998: Vol. 183., pp. 150-158.

44. Kittel, Charles. *Introduction to solid state physics.* New York: John-Willey&Sons, 1996.

45. Kovacs, J, A Ronafoldi, A Kovacs, and A Roosz. "Effect of the rotating magnetic field on the unidirectionally solidified macrostructure of Al6Si4Cu alloy." *Transactions of the Indian Institute of Metals*, 2009: Vol. 62, Iss.4-5, pp. 461-464.

46. Kurenkova, N, E Zienicke, and A Thess. "Influence of the thermoelectric effect on the Rayleigh-Bernard instability inside a magnetic field." *Physical review E*, 2001: Vol. 64, 036307.

47. Kurz, W, and D.J Fisher. *Fundamentals of Solidification.* Lausanne: Trans Tech Publications, 1984.

48. Kurz, W, C Bezencon, and M Gaumnn. "Columnar to equiaxed transition in solidification processing." *Science and technology of advanced materials*, 2001.

49. Lan, C. W. "Recent progress of crystal growth modeling and growth control." *Chemical engineering science*, 2004: Vol. 59, pp. 1437-1457.

50. Lehmann, P Moreau, R, D Camel, and R Bolcato. "Modification of interdendritic convection in directional solidification by a uniform magnetic field." *Acta Materialia*, 1998: Vol. 46, No. 11, pp. 4067-4079.

51. Lehmann, P, R Moreau, and D Bolcato, R Camel. "A simple analysis of the effect of convection on the structure of the mushy zone in the case of horizontal Bridgman solidification Comparison with experimental results." *Journal of Crystal Growth*, 1998: Vol. 183, pp. 22-66.

52. Li Xi, Zhongming Ren,Yves Fautrelle. "Effect of high magnetic fields on the microstructure in directionally solidified Bi–Mn eutectic alloy." *Journal of Crystal Growth*, 2007: Vol. 299, Iss. 1, pp. 41-47.

53. Li, F, L.L Regel, and W.R Wilcox. "The influence of electric current pulses on the microstructure of the MnBi/Bi eutectic." *Journal of Crystal Growth*, 2001: Iss. 1-2, pp. 251-264.

54. Li, J, J Ma, C Song, Y Gao, and Q Zhai. "Columnar to equiaxed transition during solidification of small ingot by using electric current pulse." *Journal of Iron and steel research international*, 2009: Vol.16, pp, 7-12.

55. Li, J, J Ma, S Changjiang, L Zhijun, G Yulai, and Z Qijie. "Columnar to equiaxed transition during solidification of small ingot by using electric current pulse." *Journal of iron and steel research international*, 2009: Vol. 16, pp. 7-12.

56. Li, X Fautrelle, Y. "Influence of thermoelectric effects on the solid-liquid interface shape and cellular morphology in the mushy zone during the directional solidification of Al-Cu alloys under a magnetic field." *Acta Materialia*, 2007: Vol. 55, Iss. 11, pp. 690-704.

57. Li, X, et al. "Columnat-to-equiaxed transitions in Al-based alloys during directional solidification under a high magnetic field." *Journal of crystall growth*, 2010: Vol. 312, pp. 267-272.

58. Li, X, et al. "Effect of a high magnetic field on the morphological instability and irregularity of the interface of a binary alloy during directional solidification." *Acta Materialia*, 2009: Vol. 57, Iss. 5, pp. 1689-1701.

59. Li, X, et al. "Solidification of metallic alloys under magnetic fields." *Transactions of the Indian Institute of Metals*, 2009: Vol.62, Iss.4-5, pp.465-467.

60. Li, X, Z Ren, A Gagnoud, O Budenkova, A Bojarevics, and Y Fautrelle. "Thermo-Electric motion and structures generated by static magnetic fields during the solidification of metallic alloys." *Journal of iron and steel research international*, 2012: Vol. 19, pp. 9-18.

61. Li, X, Z Ren, A Gagnoud, O Budenkova, A Bojarevics, and Y Fautrelle. "Thermo-electric motions and structures generated by static magnetic fields during the solidification of metallic alloys." *Journal of iron and steel research international*, 2012: Vol.19, pp. 9-17.

62. Li, X, Z Ren, and Y Fautrelle. "Effets of the simultaneous imposition of electromagnetic and magnetic forces on the solidification structure of pure Al and Al-4.5wt.%Cu alloy." *journal of Materials Processing and Technology*, 2008: Vol.195, pp.125-134.

63. Liaoa, X, Q Zhaia, J Luoa, W Chena, and Y Gonga. "Refining mechanism of the electric current pulse on the solidification structure of pure aluminum." *Acta Materialia*, 2007: Vol.55, Iss.9, pp.3103-3109.

64. Lie, K.H, J.S Walker, and D.N Riahi. "Free surface shape and AC electric current distribution for float zone silicon growth with a radio frequency induction coil." *Journal of Crystal Growth*, 1990: Vol.100, Iss.3, pp.450-458.

65. Ma, Y, L.L Zheng, and D.J Larson. "Microstucture formation during BiMn/Bi eutectic growth with applied alternating electric fields." *Journal of Crystal Growth*, 2004: Vol.262, pp. 620-630.

66. Marwaha, A.S. "The absolute thermoelelectric power of polyvalent liquid metals." *Advances in physics*, 1967: Vol. 16, Iss. 64, pp. 617-627.

67. Marwaha, A.S, and N.E Cusack. "The absolute thermoelectric power of liquid metals." *Physics letters*, 1965: Vol. 22, No. 5, pp. 556.

68. Mathiesen, R.H, and L Arnberg. "X-Ray Monitoring of Solidification Phenomena in Al-Cu Alloys." *Materials science forum*, 2006: Vol. 508, pp. 69-74.

69. Meeker, D. *www.femm.info.* 24 06 2011. http://www.femm.info/wiki/HomePage (accessed 02 13, 2013).

70. Muller, G, G Neumann, and W Weber. "Natural convection in vertical Bridgman configurations." *journal of crystal growth*, 1984: Vol.70, Iss.1-2, pp.78-93.

71. *National Institute of Standards.* 2010. http://www.nist.gov/index.html.

72. NIST. *www.metallurgy.nist.go.* 1998. http://www.metallurgy.nist.gov/phase/solder/solder.html (accessed 02 19, 2013).

73. Noeppel, A, et al. "Influence of forced/natural convection on segregation during the directional solidification of Al-based binary alloys." *Metallurgical and Materials Transactions B*, 2010: Vol. 41, pp. 193-208.

74. Otto, F, E.K Riegel, and G.A Voth. "Measurements of the steady streaming flow around oscillating spheres using 3D particle tracking velocimetry." *Physics of fluids*, 2008: Vol. 20, Iss. 9, 9 pages.

75. Pascore, G. “The thermo-EMF of tin-lead alloys.” *journal of physics E*, 1976: Vol. 9, pp. 1121-1122.

76. Phillips, R. *Crystals, Defects and Microstructures.* Cambridge: Cambridge University Press, 2004.

77. Polzin, K.A. *Liquid-metal pump technologies for nuclear surface power.* Alabama: Marshall space flight center, 2007.

78. Prescott, P.J, and F.P Incropera. "Magnetically damped convection during solidification of a binary metal alloy." *Journal of Heat Transfer*, 1993: Vol.115, pp.302-310.

79. Rabiger, D, M Leonhardt, S Eckert, and G Gerbeth. "Flow control during directional solidification of SnPb alloys using time-modulated AC magnetic fields." *3rd international conference of advances in solidification processes.* IOP, 2011.

80. *renewable-energy-concepts.* 2012. www.renewable-energy-concepts.com/solarenergy/solar-technology/production-solarcells/bridgman-furnace-process.html.

81. Roplekar, J.K. *A study of solidification with a rotating magnetic field.* ProQuest Dissertations and theses, 1999.

82. Samanta, D, and N Zabaras. "Control of macrosegregation during the solidification of alloys using magnetic field." *International Journal of Heat and mass transfer*, 2006: Vol. 49, pp. 4850-4866.

83. Schroeter, K.H. *IBSmagnet.* 2013. http://www.ibsmagnet.com/fluxdensity/flussdichte_berechnung.php?f=qd (accessed 03 03, 2013).

84. Seifert, W, P Reinshaus, and A Bachran. "Thermosolutal convection during vertcal bridgman growth of semiconductor melts." *Crystal res. technology*, 1998: Vol. 33, Iss. 6, pp. 899-910.

85. Series, R.W, and D.T.J Hurle. "The use of magnetic fields in semiconductor crystal growth." *Journal of Crystall Growth*, 1991: Vol. 113, Iss. 1-2, pp. 305-328.

86. Shen, Y, Z Ren, Xi Li, W Ren, and Y Xi. "Effect of a low axial magnetic field on the primary Al2Cu phase growth in a directional solidified Al-Cu hypereutectic alloy." *Journal of Crystal Growth*, 2011: Vol. 336, pp. 67-71.

87. Shercliff, J.A. “Thermoelectric magnetohydrodynamics.” *Journal of fluid mechanics*, 1979: Vol. 91, part 2, pp. 231-251.

88. Song, C, Y Guo, Y Zhang, H Zheng, M Yan, and Q Han. "Effect of currents on the microstructure of directionally solidified Al-4.5wt%Cu alloy." *Journal of Crystal Growth*, 2011: Vol.324, pp.235-242.

89. Steinbach, S, and L Ratke. "The effect of rotating fields on the microstructure of directionally solidified Al-Si-Mg alloys." *Materials Science and Engineering A*, 2005: Vol. 413-414, pp.200-204.

90. Szekely, J, and P.S Chhabra. "The effect of natural convection on the shape and movement of the melt-solid interface in the controlled solidification of lead." *Metallurgical and Materials Transactions*, 1970: Vol.1, Iss.5, pp. 1195-1203.

91. Tewary, S.N, R Shah, and H Song. "Effect of Magnetic-Field on the Microstructure and macrosegregation in directionally solidified Pb-Sn alloys." *Metallurgical and materials transactions A*, 1994: Vol. 25, pp.1535-1544.

92. *Thermal-Fluids Central.* 2010. https://www.thermalfluidscentral.org/encyclopedia/index.php/One-Dimensional_Steady-State_Convection_and_Diffusion (accessed 02 11, 2013).

93. Usui, M, K Iwai, and S Asai. "Crystal Alignment of Sn–Pb Alloy by Controlled Imposition of a static magnetic field and alternating electric current during solidification." *ISIJ international*, 2006: Vol. 46, pp. 859-863.

94. Vives, C. "Crystallization of aluminum alloys in the presence of vertical electromagnetic force fields." *Journal of Crystall Growth*, 1997: Vol. 173, pp. 541-549.

95. Vives, C. "Solidification of tin in the presence of electric and magnetic fields." *Journal of Crystal Growth*, 1986: Vol.76, Iss.1, pp. 170-184.

96. Vives, C, and C Perry. "Effects of magnetically damped convection during the controlled solidification of metals and alloys." *International Journal of Heat and Mass Transfer*, 1987: Vol30, Iss.3, pp.479-496.

97. Wang, J, et al. "Thermoelectric magnetic force acting on the solid during directional solidification under static magnetic field." *Applied physics letters*, 2012: Vol.101, 251904.

98. Wesseling, P. "Elements of computational fluid dynamics." *Faculty ITC lecture notes.* Delft, 2001.

99. Wettlaufer, J.S, M.G Worster, and H.E Huppert. "Natural convection during solidification of an alloy from above with application to the evolution of sea ice." *Journal of fluid mechanics*, 1997: Vol.344, pp.291-316.

100. Witkowski, L.M, and P Marty. "Effect of a rotating magnetic field of arbitrary frequency on a liquid metal column." *European Journal of Mechanics, B/Fluids*, 1998: Vol. 17, No. 2, pp. 239-254.

101. Xi, Li, Z Ren, and Y Fautrelle. "Effect of a high axial magnetic field on the microstructure in a directionally solidified Al-Al2Cu eutectic alloy." *Acta Materialia*, 2006: 5349-5360.

102. Xiaohua, M, C Changle, H Zhenyu, and W Jianyuan. "Effect of rotating magnetic field on the solidification microstructures of Pb-Sn alloys." *Science in China*, 2006: Vol.49, pp. 274-282.

103. Yasuda, H, et al. "Direct observation of stray crystal formation in unidirectional solidification of Sn–Bi alloy by X-ray imaging." *Journal of Crystal Growth*, 2004: Vol. 262, pp. 645-652.

104. Yasuda, H. "In-situ observation of solidification for understanding EPM-Solidification under a static magnetic field." 2011.

105. Yesilyurt, S, S Vujisic, S Motakef, F.R Szofran, and M.P Volz. "A numerical investigation of the effect of thermoelectromagnetic convection (TEMC) on the Bridgman growth of Ge1-xSix." *Journal of Crystal Growth*, 1999: Vol. 207, pp. 278-291.

106. Yestilyurt, S, S Motakef, R Grugel, and K Mazurk. "The effect of the traveling magnetic field (TMF) on the buoyancy-induced convection in the vertical Bridgman growth of semiconductors." *Journal of Crystall Growth*, 2004: Vol. 263, pp. 80-89.

107. Zhang, X, A Cramer, A Lange, and G Gerbeth. "Model experiments on macroscopic thermoelectromagnetic convection." *Magnetohydrodynamics*, 2009: Vol. 45, No. 1, pp. 25-42.

108. Zide, J.M, et al. "Thermoelectric power factor in semiconductors with buried epitaxial semimetalic nanoparticles." *Applied physics letters*, 2005: Vol.87, Iss.11.

Résumé

Lorsqu'un champ magnétique est appliqué au cours de la solidification directionnelle, une convection dans la phase liquide peut être induite par l'effet thermoélectrique. En effet la présence d'un gradient de température le long du front de solidification peut provoquer la circulation du courant thermoélectrique, qui interagit avec le champ magnétique appliqué pour créer un écoulement (convection thermo électromagnétique-TEMC). Les conditions de transport de soluté et de l'énergie sont affectées par cette convection, donc il y a influence sur l'espacement des dendrites et la macro-ségrégation des composants de l'alliage.

Dans ce travail, l'influence du champ magnétique sur la solidification directionnelle d'alliages métalliques est étudiée. Des travaux expérimentaux de la solidification directionnelle de Sn-Pb et Sn-Bi alliages sont réalisés. La solidification directionnelle dans la configuration Bridgman est effectuée avec ou sans champ magnétique appliqué. L'influence, sur la solidification, du champ magnétique et d'un courant électrique (AC et DC) appliqués est étudiée. Les mouvements du liquide provoquent de fortes macro-ségrégations ainsi qu'un modification des espacements interdendritiques. Les résultats expérimentaux sont interprétés à la lumière d'une modélisation heuristique.

Le cas d'un champ magnétique tournant a été aussi étudié. Ainsi, la valeur de la rotation du champ est choisie pour ralentir assez brassage électromagnétique sans pour autant supprimer les effets de TEMC. À faible vitesse de tirage et faible vitesse de rotation faible champ une macro-ségrégation en forme de spirale a pu être obtenue.

Mots clés: Convection thermoélectromagnétique, Solidification directionnelle, Sn-Pb alliage, Champ magnétique tournant, Puissance thermoélectrique absolu

Thermoelectric current and magnetic field interaction Influence on the structure of binary metallic alloys

Abstract

If magnetic field is applied during directional solidification, liquid phase convection can be induced by means of thermoelectromagnetic effect. Temperature gradient at the solidification front can cause thermoelectric current circulation, which then interacts with field and creates convection (Thermoelectromagnetic convection-TEMC). Solute and energy transport conditions are affected by this convection, thus it influences dendrite spacing and macrosegregation of the alloys.

In this work magnetic field influence on the directional solidification of metallic alloys is studied. Experimental work of directional solidification of Sn-Pb and Sn-Bi alloys is done. Alloys are directionally solidified in Bridgman setup without or with applied magnetic field. Influence on the structure by magnetic field and applied electric current (AC and DC) is studied in this work. Analytical and experimental results are compared and interpreted.

Bridgman solidification under rotating transverse magnetic field is studied as well, field rotation value is chosen to be slow enough that electromagnetic stirring does not fully suppress effects of TEMC. At low pulling velocity and low field rotation velocity spiral shaped component macrosegregation can be achieved.

Keywords: Thermoelectromagnetic convection, Directional solidification, Sn-Pb alloys, Slowly rotating magnetic field, Absolute thermoelectric power measurements